Partitioning of heavy noble gases between planetary reservoirs at high pressure

Qi Chen

To cite this version:

Qi Chen. Partitioning of heavy noble gases between planetary reservoirs at high pressure. Earth Sciences. Sorbonne Université, 2022. English. NNT : 2022SORUS136 . tel-03783505

HAL Id: tel-03783505
https://theses.hal.science/tel-03783505v1

Submitted on 22 Sep 2022

Sorbonne Université

École doctorale Géosciences, Ressources Naturelles et Environnement - ED 398

Institut de minéralogie, de physique des matériaux et de cosmochimie (IMPMC)

Partage des gaz nobles lourds entre réservoirs planétaires à haute pression

Partitioning of heavy noble gases between planetary reservoirs at high pressure

Par Qi Chen

Thèse de doctorat de Géophysique

Dirigée par Chrystèle Sanloup et Hélène Bureau

Présentée et soutenue publiquement le 11 Juillet 2022

Devant un jury composé de:

ANTONANGELI Daniele	Directeur de recherche (CNRS)	Examinateur
BUREAU Hélène	Directrice de recherche (CNRS)	Directrice
BURGESS Ray	Professeur	Examinateur
DANIEL Isabelle	Professeure	Rapporteuse
HAZEMANN Jean-Louis	Directeur de recherche (CNRS)	Rapporteur
SANLOUP Chrystèle	Professeure	Directrice
SCHMIDT Burkhard	Recherche	Examinateur

Acknowledgements

This PhD thesis could not be finished without the support from many people.

I would like to express my deepest appreciation to my PhD supervisors Chrystèle Sanloup and Hélène Bureau, for all their guidance, patience, advice and encouragement, for teaching me knowledge and training me in high pressure fields.

I would also like to thank the rest of the research group, Guozhao Zhang, Fang Xu, Igor Rzeplinski, Bin Zhao, Tobias Grutzner-handke, Francesca Miozzi, Silvia Boccato, Nicki Siersch, Marion Harmand, Daniele Antonangeli and Eglantine Boulard for their wise advice and help.

I also acknowledge:

all the beamline scientists at central facilities and in particular Konstantin Glazyrin (P02.2, DESY); Guoyin Shen (HP-CAT, Advanced Photon Source); Robert Farla (P61B, DESY) and Francesco Capitani (SMIS, SOLEIL),

Imène Esteve and Stéphanie Delbrel for assistance with the SEM analyses, Keevin Beneut for Raman spectroscopy, Yoan Guarnelli for the laser-drilling technique from IMPMC,

Omar Boudouma and Nicolas Rividi from the CAMPARIS centre,

Marta Bellato for assistance with the X-ray tomography from AST-RX.

And lastly, but definitely not the least, I would like to thank my family for their love, support, and encouragement.

Contents

Resume en Francais

Le xénon (Xe) est en déficit dans les atmosphères de la Terre et de Mars par rapport aux autres gaz rares lourds, c'est le paradoxe du Xe manquant. Une possibilité est que le Xe soit stocké dans la croûte inférieure et le manteau supérieur dans les minéraux, fluides et magmas profonds. Pour comprendre la distribution du Xe entre les différents réservoirs terrestres, il est essentiel de connaître les coefficients de partage entre phases en présence, or les valeurs publiées s'étalent sur 7 ordres de grandeur selon les études. Dans cette thèse, nous avons étudié les deux systèmes les plus importants pour le cycle géochimique du Xe: magma/minéraux et fluides/minéraux. Un nouveau protocole basé sur le signal de fluorescence X mesuré en dispersion d'énergie est établi pour mesurer *in situ* le partage du Xe en conditions de hautes pressionss. L'étude du partage du Xe a ainsi été faite pour trois minéraux majeurs de la croûte continentale (plagioclase) et du manteau supérieur (clinopyroxène et olivine) co-existant avec un magma felsique ou basaltique. Dans tous les cas, le Xe se comporte comme un élément compatible, le coefficient de partage le plus élévé étant mesuré pour le système olivine/basalte (89 ± 22) à 1270 ºC, 2 GPa. Le Xe est donc préférentiellement retenu dans les minéraux, et in fine dans les intérieurs planétaires. Dans le cas des fluides, un signal supplémentaire est observé à 3.7 Å dans les fonctions de distribution radiale en cas de dopage au Xe par rapport à l'eau pure. Cette distance suggère un environnement de type clathrate autour du Xe dans le fluide. Le coefficient de partage du Xe entre fluide et feldspath est de 11-13 à 650 ºC, 3 GPa, indiquant un lessivage préférentiel du Xe.

Abstract

Xenon (Xe) is missing from the Earth's and Mars' atmosphere relative to chondritic patterns, known as the 'missing Xe'. Studies support Xe could be stored at depth with planetary materials such as water, quartz, olivine, and in deep crustal melts. However, Xe behaviour during planetary petrological processes is not well known. One major process to infer the distribution of Xe between planetary reservoirs is partitioning. Nevertheless, published Xe partition coefficients, based on the analysis of samples quenched to room conditions, spread over 7 orders of magnitude. In this PhD thesis we focused on two most relevant systems in the framework of Xe geochemical cycle: magma/minerals and fluids/minerals. A new protocol with X-ray fluorescence signal measured in energy-dispersive probes has been established to in-situ measure Xe partitioning at high pressure. Investigation of Xe partitioning between three major Earth minerals of the continental crust (plagioclase) and upper mantle (clinopyroxene and olivine) coexisting with basaltic/felsic melts found Xe is compatible in all minerals, with a highest value of 89 ± 22 for olivine/basaltic melt at 1270 ºC, 2 GPa. Xe is thus preferentially retained in minerals, favouring the very early retention of Xe in planetary interiors. Compared to pure water, an additional Xe-O distance of ~ 3.7 Å in the radial distribution functions was observed in Xe-doped fluids, suggesting that Xe is in a clathrate-like environment in the fluids, different from Xe local environment in minerals and melts. Xe partitioning between fluids and crystal has been quantified of 11-13 at 650 ºC, 3 GPa, indicating Xe being preferentially retained within fluids.

Chapter 1: Introduction

This chapter provides an overview of previous studies of noble gases in solar system for decades, which have a complex story of its inheritance, loss, replenishment and cycle.

Section 1.1 will present basic geochemistry background of the noble gases.

Section 1.2 will review the origin and evolution of noble gases throughout the history of the Earth.

Section 1.3 will discuss the Xe paradox and existent hypotheses.

Section 1.4 will focus on Xe incorporation and distribution behaviour at depth.

1.1. Noble gas geochemistry

The noble gases (He, Ne, Ar, Kr, Xe) are unique tracers for the sources of volatiles to Earth, the mantle convection, the degassing history as well as the evolution of the atmosphere. The inertness of noble gases is the cornerstone of noble gas geochemistry. Thus, their physical properties vary systematically, their abundances within Earth materials are modified only by radioactive decay and physical processes such as melting, diffusion and vapor-phase transport, and their geochemical behavior are easier to predict than that of the major volatiles (e.g., carbon and nitrogen). Moreover, the five noble gases have a variety of stable isotopes (23 in total, Table 1-1) produced by nuclear processes. Their measurable isotopic variations help us to constrain the timing and mechanism of the geochemical evolution of the planet.

Table 1-1

Noble gas isotopes.

Element	Non-radiogenic isotopes	Radiogenic isotopes	Parent isotope	Decay mode	Half-life (Gy)
He	^{3}He	^{4}He	^{232}Th	α	14.001
			^{235}U	α	0.704
			^{238}U^{c}	α	4.468
Ne	^{20}Ne	^{21}Ne	^{232}Th	^{18}O(α, n)^{21}Ne	NA
	^{22}Ne		^{235}U	^{24}O(n, α)^{21}Ne	
			^{238}U	^{24}O(n, α)^{21}Ne	
Ar	^{36}Ar	^{40}Ar	^{40}K	e^{-} capture	1.251
	^{38}Ar				
Kr	^{78}Kr	^{84}Kr (minor)	^{244}Pu	SF	0.082
	^{80}Kr	^{86}Kr^{a} (minor)	^{238}U	SF	4.468
	^{82}Kr				
	^{83}Kr				
	^{84}Kr				
	^{86}Kr				
Xe	^{124}Xe	^{129}Xe^{b}	^{129}I	β^{-}	0.0157
	^{126}Xe	^{131}Xe^{b}	^{244}Pu; ^{238}U	SF	0.082; 4.468
	^{128}Xe	^{132}Xe^{b}	^{244}Pu; ^{238}U	SF	0.082; 4.468
	^{130}Xe	^{134}Xe^{b}	^{244}Pu; ^{238}U	SF	0.082; 4.468
		^{136}Xe^{a,b}	^{244}Pu; ^{238}U	SF	0.082; 4.468

[a] owns the highest production rates for the fission Kr or Xe isotopes; [b] represents fissiogenic isotopes, produced by spontaneous fission of ^{244}Pu or ^{238}U; ^{238}U^{c} is the major U isotope (99.27%). He, helium; Ne, neon; Ar, argon; Kr, krypton; Xe, xenon; Th,

thorium; U, uranium; Pu, plutonium; K, potassium; I, iodine; Mg, magnesium; NA, not applicable; O, oxygen; SF, spontaneous fission (from Mukhopadhyay and Parai, 2019).

Helium

Helium (He), with an extremely low abundance (5.2 ppm by volume) in Earth's atmosphere, is the only element not presently retained by the Earth's gravitational field due to its low atomic weight. ^{3}He is primordial in the Earth's mantle, whereas most terrestrial helium present today (^{4}He) is generated by the natural radioactive decay of heavy radioactive elements (e.g., thorium (Th) and uranium (U)) (Table 1-1). As a result, high ^{3}He/^{4}He ratios can represent a primordial, non-degassed end member (Clarke et al., 1969; Kurz and Jenkins, 1982). For simplicity, He isotope ratios are generally compared to the atmospheric ratio denoted as R/R$_A$, where R is ^{3}He/^{4}He ratio of the sample and R$_A$ is the atmospheric ^{3}He/^{4}He ratio of 1.39×10^6. Compared to the atmospheric value, mantle samples have much higher ratios from 3 to 30 R$_A$ (Fig. 1-1). He isotope ratios in the mid-ocean ridge basalt (MORB) have a notably uniform of 8 R$_A$ (Farley and Neroda, 1998). In contrast to the uniformity for most MORBs, ^{3}He/^{4}He ratio in ocean island basalts (OIBs) vary from 4 to 32 R$_A$ (Sarda and Graham, 1990). The variability of ^{3}He/^{4}He ratio is generally taken as the strongest evidence for a layered mantle (Kaneoka et al., 1983; Allegre et al., 1983, 1995). Particularly, high ^{3}He/^{4}He ratios in plumes have been the cornerstone of models that have invoked convective isolation of the plumes source (Mukhopadhyay and Parai, 2019). To explain the isotopic feature in OIBs, several models have been proposed: (a) the two-layer mantle model (e.g., Allègre, 1987); (2) the basal magma ocean model (e.g., Labrosse et al., 2007; Coltice et al., 2011); and (3) a hidden reservoir such as the D″ layer or outer-core material which could be incorporated in mantle plumes during their formation (e.g., Porcelli and Halliday, 2001, Bouhifd et al., 2013).

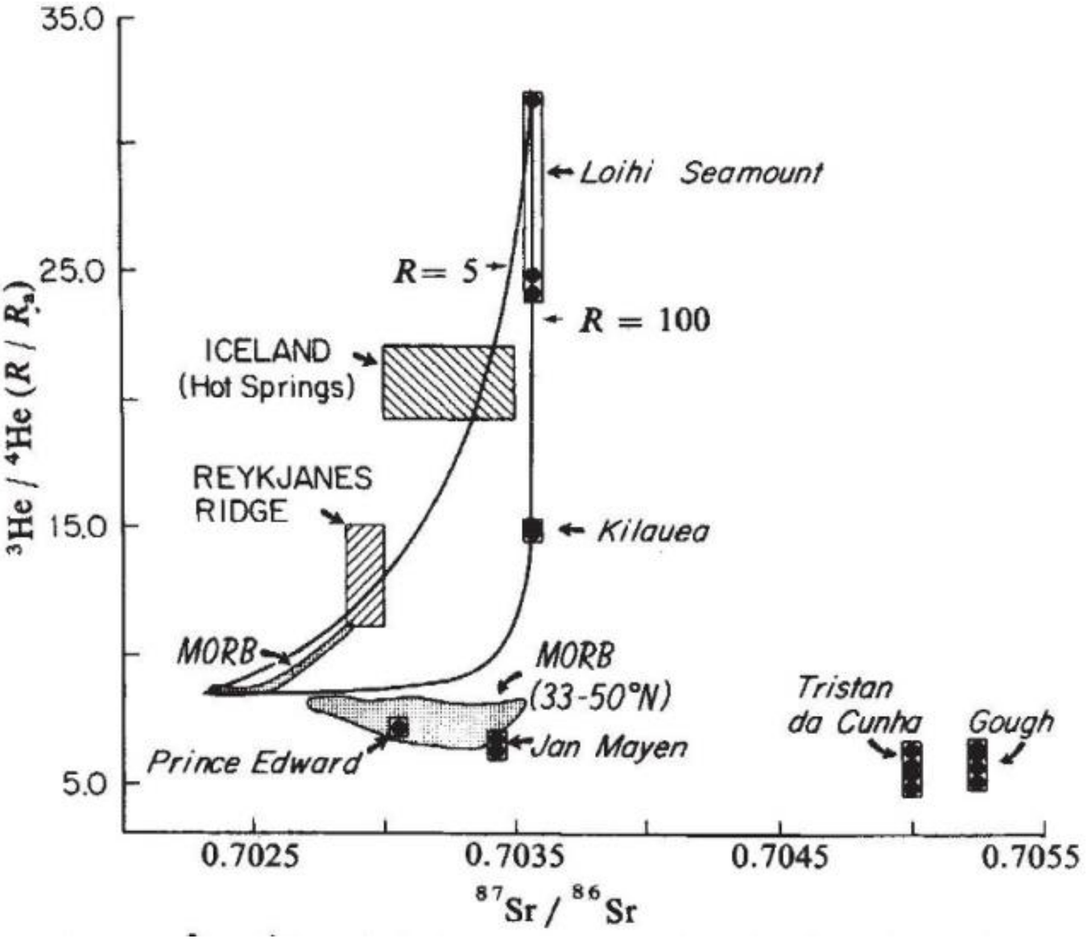

Fig. 1-1. ^{3}He/^{4}He ratio (relative to atmosphere) plotted against ^{87}Sr/^{86}Sr ratio for oceanic volcanic rocks (figure from Kurz and Jenkins, 1982 and refe. in).

Neon

Neon (Ne) has three isotopes: ^{20}Ne, ^{21}Ne and ^{22}Ne. Neon isotope measurements on diamonds (Honda et al., 1987; Ozima and Zashu, 1988), and on submarine volcanic glasses from ridges and islands (Sarda et al., 1988) show that the mantle is characterized by elevated ^{20}Ne/^{22}Ne and ^{21}Ne/^{22}Ne ratios compared to the atmosphere. High ^{21}Ne/^{22}Ne in the mantle result from nuclear production of ^{21}Ne, while the origin of the mantle excess ^{20}Ne remain debatable. ^{20}Ne/^{22}Ne ratio has played a key role in providing constraints on the acquisition of volatiles over the past fifteen years. The ^{20}Ne/^{22}Ne ratio is 13.36 ± 0.09 for nebular Ne (Heber et al., 2012); 12.5 to 12.7 for solar wind irradiated material (Moreira and Charnoz, 2016); 8 for carbonaceous (CI) chondrites (Mazor et al., 1970); 12.49 ± 0.04 for MORB source (Trieloff et al., 2000; Ballentine et al., 2005; Holland and Ballentine, 2006); ~ 13 for plume sources (Sarda et al., 2000; Yokochi and Marty, 2004; Mukhopadhyay, 2012; Péron et al., 2016; Williams and Mukhopadhyay, 2019). The ^{20}Ne/^{22}Ne ratio of plume sources is higher both than that of solar wind irradiation material and CI chondrites (Fig. 1-2), suggesting that volatile accretion started in the presence of nebular gases (persists for ∼10 Myrs) while the Earth was a planetary embryo. The mean time of accretion for Earth is limited to ∼11 Myrs (Yin et al., 2002).

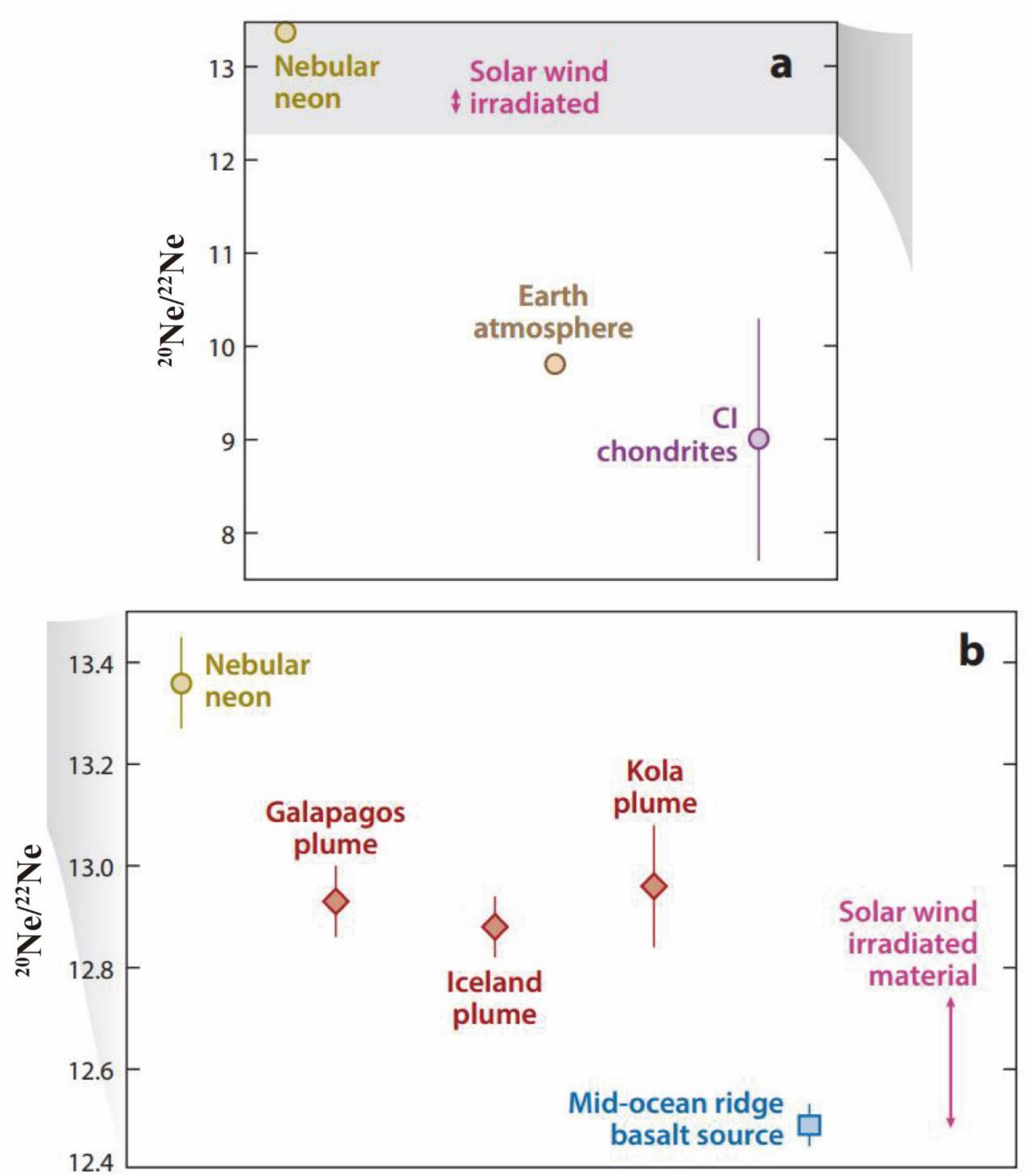

Fig. 1-2. The Ne isotopic composition of (a) solar nebula, solar wind irradiated meteoritic material, CI chondrites, and Earth's atmosphere; compared to the (b) mantle values. The nebular value from Heber et al. (2012); the range of solar wind irradiated material from Moreira and Charnoz (2016); the CI chondrite data from Mazor et al. (1970); The Galapagos, Iceland and Kola plume points represent the highest measured values from these plumes and are from Péron et al. (2016), Mukhopadhyay (2012) and Yokochi and Marty (2004), respectively; The MORB source from Holland and Ballentine (2006) (figure from Mukhopadhyay and Parai, 2019).

Argon

Argon (Ar) has three isotopes: the primordial ^{36}Ar and ^{38}Ar, and radiogenic ^{40}Ar produced by the radioactive decay of ^{40}K. ^{38}Ar/^{36}Ar ratio in the whole mantle (0.188, a primordial signature) differs from the solar composition (0.1818, Meshik et al., 2007), which may indicate a chondritic origin of primordial argon (Moreira, 2013). In addition, measured ^{40}Ar /^{36}Ar ratios range from slightly above the atmospheric value (295.5) to as high as 40000 in MORBs after correction for atmospheric contamination (Sarda et al., 1985; Burnard et al., 1997; Raquin et al., 2008), while less than 10000 in OIBs (Hiyagon et al., 1992; Honda et al., 1993; Trieloff et al., 2000; 2002; Raquin and Moreira, 2009; Mukhopadhyay, 2012), suggesting that OIBs are enriched in primordial isotopes and less degassed than the MORBs.

Krypton

Krypton (Kr) has six isotopes (^{78,80,82,83,84,86}Kr). However, none of Kr stable isotopes is purely radiogenic, with a limited production by Pu and U fission. Kr therefore cannot be used to constrain chronology of the atmosphere evolution, and has been the subject of much less focus compared to He, Ne, Ar, and Xe. Earth atmospheric Kr isotope composition has remained constant since at least 3.3 Gy (Avice et al., 2017), falls in-between solar and chondritic compositions (Pepin, 1991). However, Kr isotopic ratios in CO_2 magmatic well gases, a proxy of deep mantle gases, showed a significant enrichment in ^{84}Kr and ^{86}Kr compared to the atmosphere, indicating a source similar to a primordial chondritic component or a fractionated solar nebula source (Holland et al., 2009). Recent study found the deep-mantle sources have a deficit in the neutron-rich ^{86}Kr relative to the average composition of carbonaceous meteorites, indicative of a nucleosynthetic anomaly (Péron et al., 2021). They proposed that accretion of volatile and refractory elements occurred simultaneously. Besides, mantle-derived basalts (MORBs, OIBs) have an atmospheric Kr isotopic feature (Moreira et al., 1998), probably due to atmospheric Kr recycling at the subduction zones (Holland and Ballentine, 2006).

Xenon

Xenon (Xe) is a particularly challenging element among the other noble gases. It owns nine isotopes, several of which are produced by radioactive decay. The variations in ^{129}Xe/^{130}Xe ratios can be generated only during the first 100 Myr of Solar System history due to the decay of the extinct nuclide ^{129}I, which hence can be used to constrain the timescale of the differences between plume and MORB reservoirs. ^{129}Xe/^{130}Xe ratios in plumes, no more than 6.8 to 7.0, are much lower than that of MORBs of 7.8 to 7.9. The atmosphere has a lower ^{129}Xe/^{130}Xe ratio of 6.49 (Staudacher and Allègre, 1982; Poreda and Farley, 1992; Kunz et al., 1998; Moreira et al., 1998; Sarda et al., 2000; Trieloff et al., 2002; Holland and Ballentine, 2006; Mukhopadhyay, 2012; Parai et al., 2012; Tucker et al., 2012; Peto et al., 2013). High-precision Xe isotopic data in basalt samples from two plumes reflect distinct I/Xe ratios for the plume and MORB sources during the lifetime of ^{129}I (Mukhopadhyay, 2012; Peto et al., 2013), plotted in Fig 1-3. This shows that MORB and plume source compositions are not colinear with the atmospheric composition, thus an air contaminant to a MORB source cannot produce the ^{129}Xe/^{130}Xe ratios in plumes. As a consequence, it indicates a different I/Xe ratio between the two sources, which was set up during Earth's accretion.

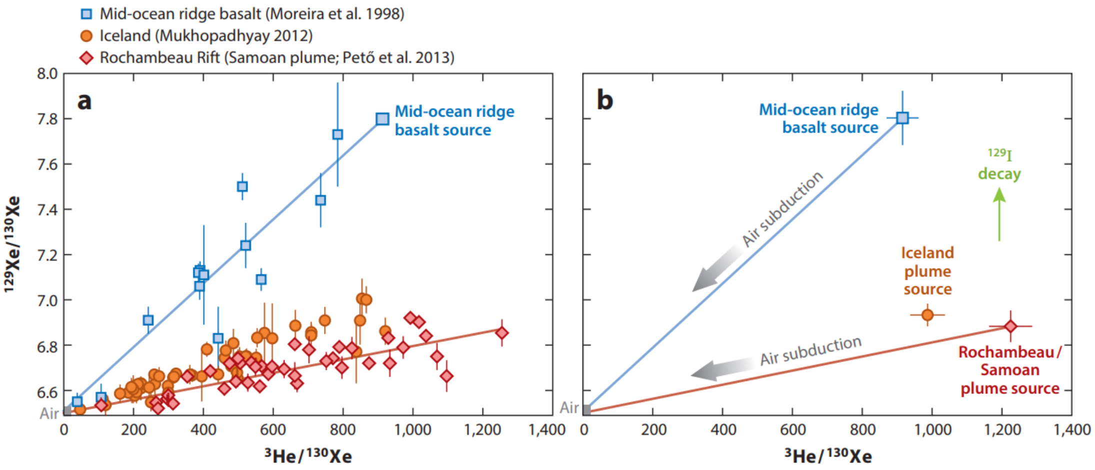

Fig. 1-3. Correlation of ^{129}Xe with ^{3}He for the MORB and the two plume sources. (a) Data from the Mid-Atlantic Ridge MORB compared to data of basalt glass from the Iceland and Rochambeau Rift plumes. (b) Comparison of the MORB source valve with the Iceland and Rochambeau plume sources (figure from Mukhopadhyay and Parai, 2019).

1.2 The origin and evolution of noble gases

1.2.1 Origin of noble gases

The origin of noble gases is a topic of continuing debate. Generally speaking, terrestrial planet formation can be divided into three periods: (1) after collapse of the Solar Nebula, planetesimals accreted and formed planetary embryos in the first 0.1-1 Myr (Chambers et al., 2004); (2) a series of giant impacts happened associated with collisions between embryos, with the last giant impact-Moon forming impact for the Earth (Canup and Asphaug, 2001; Cuk and Stewart, 2012); (3) after the giant impacts, chondritic material was delivered to the Earth by planetesimals, so called 'late veneer' (Drake and Righter, 2002; Albarède, 2009; Wang and Becker, 2013; Genda et al., 2017). Therefore, there are several sources accounting for the origin of Earth's noble gas: (1) the implanted solar wind, (2) solar nebula gas, and (3) a chondritic component and/or a cometary source. Besides, several models have proposed to explain the origin of volatiles on Earth (Péron et al., 2018): (1) the parent body model, (2) the solar nebula gas dissolution model, and/or (3) the late veneer mode.

The Parent Body Model

Some studies suggested that at the initial stage of solar system formation, the light noble gases were implanted onto the Earth's precursors by solar wind irradiation (Trieloff et al., 2000; Ballentine et al., 2005; Kurz et al., 2009; Moreira, 2013; Colin et al., 2015; Péron et al., 2016, 2017). This scenario was developed to explain the mantle Ne isotopic feature due to the similarity between implanted solar wind (not equal to solar wind composition as the implantation process could also trigger isotope fractionation) and the plume source neon composition. Additionally, Earth and enstatite chondrites share a similar isotopic composition (Trinquier et al., 2007; Javoy et al., 2010; Warren, 2011; Dauphas et al., 2014; Piani et al., 2020). This indicates that Earth and enstatite chondrites may origin from a similar reservoir between 0 and 1.5 AU (astronomical unit, equal to the distance from Earth to the Sun) (Dauphas et al., 2014), within the protoplanetary disk susceptible to irradiation by the solar wind (Moreira and Charnoz, 2016). Thus, the solar wind implantation possibly accounts for the origin of a part of mantle noble gases in the first few Myr of the solar system. Indeed, part of solar wind implanted noble gases are presumably lost during accretion. Considering that the abundances of light noble gases in solar wind are higher than in chondrites (Grevesse et al., 2005), only a small fraction of implanted sources is enough to explain the Earth's budget of light noble gases. Such scenario however, cannot explain the atmospheric Ne isotopic composition. Besides, the Earth's noble gases compositions obtained from implantation strongly depends on whether equilibrium was achieved (Moreira and Charnoz, 2016) and possible later gas loss, which are difficult to quantify.

The Solar Nebula Gas Dissolution Model

Alternatively, it is proposed that in the first few Myr, a primordial atmosphere captured by gravity from the solar nebula directly dissolved into a stirring early magma ocean to account for a fraction of Earth's noble gases feature (Mizuno et al., 1980). Although ^{20}Ne/^{22}Ne ratio of plume sources satisfied this hypothesis (cf section 1.1), there is no more signature of nebular gases found elsewhere on Earth. The MORB source Ne are similar to solar wind irradiated materials (Fig. 1-2) (Holland and Ballentine, 2006; Moreira and Charnoz, 2016) and the isotopic ratios of other volatiles (Ar, Kr, Xe, H, N) in the MORB source and in the atmosphere (with the exception of Xe) are similar to chondritic meteorites (Alexander et al., 2012; Marty, 2012; Halliday, 2013; Hirschmann, 2016). These findings may indicate that a majority of captured nebular volatiles have been lost during accretion and later replenished via delivery of chondritic volatiles (Schlichting and Mukhopadhyay, 2018). On the other hand, some volatile elements can possibly have been isolated in the core (Dasgupta et al., 2013; Hirschmann, 2016).

The Late Veneer Mode

The late veneer, with a composition of chondritic material, was firstly proposed to explain the highly siderophile elements of the mantle, accounted for about 0.5 % of the terrestrial mass (Fig. 1-4) (Drake and Righter, 2002; Kleine et al., 2005; Albarède, 2009). Consequently, a large amount of highly volatile elements can be delivered to the Earth. In addition, together with a small fraction of comets, such chondrites-comets components are used to explain the D/H, ^{15}N/^{14}N, and Xe isotopic ratios on Earth (Albarède, 2009; Marty, 2012; Halliday, 2013; Marty et al., 2016, 2017; Schlichting and Mukhopadhyay, 2018; Mukhopadhyay and Parai, 2019). The late veneer hypothesis can also account for the atmospheric ^{20}Ne/^{22}Ne ratio combined with outer solar system sources like carbonaceous chondrites or comets. However, the relatively low N/H ratio on Earth does not match any known solar system source, thus delivering all of the H and N during the late veneer presents a big challenge. Additionally, recent study on ruthenium (Ru) isotopes finds distinct Ru isotopic compositions between Earth's mantle and all chondrites, including carbonaceous chondrites, arguing that the late veneer was not the primary source of volatiles and water on the Earth (Fischer-Gödde and Kleine, 2017). Moreover, Piani et al. (2020) suggested a much smaller input of water from late veneer than if 0.5% of Earth's mass had been accreted.

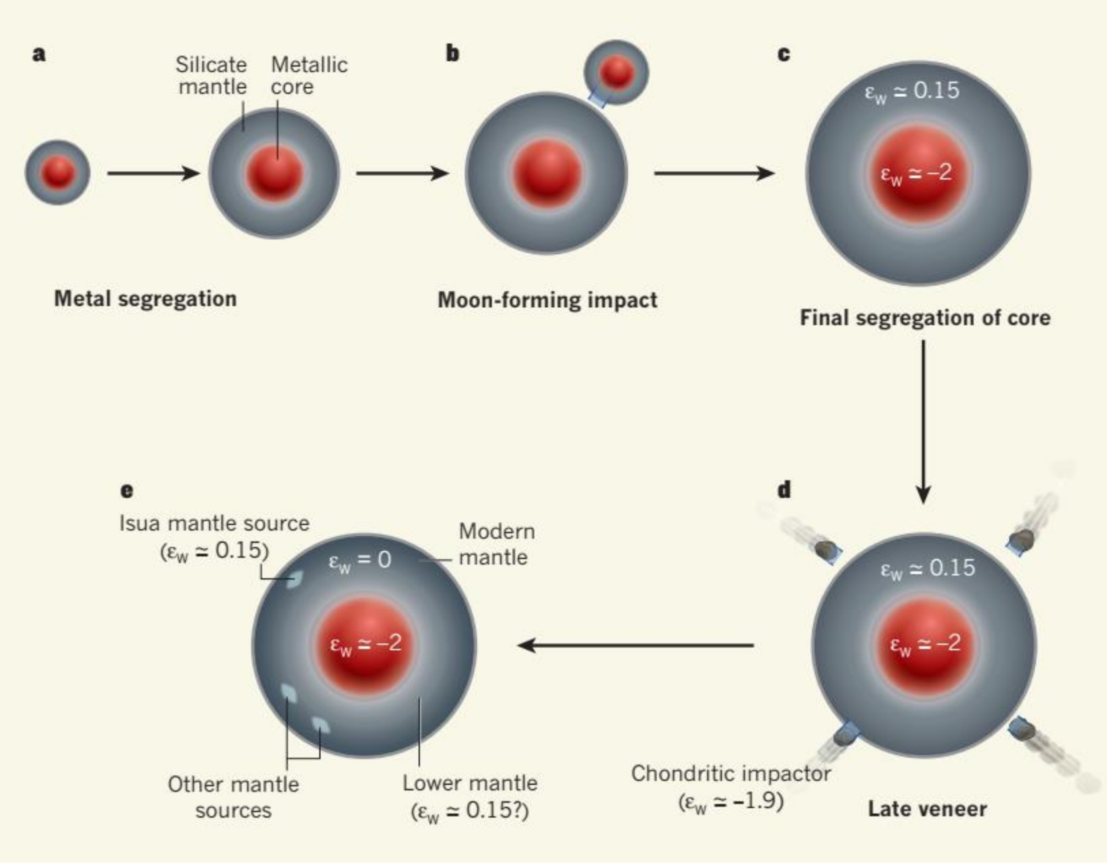

Fig. 1-4. Illustration of the late veneer. εw (ε^{182}w) shows tungsten-isotope enrichment as parts per 10,000 relative to the modern terrestrial mantle, a-c, Accretion and core formation (4.567 billion to about 4.5 billion years ago). d-e, Late accretion (about 4.5 billion to 3.8 billion years ago) following core formation. Note a, siderophiles are removed from the silicate mantle to the metallic core; and d, siderophile elements are replenished in the mantle by a late veneer of chondritic meteorites (figure from Kleine, 2005).

1.2.2 Atmospheric Loss of noble gases

As discussed in section 1.1. evidences suggest the Earth's volatiles loss during the main accretion stage. One mechanism proposed to explain the loss of volatiles is hydrodynamic escape (Pepin, 1991; Dauphas, 2003). Hydrodynamic escape can be used to explain the Xe isotopic composition in Earth's atmosphere. It requires a H-rich atmosphere and high UV flux to ionize elements, which is possible if the proto-Earth's atmosphere inherited from nebular gases (cf section 1.3.2). Kr isotopes would also fractionate during this process, leading to a much greater Kr isotopic fractionation compared to modern atmosphere. To buffer the difference, Earth's mantle has been considered to provide a solar Kr source (Pepin, 1991). However, as mentioned in section 1.1, the discovery of the enrichments of heavy Kr isotopes in deep mantle (Holland et al., 2009) suggests the hydrodynamic escape cannot produce the present volatile budget. Besides, the mass differences between different elements and isotopes require an extreme fine tuning of H_2 for the suspension of the escape (Schlichting and Mukhopadhyay, 2018). Thus, if hydrodynamic escape is real, it must happen in the early history (like embryos stage), where the signature has been overprinted by following geological processes.

Indeed, there is also a hypothesis of impact degassing (Vickery and Melosh, 1990; Ahrens, 1993). Shock experiments show that high-velocity impacts on volatile-rich minerals can cause considerable release of volatiles (Lange and Ahrens, 1982). The Moon-forming impacts that blow off the atmosphere could be a possibility for terrestrial impact degassing. However, there is no available direct evidence. Besides, the impact does not fractionate the isotopes due to the bulk ejection of the atmosphere, whereas the impact-driven losses can fractionate the element due to the different solubilities of the elements between reservoirs. For example, to explain the low $^{3}He/^{22}Ne$ and high $^{20}Ne/^{22}Ne$ ratios in plumes, it has been proposed that global magma oceans were generated from the energetic giant impact phase of planetary accretion (Abe and Matsui, 1985; Stevenson, 1987; Benz and Cameron, 1990; Tonks and Melosh, 1993; Elkins-Tanton, 2008, 2012), and during nebular ingassing into a magma ocean, the $^{3}He/^{22}Ne$

ratio of the magma ocean could be fractionated to 2.3-3 from the nebular composition (~ 1.5) due to different magmatic solubilities of He and Ne (He/Ne ratio ~ 2) (Tucker and Mukhopadhyay, 2014). With multiple magma oceans outgassing and atmospheric loss episodes, the primitive mantle ^{3}He/^{22}Ne ratios eventually increase to the value of depleted mantle (Fig. 1-5.).

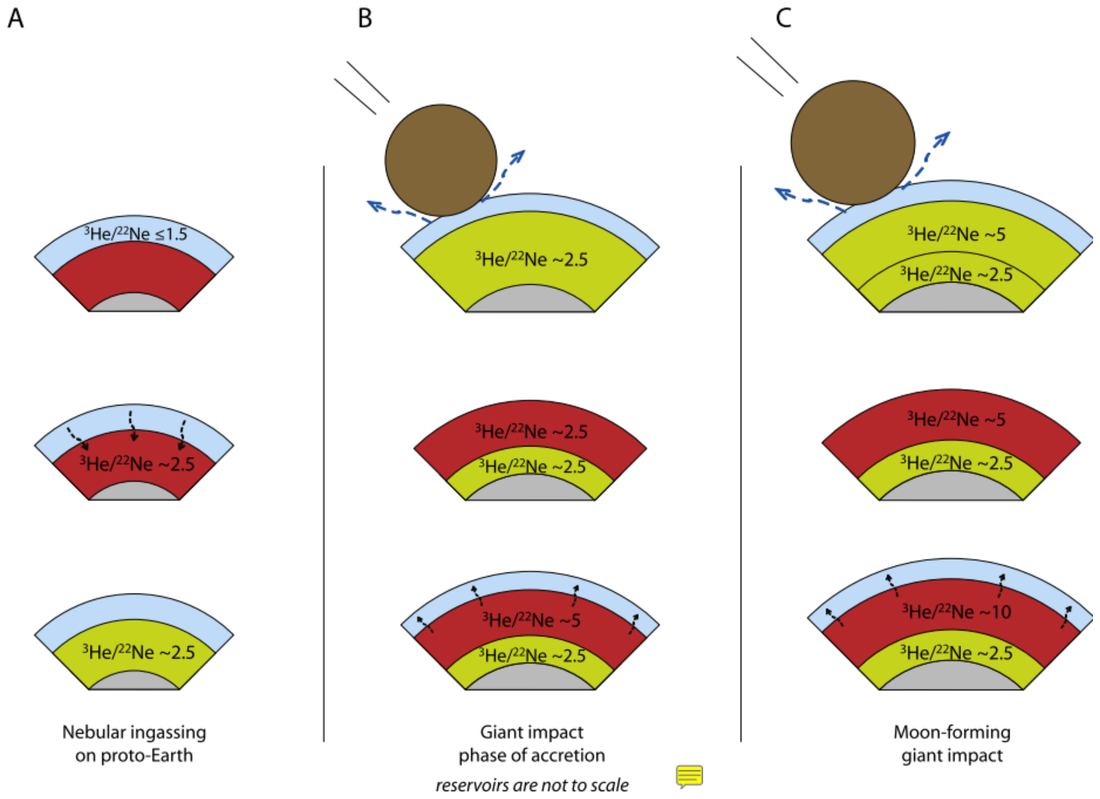

Fig. 1-5. A proposed conservative chronology of events to explain the highly fractionated ^{3}He/^{22}Ne ratio of the depleted mantle. (a) Nebular ingassing. (b) Magma ocean outgassing with a giant impact. (c) Moon-forming giant impact as a second giant impact. Color in blue: atmosphere; in red: magma ocean; in green: solidified magma ocean; in grey: core (figure from Tucker and Mukhopadhyay, 2014).

1.2.3 Degassing and recycling of noble gases

Degassing processes

Degassing processes control the distribution of terrestrial volatile elements from the interior to the surface. For example, at the region of partial melting in MORBs, volatile components (noble gases, H, C, etc.) can be dissolved in the melt due to the high pressure (*P*). As the melt rises to shallow depth, the oversaturated volatiles form gas bubbles in the melt. This less dense gas bubbles move upwards and escape from the melt into surface reservoirs. The partition coefficients thus are crucial to quantify the distribution of elements during this process (cf section 1.4.4). Mantle degassing is normally assumed to be related to (1) the early magma ocean (melt/vapor partitioning, e.g., Zhang and Zindler, 1989) and (2) mantle partial melting (solid/melt partitioning, e.g., Hamano and Ozima, 1978). The former is thought as the principal process for the release of noble gases from the solid Earth into the atmosphere (Ozima and Zahnle, 1993). On the other hand, partial melting is responsible for the continued outgassing of noble gases through geologic time, although at a much less extent than in early Earth history. The discovery of excess of helium in seawater indicates that the mantle is currently degassing (Bieri et al., 1964; Clarke et al., 1969). Plenty of investigations have been carried out to trace the degassing history using noble gas isotopes. Turekian (1959) proposed a continuous degassing model for ^{40}Ar from the solid Earth to the atmosphere assuming the degassing rate is proportional the ^{40}Ar content in Earth. Allegre and coworkers have made great contributions to the understanding of mantle degassing (e.g., Staudacher and Allègre, 1982; Sarda et al., 1985, 1988, 2000; Staudacher et al., 1986, 1990; Allègre et al., 1987; Staudacher, 1987; Staudacher and Allègre, 1989; Moreira et al., 1995, 1996, 1998; Valbracht et al., 1997; Trieloff et al., 2000; Moreira and Allegre, 2002). A multitude of isotopic data including Ne, Ar and Xe have been reported in mantle-derived rocks, and plenty of quantitative mantle degassing models have been developed. Staudacher and Allègre (1982) systematically reported Xe isotopic data in MORB and OIB. By measuring ^{129}Xe/^{130}Xe ratios, they reported a mean degassing time of within the first 10-25 Myr. Sarda et al. (1985) measured Ar isotopic data in MORB and developed a model of a very early and extensive burst degassing with a time constant of 4 Myr, and followed by a slower process to present day type with 0.5 Gy. Allègre et al. (1987) modeled He, Ar and Xe degassing history, finding that half of the Earth's mantle is extensively outgassed, outgassing occurred in an early very intense stage within the first 50 Myr of Earth history and a slow continuous stage which continues to the present day. They gave a similar mean age of the degassed atmosphere of 4.4 Gy as Sarda et al. (1985). Different quantitative degassing models were also developed in the 1980s and 1990s (Ozima, 1975; Hart et al., 1985; Allègre et al., 1987; Zhang and Zindler, 1989; Tolstikhin and O'Nions, 1994; Porcelli and Wasserburg, 1995a, b; Honda and McDougall, 1998). All these models divided the mantle into two parts: a degassed mantle (upper mantle) and a undegassed mantle (low mantle). These models are referred to a closed-system degassing, with a closed bulk silicate earth (BSE) except for the escape of He and early hydrodynamic escape to outer space.

Recycling processes

The noble gases have long been thought to be ineffectively transferred to the mantle during subduction due to their distinct isotopic composition, e.g., Staudacher and Allegre (1988) reported that up to 96% Ar and 98% Xe in altered oceanic crust is removed during subduction to maintain mantle isotopic differences. Later high precision analyses of Xe and Kr isotopes in mantle-derived well gases showed that the elemental abundance pattern of the heavy noble gases in CO_2 well gases (continental natural gases that contain a high abundance of noble gases, e.g., Hennecke and Manuel, 1975b) is remarkably close to that of sea water, distinct from modern air (Holland and Ballentine, 2006). They proposed that the convecting mantle noble gas isotopic and elemental composition can be explained by subduction of sediment and seawater-dominated pore fluids, accounting for up to 80% of current Xe and 100% of non-radiogenic Ar and Kr (Holland and Ballentine, 2006). Besides, measurements on exhumed portions of oceanic and continental lithosphere show that terrigeneous lithologies and hydrated oceanic slab are able to host significant quantities of noble gases (Kendrick et al., 2013, 2015; Baldwin and Das, 2015, Dai et al., 2016, Guo et al., 2017; Syme et al., 2017). Recent experiments on amphibole show that noble gases are strongly fractionated within hot subduction zones, implying that the mantle heavy noble gas inventory is dominated by the injection via cold subduction zones (Syme et al., 2017). In addition, the time of initiation of volatile regassing into the deep Earth was constrained from mantle Xe isotopic composition (Parai and Mukhopadhyay, 2018). Their results indicate that recycling of atmospheric xenon into the deep mantle has occurred 2.5 Gy ago, consistent with the time of 2.8 Gy when the recycling of atmospheric xenon, and likely of other noble gases could have been effective via the analyses of the fissiogenic isotopes ^{131,132,134,136}Xe (Péron and Moreira, 2018).

1.3 The Paradoxes of Xenon

Xenon, the least abundant noble gas, is a key tracer of Earth's dynamics progresses. Xenon isotopes have been wildly investigated for decades, known as Xenology (Staudacher and Allègre, 1982). Due to their non-radioactive origin, the light Xe isotopes (^{124}Xe, ^{126}Xe, ^{128}Xe, ^{130}Xe) can provide unique insight on the evolution of the terrestrial atmosphere (Pepin, 1991, 2006; Ozima and Podosek, 1999; Hébrard and Marty, 2014). In addition, the other Xe isotopes (Table 1-1) are produced by three distinct radiogenic/fissiogenic decays: (1) ^{129}Xe produced by ^{129}I with a half-life of 16 Myr during the formation of solar system; ^{131}Xe, ^{132}Xe, ^{134}Xe and ^{136}Xe produced by (2) ^{244}Pu with a half-life of 82 Myr, which happened during the formation of solar system, either; (3) ^{238}U with a half-life of 4.47 Gy. Interestingly, these three decays cover three key periods in terrestrial evolution: (1) accretion of the nebular; (2) the Archean eon and (3) the whole of Earth history, respectively.

1.3.1 The 'missing Xe' and the Xe paradox

Noble gases abundances from different end-members are summarized on Fig. 1-6a. Chondrites are taken as representative of undifferentiated planets: the isotopic composition as well as relative abundances of noble gases are similar even if the absolute values vary. Atmospheric noble gases on Earth and Mars have a similar elemental pattern as chondrites, except for Xe, which abundance is obviously lower than predicted. That's to say, compared with the chondritic patterns, the ratio of $^{132}Xe/^{84}Kr$ is one order of magnitude lower (Pepin, 1991). This depletion suggests 90% of Xe is missing from the Earth's atmosphere (Ozima and Podosek, 1999), so called the 'Missing Xenon'.

Xenon isotopic compositions for several reservoirs are shown on Fig. 1-6b. The Bravo Dome CO_2 well gases (in New Mexico, USA) was the focus of a mantle noble gas study (Ballentine et al., 2005). CO_2 well gases have probed a primordial component for Xe non-radiogenic isotopes measured with high-precision (Caffee et al., 1999; Holland and Ballentine, 2006). The Xe isotopic composition of this component significantly differs from that of solar wind (close to solar isotopic composition), indicating it cannot be solar but either chondritic or mass-fractionated solar. Martian atmosphere, terrestrial atmosphere and MORB share a similar Xe isotopic composition (Swindle et al., 1986; Moreira et al., 1998; Trieloff et al., 2002) with a depletion in light Xe isotopes compared to chondrites (Krummenacher et al., 1962). The strong mass-dependent fractionation of terrestrial Xe isotopes (enriched in its heavy isotopes relatively to chondrite and solar wind by 3-4 $\%.amu^{-1}$, i.e., atomic mass unit) is the second feature of the so-called 'Xenon Paradox'. On the contrary, terrestrial atmospheric Kr is only fractionated by 1 $\%.amu^{-1}$ (Hébrard and Marty, 2014).

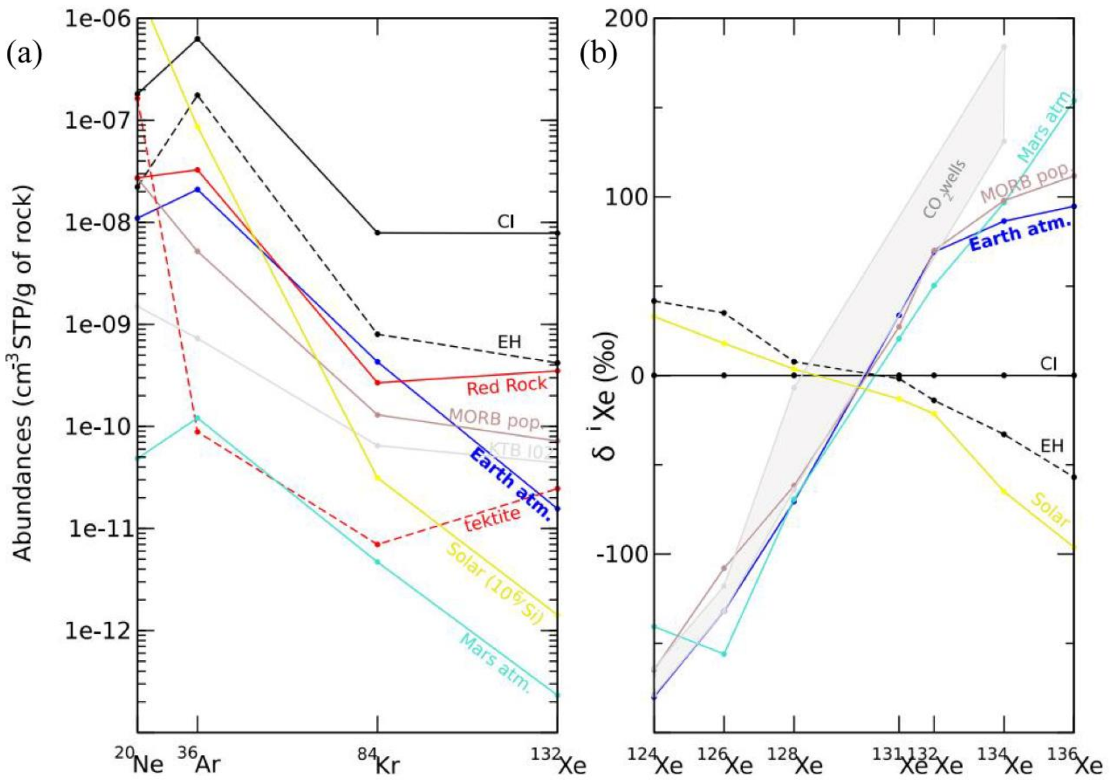

Fig. 1-6. (a) Noble gases patterns. Carbonaceous chondrite (CI) and the solar abundances are taken Lodders (2003); Enstatite chondrite (EH) from Crabb and Anders (1981); Earth atmosphere from Anders and Owen (1977); Mars atmosphere from Hunten et al. (1987); MORB popping rock from Moreira et al. (1998); Sudbury Red Rock granite from Kaneoka et al. (1977); tektites from Palma et al. (1997); and KTB I02 sample from Drescher et al. (1998). (b) Xe isotopic composition normalized to Carbonaceous chondrite (CI). Chondritic reservoirs (CI and EH) from Crabb and Anders (1981); Earth atmosphere from Basford et al. (1973); Mars atmosphere from Swindle et al. (1986); MORB popping rock from Moreira et al. (1998); CO_2 well gases from Holland et al. (2009) and the solar abundances from Lodders (2003) (figure from Sanloup et al., 2011).

Despite the elemental depletion and isotopic fractionation, there is an additional extraordinary characteristic of atmospheric Xe. The Xe isotopic fractionation is mass-dependent, which applies to almost all Xe isotopes except for the excess of ^{129}Xe due to the decay of extinct ^{129}I. However, the two heaviest Xe isotopes, ^{134}Xe and ^{136}Xe are depleted with respect to other Xe isotopes, so called 'U-Xe' component (Pepin, 1991).

U-Xe is close to solar-wind Xe for the $^{124–130}$Xe isotopes but depleted in the heavy Xe isotopes, particularly ^{134}Xe and ^{136}Xe, which has not been clearly identified in meteorites or planetary samples. It has been proposed that additional ~20% cometary Xe to meteoritic Xe may account for this peculiar composition of U-Xe (cf section 1.2.3).

1.3.2 'Missing Xe': Hypotheses

An intriguing feature of Xe isotopes is that samples have been analyzed in fluid inclusions and organic matter in Archean-aged rocks (Pujol et al., 2011; Avice et al., 2017; 2018; Almayrac et al., 2021), showing the isotopic compositions are intermediate between atmospheric and chondritic value (Fig. 1-7). Xe isotopic fractionation was found to be 13.7 ‰.u^{-1} from a 3.5 Gy Barite (Pujol et al., 2009); 10-15 ‰.u^{-1} from 3 ± 0.2 Gy hydrothermal quartz in North Pole, Australia (Pujol et al., 2011); 21 ‰.u^{-1} from a 3.5 Gy barite in the same formation (Srinivasan, 1976); 3 ‰.u^{-1} from deep fluids in the Canadian Precambrian Shield isolated since at least 1.5 Gy (Holland et al., 2013); 12.9 ‰.u^{-1} from a 3.3 Gy quartz in Barberton, South Africa (Avice et al., 2017), 0.5 ‰.u^{-1} from a 0.18 Gy barite in the Belorechenskoe deposit in North Caucasus, Russia (Meshik et al., 2001); and 11 ‰.u^{-1} and 3.4 ‰.u^{-1} from 2.8 and 2.6 Gy barites in the Kalahari Craton in South Africa and Zimbabwe (Almayrac et al., 2021). Specifically, Xe isotopic signatures in Archean-aged samples show that the ancient atmosphere was enriched in light isotopes compared to the present-day composition, and this atmosphere kept evolving, finally reaching the modern-like composition at around 2.1 Gy ago (Avice et al., 2018). Although recent study found a discontinuous evolution at 2.7 Gy in two barites (Matthieu et al., 2021), they could not exclude the possibility for the mass fractionation in barite to be the result of secondary cosmogenic production of light Xe isotopes by spallation reaction, that's to say, the sample may not represent the fractionated Archean atmosphere at all and more sample need to be analyzed in future.

Hydrodynamic escape models

Xe isotope fractionation throughout the Archean could be interpreted with the high UV flux from the young Sun. Compared to other noble gases, Xe has a lower first ionization potential (Hébrard and Marty, 2014; Zahnle et al., 2019). Extreme solar UV photons (e.g., $\lambda < 100$ nm) are able to ionize Xe, which were potentially much more abundant during the Archean and the Hadean eons than today (Ribas et al., 2005). It was proposed that the existence of organic haze in the high atmosphere could preferentially trap heavy Xe^+ isotopes and retain atmospheric Xe^+ heavy isotopes (Hébrard and Marty, 2014). However, this model did not detail the mechanism of how Xe^+ escaped to space. Recent model pointed that the lighter isotopes escaping to space is by escaping hydrogen ions formed by the photo-dissociation of water vapor, which could drag Xe^+ up (Zahnle et al., 2019). Xe escaped as an ion lifted up by H^+ along polar magnetic field lines, requiring both a H-rich atmosphere and high-energy extreme ultra-violet (EUV) irradiation from the young Sun during the Archean eon. However, it remains controversial to explain Xe isotope fractionation throughout the entire Archean eon if the UV flux decreases far more rapidly than Xe isotope fractionation (Figure 1-7).

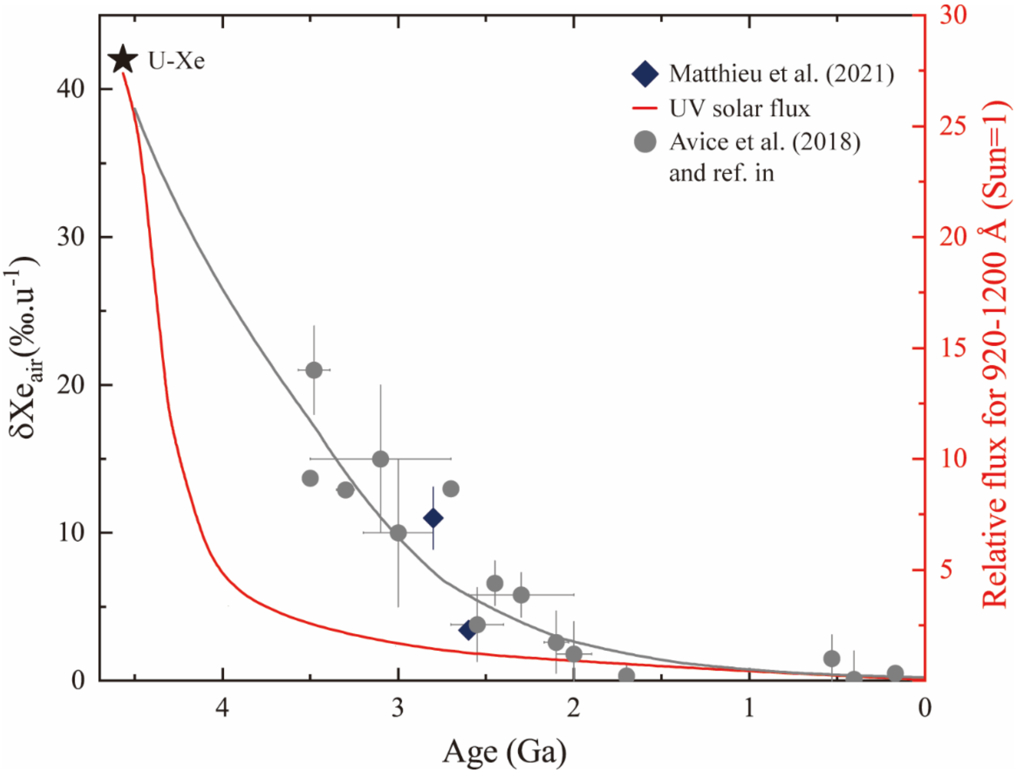

Fig. 1-7. UV solar flux and evolution of the isotopic fractionation of atmospheric Xe (in ‰.u^{-1}) with variable ages. Blue diamonds (Almayrac et al., 2021) and grey circles (Avice et al., 2018 and ref. therein) show Xe isotopic fractionation, with grey black line showing the tendency; red line is solar flux data from Ribas et al. (2005). U-Xe is the initial Xe isotopic composition of the atmosphere (Pepin, 1991).

Cometary distribution

In the non-accretion scenarios, a dual origin of the atmosphere has been proposed (Dauphas, 2003): a solar component (U-Xe) was first fractionated, followed by the addition of cometary components with low Kr/Xe ratio (Marty et al., 2016; 2017). Cometary Xe is found to be depleted in ^{134}Xe and ^{136}Xe isotopes from the analysis of Comet 67P/Churyumov-Gerasimenko by the ROSINA instrument onboard of the Rosetta spacecraft, presumably from sublimation of ice (Marty et al., 2017; Rubin et al., 2018). Combining 22 ± 5% cometary (67P/C-G) Xe and Q-Xe, the composition of U-Xe as well as 6.8 ± 0.3% ^{129}Xe excess observed in the air can be well reproduced (Fig. 1-8). And such a contribution may not have affected the terrestrial D/H ratio

(Marty et al., 2017).

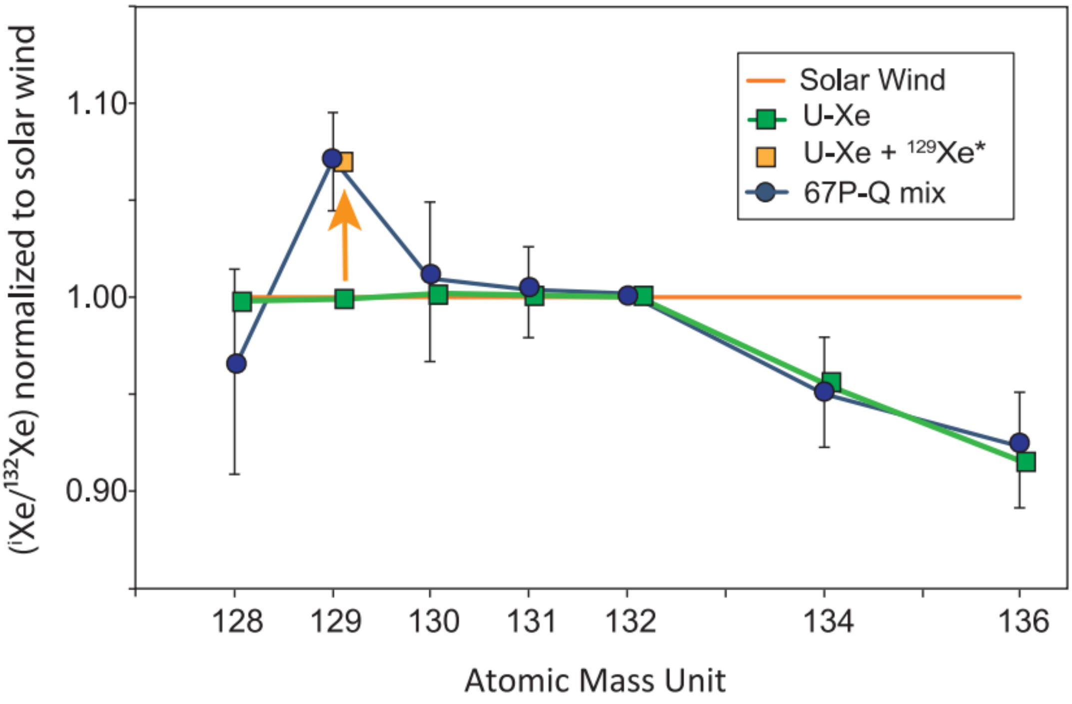

Fig. 1-8. A mix of chondritic and cometary Xe accounts for primordial atmospheric Xe (U-Xe) component. The Xe isotopes are normalized to ^{132}Xe and the solar wind composition (orange line). The U-Xe isotopic composition (green squares) is well reproduced by mixing cometary (67P/C-G) Xe and Q-Xe (67P-Q; dark blue dots). Such mixture can also reproduce the monoisotopic excess of ^{129}Xe in air (orange square) (figure from Marty et al., 2017).

However, Xe trapped in the terrestrial mantle is not U-Xe like but chondritic (Pujol et al., 2011; Broadley et al., 2020), indicating that when comets contributed volatiles to Earth, the mantle was already closed to exchanges with the surface, probably after the Moon-forming event, so called late veneer. Recent study nevertheless suggested that the volatiles, like water, may have been inherited from enstatite chondrite meteorites at the early stage of terrestrial formation (accretion period) rather than accrete anhydrously and acquired volatiles subsequently through late veneer (Piani et al., 2020). In addition, high-precision noble gas isotopic data from volcanic gases in the deep plume mantle (Yellowstone caldera, Wyoming, United States) found Kr and Xe isotopes to be chondritic in origin, similar to the MORB source mantle, while Ne showing the solar isotopic signature (Broadley et al., 2020). Differences in $^{129}Xe/^{124,126,128,130}Xe$ between plume and MORB mantle reservoirs (Mukhopadhyay, 2012) are interpreted as the two reservoirs having experienced limited mixing over the last 4.45 Gy, even during the Moon-forming impact. However, Archean-aged komatiites are depleted in siderophile elements relative to the modern mantle (Marchi et al., 2018), indicating that if siderophile elements added to the Earth during the late veneer, they were progressively mixed by mantle convection rather than directly injected into the deep mantle (Maier et al., 2009). Therefore, the chondritic heavy noble gas component in the deep plume mantle is unlikely to be inherited from chondritic material arriving to Earth during the late veneer. On the contrary, they proposed that the Earth has retained chondritic volatiles throughout accretion and the dichotomy between the main sources of heavy (chondritic) and light (solar) noble gases in the deep mantle was established within the proto-Earth's mantle during the protosolar nebula.

Hidden in the solid Earth

Alternatively, Xe could be retained in the solid Earth, and the three potential reservoirs are notionally described below.

(1) In clathrates and other cage compounds clathrates.

Hydrates have been regarded as carriers of noble gases to the giant planets by a simple adsorption on amorphous ice (Mahaffy et al., 2000). Noble gases hydrates are found to be bonded with H_2O via van der Waals interactions (Villard, 1986) and *P-T* stability conditions extending from He to Xe (Dyadin et al., 1999), with a maximum of 2.5 GPa for Xe hydrates (Sanloup et al., 2002a). Terrestrial clathrate hydrates are found in oceanic margins and pergelisols. However, first attempts to identify significant Xe reservoirs in ices, clathrates, shales and sediments have failed, despite relatively high Xe concentrations in siliceous sediments (Bernatowicz et al., 1984; Matsubara et al., 1988; Matsuda and Matsubara, 1989). The volume of sediments on the Earth is not enough to account for the whole ‘missing Xe’.

(2) In the core.

Besides, Xe was reported to be metallized at 135 GPa (Goettel et al., 1989). Electrical resistivity measurements of purely solid Xe behavior further refined the *P* condition to 155 GPa (Eremets et al., 2000). The first investigation of the Xe-iron system was conducted in 1997, showing no Xe-Fe component formation up to 150 GPa (Caldwell et al., 1997). A great variety of work followed. Ab initio quantum mechanical calculations showed that Xe can be alloyed with hexagonal close-packed (hcp) ε-iron (thought to be stable in the Earth’s inner core) through substitutional incorporation at high *P*, with a favorable enthalpy of formation for the alloy (Lee and Steinle-Neumann, 2006). They suggested that Xe solubility can be up to ~0.8 mol % in the Earth's iron-rich core. Nonetheless, there is no Xe-Fe stable compound reported below 200 GPa, either predicted from theoretical predictions with first-principles calculations (Zhu et al., 2014), or synthesis from high *P* experiments (Stavrou et al., 2018). Despite of a *P*-threshold reduced for Xe-Ni compound $XeNi_3$ to 150 GPa and 1,500 K (Dewaele et al., 2017; Stavrou et al., 2018), taking into consideration that pressure at the center of Mars is only 40 GPa (Rivoldini et al., 2011), Xe reactivity with core materials at extreme conditions cannot explain Xe being missing from both terrestrial and Martian atmospheres.

(3) In the deep crust or mantle.

On the other hand, it has been proposed that Xe could be stored in the deep crust or mantle either in high *P* melts (Leroy et al., 2018) and/or in minerals like quartz (Sanloup et al., 2005, Probert, 2010; Crepisson et al., 2019) and olivine (Sanloup et al., 2011; Crepisson et al., 2018a). Such a scenario could be plausible for ‘missing Xe’ of both Mars and Earth atmosphere due to their similar geologic structure, e.g., the early Mars could also have had a terrestrial-like continental crust (Sautter et al., 2015); and Earth’s upper mantle is similar in *P* conditions to Mars mantle (Rivoldini et al., 2011). We will specifically describe Xe incorporation and distribution in silicates in the next section (cf, section 1.4). As for xenology, a recent study found that Xe isotopic fractionation can be up to +2.3 ± 0.2‰ per a.m.u. in sanidine feldspar and olivine crystals recovered from high *P-T* experiments conducted at 3.5 GPa and up to 1100 ºC (Rzeplinski et al., 2022). This indicates the trapping of Xe in the mantle and primordial felsic crusts as they were formed and reworked during the Hadean with a preferential retention of Xe heavy isotopes, and loss of the released light Xe isotopes enriched fraction along with primary atmospheres.

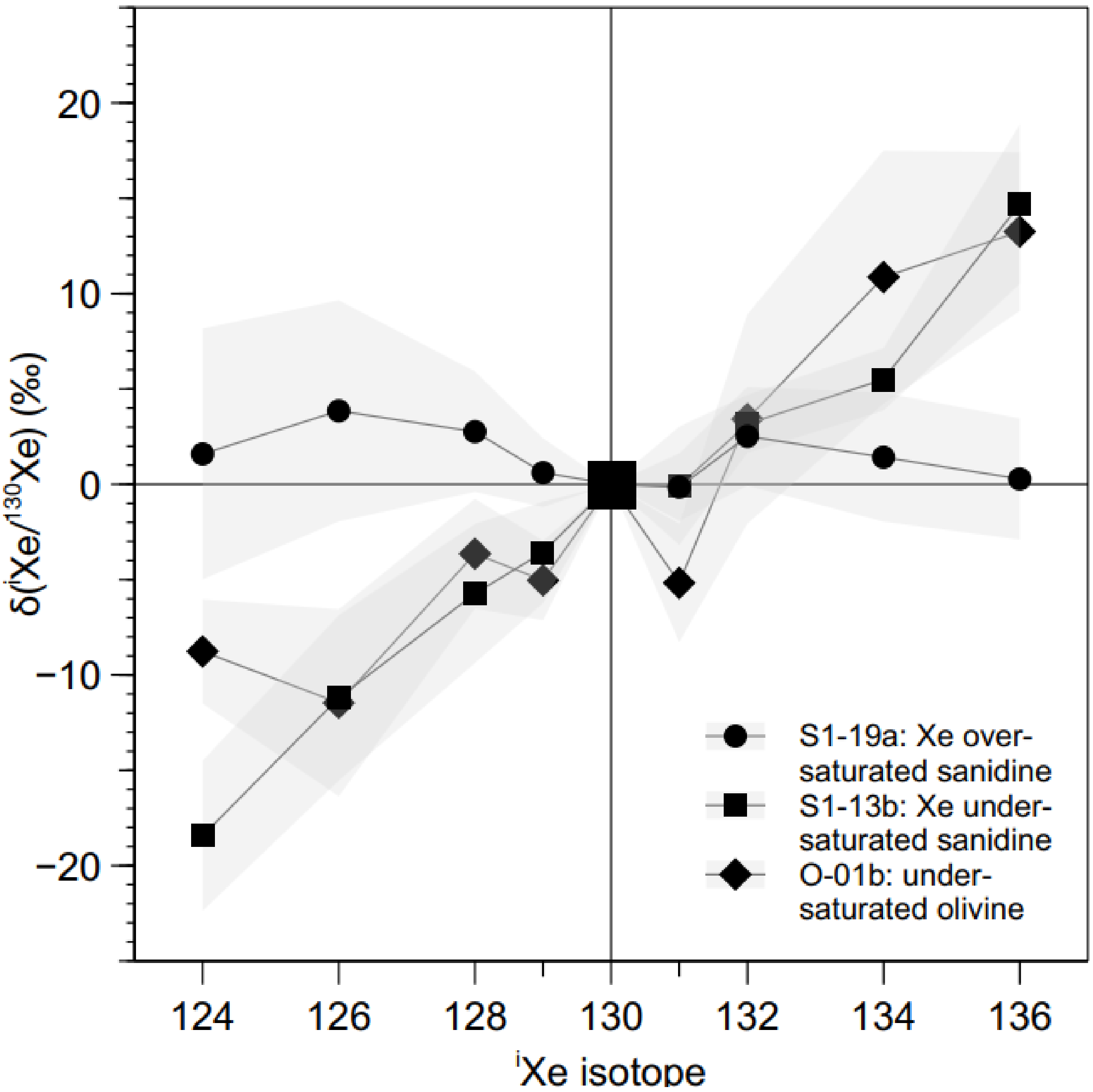

Fig. 1-9. Xenon isotopic data in sanidine feldspar and olivine crystals. Circles represent feldspar loaded with pure Xe gas; squares, feldspar loaded with 1% Xe and Kr enriched air; and diamonds, olivine loaded with 1‰ Xe and Kr enriched nitrogen. All three

samples were brought at 3.5 GPa and 1100°C for 24 h. Grey areas represent the standard error (SE) (figure from Rzeplinski et al., 2022).

1.4 Xe incorporation and distribution in terrestrial materials

Silicates, a large variety of compounds that share a silicon and oxygen structure, make up the terrestrial crust and mantle, with a majority of framework silicates such as quartz and feldspars in the crust, and a majority of olivine in the mantle, which transforms to wadsleyite and ringwoodite in the transition zone, and further decomposes into bridgmanite and magnesiowustite below 660 km (e.g., Ringwood, 1968, 1970; Helffrich, 2000; Chudinovskikh and Boehler, 2001). A lot of efforts have been dedicated into the solubility of Xe in natural samples (Table 1-3).

Table 1-3

Xe/Kr/Ar ratios in natural samples compared to air.

Sample	$^{130}Xe/^{84}Kr$	$^{130}Xe/^{36}Ar$	$\frac{(\frac{^{130}Xe}{^{84}Kr})_{sample}}{(\frac{^{130}Xe}{^{84}Kr})_{air}}$	$\frac{(\frac{^{130}Xe}{^{36}Ar})_{sample}}{(\frac{^{130}Xe}{^{36}Ar})_{air}}$
air	5.63×10^{-3}	1.17×10^{-4}	1	1
CI	0.135	1.49×10^{-3}	24	12.5
EH	0.1	7.15×10^{-4}	17.8	6.1
Mantle samples				
MORB	9.25×10^{-3}	2.2×10^{-4}	1.6	1.9
Bravo Dome fluids	$1.6\text{-}3.0 \times 10^{-2}$	$5.3\text{-}7.5 \times 10^{-4}$	**2.8-5.4**	**4.6-6.4**
Xenoliths	$0.4\text{-}3.8 \times 10^{-2}$	$0.7\text{-}19.7 \times 10^{-4}$	0.7-**6.7**	0.6-**16.7**
Felsic crust				
KTB	$1.9\text{-}90.0 \times 10^{-3}$	$1\text{-}80 \times 10^{-4}$	0.3-**16.0**	0.8-**68.7**
Red rock impact	0.199	0.163	**35.3**	**1395.7**
Tektites	0.529	4.17×10^{-2}	**94.0**	**357.2**
Lunar anorthosite	$1.6\text{-}11.9 \times 10^{-2}$	$1.3\text{-}25.8 \times 10^{-3}$	**2.9-21.1**	**11.1-220.5**

CI, carbonaceous chondrites; EH, enstatite chondrite. Ratios are from abundances given in mol·g^{-1}. Significant Xe enrichments in mantle and crust samples are given in bold characters. Reference for air (Sano et al., 2013), CI (Dauphas and Morbidelli, 2014), EH (Bekaert et al., 2020), MORB (Moreira et al., 1998), Bravo Dome fluids (Holland and Ballentine, 2006), Xenoliths (Hennecke and Manuel, 1975a; Poreda and Farley, 1992; Czuppon et al., 2009), KTB (Drescher et al., 1998), Red rock impact (Kuroda et al., 1997), Tektites (Palma et al., 1997), Lunar anorthosite (Bekaert et al., 2017) (Table from Rzeplinski et al., 2022).

1.4.1 Xe in silicate melts

Silicate melts are efficient transfer agents in the Earth's interior for heat and matter. Understanding Xe behaviour in melts is critical to constrain the early history of the Earth and its present-day degassing. Noble gases solubility in silicate melts depends on their composition and melt structure, and was assumed to occur through physical insertion in the interstitial voids of the three-dimensional network of melts (Carroll and Stolper, 1993; Shibata et al., 1998). Solubility of Ar was determined in basaltic, rhyolitic, orthoclasic, and albitic melts and glasses at pressures of 0.025-0.1 GPa and temperatures of 400-1300 ºC, showing Ar solubility in melts is strongly pressure-dependent (Carroll and Stolper, 1993). Adopting developed laser-heating high *P* diamond anvil cell techniques, Chamorro-Perez et al. (1998) found beyond 5 GPa, the Ar solubility decreased markedly by an order of magnitude, which was explained by a compression of interstitial sites in the silicate melt, but could instead be possibly due to incomplete melting of the samples (Schmidt and Keppler, 2002). In addition, by using a piston cylinder apparatus and a multi-anvil apparatus in the P range of 1-11 GPa and at T between 1500 and 2000°C, Schmidt and Keppler (2002) found a linear increase of Ar solubility up to about 4-5 GPa where it reaches a maximum of 4.0 wt% and 0.8 wt% for the haplogranitic and tholeiitic melt respectively, and remains constant at higher pressure. A similar pattern was observed by the same authors for Xe solubility in tholeiitic melt, which increased linearly up to about 6 GPa, reaching a maximum value of 0.8 wt% (Fig. 1-10).

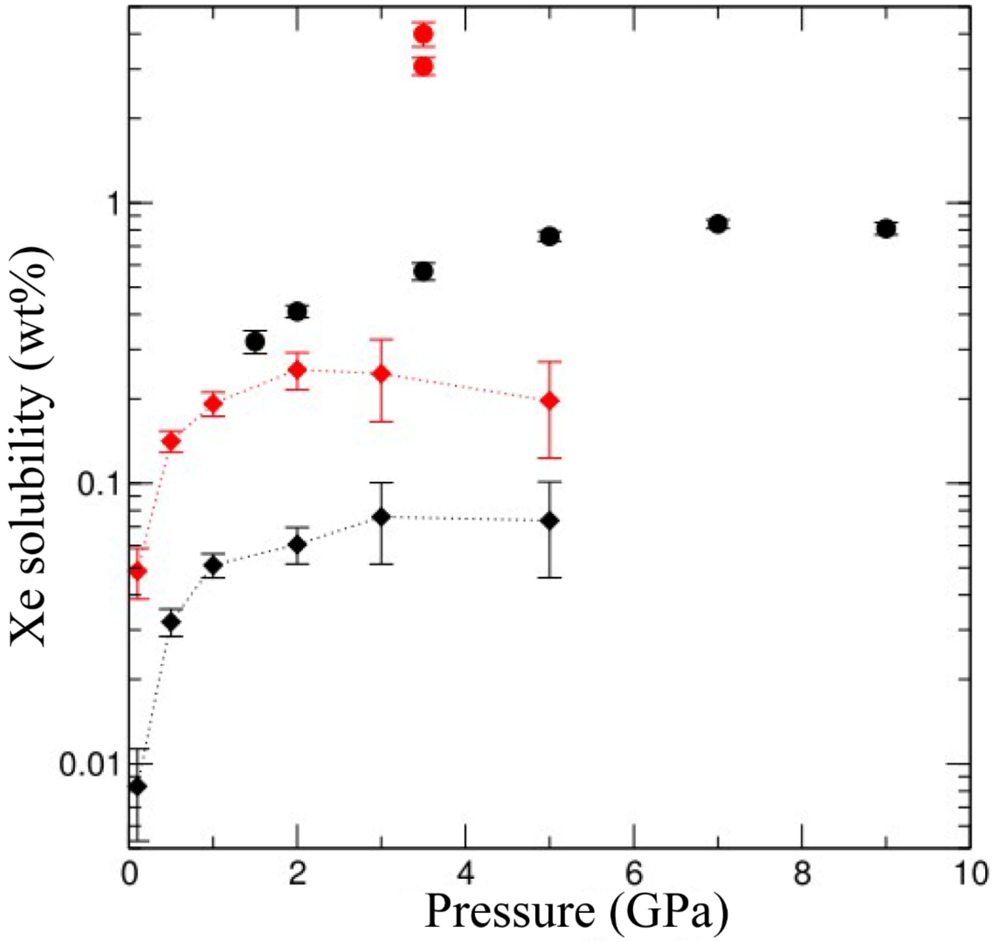

Fig. 1-10. Summarized Xe solubility data. Red circles are from hydrous haplogranitic melts (Leroy et al., 2018); black circles from tholeitic melt (Schmidt and Keppler, 2002); diamonds from theoretical calculations (Guillot and Sator, 2012) where black diamonds represent tholeitic melt, red diamonds represent haplogranitic melt (figure from Leroy et al., 2018).

Recent study carried out in compressed haplogranitic magmas with in-situ high energy synchrotron X-ray diffraction using resistive heating diamond anvil cells, found oxidation of Xe as observed by a new contribution in pair distribution functions between 0.2-4 GPa at high *T* up to 700 ºC (Leroy et al., 2018). They proposed a Xe-O bond with a bond length of 2.05 ± 0.05 Å and a coordination number of 12, implying Xe insertion in six-membered rings of the melt structure (i.e., rings formed of six SiO_4^{4-} tetrahedra) rather than in interstitial voids (Fig. 1-11). Ring structure information of silicate glasses was extracted with neutron diffraction technique (Shi et al., 2019), indicating the six-membered ring is indeed the most prominent and having an inner diameter of 4.30 Å, consistent with the Xe-O bond length.

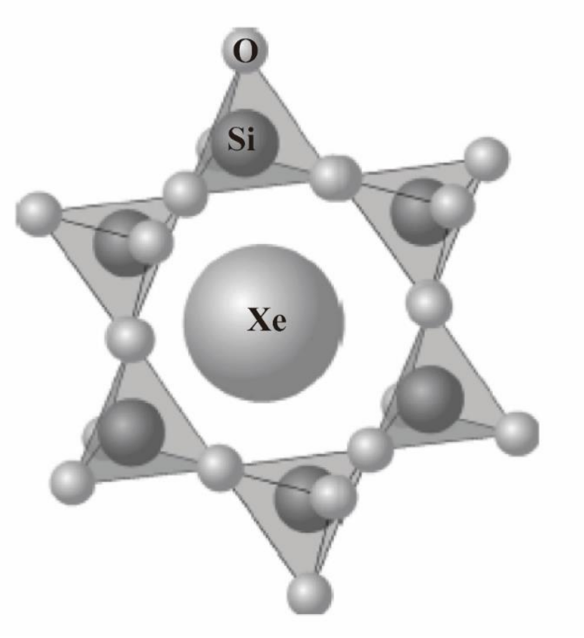

Fig. 1-11. Insertion of Xe in six-membered rings of the melt's structure.

1.4.2 Xe in stoichiometric oxides

Xenon oxides have been synthesized since the sixties from Xe-F compounds. The two xenon oxides, XeO_3 (Templeton et al., 1963) and XeO_4 (Huston et al., 1964; Selig et al., 1964) have long been known to exist at ambient pressure, but are unstable and decompose explosively above 25 °C and -40 °C, respectively. A stable xenon dioxide (XeO_2) has been synthetized by hydrolysis of XeF_4 in H_2O and 2.00 M H_2SO_4 at 0 ºC (Brock and Schrobilgen, 2011). Raman spectroscopy indicates that XeO_2 possesses an extended structure in which Xe(IV) is oxygen bridged to four neighboring oxygen atoms. The Xe chemistry at ambient *P* was later extended to H, C, O, N, S and other halogens (see reviews by Gerber, 2004; Grochala, 2007). The first experimental observation of Xe reactivity with water ice was done in laser-heated diamond-anvil cells combined with in-situ X-ray diffraction at pressures above 50 GPa and a temperature of 1200 ºC (Sanloup et al., 2013). Their results indicate the participation of H in the structure formation, giving an $Xe_4O_{12}H_{12}$ formula per unit cell and a hexagonal structure with 2 $Xe_2O_6H_6$ units (Fig. 1-12a) per unit cell. $Xe_2O_6H_6$ is metallic because of the Xe and O atoms, while the diffusivity of H atoms is similar to that of superionic ice. The xenon oxides were investigated with the compositions of XeO, XeO_2, XeO_3 and XeO_4 at 5-220 GPa using quantum-mechanical calculations (Zhu et al., 2014). The stability of xenon oxides was predicted. With increasing pressure, increasingly high oxidation states of Xe will appear: first XeO (above 83 GPa), then XeO_2 (above 102 GPa) and XeO_3 (above 114 GPa). Xenon suboxide Xe_3O_2 was found to be the first compound to become more stable than the constituting elements at about 75 GPa from first-principles calculations, and even more Xe-rich compounds at higher pressures (Hermann and Schwerdtfeger, 2014). Dewaele et al. (2016) investigated the reaction between xenon and oxygen at high pressures by using both powder X-ray diffraction, X-ray absorption spectroscopy and Raman spectroscopy with laser-heated diamond anvil cells and ab initio modelling calculation. Combining experimental and theoretical approaches, they synthesized and identified two xenon oxide structures: Xe_3O_2 (as predicted by Hermann and Schwerdtfeger, 2014) and the new Xe_2O_5 (Fig. 1-12b) at at 97 GPa and 83 GPa, respectively.

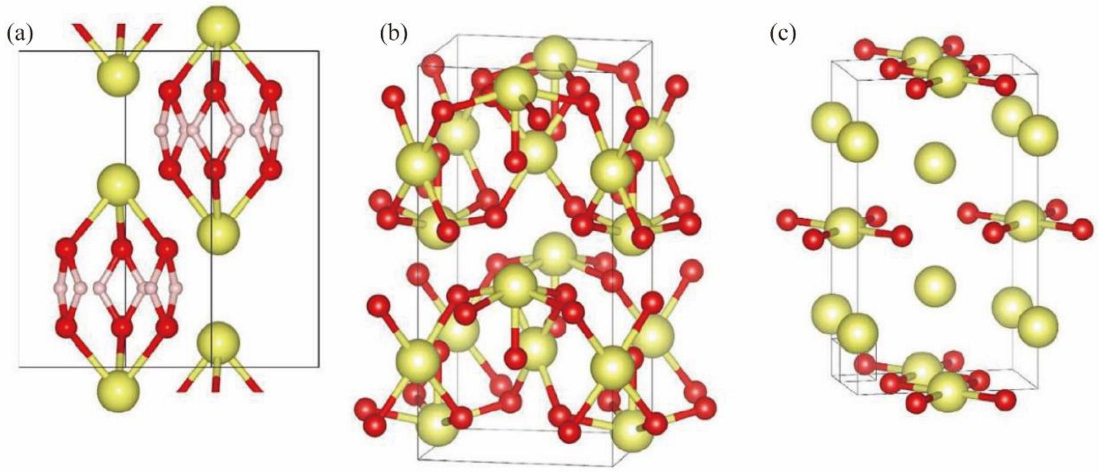

Fig. 1-12. Xenon oxides from experimentally observation and theoretically prediction. (a) $Xe_2O_6H_6$ (Sanloup et al., 2013); (b) Xe_2O_5 and (c) Xe_3O_2 (Dewaele et al., 2016). Xe atoms in yellow; oxygen atoms in red; hydrogen atoms in light pink (figure from Sanloup et al., 2020).

1.4.3 Xe as a trace element in silicate minerals

The direct evidence for chemical interaction between Xe and silica at high pressures and temperatures was found by the investigation of Xe-SiO_2 system conditions using diamond-anvil cells combined with laser heating up to 5 GPa and 1500-1750 °C (Sanloup et al., 2002b). Three very intense peaks detected in Raman spectra in the low frequency region immediately after heating attested the interaction between Xe and the silica network. Electron microprobe analysis indicated a maximum of 4 wt% Xe in this phase. A more systematic study of Xe-SiO_2 system was later carried out with in-situ x-ray diffraction measurements using Paris Edinburgh and multi anvil presses up to 6 GPa and 2000 ºC (Sanloup et al., 2005). Upon compression at ambient temperature, solid Xe was identified from the x-ray diffraction pattern, but the solid Xe signal was lost and no liquid Xe signal was ever observed when *T* increased. However, the presence of Pt_3Si was detected both in in-situ x-ray diffraction and SEM analysis on recovered samples, while quartz was the observed stable phase throughout most of the investigated *P* and *T* range. Thus, silica was reduced and released Si. The exsolution of Si from quartz/coesite was assumed through substitution of Si by Xe in the tetrahedral network at high temperature (Fig. 1-13). Olivine-Xe system was also investigated by combined chemical analysis, in-situ X-ray diffraction and Raman spectroscopy up to 7 GPa and 1700 ºC. They observed (1) a correlation between Si and Xe atomic concentrations with a slope of -1 in olivine, while the (Mg + Fe) content remains constant; (2) distortion of olivine appears systematically above the melting point with a marked increase of cell parameter a and decrease of cell parameter c; (3) a new vibrational mode in Raman spectroscopy experiments in addition to those of olivine. These finding indicate Xe enters the olivine structure by substitution to Si in the tetrahedral sites rather than in the octahedral sites. Note the fact that the substitution of Xe to Si occurs in fully polymerized phases of silica as well as in the isolated tetrahedra structure of olivine. Theoretical calculations also have confirmed this mechanism for quartz (Probert, 2010; Kalinowski et al., 2014; Crepisson et al., 2019) and olivine (Crepisson et al., 2018a), and helped refine the crystal-chemistry of Xe in these minerals. Besides, reaction between Xe and oxides in the deep crust and mantle strongly indicate that it is stored at depth as a minor or trace element, which is consistent with natural abundances of Xe (cf Table 1-3).

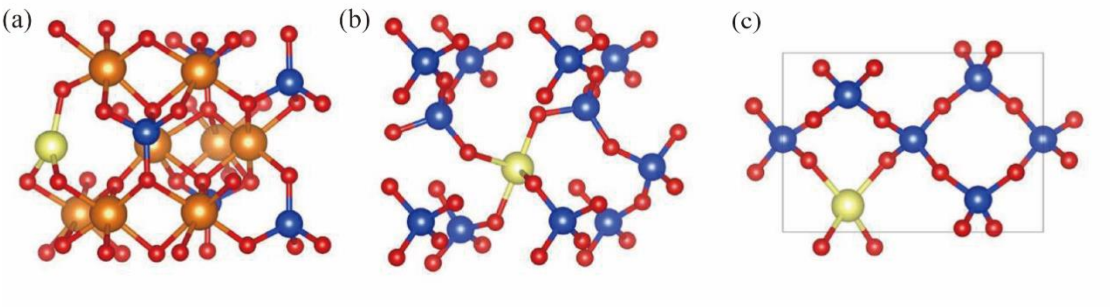

Fig. 1-13. Experimentally synthesized noble gas-silicates. (a) Xe-doped olivine Mg_2SiO_4 (Crepisson et al., 2018a); (b) Xe-doped β-quartz (Crepisson et al., 2019); (c) $(Xe,Si)O_2$ phase for which Xe site occupancy is unknown (Crepisson et al., 2019). Magnesium atoms in orange, xenon atoms in yellow, oxygen atoms in red, silicon atoms in dark blue (figure from Sanloup et al., 2020).

1.4.4 Xe partitioning behaviour

To understand Xe atypical behaviour, the mainstream method to study the relative stability of noble gases in silicate melts versus the major silicate minerals is by measuring partition coefficients, which is the ratio of the concentration of an element in a mixture of two immiscible solvents at equilibrium. For example, for silicate minerals (c^i_c) and melts (c^i_m), partition coefficient of an element i can be defined by:

$$D^i_{c/m} = c^i_c / c^i_m \quad (1.1)$$

Therefore, partition coefficients can describe how an element will be distributed between co-existing solid and liquid phases, i.e., its compatibility.

Compared to noble gases solubility in melts, much less is known about their solubility in minerals. Experiments using advances in microanalytical technique or first-principles molecular dynamics calculations have investigated the partition behaviour of noble gases at depth over the past decade (Hiyagon and Ozima, 1982, 1986; Broadhurst et al., 1990, 1992; Matsuda et al., 1993; Shibata et al., 1994; Brooker et al., 2003; Heber et al., 2007; Jackson et al., 2013; 2021; Wang et al., 2022; etc.). Among these studies, a very wide range of partition coefficients are obtained for some minerals, and their applicability to mantle melting is difficult to evaluate. In this thesis we will introduce partitioning of Xe at continental crust and mantle conditions.

Batiza et al. (1979) measured noble gas concentration in two natural volcanic rocks. Assuming that the system had been closed during magma evolution, they obtained the partition coefficients between a solid phase and a liquid phase to be 0.2 for Ne and 2-8 for Ar, Kr, and Xe. They concluded that the system may not be closed and the values were invalid. Hiyagon and Ozima (1986) performed the first investigation of Xe partitioning ($D^{Xe}_{c/m}$) for synthesized olivine -basalt system under both ambient and high *P* (0.2-1.5 GPa) at 1000-1300 ºC. They found noble gases were incompatible, with partition coefficients increasing from He to Xe. Broadhurst et al. (1992) have measured the solubilities of Ne, Ar, Kr, and Xe in natural samples of anorthite, diopside, forsterite, spinel, and in synthetic basaltic melts (Fo-An-Di-SiO_2 system) in a one-bar mixed noble gas atmosphere at 1300 or 1332 °C. All four mineral/melt pairs showed the same partitioning trend as found by Hiyagon and Ozima (1986). However, they found a surprising result that noble gases are often compatible in minerals ($D^{Xe}_{c/m}$ can be up to 90 between olivine and melt). In contrast to previous studies, Heber et al. (2007) measured partition coefficients of all noble gases between olivine (Ol) /clinopyroxene (Cpx) and melt by UV laser ablation (213 nm) and mass spectrometry analyses of individual crystals grown from melts at 0.1 GPa under mixed noble gas pressure. With this developed experimental technique, a more rigorous spatial control could be operated on the ablated phase and the grown crystals are virtually free of melt and fluid inclusions. Besides, they found bubbles of noble gases always developed within or on the surface of the growing crystals in initial experiments when samples cooled below the liquidus at constant pressure (Fig. 1-14a). To minimize bubble growth, they increased pressure by 10% at the initial stages of crystal growth in following experiments. They obtained bubble-free crystal for Cpx in this way (Fig. 1-14b), however, Ol crystals always contained bubbles (Fig. 1-14c). Thus, they used the UV laser to avoid inclusions and get bubble-free olivine pieces during ablation.

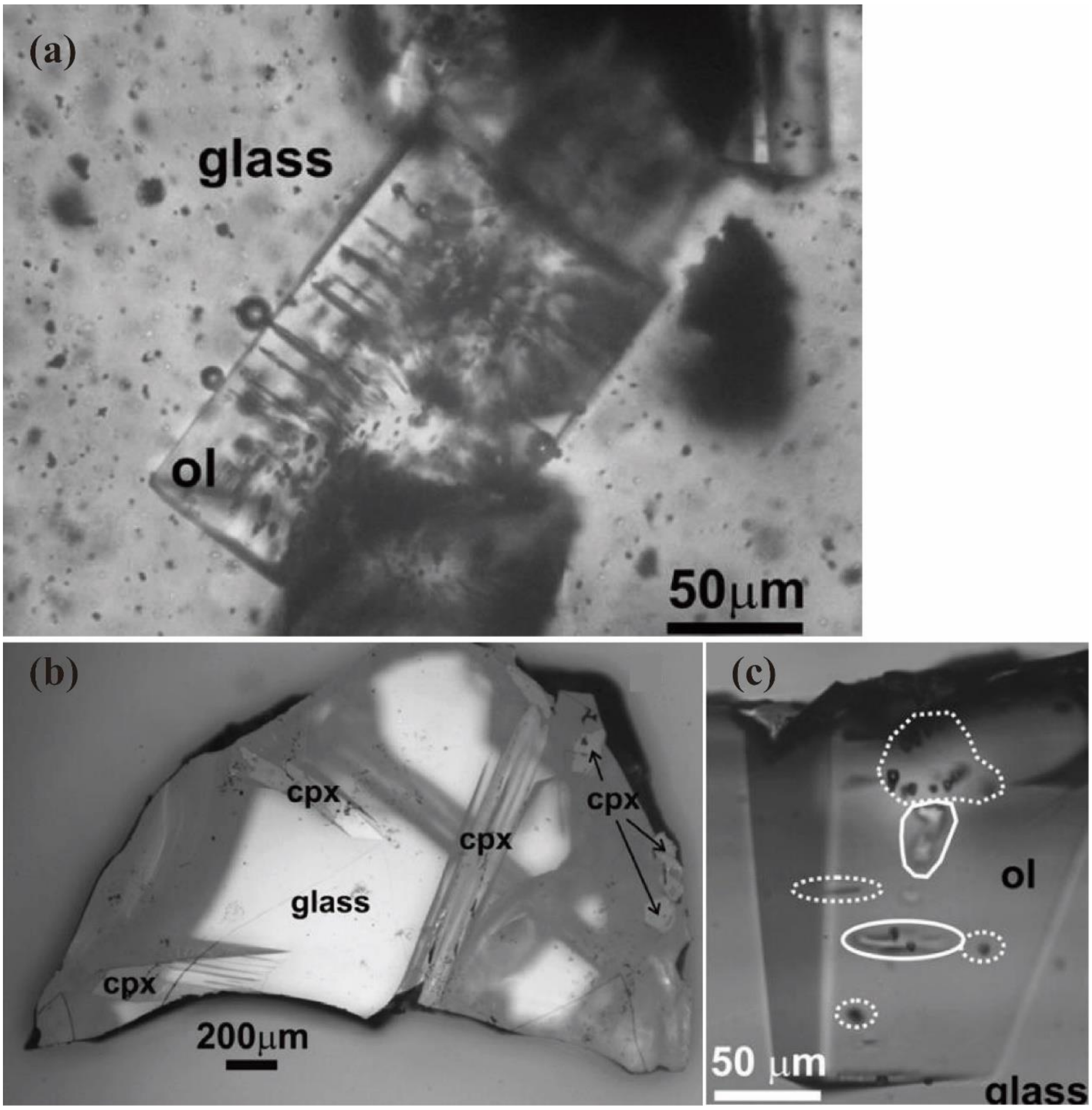

Fig. 1-14. Optical microscope image of recovered samples with different experimental approaches. (a) olivine (Ol)-melt system with a normal strategy. Bubbles seen around the Ol edge with trails extending into the crystal interior. (b) and (c) are increased pressure by 10% to minimize the bubble content. (b) clinopyroxene (Cpx)-melt system with bubble-free Cpx crystals; (c) one Ol crystal in Ol-melt system, gas bubbles (black dots, framed by dotted lines) and melt inclusions (framed by solid lines) are shown (figure from Heber et al., 2007).

Consequently, they got distinct results on partition coefficients. For olivine-melt system, $D^{Xe}_{c/m}$ can be up to 350 with bubbles analyzed but only 0.0006 for bubble-free system (Fig. 1-15). That is, the noble gas partition coefficients differ by 4-6 orders of magnitude depending on the analyses of gas bubbles. Their partition coefficients, lower by 3 or 4 orders of magnitude than in previous work, are explained by contamination either by fluid inclusions or by adsorption (Hiyagon and Ozima, 1986) and imperfect separation indicated by the rather parallel translation of the pure olivine pattern (Broadhurst et al., 1992). However, in the case of Xe reactivity with olivine (Sanloup et al., 2011; Crepisson et al., 2018a), Xe was indeed observed to be at least partly released from crystals upon quenching to room T as indicated by the appearance of pure Xe diffraction signal (Sanloup et al., 2011). In addition, Crepisson et al. (2018a) evaluated Xe contents in Xe-olivine system using first-principles calculations based on density functional theory (DFT) by comparing (1) the calculated and the X-ray diffraction measured values of cell parameters; (2) the Xe-related Raman-band intensities. Variations of cell parameters for Xe-Si incorporation site reproduce the experimentally observed increase of cell parameter a associated with small variations of cell parameter b (Sanloup et al., 2011) compared to the thermal equation of state of olivine (Liu and Li, 2006) at 0-5.7 GPa. The concentration of Xe in olivine was calculated at about 0.4% at all investigated pressures from the relative variations of a and b. They obtained a value of ~0.2 at.% Xe based on the measured Raman spectrum of Xe-rich olivine from Sanloup et al., (2011). Using the Xe solubility value of 0.2-0.4 at.% for olivine, at 0.9 GPa and 1500 ºC and 0.08 mol% Xe for a tholeitic melt at 1.5 GPa and 1500 ºC (Schmidt and Keppler, 2002), they got a partition coefficient for olivine/tholeitic melt of 2.5-5 (Crepisson et al., 2018a).

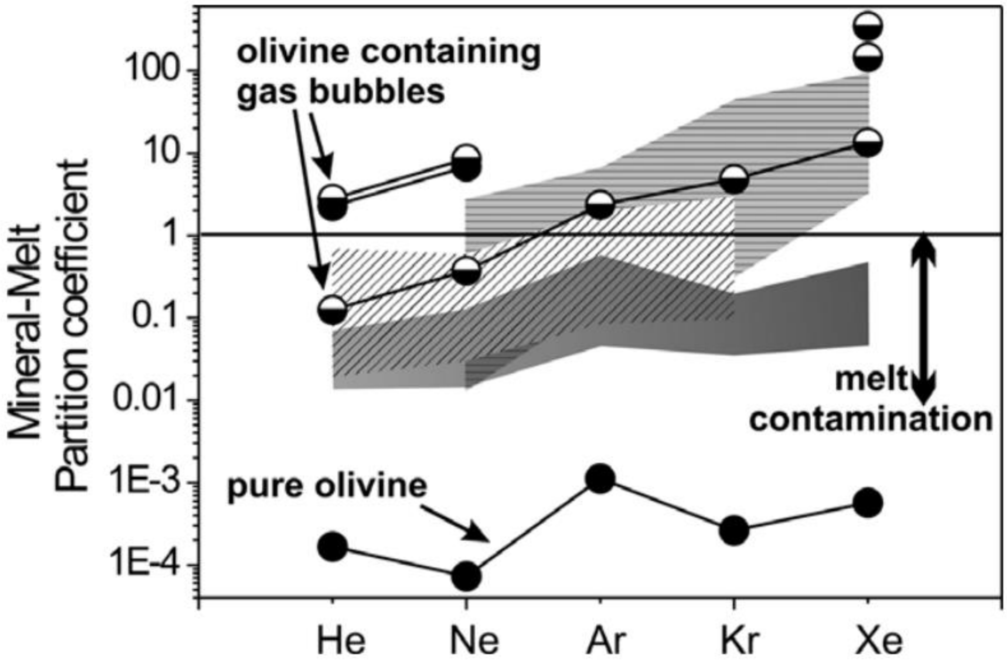

Fig. 1-15. Partition coefficients of noble gases between olivine and melt. Horizontally hatched from Broadhurst et al. (1990, 1992); diagonal hatched from Shibata et al. (1994); dark grey from Hiyagon and Ozima (1986); circles from Heber et al. (2007) where solid circles with analyses of bubble free olivine and half-filled circles with analyses of olivine that were contaminated by gas bubbles (figure from Heber et al., 2007).

Moreover, a recent study investigated Xe partitioning between granitic melt and aqueous fluid using in-situ X-ray fluorescence measurements (Leroy et al., 2019), finding that Xe degassing is strongly *T*-dependent. Partitioning coefficients between aqueous fluids and haplogranitic melt ($D^{Xe}_{f/m}$) vary from 2750 to 0.15 in the range of 680 to 850 ºC, indicating that Xe degasses only at low temperature but remains within the melt at high temperature. However, the local structure of Xe in aqueous fluids remains unknown.

The aims of this thesis

Previous studies provide profound understandings of the solubility, reactivity and mechanisms of Xe incorporation in terrestrial materials. And this will be the hypothesis explored in this PhD thesis with the following prominent questions:

(1) Xe partition behaviour is the key to understand Xe distribution at the early stages of Earth's history. However, partitioning coefficients of Xe between silicate minerals and melts span a wide range due to the existence of Xe bubbles in recovered samples. It remains debatable whether or not bubbles reflect equilibrium at high P and T or are produced upon quenching the experiment back to room conditions. Thus, Xe distribution must be measured with in-situ methods, and this is what we aim to investigate in chapters 3 and 4.

(2) The local structures of Xe in minerals and in melts have been evidently proposed. There is nevertheless no study of the local structure of Xe in aqueous fluids so far, as well as how these retention mechanisms affect Xe partitioning between mineral and fluids, and this part is conducted in chapter 5.

(3) To have a full understanding of heavy noble gases behavior in planetary interiors, and revisit the timing of key planetary processes, investigation must be extended to other noble gases like Kr. An in-situ study found Kr surrounded by oxygen atoms at 2.49 ± 0.1 Å using X-ray absorption spectroscopy at the Kr K-edge on a feldspathic Kr-bearing glass and melt up to 2.7 GPa and 1090 °C (Crepisson et al., 2018b). This suggests Kr bonding to O atoms and Kr oxidation inside cages formed by the largest aluminosilicate rings (i.e., ~12-membered-rings). It is however difficult to reach further conclusions due to the infeasibility to calculate the coordination number without Kr oxide references. Now we need to focus on how Kr incorporation in minerals and how this mechanism affects Kr partitioning behaviour. Our preliminary results for this part

are summarized in Appendix II.

Here is summary of the used beamlines at different synchrotron sources, which are highlighted related to this study.

Beamtimes sessions:

1) October-2018: Soleil, France, beamline SMIS.
On: Xe incorporation mechanisms in quartz and olivine by in-situ infrared measurement at high *P*-*T* conditions.
2) October-2019: Proposal I-20190348 EC, Petra III, Germany, beamline P02.2.
On: Partitioning of heavy noble gases between planetary reservoirs at high pressure.
3) September-2020: Proposal I-20200200 EC, Petra III, Germany, beamline P61.
On: Behaviour of Xe upon mantle melting at depth.
4) October-2020: Soleil, France, beamline SMIS.
On: Testing Xe retention in bridgmanite at lower mantle conditions.
5) December-2020: Proposal GUP 69687, APS, USA, 16-BM-B HP White-beam.
On: Iodine and xenon behaviour upon mantle melting at high pressure.
6) March-2021: Proposal GUP 69589, APS, USA, 16-BM-B HP White-beam.
On: Tracking neodymium local structure in magmas at depth.
7) June-2021: Proposal GUP 73936, APS, USA, 16-BM-B HP White-beam.
On: Behaviour of Xe upon mantle melting at depth.
8) July-2021: Soleil, France, beamline SMIS.
On: Testing argon retention in the lower mantle by mid-infrared spectroscopy.
9) September-2021: Proposal I-20210211 EC, Petra III, Germany, beamline P02.2.
On: Xenon behavior in fluids at depth.
10) October-2021: Proposal GUP 75671, APS, USA, 16-BM-B HP White-beam.
On: Iodine speciation in high pressure basaltic melts.

Chapter 2: Experimental methods

This chapter is an overview to introduce all equipment and methods used in this thesis. A series of apparatus to generate high *P-T* conditions (piston cylinder press, diamond anvil cell, multi anvil press and Paris Edinburgh Press) are summarized in 2.1. Synchrotron X-ray techniques (energy-dispersive X-ray diffraction and angle-dispersive X-ray diffraction combined with X-ray fluorescence analysis) to investigate distribution behaviour of Xe are presented in 2.2. Analyses of recovered samples (scanning electron microscopy, electron probe micro-analysis, Raman spectroscopy, and X-ray tomography probes) are covered in 2.3.

2.1 High Pressure Techniques

High pressure experiments are essential to explore partitioning behaviour of noble gases at depth. In our work, piston cylinder press was firstly used to synthesize silicate glass doped with noble gases under pressure and carry out some preliminary ex-situ experiments. In-situ experiments were further conducted in diamond anvil cells, multi anvil press and Paris Edinburgh press at synchrotron sources.

2.1.1 Piston cylinder press and gas loading process

The piston-cylinder apparatus is a solid media device, which is wildly used in experimental petrology laboratories for simultaneously accessing high pressure (up to 6 GPa) and temperature (up to 1700 ºC) at crust-mantle conditions. The first piston cylinder type device was proposed by Sir Charles Parsons, further developed by Coes (1962). The modern generation wildly used in Earth's sciences is based on the design described by Boyd and England (1960), which is constituted by three main parts: (1) the pressure generating system; (2) the pressure vessel; and (3) the assembly parts within the vessel. The principle of this instrument is to generate pressure by compressing a sample assembly between a base support and a piston, which includes a resistance furnace, inside a cylindrical tungsten carbide chamber (Fig. 2-1). The materials of the assembly (such as pyrophyllite and talc) become ductile at high *T*, transforming the axial pressure into a quasi-hydrostatic pressure. The top plate remains fixed while a hydraulic ram at the bottom put strength on the pressure plate through the injection of pressurized oil. The actual pressure at the center of the assembly can be accurately calibrated from the hydraulic oil pressure in the ram. A graphite resistive-heating furnace is used to create homogeneously high *T* for the whole capsule, which is monitored with a thermocouple next to the top of the capsule.

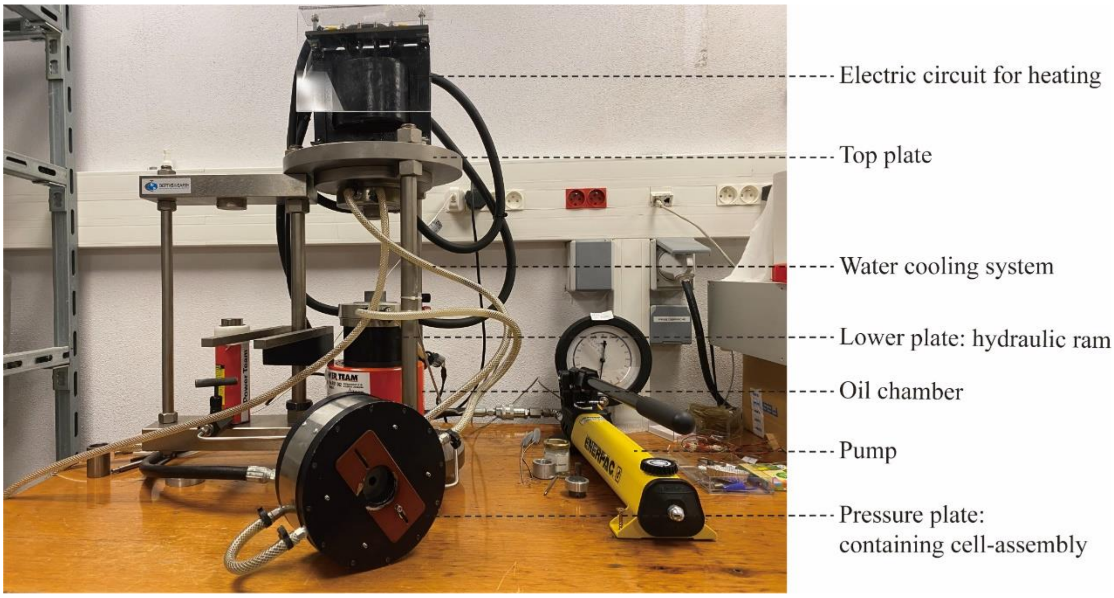

Fig. 2-1. Photo of the piston cylinder press used in IMPMC.

The silicate glasses were initially synthesized by mixing the reagent grade oxides and carbonates. Powders placed in a platinum crucible were then molten in an atmospheric Elite BRF17/5 furnace, which can reach up to 1700 ºC (Fig. 2-2).

Noble gases (Xe or Kr) were loaded with a simple device (Fig. 2-3), developed by Boettcher et al. (1989). This device uses vacuum to evacuate air from the capsule, and crimps the capsule to keep the gas sealed. A one-end welded capsule D loaded with sample firstly is inserted into B and then inserted into components E (Fig. 2-3b). When screwing A into B to seal the open-end of the capsule into C, vacuum is initiated on the line I and gas is introduced with the connection of one bottle of pressurized gases. At last, B and E are pulled apart, the capsule and B are placed on a vise and the gas remains on until the capsule is crimped. The capsule is then cut along the top edge, welded and ready for experiments. The amount of gas is constrained by weighing the capsules before and after loading.

Fig. 2-2. Photo of BRF17/5 furnace used in our experiments.

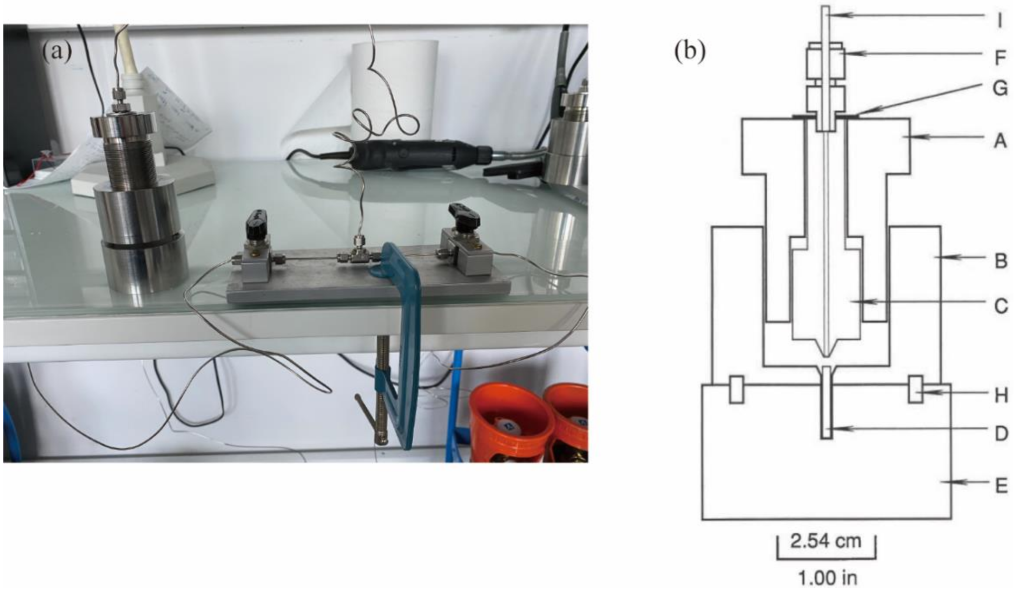

Fig. 2-3. (a) Photo of gas loading device (b) Schematic arrangement of the loader, from

Boettcher et al. (1989).

High *P* syntheses were carried out on an end-loaded piston cylinder press at the IMPMC. We use a half-inch talc pyrex assembly (Fig. 2-4), composed by a graphite heater, one or two platinum (Pt) capsules (5 mm height for two capsules, 10 mm height for one capsule) with dried MgO powder packed around as a pressure transmitter, and a type D thermocouple ($W_{74}Re_{26}$-$W_{95}Re_5$) separated by an alumina disk. The uncertainty of *T* is related to the location of the thermocouple in the upper part of the assembly and the size of the sample, which can be up to 200 ºC for a 19 mm assembly due to the existence of thermal gradients (Watson et al., 2002). Pressure was slowly increased under 1 GPa to protect the assembly. Eventually, the initial pressure was always increased to 10% plus of the desired run pressure displayed on the pressure gauge to overcompensate for friction that is present at low *T*. Especially for low pressure experiments (less than 1 GPa), the pressure was initially increased up to 1.5 GPa to make sure the furnace assembly was compacted. After reaching the appropriate pressure (1-2h), the temperature was increased with the rate of 100 ºC/min. During the *T* increased, *P* was monitored and adjusted to maintain the target *P*. Experiments were run for different duration and followed by rapid *T* quenching (a few minutes) and decompression at room *T*.

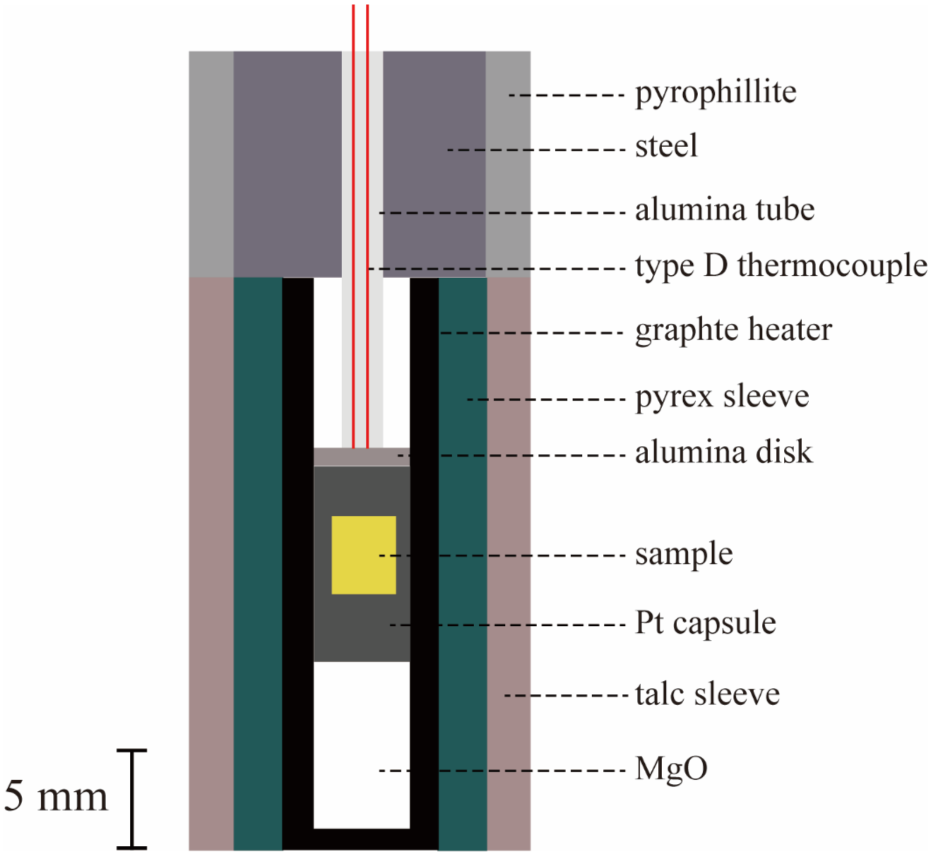

Fig. 2-4. Scheme of the cell assembly used in piston cylinder.

2.1.2 Diamond Anvil Cell

A diamond anvil cell (DAC) is a one of the most popular devices that enables the compression of a small (sub-millimeter-sized) piece of material to create extreme pressures (up to hundreds of GPa). The first diamond anvil cell was proposed by Charlie Weir in 1958, and developed as one most powerful high-*P* device during the following decades. The principle of DACs is very simple: two opposing diamonds with a sample compressed between the polished culets (Fig. 2-5). A gasket inserted in between not only provides containment for the pressure medium, but also acts as a supporting ring to prevent anvils from touching. Pressure is induced by forcing the two diamond culets toward each other. High temperature can be achieved by three different ways: (1) by using an external furnace, for which *T* can reach up to 500 ºC; (2) by using an internal heater, i.e., a resistive heater surrounding the diamonds and gasket assemblage or the supports for the diamonds (usually WC), for which *T* can reach up to 1400-1600 ºC within the vacuum (Zha et al., 2008; Yan et al., 2021); (3) by using laser heating technique based on the principle of absorption of infrared laser light by the sample with minor intensity loss when it passes through the diamond, for which *T* can reach up to several thousand degrees (Errandonea et al., 2003; Meng et al., 2006). The DACs can be homogeneously heated via the two first ways. However, it suffers from *P*-*T* limitations due to the oxidation of diamonds and seats at temperatures over 1000 °C as well as softening of the metallic gaskets. On the other hand, only a portion of the sample (tens of microns) is heated when laser heating is used, which will lead to large temperature gradients within the sample. In addition, to optimize X-ray diffraction patterns, symmetric large opening DACs (70°) equipped with Boelher-Almax seats (Boehler et al., 2004) were used to generate high *P*-*T* conditions. In this thesis, we mainly focus on two types of resistive-heating DACs (RH-DAC): graphite-heater DAC and Pt-wire-heater DAC.

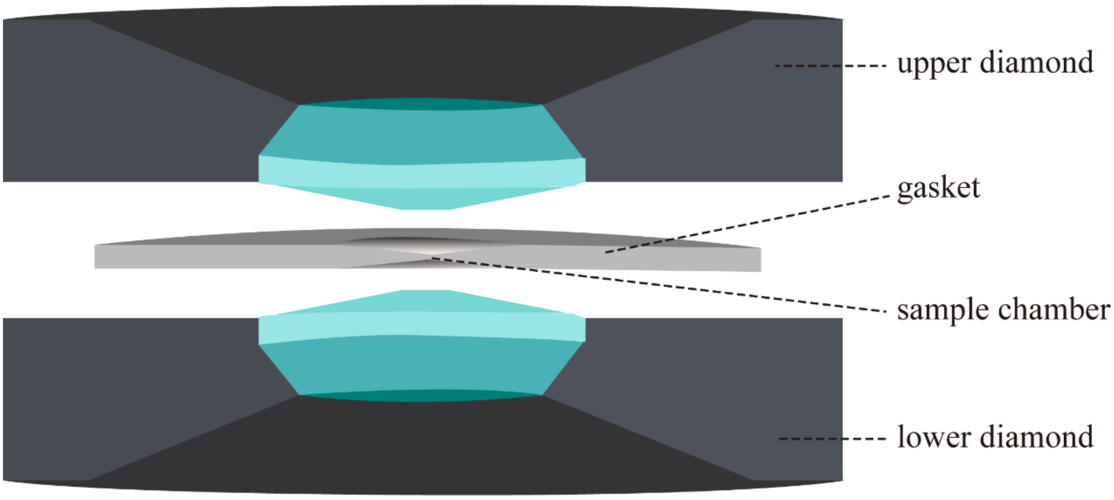

Fig. 2-5. Schematic of the employed DAC (Boehler-Almax design). Diamond anvils are supported by tungsten-carbide seats and separated by a rhenium (Re) gasket.

Graphite-heater DAC

Diamond anvil cell with a specific design, equipped with a graphite heater (Fig. 2-6) was applied in the experiments at P02.2, Petra III, Hamburg, Germany (Lierman et al., 2009) to reach relatively high *T*. Graphite is an ideal material to use for heating because it is a good thermal and electrical conductor. The diamond anvil was affixed on the tungsten carbide (WC) seat. Graphite pieces were placed at the center. Laser drilled Re gasket was used as sample chamber. Two Mo rods were used to supply power to graphite heater disposed under and above the gasket. *T* was recorder by R-type (Pt + Rh/Pt) thermocouples near to the diamond anvil, with uncertainties of ± 60 ºC (Lierman et al., 2009). When we did Raman analysis, the whole assembly was put into a vacuum vessel to protect diamonds, Mo rods as well as WC seats (Fig. 2-6b).

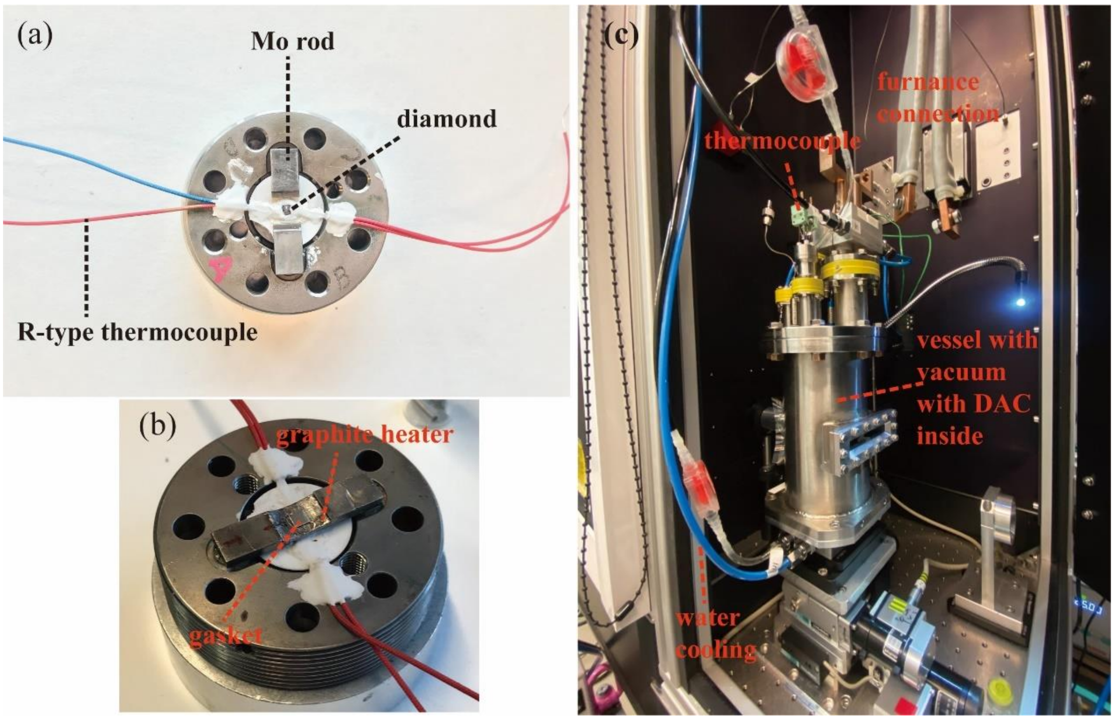

Fig. 2-6. (a) Half part of graphite heater DAC; (b) focus on the graphite heater (c) Experimental set-up on P02.2 for graphite heated DAC with in-situ Raman spectroscopy. Reached maximal T is 1250 ºC.

Platinum-wire-heater diamond anvil cell

Diamond anvil cell with Pt-wire heater (Fig. 2-7) was made using the design by Y. Fei (Carnegie Institution of Washington) for Mo-wire heater, and adapted to symmetric cell by C. Sanloup. Resistive-heating was achieved using the internal heating technique developed by Fei and Mao (1994). Because of the high ductility and of oxidation behaviour, Pt has great advantages to coil thin wires and resist oxidation, as only a very thin PtO_2 layer is formed at high *T* but disappears with further heating (Chaston, 1975). Pt wire was coiled around an alumina ring and connected to Mo tubes, then placed at the center of a piece of pyrophyllite, covered with heat-proof cement. Laser drilled Re gasket was inserted at the center of the alumina ring as sample chamber. Two Mo needles were inserted into the Mo tubes to supply power to Pt wire. *T* was recorded by a type S thermocouple located on the edge of the gasket closed to the sample chamber. A piece of mica plate was placed on the both sides of the pyrophyllite to avoid the electrical short-cuts. Pt-wire heater was also applied in the experiments at P02.2, Petra III, Hamburg, Germany (Fig. 2-8). Pressure at ambient *T* was measured by ruby fluorescence, and was monitored at high *T* via (1) the volume of a piece of gold inserted in the sample chamber using its X-ray diffraction (XRD) signal; (2) Raman signal of a piece of ruby (Dewaele et al., 2008); (3) Raman signal of a piece of $SrB_4O_7:Sm^{2+}$ (Rashchenko et al., 2015). However, the *P* given by ruby at high *T* is inaccurate due to several factors: (1) the linewidth of the fluorescence lines rapidly increases with *T* and the doublet R_1–R_2 becomes a broad band above 200 °C; (2) signal becomes increasingly noisy with *T*; and (3) the *T* dependence of the R_1 wavelength is relatively large. The error on *P* reading can be affected by the one on *T* (Datchi et al., 2007). With an isolated, narrow and intense fluorescence line at 685.41 nm with a very small temperature dependence, $SrB_4O_7:Sm^{2+}$ is a more ideal pressure sensor at $T < 600$ °C. However, we observed it to be dissolved with liquid water around 500-600 °C. Besides, for preventing the DAC stage motors to heat up, the DAC is surrounded by a pyrophyllite holder, further packed with water cooling system (Fig. 2-8). H_2/Ar flux was adopted during experiments to prevents rapid oxidation of the cell.

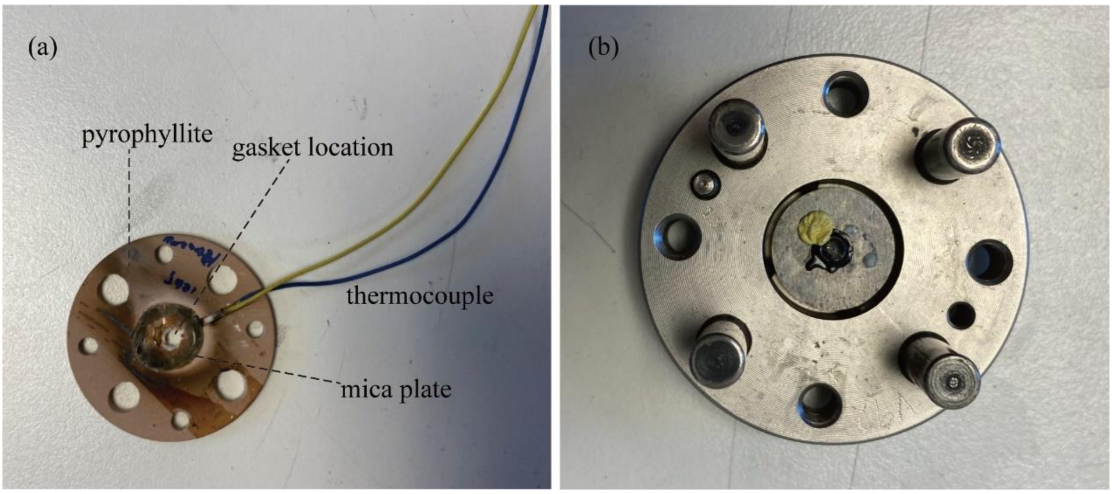

Fig. 2-7. (a) Mo-wire heater. (b) lower part of the DAC.

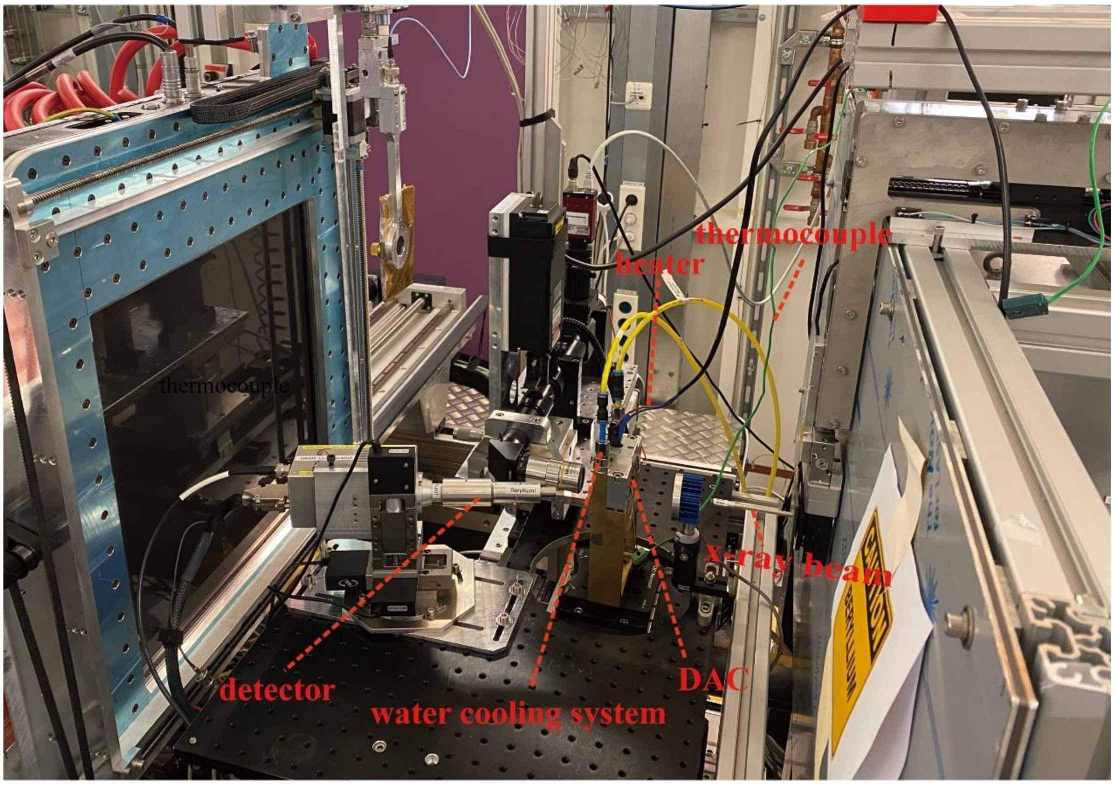

Fig. 2-8. Experimental set-up on P02.2 (beamline at DESY, Petra III, Hamburg, Germany) for Pt-wire heated DAC with in-situ angle-dispersive X-ray diffraction. DAC is surrounded by a pyrophyllite holder, further packed with water cooling system. Reached maximal *T* is 1060 ºC.

Temperature estimation for Pt-wire-heater DAC

In this thesis, we have used the same RH-DACs as described in de Grouchy, PhD thesis (2016). The only difference is that we adopted type S thermocouple (TC) rather than type K for a better stability of TC at high *T*. The Pt-wire heater was made by coiling a 250 μm diameter Pt wire with at least 20 turns around a 10 mm outer diameter alumina ring, with no contacts between the coils. The maximal *T* of one heater depends on the number of coils and coil spacing. However, abnormal display of TC can occur when TC either is far away or touch the diamond. Therefore, it is essential to establish the *T*-calibration curve to estimate the error on the TC reading, and any possible *T* variation due to the distance from the sample chamber. One effective way is to use samples of known melting temperature. By loading Pt and NaCl in separate holes in the gasket, De Grouchy obtained a calibration curve at different pressures and the average temperatures. Here we collected all our experimental data with de Grouchy's results (Fig. 2-9). Most data are consistent with established calibration curve, suggesting the reproducibility of the heater. Note *T* measurements in some experiments deviate from TC calibration curves, indicating that the TC was far away from the sample chamber during experiment. The heater used in all experiments were prepared in a same way with similar number of coils. Thus, temperature was estimated from the established power-*T* curve for the TC-failed experiments, with uncertainties of ~ 80 ºC.

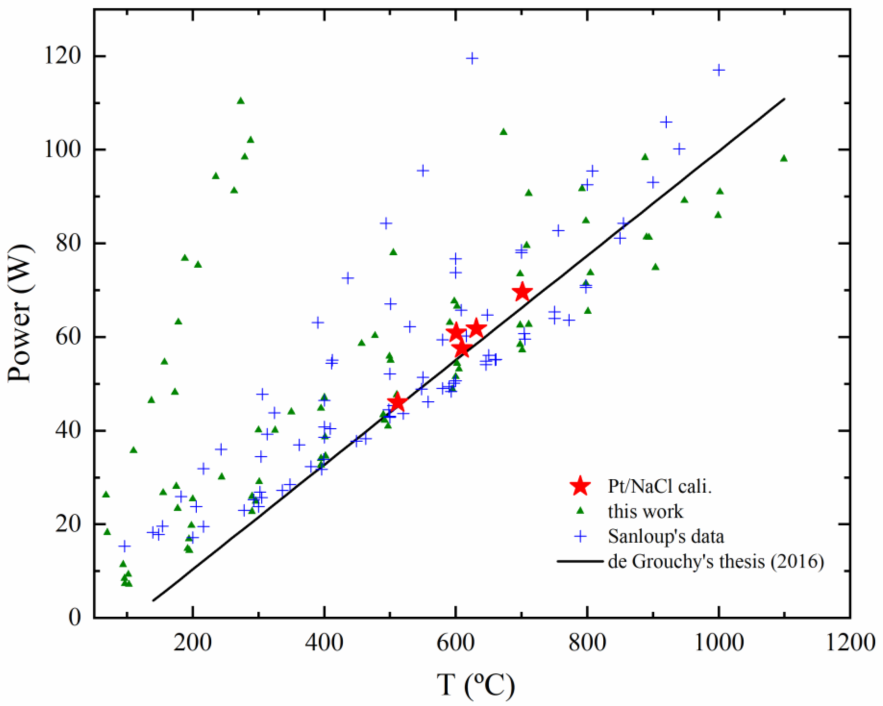

Fig. 2-9. Power vs *T* relations in Pt-wire-heater DAC. Solid line and stars represent TC calibration curve and Pt/NaCl extrapolation up to 1100 ºC, respectively (from de Grouchy's thesis, 2016). Green triangles and blue crosses are data collected in RH-DAC's experiments, from our work and from Sanloup's experiments, respectively. Note *T* measurements in some experiments far deviate with TC calibration curves, indicating the necessity for *T* calibration in RH-DAC experiments.

2.1.3 Multi anvil press

A multi-anvil press is a type of device related to a machine press that is used to create extraordinarily high pressures within a small volume. Tracy Hall firstly invented the multi-anvil apparatus in 1958, attaining 10 GPa and above 3000 ºC. It has evolved progressively in the past half century and can now reach pressures close to 100 GPa. In the early 1960s, cubic-anvil apparatus was developed, in which six orthogonal pistons compress a cubic cell volume. A typical 8-6 multi anvil apparatus uses air pumps to pressurize oil, which drives a vertical hydraulic ram to compress a cylindrical cavity. The cavity is filled with six steel anvils, gathering on a set of eight tungsten carbide cubes. To fit an octahedral assembly, the interior corners of these cubes are truncated. When compressed, the assembly extrudes out between the cubes, forming a gasket.

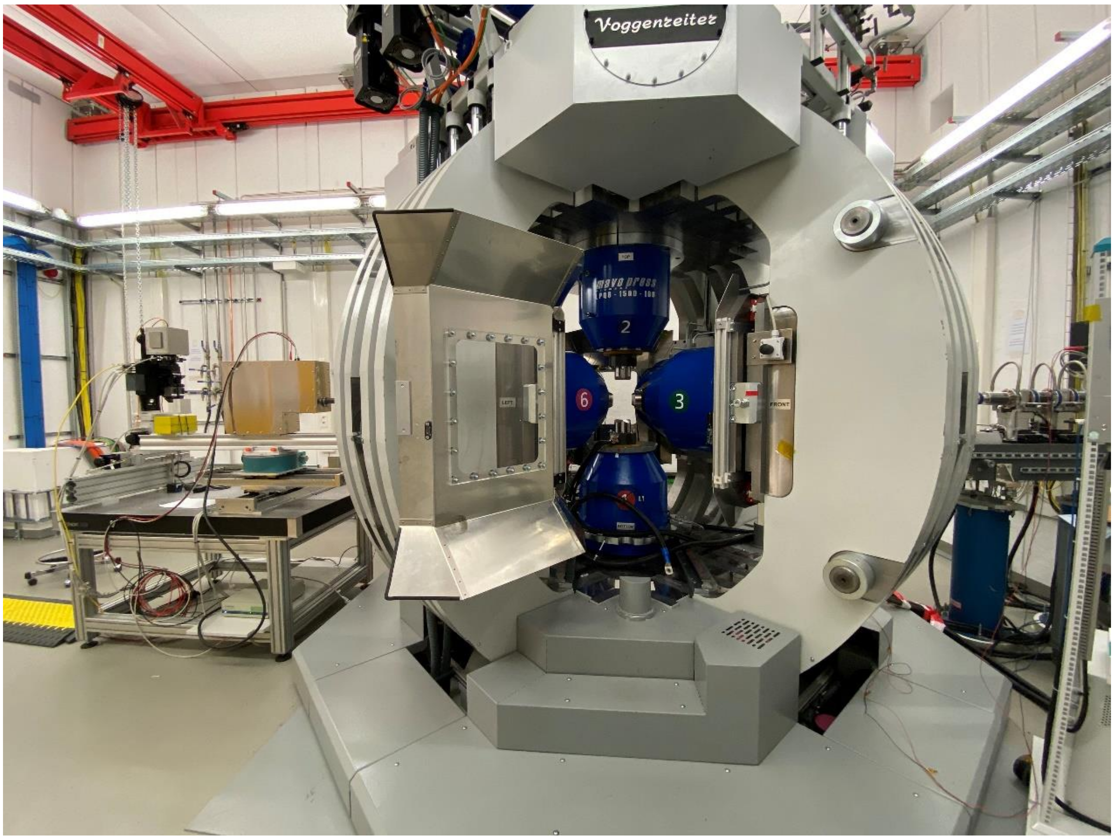

Fig. 2-10. Experimental set-up on P61B (beamline at DESY, Petra III, Hamburg, Germany) for multi anvil press with in-situ energy-dispersive X-ray diffraction, compressed by the large blue hydraulic rams.

In our work, a modern version of the Hall-type press (Hall, 1967) was used in P61B, Petra III, Hamburg, Germany, combined of 6 first-stage anvils and 8 tungsten carbide (WC) second-stage anvils (Fig. 2-10). The six independent plunger pumps are mounted on top of the press frame. They are mounted perpendicular to each other as three pairs inside a spherical press frame, which control the rams individually. This design minimizes and fixes the hoses connecting each ram and plunger despite the movement of the press by the alignment stage mentioned later. The pressure of each plunger pump is up to 70 MPa and with a precision of 50 kPa (Farla et al., 2022). The wide openings between the hydraulic rams permits vertical and horizontal diffraction angles of 30º and 23º, respectively. Via isotropic compression, quasi-hydrostatic pressure was generated in the sample using eight cubic inner anvils with a triangle-shaped truncation and an octahedral pressure medium (Fig. 2-11). We used the 18/11 cell-assembly with truncated edge lengths of 11 mm, doped octahedra MgO with a graphite heater, ZrO_2 thermal isolator and MgO as the capsule container (Fig. 2-12). *P* was derived from the equation of state of MgO (MgO cylinder surrounding the sample capsule) by recording its diffraction pattern. *T* was monitored using a type C thermocouple. To constrain the X-ray path length through the sample, and preserve the sample cylindrical geometry, diamond cylinder was used and sealed under pressure by platinum-rhodium caps, filled with sample.

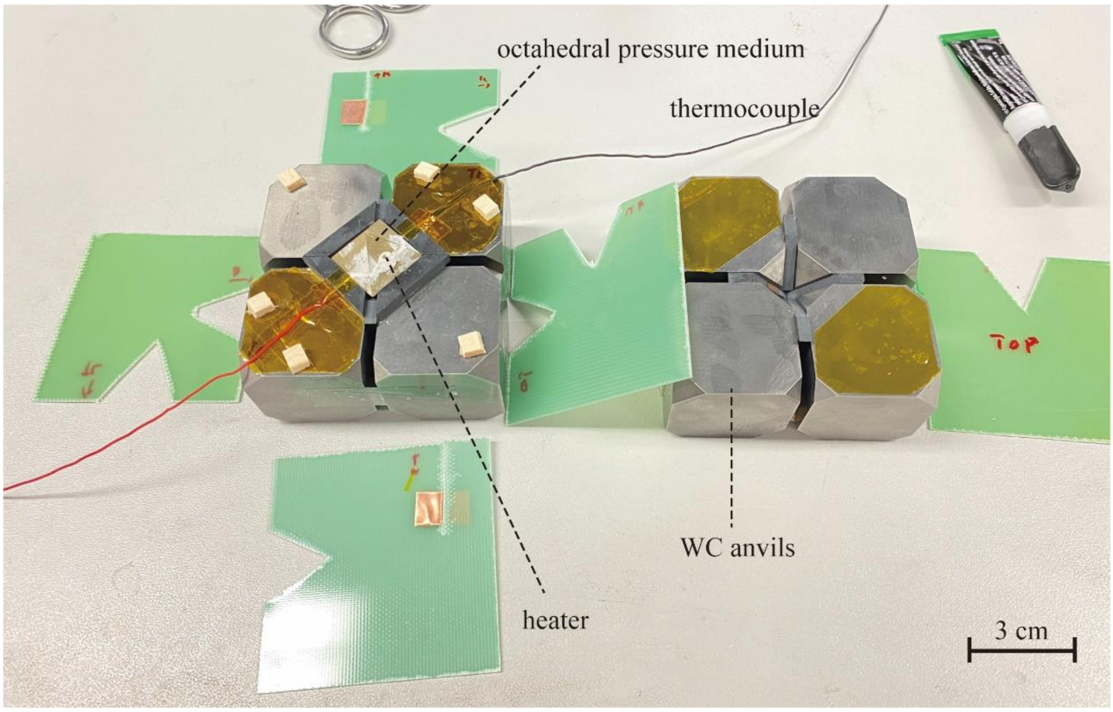

Fig. 2-11. Assembly for the 'Kawai' compression geometry. The octahedral pressure medium with a sample inside is compressed by eight WC cube-shaped anvils.

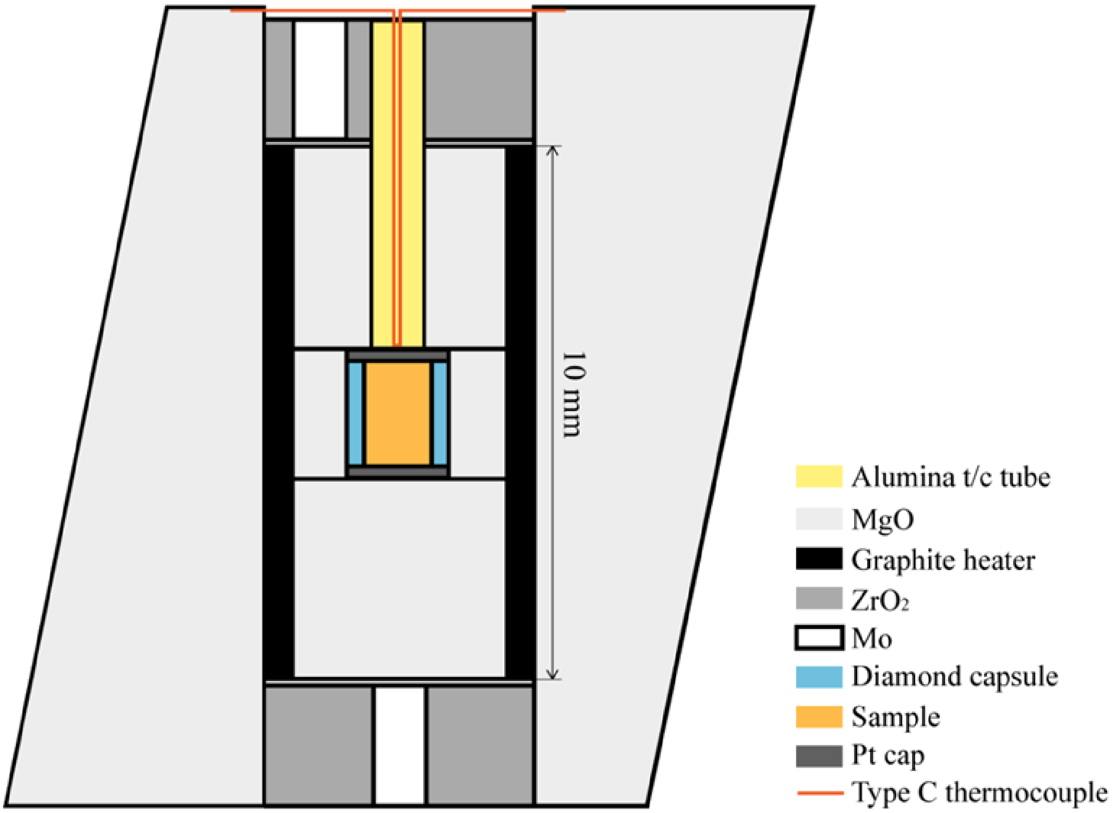

Figure 2-12. Schematic illustration for sample chamber of the Hall-type design of multi anvil press.

2.1.4 Paris-Edinburgh Press

Paris-Edinburgh Press (PEP) is a small solid medium apparatus (~25 cm^3 × 25 cm^3 × 25 cm^3 and a mass of only 50 kg for a standard design, Philippe et al., 2016), which was initially developed to conduct in-situ neutron measurements at high *P*-*T* conditions in 1992 (Besson et al., 1992). It is based on the injection of pressurized oil into a chamber which acts on a piston. With the benefit of available large volume samples (up to 2 mm^3) and wide detector windows, it has been adapted for X-ray measurements since the 1990s. The PEP can generate quasi-hydrostatic *P* up to 17 GPa (Morard et al., 2011), and high temperatures up to 2300 K at 10 GPa (Kono et al., 2014). Compared to multi anvil press, its wide detector window allows a very large X-ray access to the sample for angle-dispersive diffraction: 60° horizontally and 15° vertically (Morard, 2006). During experiments, the sample was contained within a deformable gasket compressed by two opposed tungsten carbide anvils (Figure 2-13). High temperature conditions were reached by resistive heating through an internal graphite furnace. *T* was estimated using previous power consumption and temperature calibrations (Kono et al., 2014). Uncertainty in temperature was within 10% (Yamada et al., 2011). Semi-sintered MgO acted as a *P*-transmitting medium to the sample, which was placed in the path of the X-rays (Fig. 2-14) and was also used for pressure measurement (Speziale et al., 2011). A boron epoxy (BE) ring was used as a gasket, which was isolated from the graphite heater by MgO rings. Two boron epoxy windows were used for the purpose of reduction of the absorption and improvement of signal/noise ratio.

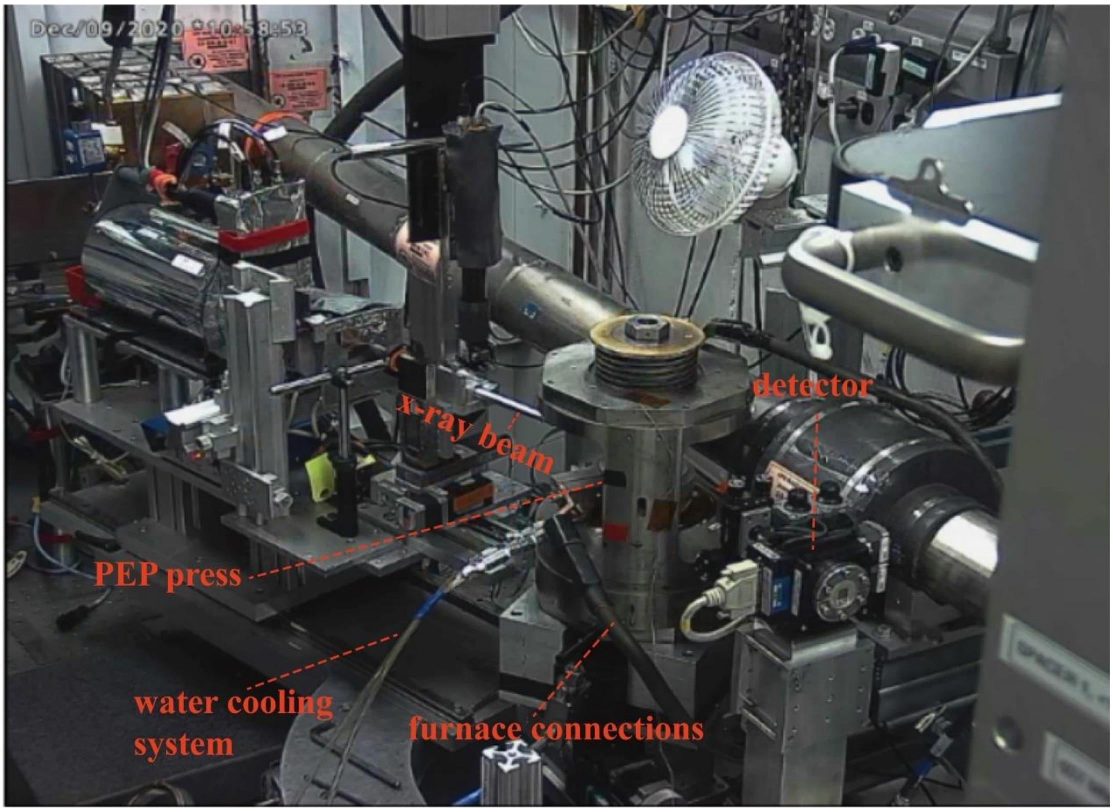

Fig. 2-13. Experimental set-up on 16-BM-B beamline (HPCAT at the APS, Argonne National Laboratory) for PEP with in-situ energy-dispersive X-ray diffraction.

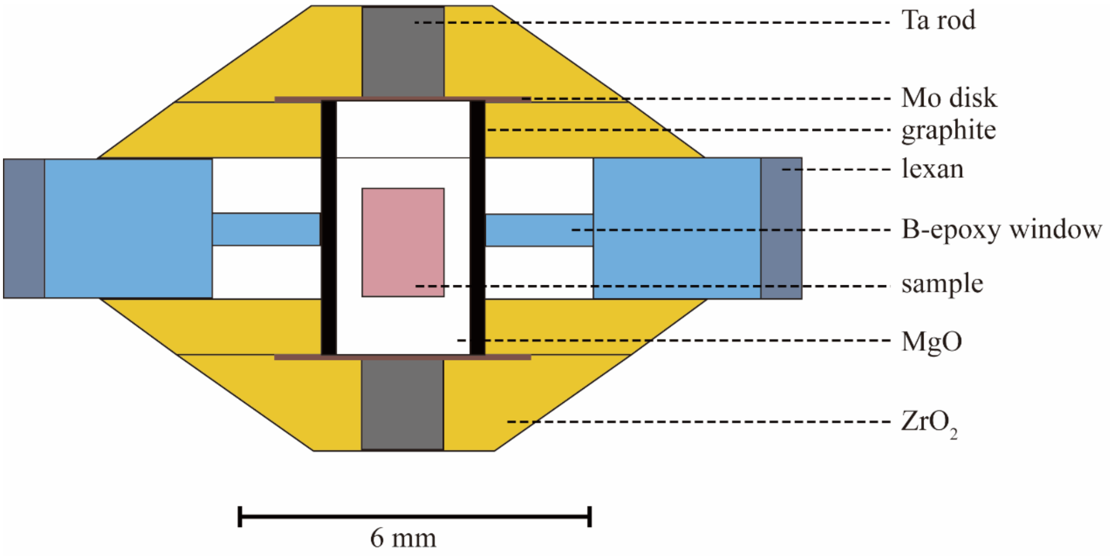

Fig. 2-14. PEP basic cell designs (zirconia cap design) used in thesis (figure modified from Yamada et al., 2011).

2.2 In-situ Synchrotron X-ray Sources

Synchrotron radiation has a significant impact on many scientific fields. A synchrotron light source is a source of electromagnetic radiation, which is usually produced by a storage ring and other specialized particle accelerators, typically accelerating electrons (Fig. 2-15). Once the high-energy electron beam has been generated, it is directed into auxiliary components such as bending magnets and insertion devices (undulators or wigglers) in storage rings, which supply the strong magnetic fields perpendicular to the beam to convert high energy electrons into photons and keep the accelerated electrons in a curved path. X-ray radiation is emitted and delivered to each beamline from the accelerated electrons as they change direction. Four generations of synchrotron sources have been generally defined. The first generation was built to understand the fundamental particle interactions and laws of matter. The second generation was initially built to produce X-rays. Synchrotron storage rings optimized for insertion devices are called the third-generation light sources. The first high-energy fourth-generation synchrotron was to employ a new magnetic configuration to circulate and focus the electrons at the European Synchrotron Radiation Facility (ESRF), Grenoble, France, which can produce an X-ray beam 100 times more brilliant and coherent than before. User beamlines comprise crystal and/or mirror optics designed to tailor the electron beam for specific types of experiments. On a beamline, the desired energy is selected using a monochromator and delivered in the experimental hutch.

Fig. 2-15. Synchrotrons used in our study: left: PETRAIII (Hamburg, Germany) and right: APS (Argonne National Laboratory, Argonne, USA).

2.2.1 X-ray fluorescence

X-ray fluorescence (XRF) is the emission of characteristic "secondary" (or fluorescent) X-rays from a sample, which has been excited by being bombarded with high-energy X-rays or gamma rays. Specifically, when samples are excited by a primary beam of X-rays, interaction of X-ray photons and atoms causes the ionization of inner shell orbital electrons by so called photo-electric effect. Such an atom is unstable and decay to a more stable electronic configuration via transition of an outer shell electron to fill the vacancy caused by ionization. In falling, this electron release energy as a secondary "fluorescence" X-ray photon, the energy of which is equal to the energy difference of the two orbitals involved. After correction for X-ray absorption and enhancement effects, the intensity of measured characteristic fluorescence radiation is proportional to the atomic concentration of the element. Besides, XRF is normally insensitive to the oxidation state of elements because X-ray emission involves inner shell electrons.

Additionally, the energy difference between electron orbital energy levels increases systematically with the atomic number of the element, resulting in an increase in the energy of X-ray fluorescence emissions (Janssens et al., 2000).

Since excitation of atoms results in the emission of several fluorescent lines, individual lines are normally identified by the orbital level in which the electron vacancy was created. The most sensitive response is generally obtained by fluorescence of K-lines, which result from transitions following ionization of a K-shell electron. Two principal K-lines are K_α (L to K orbital shells) and K_β (M to K orbital shells). The K_α emission is the most intense, which is usually chosen for analytical measurements (Potts and Webb, 1992).

The first X-ray fluorescence microprobe was reported in 1972, using a pinhole and a condensing mirror (Horowitz and Howell, 1972). The first X-ray microprobe was constructed in 1977, designed to test for superheavy elements (Spark et al., 1977), employing a 30-150 μm beam of 37 keV energy. At the second-generation synchrotron rings, the geological rare earth element (REE) was preferably analyzed by using their L lines (Janssens et al., 1998). To resolve the multiple lines of REE, a wavelength-dispersive (WD) rather than energy-dispersive (ED) detection of the fluorescent radiation was used. After the third-generation synchrotron facilities, Rindby et al. (1997a, b) have reported that with the use of a 13 keV monochromatic beam, relative detection limits in organic samples for the element Ca-Zn were in sub-ppm level.

Thus, XRF has a justifiable reputation for the high precision of analytical measurements. It is capable to determine a wide range of trace elements with up to ppm detection limits. Even XRF measurements depends on matrix dependent X-ray absorption effects, mathematical models for the correction of these phenomena are well-characterized and have attained a high degree of accuracy. And this method will be used to investigate Xe distribution behaviour in chapters 3, 4 and 5.

2.2.2 X-ray diffraction

This part gives brief background information of the principles of the X-ray diffraction techniques before focusing on angle-dispersive and energy-dispersive X-ray diffraction. The wavelength of X-rays has similar range as interatomic distances or unit cell sizes (0.1 to 100 Å), diffraction thus can be produced by the elastic scattering of X-rays. The scattering power of an atom depends on its number of electrons because X-rays are scattered by electrons. Scattering factor decreases with the scattering angle due to the interference between scattered waves from different portions of the electronic cloud of an atom. In Bragg's representation, X-ray diffraction can be used to determine the d-spacings of different lattice planes (hkl). The X-ray diffraction condition can be described by the following Bragg equation:

$$2d_{hkl}sin\theta_{hkl} = n\lambda \tag{2.1}$$

where λ is the incident X-ray wavelength, θ is the diffraction angle and n is an integral number. There are two frequently used X-ray diffraction techniques: single crystal diffraction. We will focus on the latter in this thesis as only it is used in our work. Good particle statistics are crucial to obtain powder diffraction patterns. The powder diffraction at high *P* can be combined with either energy-dispersive X-ray diffraction or angle-dispersive X-ray diffraction. However, due to the isotropy, diffraction patterns from all of the lattice plane families can overlap. Consequently, crystal structure determination is extremely challenging from powder diffraction.

2.2.3 Angle-dispersive X-ray diffraction (ADXRD) combined with X-ray fluorescence

Angle-dispersive X-ray diffraction (ADXRD) is a non-destructive tool for the determination of crystal structure, which use a monochromatic energy beam to excite the sample, and the full diffractogram is obtained by measuring at multiple scattering angles (Fig. 2-16). The diffraction patterns are recorded by a 2D detector (area detector).

The factor determining the quality of diffraction data is the resolution, defined as the ratio of the uncertainty and d-spacing ($\Delta d/d$). According to equation 2.1, Δd depends on the deviations of Bragg angle, $\Delta\theta$, and of X-ray energy, ΔE:

$$\frac{\Delta d}{d} = \frac{\Delta E}{E} + |cot\theta|\Delta\theta \qquad (2.2)$$

High resolution (i.e., $\Delta d/d < 10^{-4}$) indicates peak positions are more accurately determined and signals can be better resolved. ADXRD always has much better resolution compared to EDXRD signal.

In our experiments, angle-dispersive diffraction patterns were recorded on a CsI bonded amorphous silicon detector (Perkin Elmer XRD 1621), while XRF signal was collected on a Vortex® 60-EX silicon drift detector. The volume sampled by XRF was slightly smaller than the volume probed by XRD and great care must be taken to align the XRF detector with the XRD focal point (cf. section 3.3.1).

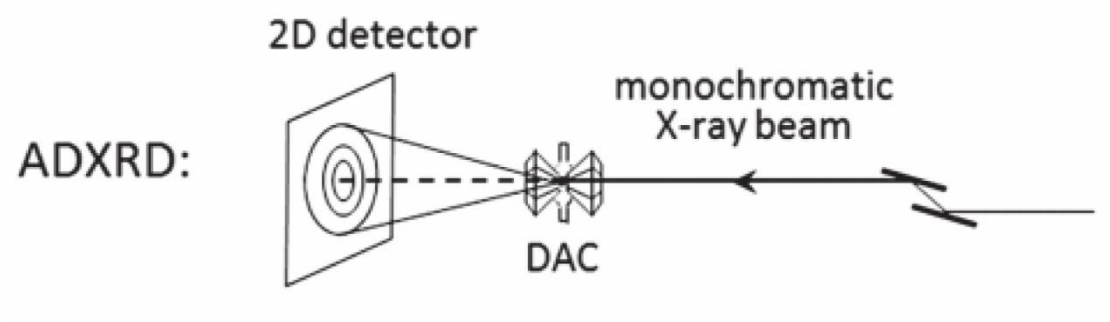

Fig. 2-16. Geometry of ADXRD used with diamond anvil cell, from Liu (2016).

2.2.4 Data treatment for angle-dispersive X-ray diffraction (ADXRD)

As discussed above, we can obtain a diffraction pattern using an 2D plate from ADXRD, with the intensity as a function of the diffraction angle (Fig. 2-17a). For both crystal and amorphous phases data processes in our work, the first step is to correct the raw data before analysis of the diffraction data. It includes:

(1) Remove the Bragg peaks from the image plate due to scattering from the single crystal diamond anvils (Fig. 2-17b), and the geometry of the cells with signal cut-off

caused by the limited opening of the tungsten carbide seats (~80°) (Fig. 2-17c) by applying a mask in Fit2D (Hammersley, 1998) or Dioptas (Prescher and Prakapenka, 2015) software.

(a) without mask

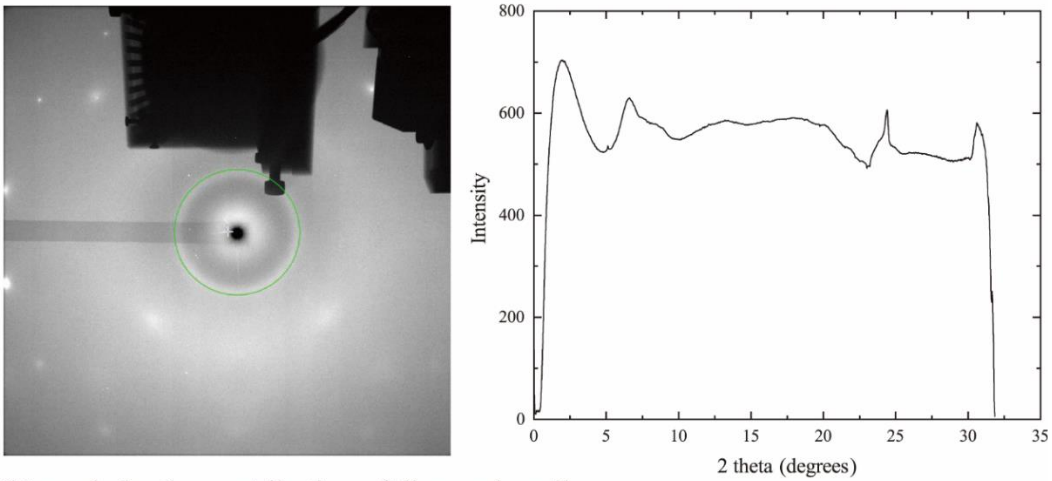

(b) mask the the contribution of diamond anvil

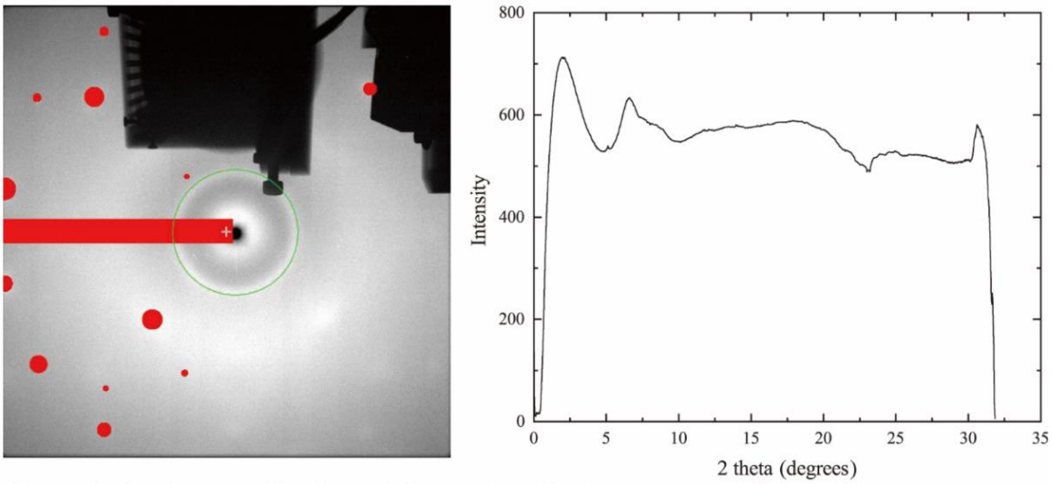

(b) mask the the contribution of diamond and the geometry of the cell

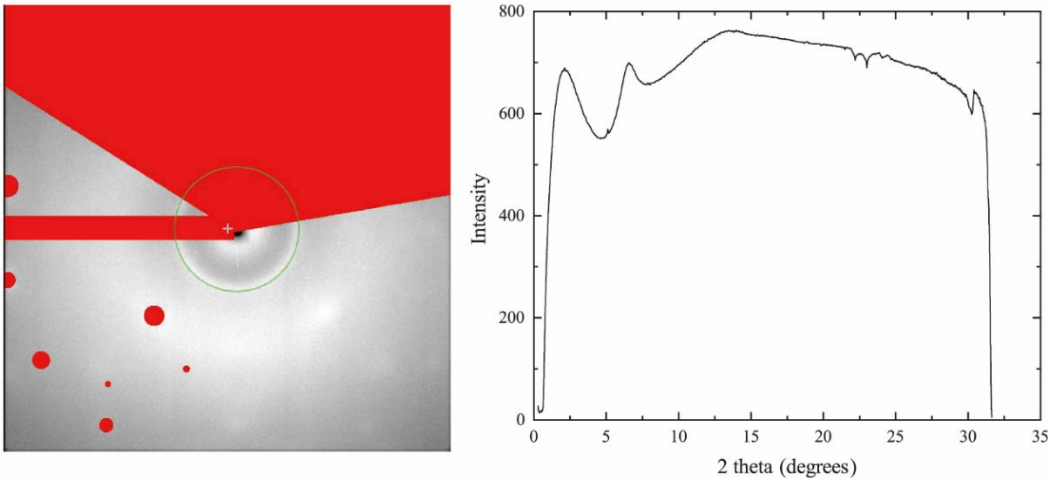

Fig. 2-17. Image plates and integrated spectra processed with Fit2D. (a) Without mask; (b) corrections of diamond diffraction signal; and (c) correction of cell geometry.

(2) After step (1) we can get an intensity with scattering from both sample and background (Fig. 2-18). Background removal is the trickiest but the most significant step. In order to remove this from the sample signal, we collected X-ray diffraction patterns with an empty gasket inserted in the DAC at room conditions, filtered by the gasket aperture and surrounding air before every experiment. To ensure the same corrections for polarization and flux normalization, we used the same mask for the sample (plus background) signal and empty gasket signal. The background spectra was then integrated from the image plate and scaled to the sample (plus background) signal.

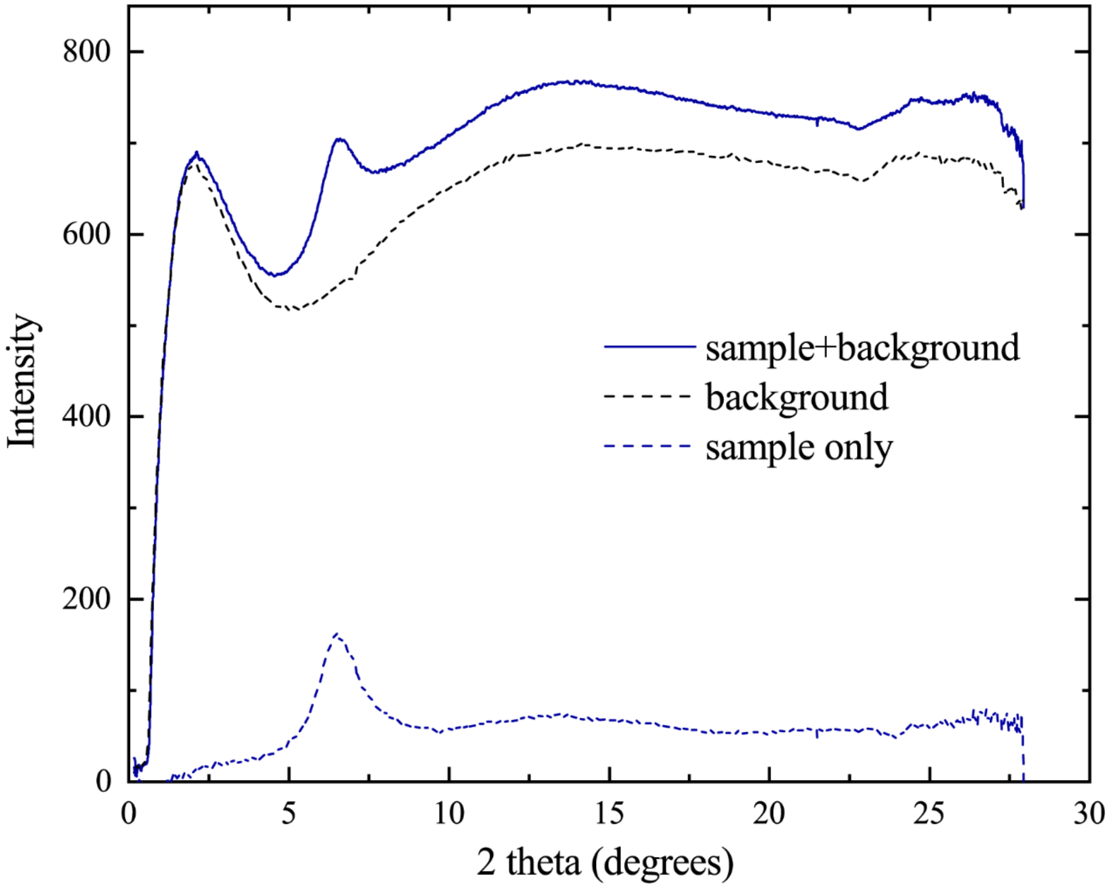

Fig. 2-18. Process of background scaling and removal for H_2O coexisting with plagioclase system in a resistively heated DAC.

(3) After baseline subtraction, the crystal diffraction pattern is treated using Rietveld refinement (Rietveld, 1967, 1969) through many programs such as Fullprof (Rodriguez-Carvajal, 1990) and GSAS (Larson and Von Dreele, 1994). A theoretical diffraction pattern was firstly established via crystal structure, instrumental and microstructural information, and a least squares algorithm was further used to minimize the difference between the calculated and observed pattern by adjusting model parameters (cf, section 3.3.2). While for the amorphous phase, the measured signal can be used to obtain the structure factor $S(q)$ and the pair distribution function, G(r) following Sanloup and de Grouchy (2018) (cf, section 5.3.1). The wave vector (momentum transfer) q, is given by:

$$q = 4\pi \cdot sin\theta/\lambda \tag{2.3}$$

where θ is the diffraction angle, and λ is the wavelength of the beam.

The structure factor $S(q)$ can be defined as:

$$S(q) = \frac{\alpha I_{ech}(q)}{Z^2 f(q)^2} \tag{2.4}$$

where $I_{ech}(q)$ is the sample signal as a function of the wave vector, Z is the average atomic number, $f(q)$ is the effective form factor, and α is the normalization factor:

$$Z = \sum_i \chi_i Z_i \tag{2.5}$$

$$f(q) = \frac{\sum_i \chi_i f_i(q)}{Z} \tag{2.6}$$

$$\alpha = \frac{-2\pi n + \int_0^{q_{max}} (\frac{\sum I_{incoh}(q)}{Z^2 f^2(q)} + S_\infty)}{\int_0^{q_{max}} (\frac{\sum I_{coh}(q)}{Z^2 f^2(q)} + S_\infty) q^2 dq} \tag{2.7}$$

$$n = \rho N_A / M \tag{2.8}$$

where Z is the average atomic number, χ_i the proportion of the element i, Z_i the atomic number of the element, f_i the shape factor of the element, q_{max} the maximum experimental wave vector, n the atomic density, N_A the Avogadro number, ρ the mass density, M the molar mass of the sample, S_∞ the value of the structure factor at infinity, I_{incoh} and I_{coh} the incoherent and coherent scattering signals of the sample.

The total radial distribution function, G(r) can be calculated by Fourier transform of the structure factor:

$$g(r) = \frac{1}{2\pi^2 rn} \int_0^\infty qS(q)\sin(rq)\,dq \qquad (2.9)$$

where r is the distance in Å.

2.2.5 Data treatment for X-ray fluorescence

There are basically three different concepts of quantification: alpha-coefficient, fundamental parameter (FP) and Monte Carlo (MC) simulations methods. The first one need multitudes of standards similar to the unknown sample, while the latter two need a set of reference standards which are not necessarily similar to the measured sample. The fundamental parameter method (Criss and Birks, 1968) is widely used for reference free quantification due to the moderate computation complexity in comparison to MC simulations. The FR method uses the theoretical relationship between weight fractions and net X-ray intensities. The initial beam flux I_0 will reduce to the intensity $I(z)$ at a depth (z) of the sample:

$$I(z) = I_0 e^{-\mu(E_0)\cdot\rho\cdot z\cdot sin(\alpha)} \qquad (2.10)$$

where ρ is the density, α angle of incidence on the sample, and μ the mass absorption coefficient and is equal to:

$$\mu(E_0) = \sum_i w_i\, \mu_i(E_0) \qquad (2.11)$$

where w is the weight fraction of analyte i.

The primary fluorescence intensity of one element can be expressed by: (1) the attenuation of the exciting radiation; (2) the attenuation of the fluorescence radiation on the path to the detector; and (3) the production of the fluorescence radiation at depth z. Generally speaking, quantification of X-ray fluorescence data needs two steps: (1) evaluate the spectrum to extract the net peak areas; (2) convert the net peak areas into concentrations.

In our work, the XRF data was processed with PyMcA software (Solé et al., 2007). The calibration for energy vs channels of XRF data was done by measuring two NIST standards glasses: NIST610 and NIST612 (Pearce et al., 1996). Concentration that converted from XRF data was calibrated not only from the measurements on two double-polished glasses: one basalt glass with 0.48 wt% I and one haplogranite glass with 3.54 wt% Xe, but also by measuring sanidine glass with 2.60 wt% Xe loading in a gasket placed in DAC (Fig. 2-19).

For a homogeneous sample with thickness d (one layer), the count rate of the areas A of an element group of lines can be defined as:

$$A = I_0 c \frac{\Omega}{4\pi} \sum_j \frac{R'_j}{\sum_j R'_j} \tag{2.12}$$

where I_0 is the incident beam rate, c the mass fraction of the element in the sample, $\Omega/4\pi$ the detector geometric efficiency, R_j' the relative intensity ratios:

$$R'_j = \frac{w_j P_j(E_0) R_j T_A [1 - T_D(E_j)]}{\mu_T(E_0) + \mu_T(E_j)\, sin\,\psi_1 / sin\,\psi_2} \times \{1 - \exp\,[(\frac{\mu_T(E_0)}{sin\,\psi_1} + \frac{\mu_T(E_j)}{sin\,\psi_2})\rho d]\} \tag{2.13}$$

where T_A the absorption correction term, ω_j the fluorescence yield of the considered shell, P_j the possibility to have a vacancy in the j shell, μ_T the total mass attenuation coefficient of the sample, E_0 and E_j the incident photon beam energy and the energy of X-ray line, ρ the density, ψ_1 and ψ_2 the angels of the incoming and fluorescent beam respect to the sample surface.

As for a sample containing more than one phase, the data was dealt with a multi-layer way. For multilayered sample, attenuation of both the incoming and outgoing beams through the different layers were considered. Thus, the program gives a concentration of the entire signal from each layer. To estimate each layer's contribution, the thicknesses of layers need to be figured out.

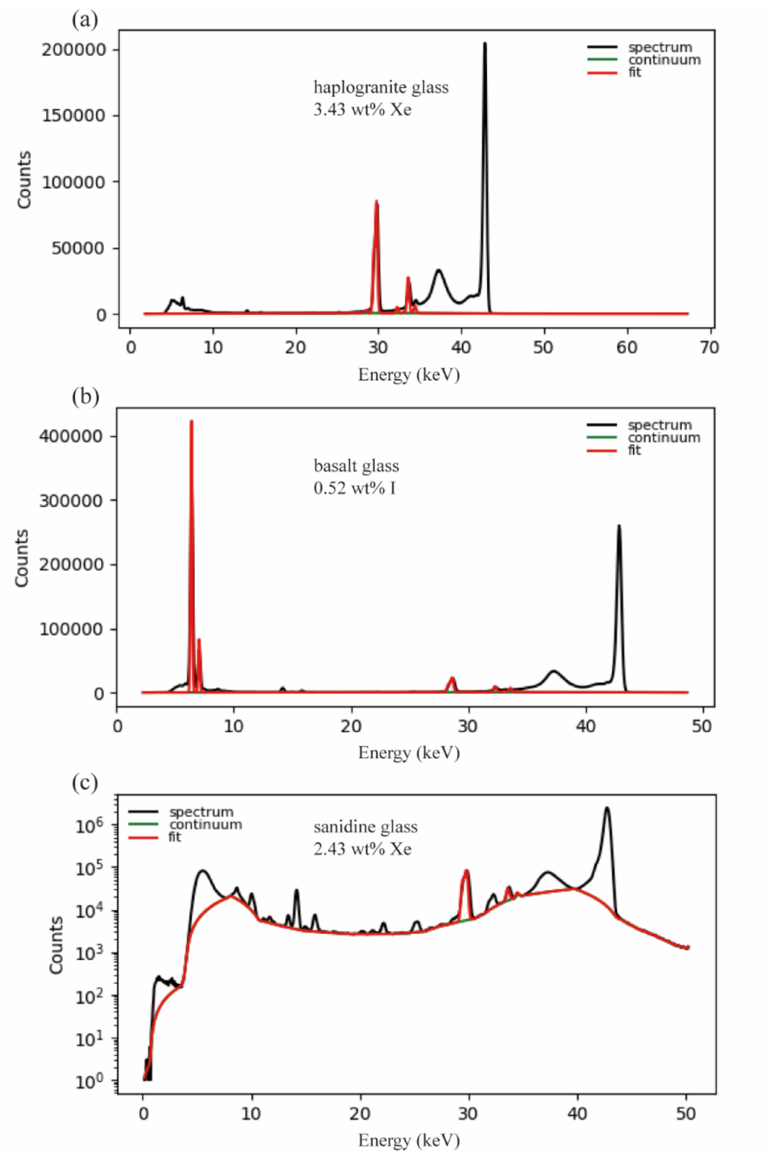

Fig. 2-19. XRF data calibration with (a) haplogranite glass with 3.54 wt% Xe; (b) basalt glass with 0.48 wt% I; and (c) sanidine glass with 2.60 wt% Xe loading in DAC. Numbers in the figure are calculated values using PyMca software.

2.2.6 Energy-dispersive X-ray diffraction (EDXRD) and X-ray fluorescence

In contrast to ADXRD, EDXRD uses a polychromatic (actually a white beam) energy beam to excite the sample. A solid-state detector (SSD) with energy resolution is held at a fixed scattering angle (Fig. 2-20). Consequently, the signal is acquired as intensity vs. energy of the diffracted photons, with XRF lines simultaneously detected. The detector angle is always calibrated with a diffraction standard. However, due to the limited energy resolution (e.g., 25 eV for Ge detector), EDXRD diffraction signals are typically broad and overlapped at higher energies, making it difficult to fit the positions and intensities. Xe concentrations obtained from energy- dispersive X-ray fluorescence signal were processed following the method described in Simabuco and Nascimento, (1994), where the absolute intensity of the fluorescence signal depends on the five following factors: (1) beam intensity, (2) Xe concentration in the sample, (3) volume of the sample probed by X-rays, (4) absorption by the sample and the surrounding cell-assembly, (5) detector sensitivity (cf section 3.3.2):

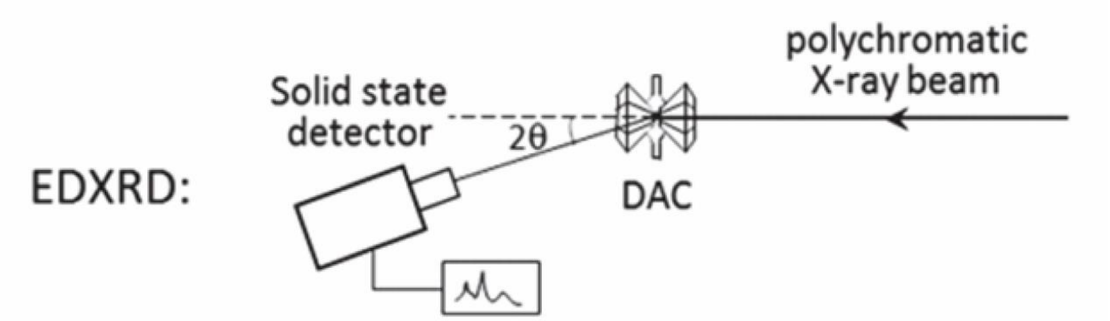

Fig. 2-20. Geometry of EDXRD used with diamond anvil cell, from Liu et al. (2016)

2.3 Ex-situ characterization

To characterize the starting glasses and the samples recovered from the high pressure and high temperature (*HP-HT*) experiments, several pieces in different areas of the capsule of each sample (to be representative of the entire sample) or the whole sample were embedded in epoxy resin, then polished and metallized with carbon. The samples were measured via following analytical techniques:
Scanning Electron Microscopy (SEM), Electron Microprobe analysis (EPMA), Raman spectroscopy and X-ray tomography technique.

2.3.1 Scanning Electron Microscopy

A SEM is a type of electron microscope that uses a focused beam of high-energy electrons to create images of a sample at the surface. The signals to produce an image result from interactions of the electron beam with atoms at various depths within the sample, which produce various types of signals including secondary electrons (SE), backscattered electrons (BSE), characteristic X-rays and light (cathodoluminescence) (CL), absorbed current and transmitted electrons. SE are valence electrons ejected from the sample during inelastic scattering interaction with the incident electron beam, which have very low energies (< 50 eV). Consequently, SE can only originate from within a few nanometers below the sample surface. However, BSE are beam electrons that are reflected from the sample by elastic scattering, which consist of high-energy electrons produced by backscattering nearly perpendicularly to the incident electron beam. Since they have much higher energy than SE, they are probing from deeper locations (few micrometers of the sample) and result in the less resolution than SE images. Since heavy elements backscatter electrons more strongly than light elements, BSE are sensitive to chemical composition, that is, high-Z atoms backscattered electrons more efficiently, and thus appear brighter in the image (Fig. 2-21). Characteristic X-rays that are produced by the interaction of electrons with the sample can also be detected in an SEM equipped with energy dispersive X-ray spectroscopy. Analysis of the X-ray signals can therefore be used to map the distribution and estimate the abundance of elements in the sample. A high energy beam is required to excite inner-shell electrons for identification of heavy elements (e.g., 15- 20 KeV for Xe).

In our work, recovered samples were analyzed with a Zeiss Ultra 55 field emission SEM both at IMPMC and OSU Ecce Terra, Sorbonne Université with an acceleration voltage of 15-20 keV and a working distance of 7.5 mm in backscattered mode. As discussed above, Xe is much heavier than Ca, Si, Mg, Al or O and backscatter electrons far more intensely than the surrounding silicate material, appearing brighter (Fig. 2-21).

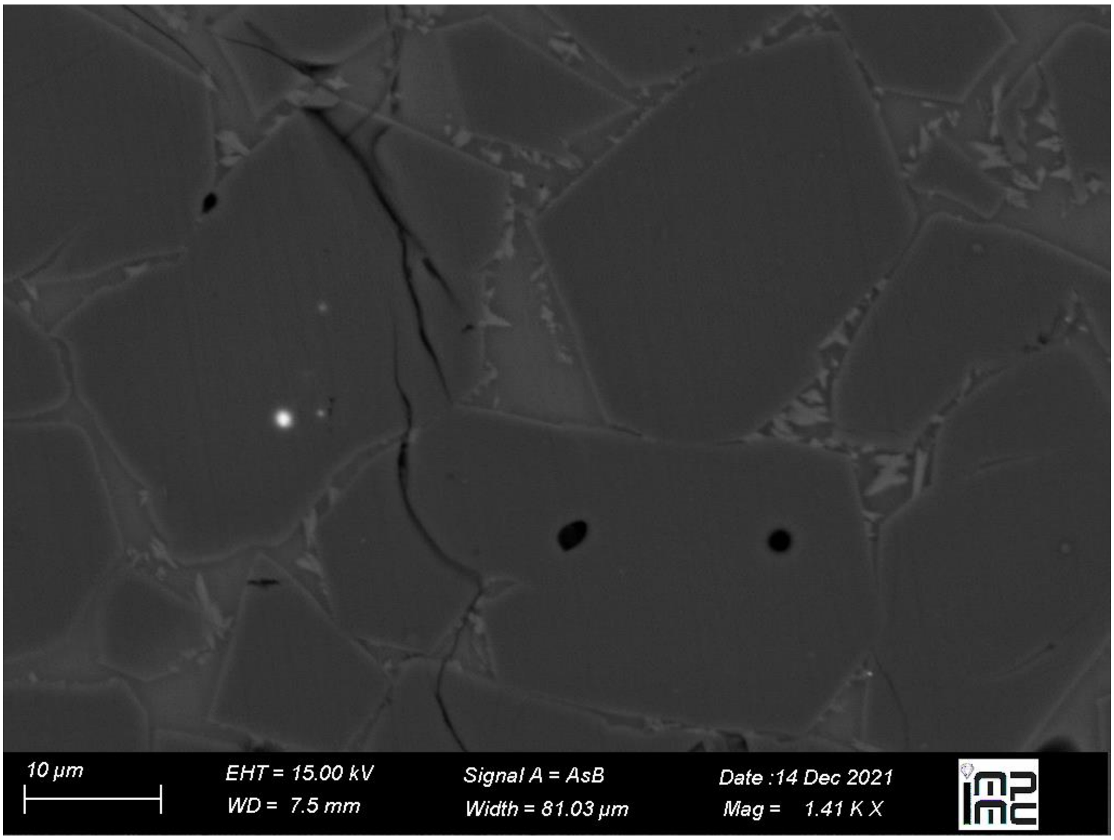

Fig. 2-21. SEM image of Run PC252b. Black crystal is olivine, brighter crystal is pyroxene, coexisting with melt (grey area). Bright bubbles in olivine crystal are Xe bubbles, black roundish shapes inside crystal are bubbles open upon polishing or under the electron beam.

2.3.2 Electron Microprobe analysis

EPMA (electron probe microanalysis) is an microbeam instrument to non-destructively determine the chemical composition of small volumes of solid materials. It works similarly to SEM. Low-energy electrons are generated from a tungsten filament, a lanthanum hexaboride crystal cathode or a field emission electron source, and accelerated by a positively biased anode plate to 3-30 keV. The electrons are then collimated and focused by a series of magnetic lenses and apertures (Fig. 2-22). During the resulting beam electrons interact with bound electrons in the innermost electron shells of various elements' atoms in the sample, the bound electrons can be scattered from the electron shell and ionize the atom. A photon will be emitted by the binding energy difference between the electron shell in which the vacancy was produced and the shell from which the electron fills the vacancy, emitting characteristic X-rays of the analyzed elements. Instead of an energy dispersive X-ray spectrometry (EDS), wavelength dispersive spectrometry (WDS) is used, thus EPMA has difficulties to determine low-Z elements (such as H and Li), and relatively volatile elements such as Na, or K. The quantification is done by comparison of the intensity of a line characteristic of an element emitted by the sample with that of reference standards.

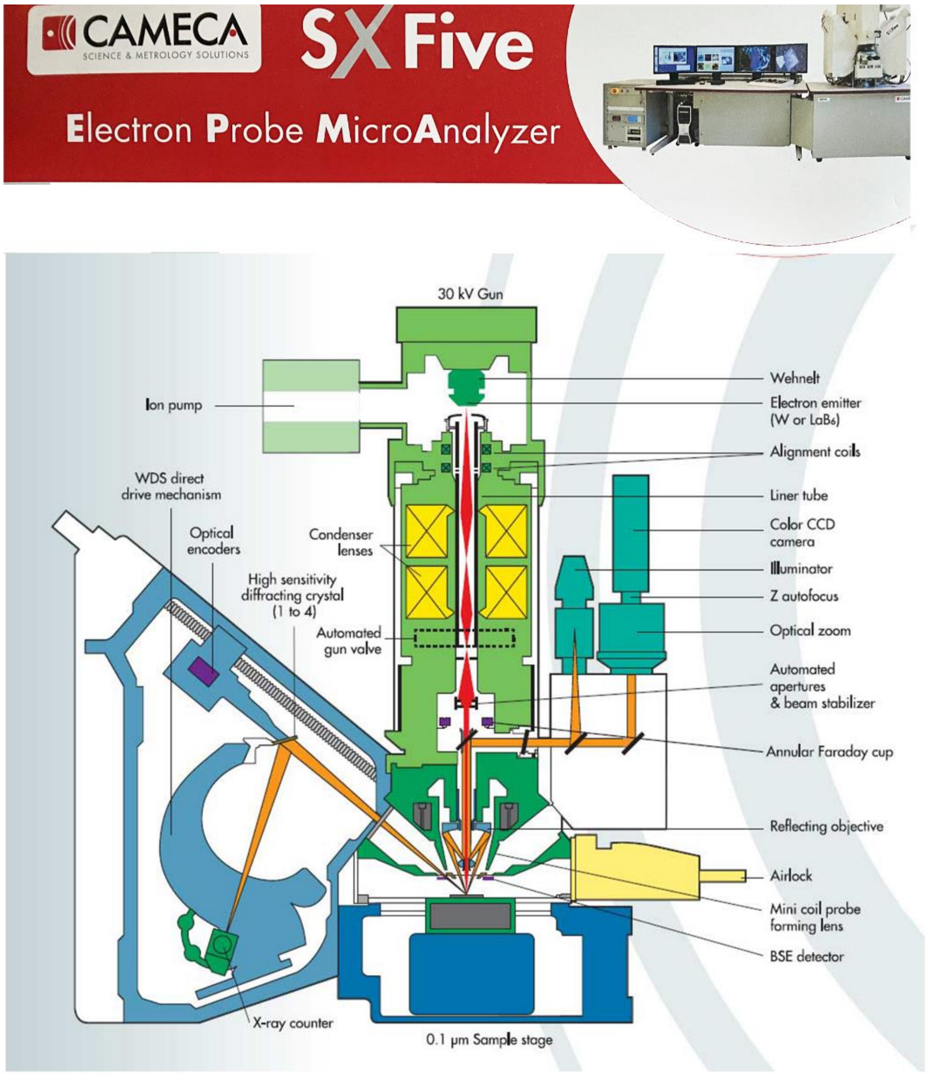

Fig. 2-22. Schematic sketch of a cross-section for the electron microprobe Cameca SX-FIVE.

In our work, major elements were analyzed using a Cameca SX-FIVE electron microprobe analyzer (EPMA) on the Camparis platform at OSU Ecce Terra, Sorbonne Université. Accelerating voltage was set to 15 kV, and we used two different conditions with an overall measurement time of 4min, i.e., a counting time between 10s and 20s per element. The first program, with an accelerating voltage of 15keV and a current of 4-5 nA, allows to measure the major elements on the five different spectrometers: Na Kα, Si Kα, Al Kα, K Kα, Ca Kα, Fe Kα, and Mg Kα. The second program with a current of 40 nA makes it possible to measure Xe on two spectrometers on Xe Lα. To avoid damage such as Na loss and the destruction of the sample, we used a delocalized beam focused to 15 μm diameter on the sample. For each sample, 10-30 points measurements were acquired to get an average value. Xe calibration was established following the procedure developed by Montana et al. (1993) by measuring the counts for the neighbouring elements, I (CuI) and Cs (CsCl). And a Xe-bearing sanidine glass PC53 was used as the standard (cf., section 3.2.5).

2.3.3 Raman spectroscopy

Raman spectroscopy is a no-destructive chemical analysis technique to provide information of vibrational modes of molecules, which depends on inelastic scattering of photons, known as Raman scattering. The laser light interacts with molecular vibrations, leading to the shift in energy of the laser photons. Inelastic scattering indicates the energy of the emitted photon is lower or higher than the incident photon. The scattered photon will shift to keep the same total energy. If the final state is higher than the initial state, the scattered photon will be shifted to a lower frequency, so called a Stokes shift. Conversely, If the final state is lower, the scattered photon will be shifted to a higher frequency, called an anti-Stokes shift (Fig. 2-23).

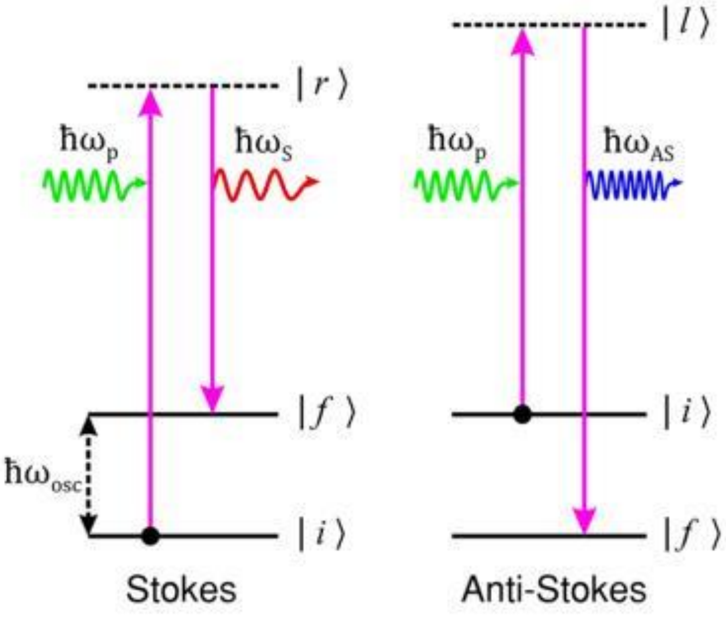

Fig. 2-23. Energy transfer process in Stokes (left) and anti-Stokes (right) Raman scattering, from Jones et al., (2019).

Typically, a Raman spectrum features peaks with the wavelength position and intensity of the Raman scattered light, corresponds to the specific molecular bond vibrations. Identification of the sample can be easily done by comparison with the Raman spectral libraries. In addition, the intensity of the peak is related to the concentration. Quantitative information can be calculated with the relative peak intensities (cf, section 3.2.6).

Most of Raman analyses in this thesis were performed in the Raman lab at IMPMC on a Jobin-Yvon Horiba HR460 spectrometer using a single-grating monochromator with 1500 gratings/mm and an argon laser (514.5 nm wavelength) with the power of 1-11.4 mW on the sample. Spectra were acquired for 45-60s with 2 accumulations at room conditions.

2.3.4 X-ray tomography technique

X-ray tomography uses X-rays to penetrate objects and create cross-sections, which can be used to undamaged recreate a 3D model (Fig. 2-24). When the radiation emitted by an X-ray source passes through the sample, part of the X-ray radiation is absorbed, and the residual radiation is captured by an X-ray detector as a two-dimensional radiographic image. The grayscale of the image depends on the X-ray attenuation, that is it, the proportion of absorbed X-rays, which is controlled by the density and attenuation coefficient of the object. The measured sample is rotated step by step to get hundreds of this two-dimensional image in sequence. The three-dimensional information can be extracted using a suitable program such as ImageJ (Abràmoff et al., 2004). Thus, it has great benefit to get phase fractions of recovered samples, which is needed to interpret the X-ray fluorescence signal.

Fig. 2-24. X-ray tomography set-up in the AST-RX platform.

To locate the phase boundaries between phases in the sample (e.g., melt and crystal phases in our work), the contrast of the X-ray image (grayscale in the image from black to white) obtained from the difference in absorption of X-rays by the phases, is required to be large enough (Fig. 2-25a). The X-ray attenuation of a sample can be determined from the Beer-Lambert law:

$$I = I_0 \cdot \exp(-(\mu/\rho) \cdot \rho \cdot d) \tag{2.12}$$

where I_0 and I are the intensities of the incident and transmitted X-rays, respectively; μ, linear attenuation coefficient; ρ, density; d, thickness of the sample.

The mass attenuation coefficients (μ/ρ) can be written as:

$$\mu/\rho = \sum \omega_i (\mu/\rho)_i \tag{2.13}$$

where ω_i is the atomic mass fractions.

Thus, the sample with heavier atoms would have higher mass attenuation coefficients and absorb more X-rays (Fig. 2-25b). H_2O, CH_4 hydrate, and CO_2 have similar mass attenuation coefficients. On the contrary, attenuation coefficients Xe and Kr hydrates are much higher because of the heavy Xe and Kr atoms as the guest species and high mass fractions in the hydrate structure (Takeya et al., 2020).

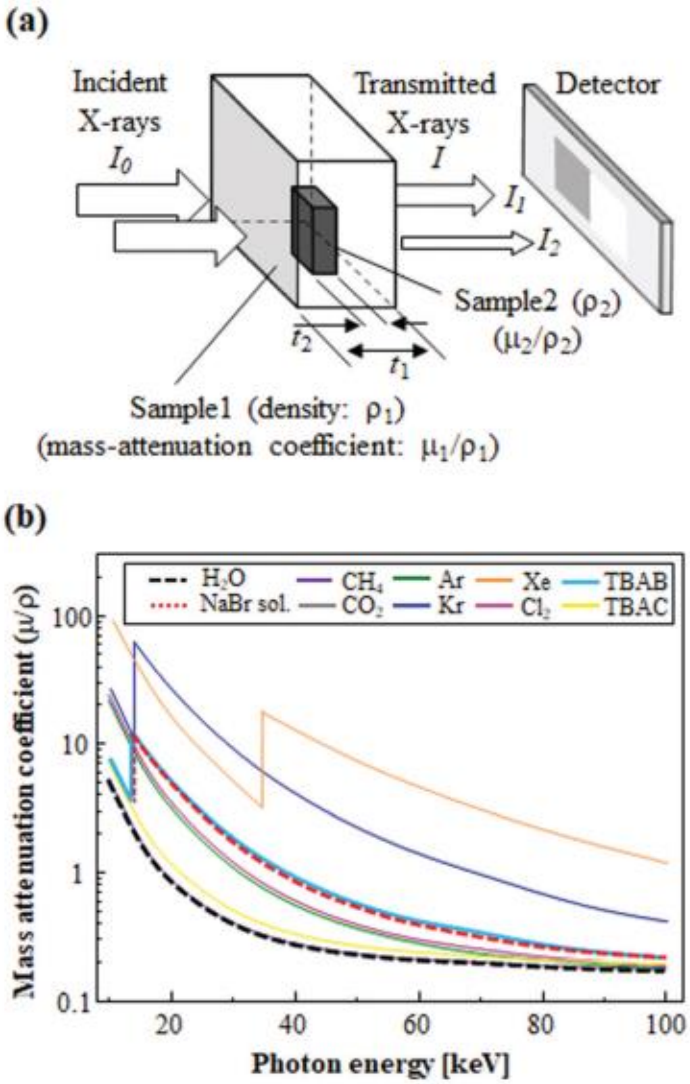

Fig. 2-25. (a) Schematic diagram of X-ray absorption, and (b) mass attenuation coefficient of clathrate hydrates vs photon energy. H_2O, CH_4 hydrate, and CO_2 hydrate overlap. The NaBr line represents a 10 wt% NaBr solution (figure from Takeya et al., 2020).

In our work, the quenched samples were analyzed using X-ray tomography technique at the platform AST-RX (Muséum national d'Histoire naturelle, Paris) (cf section 3.2.4).

Chapter 3: Probing the partitioning behaviour of Xe using in situ X-ray Synchrotron techniques at high P-T conditions

This paper (submitted to High Pressure Research) establishes existing but so far not used technique in Earth's sciences to determine element concentration in phases using x-ray fluorescence signal on energy dispersive diffraction data, and compares it with more classical XRF data obtained using monochromatic x-ray beam. For this purpose, the target system is hydrous albite-anorthite as its melting point is achievable using resistive-heating DACs (used for "classical" XRD). XRF from EDX data is compatible with the use of large volume presses on synchrotrons such as DESY and the APS, and hence allows to probe geological systems at higher temperatures (and higher pressures). Albeit the fact that laser-heating DAC could also produce higher *T*, it does not allow to heat the whole sample as required here.

Abstract

Understanding how xenon (Xe) partitions between crystal and melt at depth, *i.e.* where magmas form, is key to properly trace planetary processes using Xe isotopes. Partition coefficients measured on experimental samples recovered at room pressure (*P*) and temperature (*T*) span six orders of magnitude, potentially due to Xe exsolution from crystals upon quenching. We chose two *in situ* synchrotron X-ray methods to investigate Xe crystal/melt partitioning under high *P* and *T* up to 3 GPa and 1050 °C using (1) resistive-heated diamond anvil cell with angle dispersive diffraction and X-ray fluorescence, and (2) a new protocol using large volume press with energy dispersive diffraction set-up. Results from both methods agree within uncertainties, and Xe is found to become compatible at depth, suggesting the continental crust could be a Xe-rich reservoir.

This new protocol advances research to probe geological systems at the higher *P-T*

conditions accessible with large volume presses compared to resistive-heating diamond anvil cells limited to 1100 °C while maintaining homogeneous T throughout the sample.

3.1. Introduction

Noble gases, which have been extensively studied by geoscientists, play a key role to track several processes in Earth and planetary sciences, ranging from planetary and atmosphere formation (Staudacher and Allègre, 1982; Pepin, 2006), mantle convection (Allègre et al., 1983; Gonnermann and Mukhopadhyay, 2009) and tracking underground nuclear tests (Bowyer et al., 2002). However, Xe stands out amongst other heavy noble gases as it is strongly depleted relative to chondritic patterns. Up to 90% Earth's and Mars' Xe is missing from the atmosphere, which is known as the 'missing Xe paradox' (Anders and Owen, 1977; Ozima and Podosek, 1999). This issue has become one of the most challenging riddles in the planetary sciences for decades. Xenon could have escaped from the atmosphere (Zahnle et al., 2018; Avice et al., 2018), and/or could be trapped at depth. The latter scenario is supported by the demonstration of Xe reactivity at much lower pressures as a trace/minor element with planetary materials such as olivine and quartz, through the formation of Xe-O bonds (Probert, 2010; Kalinowski et al., 2014; Sanloup, 2020 and refs therein), also evidenced in deep crustal melts (Leroy et al., 2018).

However, there are still many fundamental unknowns about the chemical behaviour of Xe with planetary materials. To better constrain Xe distribution, one of the most effective ways is to investigate the partition coefficients between major silicate minerals and melts in melting and crystallizing processes. *Ex situ* measurements of partition coefficients of Xe ($D^{Xe}_{crystal/melt}$) on quenched samples span over 6 orders of magnitude (*e.g.*, 6×10^{-4} to 350 for olivine/melt partitioning) from ambient P to 1.5 GPa and 1000-1300 ºC (Hiyagon and Ozima, 1986; Broadhurst et al., 1992; Heber et al., 2007). However, Xe is found partly located in gas bubbles in these samples, resulting in inconsistencies in Xe solubility and partition coefficients whether or not bubbles are analyzed, *i.e.* whether or not bubbles reflect equilibrium at high *P*-*T* or are produced upon quenching the experiment back to room conditions. Therefore, it is questionable whether the measured solubility and partition coefficient faithfully reflect the equilibrium solubility and partition coefficient at experimental high *P*-*T* conditions. Consequently, it is essential to carry out *in situ* measurements at high *P* and *T* to evaluate partitioning of volatile elements such as Xe at depth. First *in situ* partitioning experiments between aqueous fluids and haplogranitic melt ($D^{Xe}_{f/m}$) under high *P* showed that Xe degassing is strongly *T*-dependent, varying from 2750 to 0.15 in the range of 680 to 850 ºC (Leroy et al., 2019), indicating that Xe is preferentially retained in deep crust melts in hot contexts but otherwise very efficiently degassed in the fluid. There are so far no *in situ* measurements on Xe crystal/melt partitioning at depth. Here we present a method to investigate partitioning of Xe in crystal/melt system using large volume press (LVP) with *in situ* synchrotron energy dispersive set-up (EDX), which allows simultaneous collection of diffraction and fluorescence signal under high *P*-*T*. To demonstrate the feasibility of this technique, we also conducted experiments using the more established combination of resistive-heating diamond anvil cell (DAC) with *in situ* synchrotron angle dispersive X-ray diffraction (ADX) and X-ray fluorescence analysis (XRF). Experimental data were collected up to 3 GPa and 1050 °C (Table 3-1), the maximum *T* achievable using our resistive-heating DACs. We consequently focussed this first investigation of Xe crystal/melt partitioning on a silica-rich hydrated composition which liquidus is relatively low, co-existing with either plagioclase or clinopyroxene (jadeite or omphacite, cf Table 3-1). This melt composition is a good analogue of continental crust melts, while plagioclase and clinopyroxene are two main rock-forming minerals making up the Earth's crust (Wood et al., 1970).

3.2. Methods

3.2.1 Synthesis of glasses

Starting glasses were prepared from reagent grade carbonates (Na_2CO_3 and $CaCO_3$) and oxides (Al_2O_3 and SiO_2) powders with a nominal composition of 80/20 mol% albite/anorthite ($Ab_{80}An_{20}$). Powders were firstly ground and decarbonated by slowly heating in a platinum (Pt) crucible in an atmospheric furnace from room *T* to 1000 °C, run for 10 hours, molten at 1650 °C for 1 hour, and then quenched in water. Recovered glass was crushed into powder again, and remolten twice to ensure homogeneity.

For hydration and Xe doping processes, recovered $Ab_{80}An_{20}$ glass was first loaded into one-end welded Pt capsule to which were added 12 wt% water, and Xe using a gas loading device (Boettcher et al., 1989). The capsule was brought to 2 GPa and 1500 °C using a piston-cylinder apparatus with a half-inch talc pyrex assembly, a graphite heater, and dried MgO powder packed around the Pt capsule, followed by rapid *T* quenching and decompression at room *T*. To assess the potential effect of Xe content on its distribution, glasses with two different Xe contents were used, 0.14 wt% and 0.02 wt% respectively (Table 3-2), which are far less than Xe solubility (0.32-0.41 wt%) measured in tholeiitic melt at 1.5-2 GPa (Schmidt and Keppler, 2002). There are no available data on Xe solubility in albite-anorthite melts. However, knowing that noble gases solubility increases with SiO_2 melt content (Carroll and Stolper, 1993), our experiments are well below Xe-saturated condition.

For DAC experiments, only few pieces of starting glass were needed. For large volume press experiments, more starting glass was extracted from the Pt capsule as larger amounts of sample were needed, which accidentally brought some MgO packed outside the Pt capsule into the sample, resulting in growth of clinopyroxene omphacite at high *P* (see section 3.2.5 and Table 3-1).

3.2.2 Diamond-anvil cell experiments with angle-dispersive set-up

Symmetric large opening DACs (70°) equipped with Boelher-Almax seats and 800 µm diameter culet diamonds were used to generate high *P*-*T* conditions (Boehler et al., 2004). Laser drilled Re gasket was used as sample chamber filled with Xe-doped hydrous plagioclase glass. Resistive-heating was achieved using the internal heating technique developed by Fei and Mao (1994) modifier by using a Pt wire. *T* was recorded by a type S thermocouple located on the edge of the gasket closed to the sample chamber. Pressure at ambient *T* was measured by ruby fluorescence, and was monitored at high *T* from the cell volume of a piece of gold inserted in the sample chamber.

Synchrotron experiments were performed at the beamline P02.2, Petra III (DESY, Hamburg) using a 3×8 mm^2 focused monochromatic X-ray beam at 42.7 keV, following the same strategy as in previous studies (Bureau et al., 2016; Leroy et al., 2019). At each *T* step, ADX patterns were recorded on a CsI bonded amorphous silicon detector (Perkin Elmer XRD 1621) to identify phases (*i.e.*, crystalline *vs* molten) and monitor *P* from the cell volume of the Au internal calibrant. The X-ray diffraction patterns were integrated from the images with Fit2D software (Hammersley, 1998), and the diffraction signal was Le Bail fitted using Fullprof software (Rodríguez-Carvajal, 1993) to obtain phase identification, crystal cell-volume, and melt fraction for melt + crystals data-sets. XRF signal was collected on a Vortex® 60-EX silicon drift detector with a collection time of 900-1800 s.

3.2.3 Large-volume press experiments with energy-dispersive set-up

High *P*-*T* experiments were carried out using a Hall-type press equipped with 6 hydraulic rams (mavo press LPQ6-1500-100 by Voggenreiter) at the P61B LVP-EC beamline, PETRA III (DESY, Hamburg), using a combination of 6 first-stage anvils and 8 tungsten carbide (WC) second-stage anvils. We used the 18/11 cell-assembly with truncated edge lengths of 11 mm, doped octahedra MgO with a graphite heater, ZrO_2

thermal isolator and MgO as the capsule container (cf section 2.1.3). *T* was monitored using a type C thermocouple. To constrain the X-ray path length through the sample (cf section 3.3.1), and preserve the sample cylindrical geometry, diamond cylinder (2 mm height x 1 mm inner diameter) was used as sample capsule sealed under *P* by platinum-rhodium caps.

Energy-dispersive diffraction and fluorescence signals were collected using a low energy Germanium detector (LEGe) and a diffracted beam collimated to 50×300 mm^2. The radiographic imaging system is composed of a GGG:Eu scintillator (40 μm thickness), an objective lens with 5x magnification, a mirror and a sCMOS camera. The scattering angle 2θ was calibrated by measuring MgO each time before compression, which remained constant at 7.1315° ± 0.0003°. Based on the detector position and the incident beam and collimator slit size (both 50 μm), the maximum size of the gauge volume from where the diffracted X-rays were collected in the sample is no larger than 0.6 mm^3. Pressure was derived from the equation of state of MgO (MgO cylinder surrounding the sample capsule) by recording its diffraction pattern before and after each measurement on sample to ensure that *P* was kept constant. In case the thermocouple broke down during experiments, *T* was then determined using the power *vs T* calibration curve established before failure (Fig. 3-1). Experimental conditions are reported in Table 3-1. EDX data were collected for 60 seconds for both MgO and sample, and iterated a large number of times (50-175) on the sample and averaged to optimize the signal to noise ratio for the Xe fluorescence peaks. For run HH357, the pyrophyllite gaskets on the anvils were modified with two boron-epoxy windows to reduce X-ray absorption for both the incident and diffracted X-rays. Explored *P-T* conditions along with observed phases are summarized in Table 3-1.

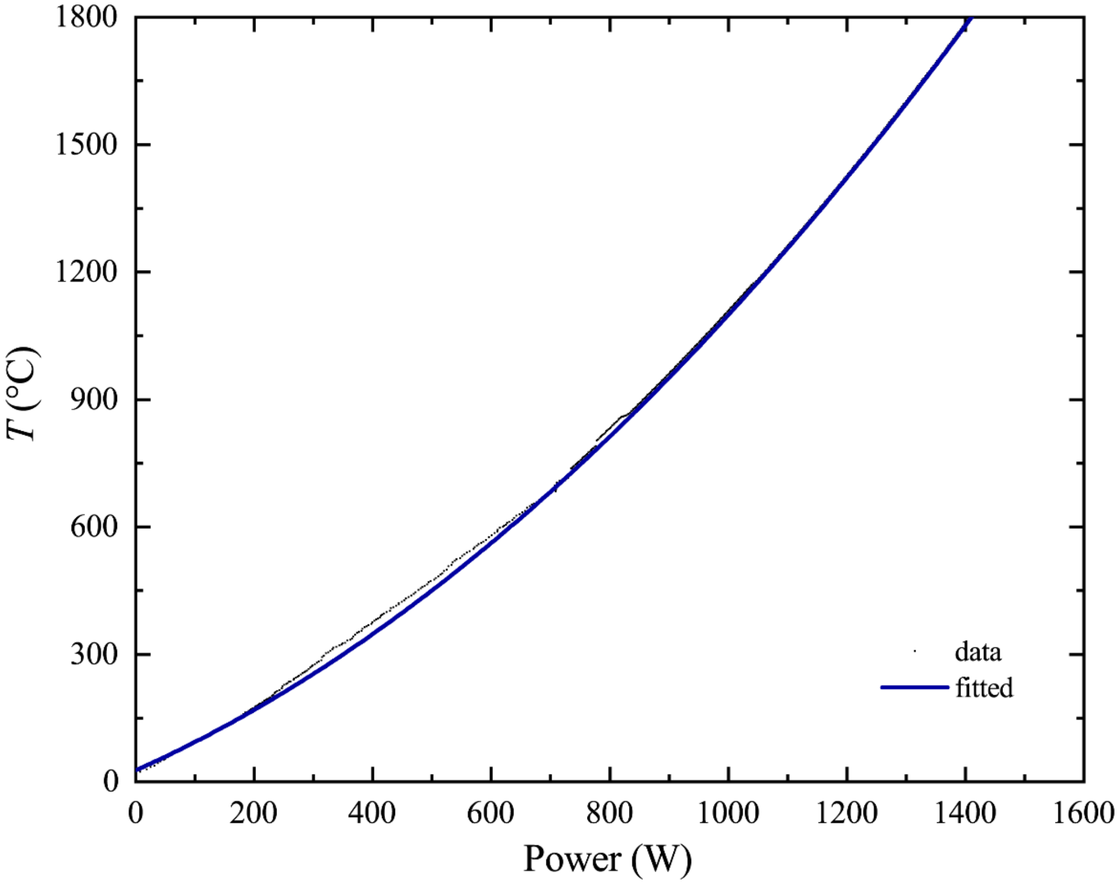

Fig. 3-1. Power-*T* calibration curve of Large-volume press experiments.

To ensure equilibrium, *T* was initially increased above the melting point, then decreased stepwise until both crystalline and molten phases co-exist, and hold for 1800s before data collection. At the targeted *P*-*T* conditions, X-ray radiography was firstly done to record sample positions, followed by EDX on the sample at two positions (one optimizing crystalline signal = 'crystal-rich', and one optimizing melt signal = 'melt-rich' with eventually pure melt), EDX on the *P* calibrant, and a final quench of the graphite furnace. For run HH357, the pyrophyllite gaskets on the anvils were modified with two boron-epoxy 'windows' to reduce X-ray absorption for both the incident and diffracted X-rays.

Table 3-1

Experimental conditions.

Run	*P* (GPa)	*T* (°C)	Duration (h)	#	State
Cell5	2[a]	1010[a]	6.5	1	melt + plagioclase
HH354	3.5	25	7.5	96	starting glass
	3.2	800		1	fully crystalline
	2.5	800		1	fully crystalline
	1.7	1000		3	melt
	1.8[a]	950[a]		93 (melt), 50 (crystals)	melt + jadeite
HH355	2.8	950	15	1	fully crystalline
	1.4	950		3	melt
	2.1	1050		15	melt + jadeite
	1.7	800		1	melt + jadeite
	1.6[a]	700[a]		107 (melt), 118 (crystals)	melt + jadeite
HH357	2.0	25	14.5	152	starting glass
	2.3	700		1	fully crystalline
	2.0	800		1	fully crystalline
	1.1	850		1	melt
	1.7[a]	850[a]		146 (melt), 175 (crystals)	melt + omphacite

Run Cell5 was conducted in DAC; Runs HH354 to 357 were conducted in LVP; # = number of scans; Duration = duration of the run at high-*T*; a, quenched *P*-*T* conditions; uncertainty on *P* is 0.3 GPa, on *T* is 50 °C. Note that run HH355 is the next-day continuation of run HH354.

3.2.4 X-ray tomography on recovered samples

For X-ray diffraction patterns that display a mixture of crystalline and molten phases (Table 3-1), it is necessary to determine the phases fractions to constrain Xe partitioning. This can be obtained from fitting the proportions of melt and crystals on diffraction data (see section 3.3.2), and was cross checked in the case of LVP experiments by carrying X-ray tomography scans on recovered samples. For this purpose, the diamond capsule, still containing the sample, was extracted from two recovered cell-assemblies after the experiments. The cell-assembly is indeed very absorbing which impedes the detection of absorption contrast between crystals and melt *in situ* at high *P-T* conditions.

X-ray tomography scans were done at the micro-CT scan facilities at the National Museum of Natural History in Paris (AST-RX platform). The voltage used was 160 kV, and the power on sample was 10 W. Detector size was 400 × 400 mm^2 with a 2024 × 2024 pixels matrix. The voxel size was approximately 2 μm, with an acquisition time of 2 seconds per frame.

3.2.5 Chemical analyses

Quenched samples together with starting glasses were put in epoxy resin and polished for Raman analysis, scanning electron microscopy, and electron microprobe analyses.

A Zeiss Ultra 55 field emission scanning electron microscope (SEM) was used with a working distance of 7.5 mm and a voltage of 20 kV for detection of Xe. Major elements were analyzed using a Cameca SX-FIVE electron microprobe analyzer (EPMA) on the Camparis platform. The beam was focused to 15 μm diameter on the sample. Accelerating voltage was set to 15 kV, with 5 nA beam current for Na, Ca, Al, Si and 40 nA for Xe, 10 s counting time for per element on both peak and background. Xe calibration was established following the procedure developed by Montana et al. (1993) by measuring the counts for the neighbouring elements, I (CuI) and Cs (CsCl). This method had been previously confirmed by analyzing one Xe-bearing glass PC53 (2.6

wt% Xe; haplogranite glass from C. Crépisson's PhD thesis [30]), for which Xe content was assessed by Particle induced X-ray emission (Leroy et al., 2018).

All analyses are summarized in Table 3-2. Based on SEM and EPMA analyses, the synthesized starting glass $Ab_{80}An_{20}$ is chemically homogeneous. Low Na_2O content likely is an artefact caused by Na loss during EPMA analysis, and the relatively low total may account for Na loss. The numerous lighter roundish zones observed by SEM in PC162a and b are too tiny to get quantitative insights (Fig. 3-2a and 2b), but are most likely Ca-rich seeds, Ca being the only major heavier element. For LVP experiments, H_2O content determined using is similar within the uncertainties in starting and quenched glasses (cf section 3.2.6), attesting that the sample remained sealed. However, H_2O losses were found for DAC experiments, which must have occurred during the quenching process because if H_2O had been lost during experiments, no melt should have been detected at experimental *T* based on hydrous albite phase diagram (Shimada, 1972).

Table 3-2.

Chemical analyses on starting glasses and recovered high *P-T* samples in wt% obtained from EPMA. Analyses are based on 10-20 data points, in brackets: standard deviation.

	Na_2O	SiO_2	CaO	Al_2O_3	MgO	Xe	H_2O*	total
$Ab_{80}An_{20}$	8.64	62.82	4.47	25.45				101.41
	(0.47)	(0.46)	(0.08)	(0.39)				
PC162a^1	4.92	57.63	3.71	21.94		0.14	10..89	99.23
	(0.19)	(1.48)	(0.13)	(0.62)		(0.01)	(1.37)	
PC162b^1	4.98	56.74	3.42	20.51		0.02	12.02	97.69
	(0.27)	(0.77)	(0.15)	(0.32)		(0.01)	(1.50)	
HH355m^2	4.84	66.80	1.22	14.80	0.01	0.05	10.76	98.49
	(0.57)	(2.02)	(0.12)	(0.67)	(0.01)	(0.01)	(1.57)	
HH355c^2	7.76	54.99	11.86	23.23	4.94	< DL		102.78
	(1.02)	(0.95)	(1.91)	(1.82)	(1.35)			
HH357m^2	7.72	60.08	2.46	17.52	1.02	< DL	11.66	100.46
	(0.98)	(0.99)	(0.12)	(0.46)	(0.15)		(1.07)	

HH357c[2]	6.81	55.57	13.45	18.57	8.37	< DL		102.77
	(0.96)	(1.11)	(1.3)	(0.94)	(0.8)			
Cell5m[3]	7.55	63.46	4.50	24.04		0.14		99.75
	(0.73)	(0.95)	(0.19)	(0.58)		(0.01)		

$Ab_{80}An_{20}$ is the dry starting glass; [1]: hydrated glasses from piston cylinder runs, [2]: samples recovered from *in situ* LVP experiments, [3]: sample recovered from *in situ* DAC experiment; H_2O* is estimated from Raman spectra (see Supplemental file for details); m = melt; c = crystal; DL = detection limit (230-260 ppm).

Note that MgO is detected in all quenched phases from LVP experiments (samples HH355 and HH357) resulting in growth of clinopyroxene due to the MgO contamination before *in situ* high *P-T* experiments (Table 3-2 and section 3.2.1). Recovered clinopyroxene crystals from LVP experiments were caracterized by Raman spectroscopy (Fig. 3-3) and SEM analyses showing calcic-magnesic cores and more sodic rims (Fig. 3-2d to 2f). This indicates that the contamination of MgO results in the transformation of albite ($NaAlSi_3O_8$)-anorthite ($CaAl_2Si_2O_8$) join to jadeite ($NaAlSi_2O_6$)-omphacite ($(CaNa)(MgAl)Si_2O_6$) join at high *P* (Bell and Davis, 1969), also confirmed by the observation of additional alumina silicate (Al_2SiO_5) in recovered sample HH357 (Fig. 3-2f). No Xe bubbles are observed in or at the periphery of quenched crystals (Fig. 3-2e and 2g). Chemical analyses show that the inclusion in the middle of clinopyroxene crystals (Fig. 3-2f) has the same composition as the melt.

In addition to H_2O, CH_4 vibrational modes are detected in the quenched glass by Raman spectroscopy (Fig. 3-4). Holes observed in recovered sample HH355 (Fig. 3-2d and 2e) thus are assumed to be exsolution of H_2O upon quenching, plus CH_4 produced at experimental conditions by reaction with the diamond capsule, also attested by the presence of some graphite crystals in the glass in one run (Fig. 3-2f and 2g).

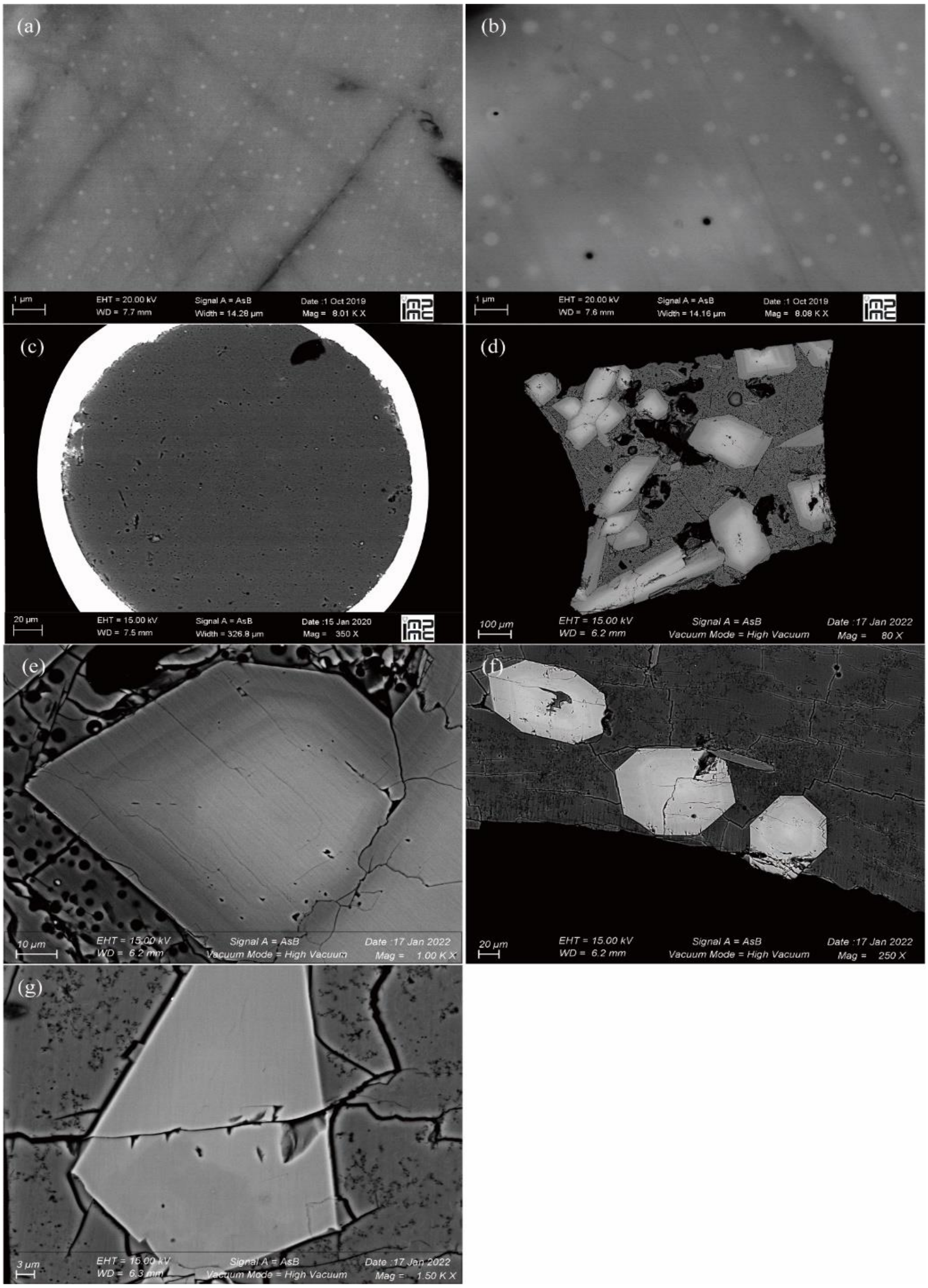

Fig. 3-2. SEM images of starting materials and high *P-T* quenched samples. Starting glasses PC162a (a) and PC162b (b); bright dots may indicate Ca-rich plagioclase seeds. (c) Quenched sample Cell5 from DAC experiments surrounded by Re gasket (bright periphery); quenched sample is mostly glass, with a few plagioclase crystals near the gasket edge. (d) Quenched sample HH355 from LVP experiment; (e) zoomed on

clinopyroxene crystal; holes are assumed to be H_2O and CH_4 bubbles open upon polishing. (f) Quenched sample HH357 and (g) zoomed on clinopyroxene crystal; grey area is melt while brighter areas are clinopyroxene crystals (Ca-rich core and Na-rich rims); black dots in the glass are graphite crystals; about 2% alumina silicate (columnar crystals) is detected.

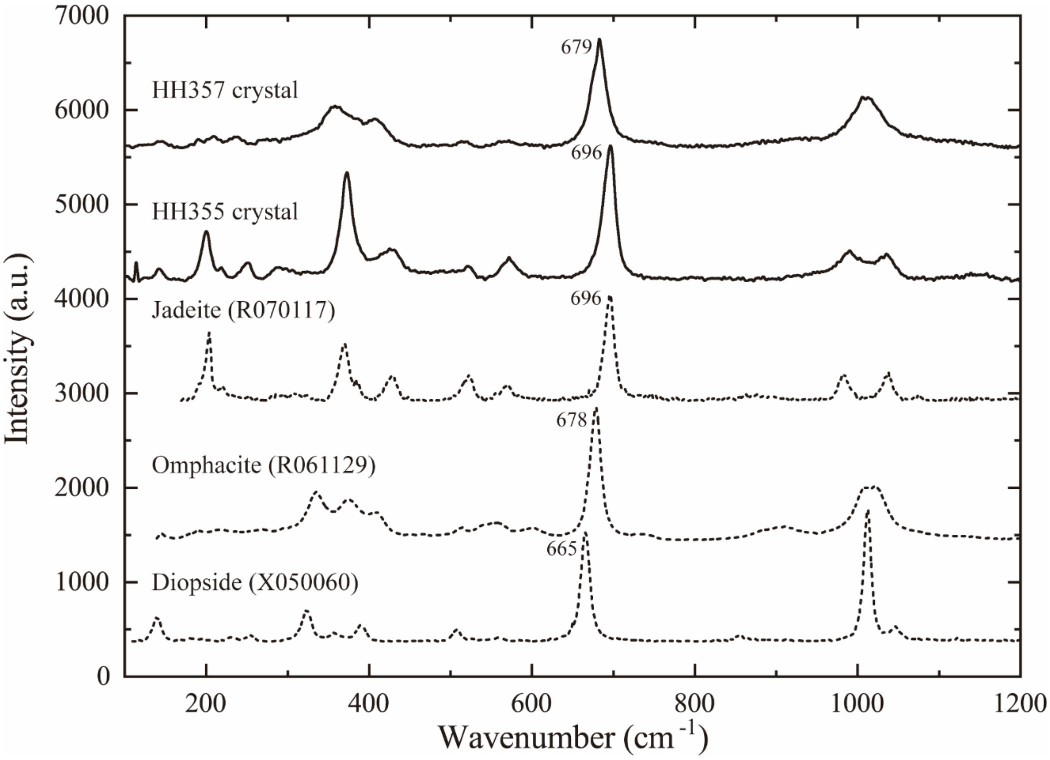

Fig. 3-3. Raman spectrum of crystals recovered from run HH355 and HH357. For comparison, Raman spectra of reference jadeite (RRUFF ID: R070117), omphacite (R061129), and diopside (X050060) from the database of RRUFF are shown.

3.2.6 Calibration of H_2O content

To constrain H_2O content in starting and recovered glasses, Raman spectra were recorded on a Jobin-Yvon Horiba HR460 spectrometer equipped with a Peltier-cooled CCD camera, a single-grating monochromator with 1500 gratings/mm and an argon laser (514.5 nm wavelength). Calibrations for spectra are performed on a Si standard firstly and then focused on the sample with power of 11.4 mW. All spectra were acquired at room *T* with accumulation time of twice 45 s. Low frequency Raman modes around 490 cm^{-1} and a shoulder near 570 cm^{-1} are associated with motions of bridged oxygen in T-O-T linkages (T = Si, Al); peak around 880 cm^{-1} is ascribed to Al-O stretching, and peak around 1000-1100 cm^{-1} to Si-O stretching in tetrahedral groups (McMillan et al., 1994; Neuville and Mysen, 1996; Neuville et al., 2006); while high-frequency modes (3000-4000 cm^{-1}) are attributed to H_2O (and OH may be) dissolved in glass (McMillan et al., 1983; Malfait, 2018).

The intensity of spectra (Fig. 3-4) was normalized to absolute intensity (I_{obs}) using the Long correction for temperature and excitation line effects (Long, 1977; Neuville and Mysen, 1996).

$$I = I_{obs}\left\{\nu_0^3\left[1-\exp\left(-\frac{hc\nu}{kT}\right)\right]\nu/(\nu_0-\nu)^4\right\} \tag{1}$$

where h is the Planck constant ($h = 6.62606957\cdot 10^{-34}$ Js), k is the Boltzmann constant ($k = 1.3806488\cdot 10^{-23}$ J/K), c is the speed of light ($c = 2.9979\cdot 10^{10}$ m/s), T is the absolute temperature, v_0 is the wavenumber of the incident laser light, and v is the measured wavenumber in cm^{-1}.

The water content was then obtained using an empirical linear relationship:

$$C_{H_2O}(wt\%) = 100\cdot A\cdot\frac{R_{w/s}}{1 + A\cdot R_{w/s}} \tag{2}$$

where A is a fitted constant, A: 0.007609; $R_{w/s}$ the relative Raman contributions of glass and dissolved water, expressed by peak area ratio (Le Losq et al., 2012).

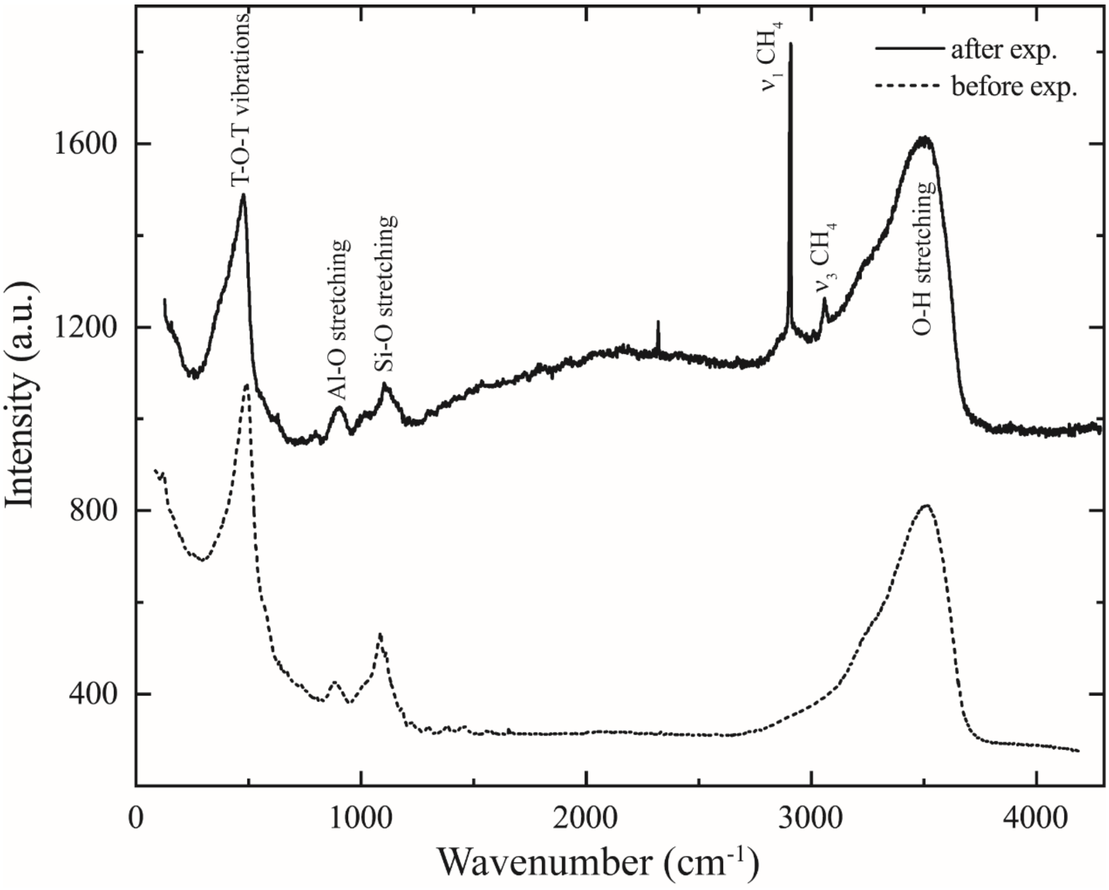

Fig. 3-4. Raman spectrum of the hydrated $Ab_{80}An_{20}$ starting glass PC162a (dash) and the quenched glass of run HH355 (solid). T = Al or Si. Both H_2O and CH_4 signals were detected in the quenched glass of HH355.

3.3. Xe crystal/melt partitioning measurements

3.3.1 In-situ determination of Xe content in crystals and melt

For large volume press experiments, *T* was initially increased above the melting point to ensure equilibrium, then decreased stepwise until both crystalline and molten phases co-exist, and hold for 1800 s before data collection. For resistive-heating diamond-anvil cell experiments, full melting was almost reached, with some crystals nonetheless preserved on the edge of gasket (Fig. 3-2c).

While it is difficult to distinguish crystals *vs* melt from visual observations (DAC experiments) or *in situ* radiographic imaging (LVP experiments), X-ray diffraction allows unambiguous phase determination (Fig. 3-5a, 6, 7). Therefore, at the targeted *P-T* conditions, samples were scanned while collecting X-ray diffraction data until best positions were found: one optimizing crystalline diffraction signal (further referred as 'crystal-rich'), and one optimizing melt diffuse signal (further referred as 'melt-rich') with eventually pure melt.

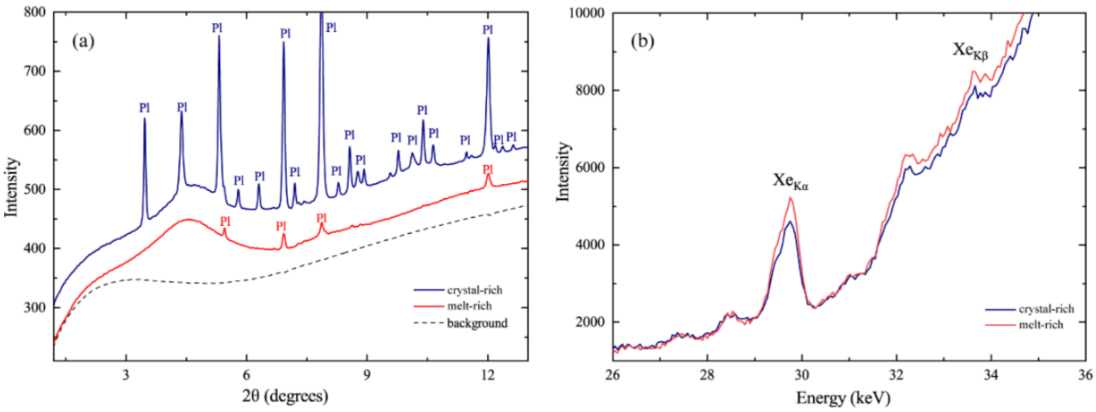

Fig. 3-5. (a) Angle-dispersive X-ray diffraction data collected at 2 GPa and 1010 °C in resistive-heating diamond-anvil cell (run Cell5); (b) corresponding X-ray fluorescence spectra. Pl, plagioclase; dotted line: background obtained using an empty gasket in the DAC. The Xe K_{α} and K_{β} fluorescence rays are observed at 29.78 keV and 33.62 keV, respectively.

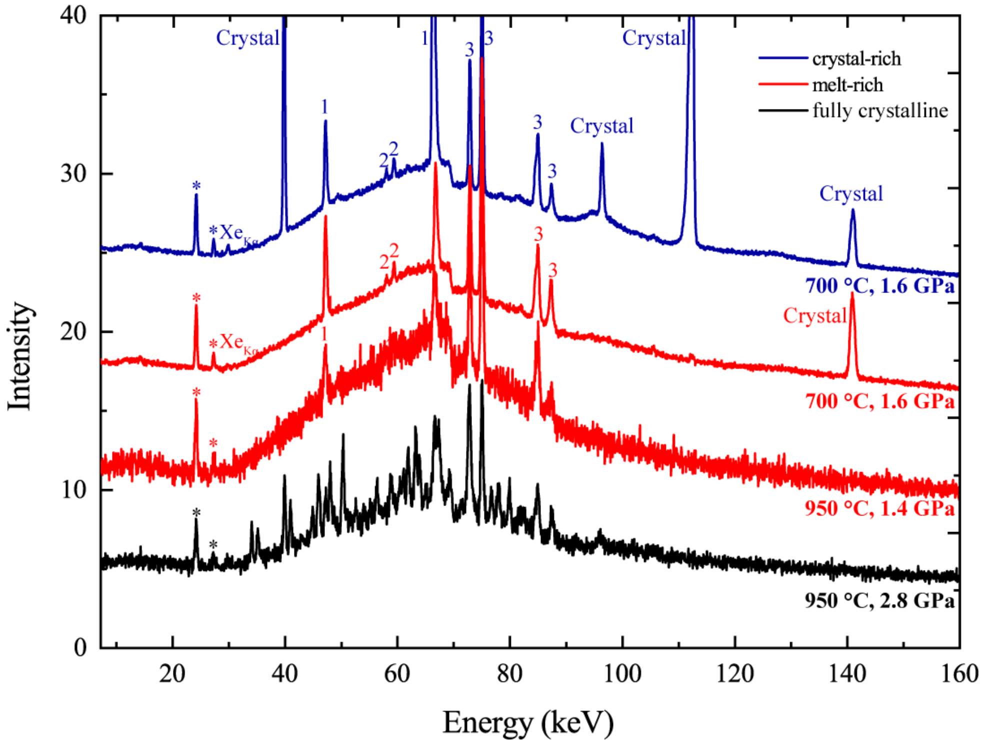

Fig. 3-6. *In situ* energy-dispersive patterns collected in large volume press (run HH355). *, Ge fluorescence from detector; 1, MgO diffraction from cell-assembly; 2, W fluorescence from entrance slits, and 3, Pb fluorescence from beamline elements.; note the W absorption edge at 69 keV. Due to the large crystal size (cf Fig. 1), not all diffraction peaks are observed but only a few depending on their orientation. From Raman spectra, crystalline phase was determined to be jadeite at 700 ºC, 1.6 GPa.

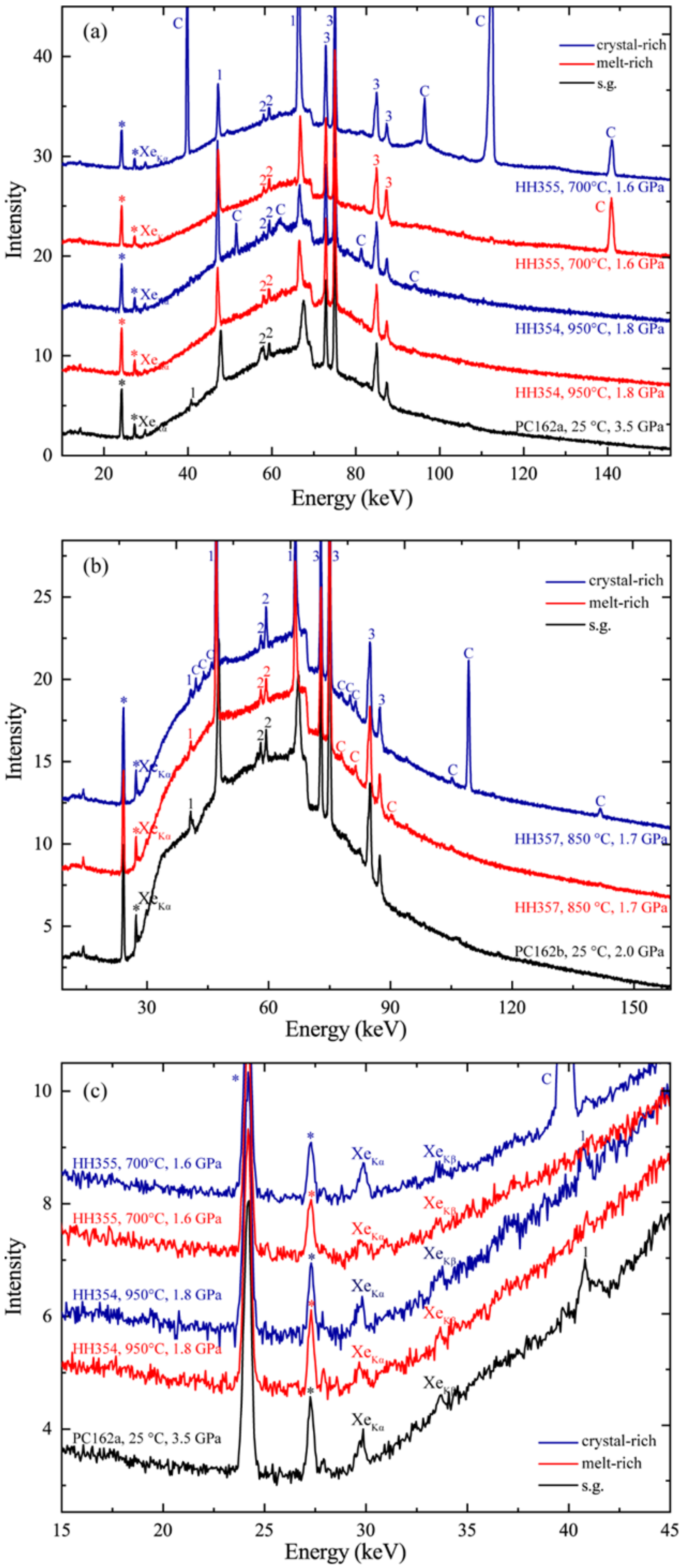
(a)
Intensity
Energy (keV)
crystal-rich
melt-rich
s.g.
HH355, 700°C, 1.6 GPa
HH355, 700°C, 1.6 GPa
HH354, 950°C, 1.8 GPa
HH354, 950°C, 1.8 GPa
PC162a, 25 °C, 3.5 GPa
$Xe_{K\alpha}$
(b)
Intensity
Energy (keV)
crystal-rich
melt-rich
s.g.
HH357, 850 °C, 1.7 GPa
HH357, 850 °C, 1.7 GPa
PC162b, 25 °C, 2.0 GPa
$Xe_{K\alpha}$
(c)
Intensity
Energy (keV)
HH355, 700°C, 1.6 GPa
HH355, 700°C, 1.6 GPa
HH354, 950°C, 1.8 GPa
HH354, 950°C, 1.8 GPa
PC162a, 25 °C, 3.5 GPa
$Xe_{K\alpha}$
$Xe_{K\beta}$
crystal-rich
melt-rich
s.g.

Fig. 3-7. Full *e*nergy-dispersive spectra data-set from large-volume press experiments. (a) Run HH354 and HH355; (b) HH357 and (c) zoom on Xe fluorescence signal. *, Ge fluorescence from detector; 1, MgO diffraction from cell-assembly; 2, W fluorescence and 3, Pb fluorescence from beamline elements. C, crystal; s.g., starting glass. Note the W absorption edge at 69 keV. For (b) run HH357 with sharper background is due to the reduction of the absorption by the use of the boron epoxy windows, which however does not significantly improve the signal/noise ratio.

At each position, Xe content is determined using the fluorescence signal of Xe K_α and K_β lines (29.78 and 33.62 KeV) lines either on a specific fluorescence detector for angle-dispersive set-up (DAC experiments, Fig. 3-5b) or on the same detector used for diffraction for energy-dispersive set-up (LVP experiments, Fig. 3-5 and 7).

For angle-dispersive DAC experiments, energy calibration and quantification of Xe content from signal intensity were calibrated *in situ* in the DAC at room conditions by filling a gasket with a Xe-doped glass PC53 (2.6 wt% Xe; unpublished data, haplogranite glass from C. Crépisson's PhD thesis, 2018) previously analyzed by both EPMA and Particle X-ray Emission (Leroy et al., 2018). XRF data are processed with PyMCA software with the declaration of attenuation by absorption of Be window and diamond anvils (Solé et al., 20017). At 1010 °C, melt proportion (see section 3.3.2 for determination of phases fractions) is more than 97% in the 'melt-rich' pattern thus we assume it can represent the Xe content in pure melt (Table 3-3). As for 'crystal-rich' pattern which contains a mixture of crystals and melt, data are further treated in a multilayer way. We assume there are two layers (melt and crystalline) in 'crystal-rich' pattern, sample thickness is assumed to be equal to that of the recovered gasket and proportions are taken as the relative layer thickness. Xe content in crystals is then obtained from mass balance calculation in PyMCA software, as the bulk Xe content of the starting glass before heating is known and Xe content in the melt is taken from the 97% melt-rich pattern.

Fluorescence peaks on energy-dispersive patterns from LVP experiments are fitted following Simabuco and Nascimento (1994) whereby the absolute intensity of the fluorescence signal depends on the five following factors: 1) beam intensity, 2) Xe concentration in the sample, 3) volume of the sample probed by X-rays, 4) absorption by the sample and the surrounding cell-assembly, 5) detector sensitivity. Note that these underlying physics are the same as implemented in the PyMCA software used above. They can be expressed by:

$$I_i = Xe_i \times \rho_i \times S \times D_i \times I_i^0 \times 10^{-A} \tag{3.1}$$

where Xe_i is Xe weight fraction in the volume probed by X-rays at a given position i; ρ_i, the average density; D_i, the sample thickness along X-ray beam path; S, the X-ray sensitivity of the spectrometer; I_i^0, the total beam intensity; A, the absorption by the sample and the surrounding cell-assembly.

As we know the Xe content in the starting glasses, the $S \times I_i^0 \times 10^{-A}$ product can be calculated (cf equation 3.1). We specifically used diamond capsules as those do not deform under our P-T conditions hence the path length, D_i, through the sample can be calculated knowing the position of the X-ray beam slits relative to the diamond capsule edges (cf X-ray radiograph on Fig. 3-10b).

Assuming that the intensity of diffraction peak can be expressed by the peak area, Xe_i can be written as:

$$Xe_i = Xe_{starting\ glass} \times \frac{peak\ area\ at\ position\ i}{peak\ area\ for\ starting\ glass} \times \frac{\rho_{starting\ glass}}{\rho_i} \tag{3.2}$$

The average density, ρ_i, is calculated using a 3rd order Birch-Murnaghan equation of state assuming ideal mixing of H_2O and silicate melt (Malfait et al., 2014), and the density of crystals using the molar volumes of plagioclase $Ab_{80}An_{20}$ predicted from the Murnaghan equation of state (Holland and Powell, 1998), the thermal expansion of plagioclase feldspars (Tribaudino et al., 2010), and the molar volumes of clinopyroxene calculated from high-T Birch-Murnaghan equation of state of diopside as a proxy (Zhao et al., 1998). All densities for crystals and melt are summarized in Table 3-3.

Xenon weight fraction in crystals can finally be obtained from mass balance calculations using phase proportions as determined in section 3.3.2 below:

$$Xe_i = x_m^i Xe_m + \left(1 - x_m^i\right) Xe_c \tag{3.3}$$

where Xe_m is the Xe weight fraction in the melt, Xe_c, the Xe weight fraction in crystals, and x_m^i, the melt fraction in pattern i. At each P-T point, Xe_m is taken from pure melt pattern except for one P-T condition (run HH355 1.6 GPa-700°C) for which we did not succeed to localize a pure melt zone, and had to solve a set of two mass-balance equations, one for the crystal-rich zone and one for the melt-rich zone.

3.3.2 Determination of phase fractions

To obtain phase fractions for patterns collected on mixture of crystals and melts, angle-dispersive diffraction data (DAC experiments) are processed by LeBail refinement (Fig. 3-8), adopting the procedure developed by Hermans and Weidinger (1948) for crystallinity quantification which relies on the proportionality between (a) amorphous (*i.e.* molten) fraction and measured amorphous intensity; (b) crystalline fraction and measured crystalline intensity.

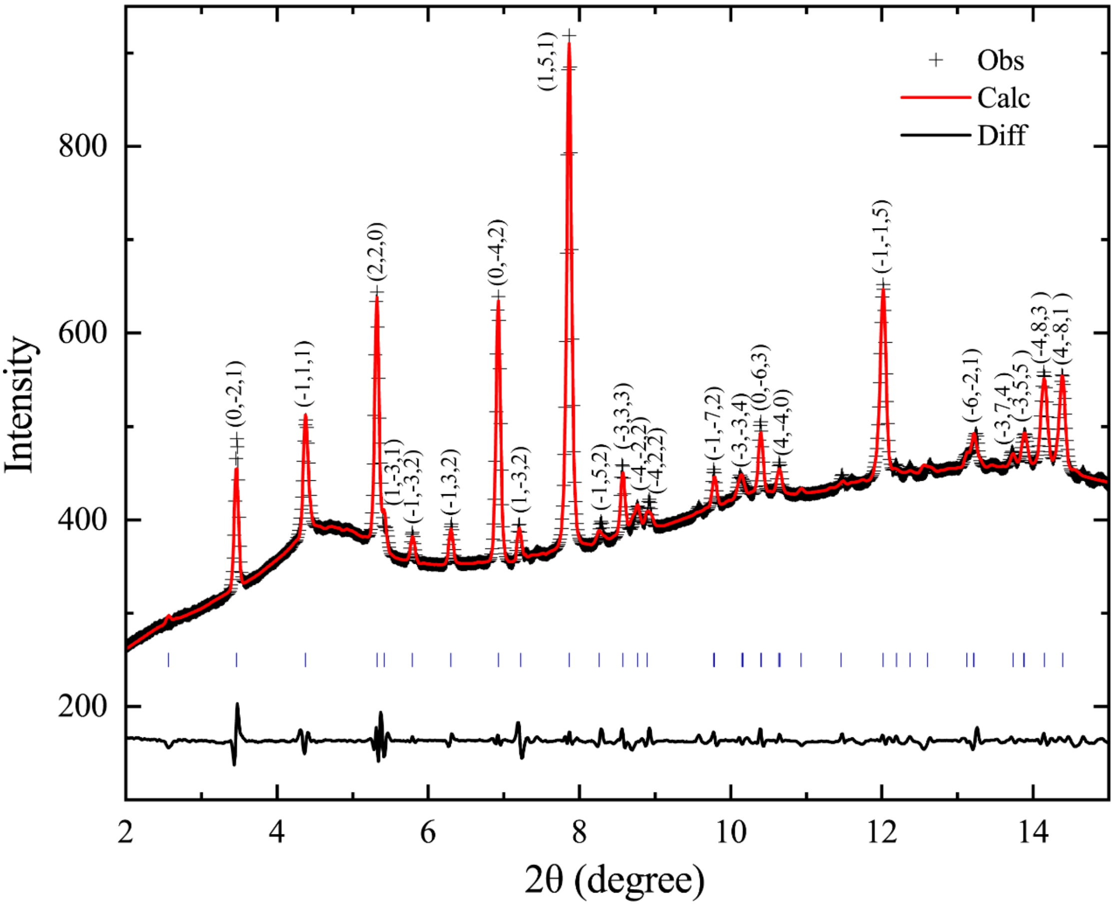

Fig. 3-8. Le Bail refinement for crystal-rich zone at 2 GPA and 1010 °C (Run 5). Pattern is fitted with $Ab_{84}An_{16}$ plagioclase (Phillipsi et al., 1971). $\lambda = 0.2898$ Å, the melt diffuse signal is most noticeable between 4 and 6°. Background is drawn from XRD measurements on DAC with empty gasket.

For energy-dispersive diffraction data (LVP experiments), diffraction signal was processed by normalizing intensities by time and slits size, and converting energy to scattering vector, $q = E sin\theta / hc$, where E is the photon energy, 2θ, the scattering angle, *h*, the Planck constant, and *c*, the speed of light (Fig. 3-9). Melt phase proportion was obtained from the ratio between diffuse melt intensity in a given EDX pattern and that observed for pure melt pattern, both after subtraction of the background signal taken from EDX pattern collected on surrounding MgO. Crystal fraction is then obtained by difference to 100%. This method was cross-checked for two samples by image processing of X-ray tomography scans (cf section 3.2.4) on two recovered diamond capsules (runs HH355 and HH357) extracted from the cell-assembly, assuming that crystal *vs* melt fractions are not affected by the quenching process. The data were processed with ImageJ software for 3-D reconstruction (Fig. 3-10) (Abràmoff et al., 2004). After that, melt and crystals phase fractions were calculated for each beam path as defined by the position of collimating slits recorded on X-ray radiographs during *in situ* EDX experiments (Fig. 3-10c and 10d).

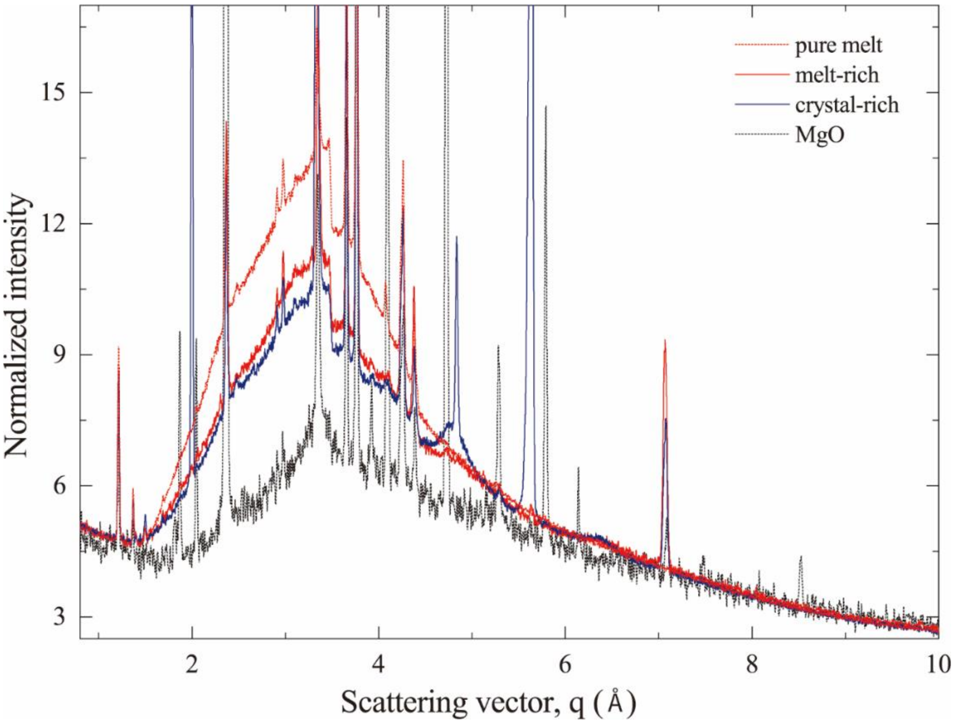

Fig. 3-9. Scattering vector (q) calculated from equation (3.6) for run HH355 at 1.6 GPa,

700 ºC. Pure melt is measured at 1.4 GPa, 950 ºC. The scattering angle is at 7.1315º ± 0.0003º, with typical ~ 56% melt fraction and ~ 73% on crystal-rich and melt-rich fraction, respectively.

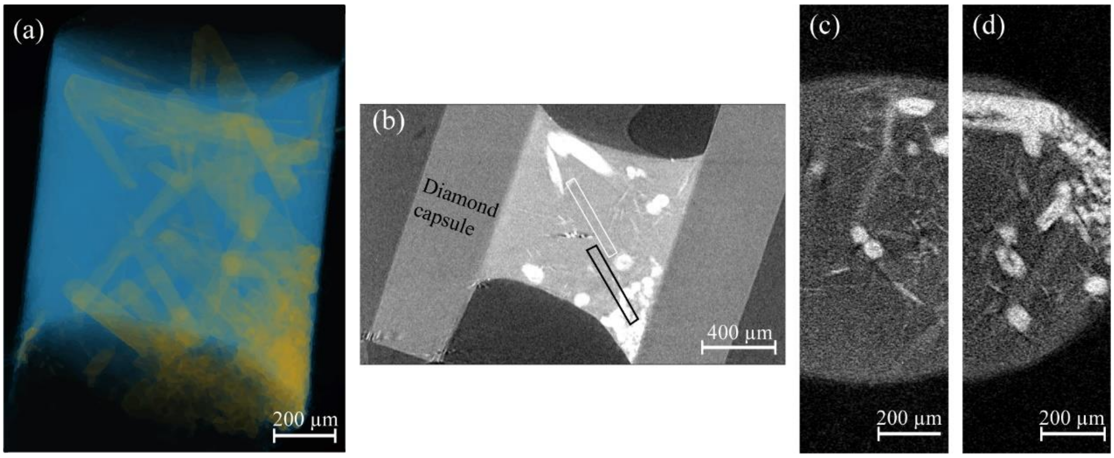

Fig. 3-10. X-ray tomography slice reconstruction on the recovered large-volume press sample (HH357). (a) Crystallized omphacite (yellow) coexisting with partial melt quenched as a glass (blue); (b) recovered sample with the beam slits position on melt-rich (white rectangle) and crystal-rich areas (black rectangle); reconstructed cross sections at 'melt-rich' (c) and 'crystal-rich' positions (d).

The results obtained using both X-ray tomography and intensity ratio calculation of EDX data tested on run HH355 are within the 10% uncertainty, with 73% melt at the melt-rich position and 56% melt at the crystal-rich position (from X-ray tomography) *vs* 68% and 55% respectively (from intensity ratio calculation).

3.4. Results and discussion

3.4.1 Results: Xe partitioning behaviour

The higher Xe concentrations are systematically found in crystal phase for clinopyroxene/melt system at all investigated *P-T* conditions, indicating Xe preferentially goes into clinopyroxene rather than into the melt (Fig. 3-11 and Table 3-3). Our *in situ* high *P-T* measurements thus show that Xe is a compatible element in clinopyroxene at depth with $D^{Xe}_{clinopyroxene/melt}$ reaching 3.36 at 700°C, and linearly decreasing with increasing *T* (Fig. 3-12 and Table 3-3). Only one data point is collected for plagioclase/melt system using DAC, at the highest *T* investigated (1010 °C), with higher Xe content retained in melt. Consequently, for plagioclase/melt system, Xe is found to preferentially partition into the melt ($D^{Xe}_{plagioclase/melt} = 0.50 \pm 0.20$) at 1010 °C. Note that his lower value is consistent with the negative *T*-trend that we report for Cpx/melt partitioning (Fig. 3-12).

Table 3-3

Phase proportions, phase densities, Xe weight fractions, and Xe partition coefficients.

Run	starting glass	*P*	*T*	Density (g/cm^3)		melt-rich	crystal-rich	Xe_c	$Xe_{m/g}$	$D^{Xe}_{crystal/n}$
		(GPa)	(°C)	ρ_c	$\rho_{m/g}$	x_m	x_m	(wt%)	(wt%)	
HH354	PC162a	3.5	20		2.532			0.14 (0.01)		
		1.8	950	3.264	2.253	100	82	0.19 (0.02)	0.12 (0.01)	1.63 (0.19)
HH355	PC162a	1.6	700	3.288	2.252	73	56	0.26 (0.02)	0.08 (0.01)	3.36 (0.25)
		0.0	20					< DL*	0.06* (0.01)	
HH357	PC162b	2.0	20		2.354			0.02 (0.01)		
		1.7	850	3.273	2.216	95	77	0.03 (0.01)	0.01 (0.01)	2.76 (0.32)
		0.0	20					< DL*	< DL*	
Cell5	PC162a	2.0	1010	2.518	2.267	97	57	0.11 (0.02)	0.14 (0.02)	0.78 (0.21)
		2.0	1010	2.518	2.267	97	57	0.07^a (0.02)	0.15^a (0.02)	0.50^a (0.20)
		0.0	20					< DL*	0.14* (0.01)	

x_m , melt % fraction; Xe_c, Xe content in crystal; $Xe_{m/g}$, Xe content in melt or glass; uncertainties (in brackets) derived from noise to signal ratio of fluorescence signal intensity (10-20 %) and phases proportions (~10 %); [a], calculated with PyMCA software; ∗, EPMA analysis on quenched sample; DL, detection limit (230-260 ppm for Xe).

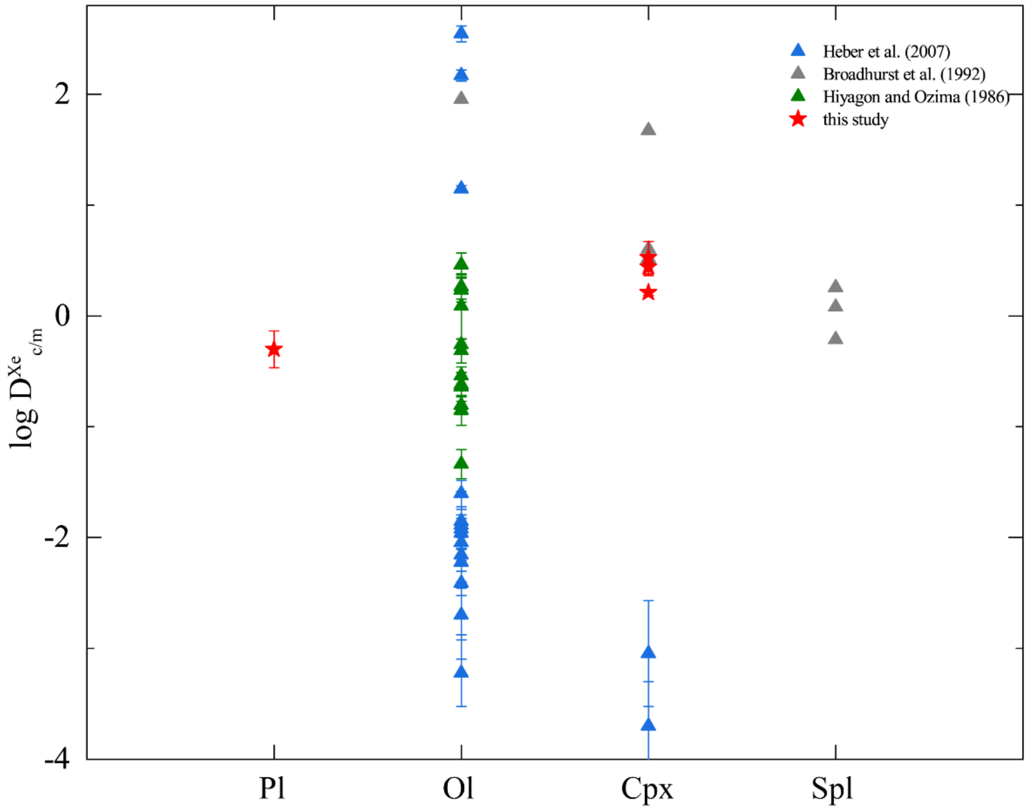

Fig. 3-11. Crystal-melt partitioning coefficients of Xe. From our experiments (red stars) and compared with literature data. Pl, plagioclase; Ol, olivine; Cpx, clinopyroxene; Spl. spinel.

These results are two orders of magnitude below the upper range of former Xe partitioning studies on olivine/melt and clinopyroxene/melt systems (Fig. 3-11) but clearly near/above unity, implying that one cannot systematically discard Xe bubbles in quenched samples as those must have at least partly been formed upon quenching to ambient conditions. In the case of Xe reactivity with olivine at high *P*-*T* conditions through Xe substitution to Si (Crepisson et al., 2018a), Xe was indeed observed to be at least partly released from crystals upon quenching to room *T* as indicated by the appearance of pure Xe diffraction signal (Sanloup et al., 2011).

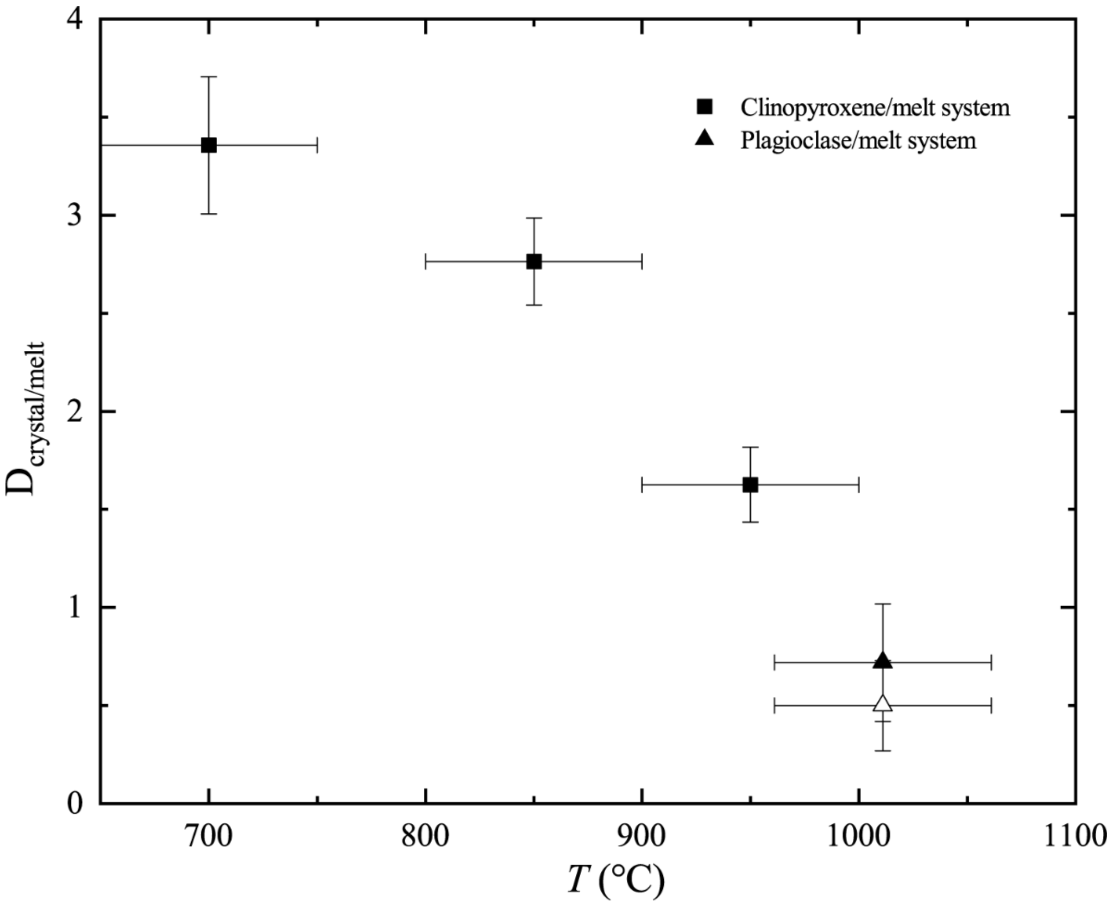

Fig. 3-12. Temperature effect on Xe crystal/melt partitioning under *P*. Solid symbols: $D^{Xe}_{c/m}$ obtained using method from Simabuco and Nascimento (1994); empty symbols: using method from Solé et al. (2007).

Noble gases retention sites in silicate melts are inside rings and cavities of the three-dimensional network. Their solubility depends on the melt composition and structure, it increases with the SiO_2 content and with *P* up to approximately 5 GPa but is independent on *T* for Ar and Xe (Carroll and Stolper, 1993; Schmidt and Keppler, 2002). Xe-O bonds have been reported to form in hydrous silica-rich melts when compressed with a coordination number of about 12, consistent with Xe insertion in the most abundant 6-membered rings (Leroy et al., 2019). However, the Xe-O coordination number shows no dependence on either *T* or *P* at the experimental conditions. Consequently, Xe solubility in melts cannot be simply explained by Langmuir adsorption model. On the other hand, Xe reacts with minerals by substituting to Si, bonding to either 4 oxygen atoms in silica polymerized phases (Crepisson et al., 2019) or to 3 oxygen atoms in olivine depolymerized structure (Crepisson et al., 2018a), with oxidation state between + 2 and + 3. Yet there is so far no data about the exact oxidation state of Xe in magmas.

Xe solubility in olivine is promoted by the existence of Si-vacancies owing to an increased concentration of Fe^{3+} cations at the high experimental *T* (Mackwell et al., 1988), also evidenced in quartz (Probert, 2010). Based on the EPMA analyses on quenched samples (Table 3-2), less Al^{3+} is retained in clinopyroxene when *T* increases, and it results in the lack of the vacancy-forming element in clinopyroxene. In consequence, the crystal could retain less Xe. Therefore, we suggest the negative relationship between $D^{Xe}_{c/m}$ and *T* (Fig. 3-12) is due to the decrease of trivalent elements in clinopyroxene phase.

3.4.2 Xe storage in the deep crust and the missing Xe

Xe can be stored within major minerals of the deep continental crust (Sanloup et al., 2005; Probert, 2010) and upper mantle (Sanloup et al., 2011; Crepisson et al., 2018a). Xe crystal/melt partition coefficients obtained from our experiments (0.50 to 3.36) indicate that Xe is moderately incompatible to compatible at continental *P*-*T* conditions. This range of values confirms the compatibility of Xe in minerals. Xenon compatibility in crystalline silicates at depth is attributed to its *P*-induced chemical reactivity, with the formation Xe-O bonds (Probert, 2010; Crepisson et al., 2018a; Crepisson et al., 2019). This short bond length is due to Xe being oxidized, not neutral. Compared to other noble gases, Xe is therefore preferentially retained into the crystal fraction during partial melting processes, rather than degassed from the melt. Xe is recycled at depth by subduction processes, leading to the mantle noble gas isotopic composition (Holland and Ballentine, 2006). Besides, Xe is detected up to 0.2 ppb (part per billion) in deep sea siliceous fossils (Matsuda and Matsubara, 1989), that eventually also are recycled into the mantle at subduction zones. In the case of haplogranite, Xe degasses strongly or is preferentially retained within the haplogranitic melt, depending on *T* (Leroy et al., 2019). Thus, in the presence of aqueous fluids, Xe is not necessarily degassed upon rock melting. Xe released from subducted plates along aqueous fluids could be therefore stored in silicate melts or minerals. Xenon stored or recycled at depth is expected to be only partially released during partial melting process, and mostly remains in crustal minerals with upwelling of magma. Thus, our results support the hypothesis of Xe storage in the continental crust. This is consistent with natural Xe enrichments of 1 to 3 orders of magnitude compared to Kr that have been reported in exhumed Red Rock granite (^{130}Xe/^{84}Kr ~ 0.2) from the Sudbury structure, Canada, formed by an asteroid impact [45] and in North America tektites (^{130}Xe/^{84}Kr ~ 0.5) (Palma et al., 1997). While in common rocks, ^{130}Xe/^{84}Kr is 0.004-0.012 in granites (Kuroda et al., 1977) and 0.007-0.033 in igneous rocks (Miura and Nagao, 1991). The time scale is very different between natural shocked rocks and slowly exhumed ones that likely underwent episodes of metamorphism/magmatism resulting in Xe loss. Thus, only shocked rocks, and to lesser extent fast ascent rocks (*e.g.*, xenoliths) may preserve Xe excess.

3.4.3 Advantages of the new EDX protocol for in situ partitioning experiments

For the angle-dispersive set-up, the volume sampled by XRF is slightly smaller than the volume probed by XRD, and great care must be taken to align the XRF detector with the XRD focal point (Fig. 3-13a). While for the energy-dispersive set-up, both structural information (*i.e.* diffraction) and chemical information (*i.e.* fluorescence) are collected using one single detector with the exact same gauge volume and geometry of sample probed (Fig. 3-13b). The obtained diffraction pattern is therefore more accurate.

-

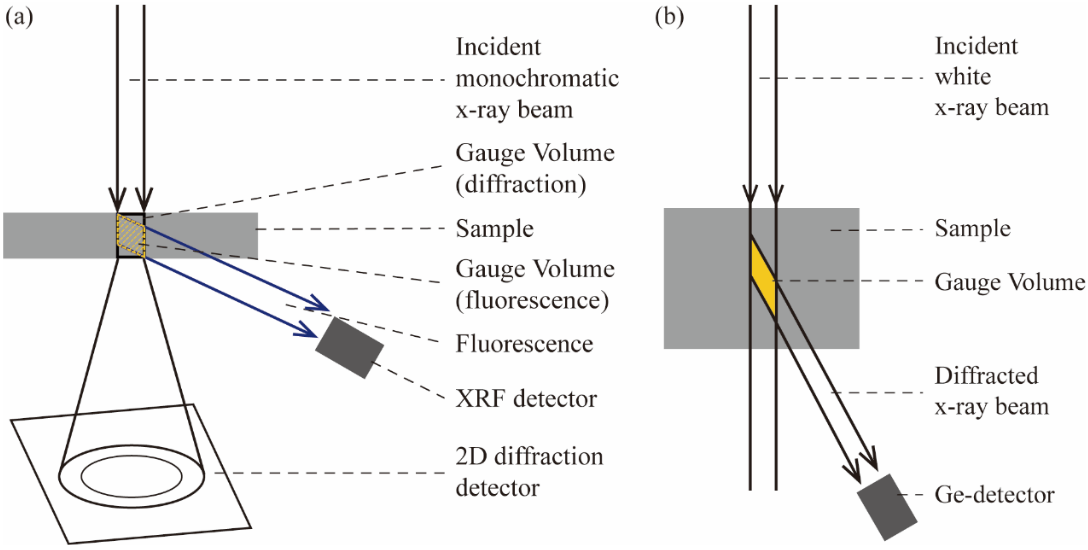

Fig. 3-13. Schematic geometry of (a) the angle-dispersive x-ray set-up (at P02.2 PETRAIII) and (b) energy-dispersive x-ray set-up (at P61B PETRAIII).

Another disadvantage of the ADX set-up is that fluorescence signal scattered from sample environment (*e.g.* diamond anvils, rhenium gasket, body cell) is also detected, which can impede detection of some elements at low concentrations. This problem is circumvented in the EDX set-up due to the collimation tip placed in front of the Ge-detector. Note that the situation can be improved with an ADX set-up by placing an additional polycapillary X-ray half-lens in front of the fluorescence detector (Wilke et al., 2010).

To evaluate the consistency between the two data processing methods (*i.e.* PyMCA software and equation 3.1-3.2 following Simabuco and Nascimento, 1994), both of them have been tested on the DAC fluorescence data. Results agree within uncertainties (cf Table 3-3 and Fig. 3-12). Thus, the feasibility of the new protocol is well demonstrated, with advantages of the congruent geometry of sample probed.

This new technique therefore offers a new avenue to determine elements concentration, including for volatile elements, in phases using X-ray fluorescence signal on energy dispersive diffraction data. Besides, by using large volume press instead of resistive-heating DAC, this protocol allows to probe geological systems at higher *P*-*T* conditions, with potential for significant impact in the experimental petrology and Earth's sciences community. Higher *P*-*T* conditions can be achieved in laser heated DACs, and fluorescence data. However while the whole sample is at constant *T* in a resistive heated DAC, only the central part of the laser heated spot is homogeneous for *T* in a laser heated DAC, making equilibrium measurements between co-existing phases very challenging (Petitgirard et al., 2012). The present method is nonetheless restricted to the investigation of elements with fluorescence signal between 15 keV and 120 keV for most synchrotron sources.

Chapter 4: Xe retention in crystallising planetary magma oceans

This chapter continues with the subject of Xe partition behaviour between minerals and melts but with more focus on the basaltic system. Using Paris-Edinburgh press and in-situ EDX probes analyses, Xe distribution between three types of crystals (olivine, anorthite and clinopyroxene) and basaltic melt has been determined. This is a draft article summarizing Xe partitioning data between all crystals and basaltic melt and its implications for sequestration of Xe during planetary magma ocean stages.

Abstract

Xenon (Xe) is missing in the Earth's and Mars' atmospheres. Partial crystallization of magma oceans (MO) plays a pivotal part in determining large-scale differentiation of terrestrial planets and embryos. We report partition coefficients of Xe between silicate crystals and basaltic melt ($D^{Xe}_{c/m}$) using *in situ* synchrotron x-ray probes at high pressures (P) and temperatures (T). Obtained values indicate a compatible behaviour of Xe at depth with $D^{Xe}_{c/m}$ = 3.27 ± 0.63 for plagioclase/melt, 1.72 ± 0.13 for clinopyroxene/melt and up to 88.69 ± 21.87 for olivine/melt. In stark contrast to other noble gases, Xe is thus preferentially retained in minerals upon solidification of magma oceans, and only partially degassed, favouring the very early retention of Xe as a trace element in planetary interiors.

4.1. Introduction

Noble gases can provide unique clues to unravel the geochemical evolution of volatile elements (Ozima and Podosek, 2002). However, compared to krypton, atmospheric Xe in Earth and Mars is depleted by a factor of ~20 in regard to chondritic meteorites (Pepin, 1991) and referred to as the 'missing Xe' problem. The Earth's noble gas budget are referred to four potential attributions: implanted solar wind (Péron et al., 2017); solar nebula gas (Harper and Jacobsen, 1996); chondrites (Albarede, 2009; Halliday, 2013; Broadley et al., 2020); and comets (Dauphas, 2003; Marty et al., 2017). Ne isotopic feature indicates nebular volatiles trapped in embryo-sized bodies during accretion (Schlichting and Mukhopadhyay, 2018). Nebular volatiles may later lose and replenished through delivery of chondritic volatiles (Mukhopadhyay and Parai, 2018). In addition, the origin of Earth's water was reported by the contribution of Enstatite chondrite (EC) meteorites during the accretion of Earth (Piani et al., 2020). As protoplanets grow toward being planets, magma oceans (MOs) are developed from the energy released by radiodecay and multiple accretion events (Abe and Matsui, 1985; Wetherill, 1990; Tonks and Melosh, 1993; Elkins-Tanton, 2008, 2012; Tucker and Mukhopadhyay, 2014). In the case of the Earth, the final major equilibration is linked to the giant impact that formed the Moon (Tonks and Melosh, 1993). MOs are key agents of the transfer of elements between reservoirs according to their geochemical affinities (Goldschmidt, 1929). Noble gas degassing within the solid Earth occurred during the solidification of MOs (Ozima and Zahnle, 1993). If the noble gases planetary budget was established at the early stage like water, the partition behaviour of noble gases during the MOs could be a crucial clue to understand their distribution and evolution between the interior and the surface.

Xe could be retained in minerals by substituting to Si, bonding to either 4 oxygen atoms in silica polymerized phases (Crepisson et al., 2019) or to 3 oxygen atoms in olivine depolymerized structure (Crepisson et al., 2018a) at the modest *P*-*T* conditions of the deep crust and upper mantle, with oxidation state between + 2 and + 3 (cf Probert, 2010; Kalinowski et al., 2014; Crepisson et al., 2018a, 2019). *P*-induced oxidation is therefore the incorporation mechanism of Xe in silicate minerals at depth. Besides, Xe-O bond in magmas with a coordination number of about 12 was found at deep continental crust conditions, indicating Xe insertion in rings of the melt structure, albeit the oxidation state is not known. Partition coefficient is essential to understand the atypical behaviour of Xe at depths. Reported Xe partition coefficients between olivine, pyroxene, spinel and basaltic melt ($D^{Xe}_{c/m}$) based on the analysis of samples recovered from high *P-T* conditions span up to 6 orders of magnitude (e.g., from 6×10^{-4} to 350 for olivine/melt) depending on the interpretation of bubbles and inclusions, i.e., whether they should be excluded from measurements or not (Hiyagon and Ozima, 1986; Broadhurst et al., 1992; Heber et al., 2007). In addition, $D^{Xe}_{c/m}$ for olivine/melt estimated from density functional theory was found to 2.5 to 5 by comparing the calculated relative variations of cell parameters with that measured in high *P-T* experiments in the 0-5.7 GPa range (Crepisson et al., 2018a). Recently, we developed a new method combining in-situ x-ray probes (Chen et al., 2022) to circumvent these problems, from which partition coefficient of Xe between plagioclase/felsic melt was successfully determined. Xe was found to be moderately incompatible to compatible (0.50 ± 0.20 to 4.46 ± 0.37) from 700-1010 ºC, consistent with natural Xe enrichments of 1 to 3 orders of magnitude compared to Kr that have been reported in Red Rock granite from the Sudbury structure (Kuroda et al., 1977), in North America tektites (Palma et al., 1997), and in the deep crust drilled by the KTB project (Drescher et al., 1998). Here we focus on Xe partitioning behaviour during MO crystallization at the early stage.

4.2. Methods

4.2.1 Synthesis of glasses

Basaltic glass was prepared from reagent grade oxides and carbonates powders with the composition relevant for lunar magma ocean at the stage of anorthite crystallization (Sakai et al., 2014). Powders were firstly ground and decarbonated by slowly heating in a platinum crucible in an atmospheric furnace from room temperature to 1000 °C, run for 10 hours, molten at 1500 °C for 1 hour, and then quenched in water. Recovered glass was crushed into powder again and remolten twice to ensure homogeneity. For Xe doping processes, recovered basaltic glass was first loaded into one-end welded Pt capsule to which were added Xe using a gas loading device (Boettcher et al., 1989). The capsule was brought to high *P*-*T* conditions using a piston-cylinder apparatus with a half-inch talc pyrex assembly, a graphite heater, and dried MgO powder packed around the Pt capsule, followed by rapid *T* quenching and decompression at room *T*. In addition, two types of natural plagioclase were used: Na-K feldspar (Brevik, Norway) and labradorite (Spectrum Mine, Plush, Lake Co., Oregon).

4.2.2 Partitioning experiments

Ex-situ experiments were conducted using piston-cylinder (PC) press (IMPMC, Paris) with similar assembly discussed above. In-situ experiments were carried out using a large-volume Paris-Edinburgh (PE) press combined with synchrotron energy dispersive diffraction probes at 16-BMB synchrotron beamline at the Advanced Photon Source, Argonne National Laboratory (Table 4-1). To constrain the X-ray path length through the sample and preserve the sample cylindrical geometry, diamond capsules were used as the capsule container and sealed under pressure by platinum-rhodium caps. MgO cylinder was modified with two boron-epoxy windows to reduce X-ray absorption for both the incident and diffracted X-rays. Due to the lack of a thermocouple in PE press, temperature was established using an empirical power-*T* curve (Kono et al., 2014), with an uncertainty of ± 5% based on well-known melting temperatures of salts (Kono et al., 2013). MgO was used as internal *P* calibrant by using an equation of state (Kono et al., 2010), with an uncertainty of ± 0.3 GPa (Kono et al., 2014). During experiment, *T* was initially increased above the melting point, and then decreased stepwise until both crystalline and molten phases co-exist in order to insure thermodynamical equilibrium. At the targeted *P*-*T* conditions, X-ray radiography was firstly done to record sample positions, followed by EDX on the sample at two positions (one optimizing crystalline signal = 'crystal-rich', and one pure melt), EDX on the *P* calibrant, and a final quench of the graphite furnace. EDX data were collected on a Ge solid-state detector with slit size of 100 x 100 μm^2, with collection time of 1800s to 6700 s to optimize the signal to noise ratio for the Xe fluorescence peaks, and with the scattering angle (2θ) at 10.0310° ± 0.0007° and/or at low angle of 2.0023° ± 0.00161° to avoid the overlap of Xe fluorescence and crystal diffraction that occurs at higher 2θ angle values.

Table 4-1

Experimental conditions.

Run	*P* (GPa) (± 0.3 GPa)	*T* °(C) (± 80 °C)	Starting materials	Description	Quenched products
PC197	1.1	1250	K-Na fledspar + basalt glass + Xe	PC press	An (95) + Cpx (5) + melt
PC202	2.1	1600	basalt glass + Xe	PC press	melt
PC223	3.3	1450	plagioclase + Kr	PC press	Pl + melt
PC229	2.5	1300	basalt glass + Xe	PC press	Cpx + melt
PC265	1.3	1200	basalt glass + Xe	PC press	Ol + melt
HPT1	2.2	1140	PC202+ labradorite	PE press	Cpx + melt
HPT2	2.0	1270	PC202	PE press	Ol + melt
HPT3	1.4	1290	PC202+ labradorite	PE press	An + melt
HPT4	1.2	1200	PC202+ labradorite	PE press	Cpx (40) + An (60) + melt

An, anorthite; Pl, plagioclase; Ol, olivine; Cpx, clinopyroxene; labradorite with an anorthite percentage (%An) between 50-70, from Spectrum Mine, Plush, Lake Co., Oregon. *P*-*T* conditions in PE press represent quenched *P*-*T* conditions. Number in brackets is the proportion of the phase.

4.2.3 Ex-situ chemical analyses

Recovered samples together with starting glasses were put in epoxy resin and polished for scanning electron microscopy and electron microprobe analyses.

SEM images were obtained using a Zeiss Ultra 55 field emission scanning electron microscope (IMPMC), with a working distance of 7.5 mm and a voltage of 20 kV for detection of Xe. Major elements were analyzed using a Cameca SX-FIVE electron microprobe analyzer (EPMA) on the Camparis platform. Accelerating voltage was set to 15 kV, with 5 nA beam current for Na, Ca, Al, Si and 40 nA for Xe, 10s counting time for per element on both peak and background. Xe calibration was established following the procedure developed by Montana et al. (1993) by measuring the counts for the neighbouring elements, I (CuI) and Cs (CsCl), and also previously confirmed by analyzing one standard Xe-bearing glass PC53, for which Xe content was also assessed by Particle induced x-ray emission (Leroy et al., 2018).

4.3. Results and discussion

4.3.1 In-situ determination of Xe partitioning

Xe partition coefficients between olivine (Ol), clinopyroxene (Cpx), anorthite (An) and coexisting basaltic melt have been measured up to 2.5 GPa and 1400 °C. The initial basaltic glass contained only 0.05 wt% Xe (Table 4-2), far less than the 0.4 wt% Xe solubility in tholeiitic melt at 2 GPa (Schmidt and Keppler, 2012) and as low as possible to still have a quantitative analysis. The system hence is Xe-unsaturated. At the targeted *P*-*T* conditions, Xe Kα fluorescence ray at 29.78 keV was identified in both melt and crystal-rich signals, except for melt co-existing with olivine. For all three investigated systems, Xe fluorescence signal in ‘crystal-rich’ pattern was more intense than in that of melt pattern, indicating Xe preferentially goes into crystal phase rather than into melt phase (Fig. 4-1).

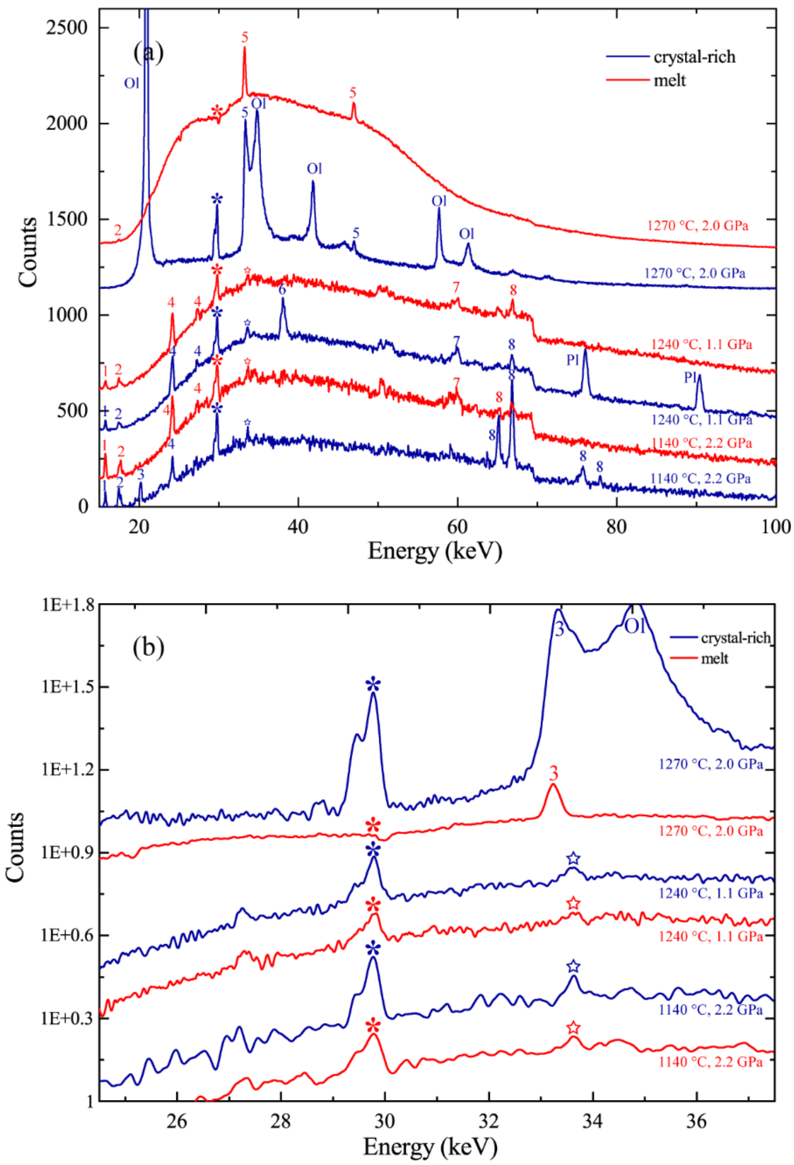

Fig. 4-1. In situ energy-dispersive patterns for three systems investigated from PE press experiments. (a) EDX spectra for coexisting melt (red) and crystal-rich (blue) patterns. (b) zoom on Xe fluorescence signal. From bottom to top: clinopyroxene with basaltic melt; plagioclase with basaltic melt; olivine with basaltic melt, respectively. The first two collected at 2.0023º while the latter collected at 10.0310º. Asterisks denote Xe Kα fluorescence ray (29.78 keV) and stars the Xe Kβ fluorescence rays (33.62 keV); Ol, olivine; Pl, anorthite plagioclase; 1-8 are from beamline elements: 1, Zr fluorescence; 2, Mo fluorescence; 3, Rh fluorescence; 4, In fluorescence; 5, MgO diffraction; 6, Pm fluorescence; 7, W fluorescence; and 8, Pt fluorescence. The W absorption edge appears at around 69 keV. Note there is no Xe fluorescence signal detected in melt coexisting with olivine.

To obtain phase fractions in ‘crystal-rich’ patterns, EDX data were processed by normalizing intensities with live time and slits size, and converting energy to scattering vector, q (Fig. 4-2), which can be defined by

$$q = Esin(\theta)/(hc) \tag{4.1}$$

where E, the photon energy; 2θ, the scattering angle; h, the Planck constant; and c, the speed of light.

EDX collected on MgO was taken as the background, phase proportions in ‘crystal-rich’ signals were driven from the ratio of areas of the intensity.

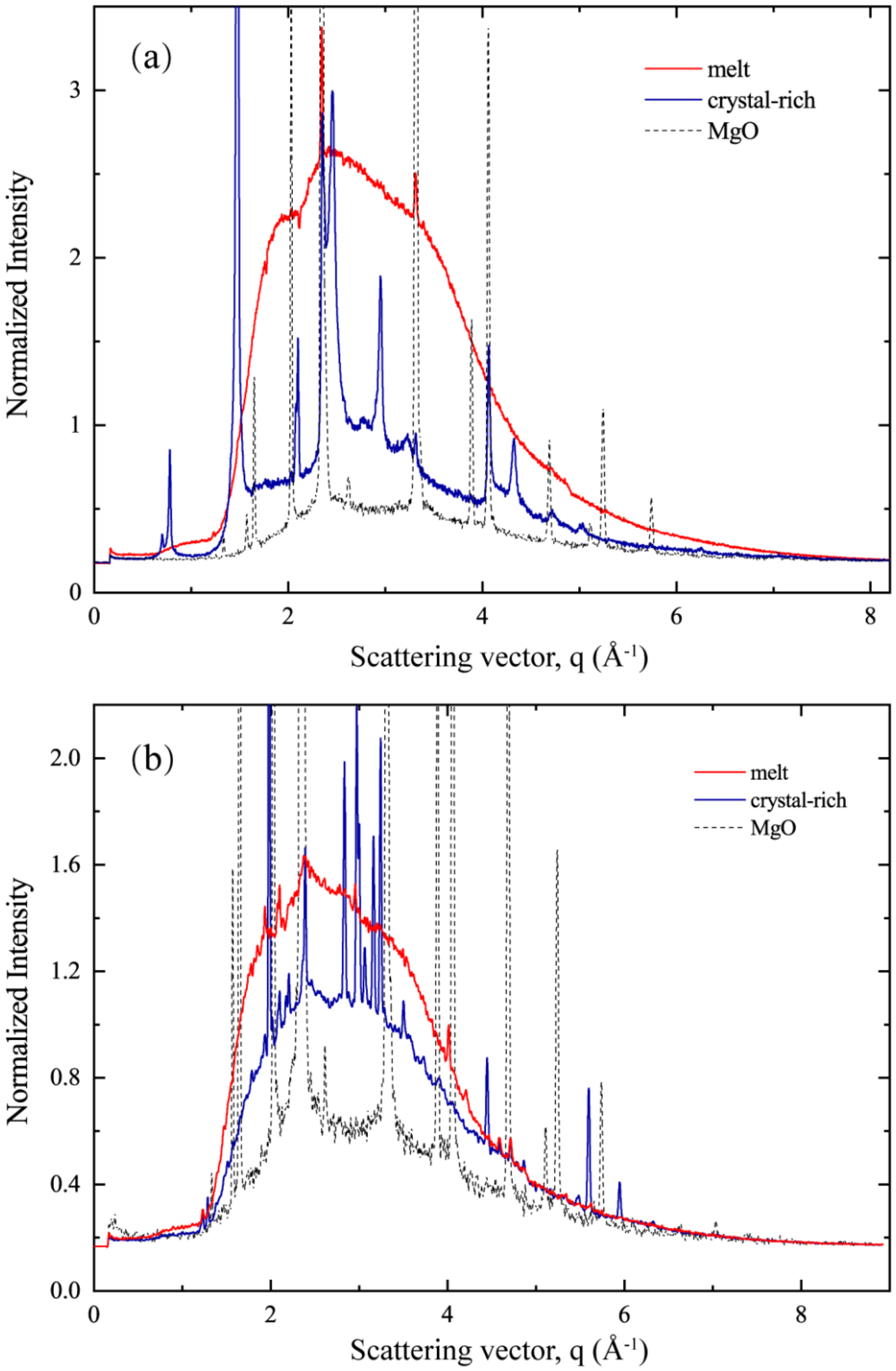

Fig. 4-2. Scattering vector (q) calculated from equation (4.1). (a) Olivine-melt system at 1270 °C, 2 GPa. The scattering angle (2θ) is at 10.0310° ± 0.0007°, with typical ~ 14% melt fraction on this crystal-rich fraction. (b) Plagioclase-clinopyroxene-basalt system at 1160 °C, 1.2 GPa. The scattering angle (2θ) is at 10.0252° ± 0.0005°, with typical ~ 47% melt fraction on this crystal-rich fraction. The uncertainty of melt faction is about 10%.

The densities of basaltic melt at experimental conditions are predicted from the 3rd Birch-Murnaghan EOS (Agee, 1998), where the compositional dependence as well as its temperature dependence can be calculated using the ideal mixing model (Lange and Carmichael, 1987; Lange, 1997). The densities of crystal are calculated from the molar volumes, which are estimated using the Murnaghan equation of state (EOS) and the thermal expansion as functions of *P* and *T* (Holland and Powell 1998; Tribaudino et al., 2010) for anorthite plagioclase; and using the 3rd Birch-Murnaghan equation of state for olivine (Liu and Li, 2006) (Table 4-2).

Table 4-2

Phase proportions, densities and Xe concentrations. in brackets: uncertainties

			density (g/cm^3)		melt-rich		crystal-rich		Xe content		
Run	P (GPa)	T (°C)	ρ_c	ρ_m	X_c (%)	X_m (%)	X_c (%)	X_m (%)	$Xe_{m/g}$ (wt%)	Xe_c (wt%)	$D^{Xe}_{c/m}$
HPT1	1.8	1190	3.194	2.920	0	100	40.7	59.3	0.037 (0.008)	0.054 (0.010)	1.505 (0.372)
	2.2	1140	3.216	2.972	0	100	69.6	30.4	0.033 (0.006)	0.057 (0.016)	1.724 (0.728)
HPT2	0.4	25		2.943					0.050		
	2.0	1270	3.865	2.928	0	100	86.5	13.5	0.002* (0.000)	0.145 (0.036)	88.685 (21.871)
HPT3	1.1	1240	2.657	2.830	0	100	31.3	68.7	0.028 (0.001)	0.094 (0.011)	3.349 (0.545)
	1.4	1270	2.664	2.862	0	100	39.9	60.1	0.028 (0.002)	0.091 (0.002)	3.271 (0.253)
	1.4	1290	2.666	2.870	0	100	30.6	69.4	0.031 (0.001)	0.122 (0.007)	3.904 (0.626)
	1.4	1290	2.666	2.870	0	100	14.4	85.6	0.043 (0.008)	0.148 (0.033)	3.760 (0.854)

* represents the value measure from recovered sample using mass spectrometry analyses.

Xe concentrations obtained from x-ray fluorescence signal were processed following the method described in Chen et al. (2022), where the absolute intensity of the fluorescence signal depends on the five following factors: (1) beam intensity, (2) Xe concentration in the sample, (3) volume of the sample probed by x-rays, (4) absorption by the sample and the surrounding cell-assembly, (5) detector sensitivity (Simabuco and Nascimento, 1994). Note the factors (1), (3), (4) and (5) are identical between crystal-rich and melt patterns. Hence the ratio of Xe content in crystal-rich and melt areas is simply the ratios of Xe fluorescence areas in respective EDX patterns. Xe crystal/melt partition coefficient is then obtained by determining the crystal and melt fractions in the crystal-rich pattern (cf, section 3.3.2). We find partition coefficients of Xe ($D^{Xe}_{c/m}$) at experimental conditions are 3.17 to 3.90 for $D^{Xe}_{An/m}$ between 1240-1290 ºC, and 1.51 to 1.72 for $D^{Xe}_{Cpx/m}$ between 1140-1190 ºC (Table 4-2).

In the case of Xe-olivine system, there is no resolvable Xe fluorescence peak in the melt patterns (Fig. 4-1). In order to further constrain Xe concentration in basaltic melt coexisting with olivine, additional mass spectrometry analyses were carried out by Denis Horlait at L2I, Laboratoire de Physique des deux infinis, Bordeaux (Horlait et al., 2021) on tiny pieces of glass recovered from APS experiments, and larger samples additionally synthesized at IMPMC using the piston-cylinder press at similar *P*-*T* conditions (Table 4-1). From the latter, pieces of pure glass could be separated from pieces of mostly, ~ 83 ± 10 % olivine crystal (cf, Fig. 4-7d and 7f, proportions obtained from ImageJ software), and give a range of $D^{Xe}_{Ol/m}$: 6.3-285.4 (Table 4-3). This variation could depend on possible heterogeneous distribution of Xe in crystals and/or ‘contamination’ by olivine of glass fragment (the third glass sample having one more order of magnitude of Xe concentration compared to the two others could be explained by only a 10-25% ‘contamination’ by olivine). Thus, in all likelihood the true value of $D^{Xe}_{Ol/m}$ is rather in the higher range (e.g., 59.5-285.4). Besides, on account of undetected Xe fluorescence signal in the molten phase of in-situ olivine/basalt experiment (Fig. 4.1), here we took the Xe content of melt (16.24 ± 2.07 ppm) measured from recovered glass and Xe content of crystal (0.145 ± 0.036 wt%) measured from in-situ experiment for determination of $D^{Xe}_{Ol/m}$, which is up to 88.7 ± 21.9 at 1270 °C

(Table 4-2), revealing that Xe turns to be a compatible element at depth.

Table 4-3

Xe content measured with mass spectrometry analyses. In brackets: uncertainties.

sample	phase	Xe atoms /wt %	Xe content (wt%)
HPT2	glass	$8.4 (0.3) \times 10^{18}$	$1.8 (0.7) \times 10^{-3}$
HPT2	glass	$6.5 (0.3) \times 10^{18}$	$1.4 (0.7) \times 10^{-3}$
PC265	glass	$4.1 (1.7) \times 10^{17}$	$8.9 (0.4) \times 10^{-5}$
PC265	glass	$4.3 (1.5) \times 10^{17}$	$9.4 (2.8) \times 10^{-5}$
PC265	glass	$4.0 (1.3) \times 10^{18}$	$8.7 (0.3) \times 10^{-4}$
PC265	olivine-rich	$9.3 (2.8) \times 10^{19}$	$2.0 (0.6) \times 10^{-2}$
PC265	olivine-rich	$2.2 (0.7) \times 10^{19}$	$4.8 (1.5) \times 10^{-3}$

Olivine-rich is the analyzed piece of 83 ± 10 % olivine crystals coexisting with 17 ± 10 % melt.

These results end the controversy on Xe partitioning studies, suggesting the relative higher range of previously published partition coefficients are reliable based on the analysis from the quenched experiments (Fig. 4-3b).

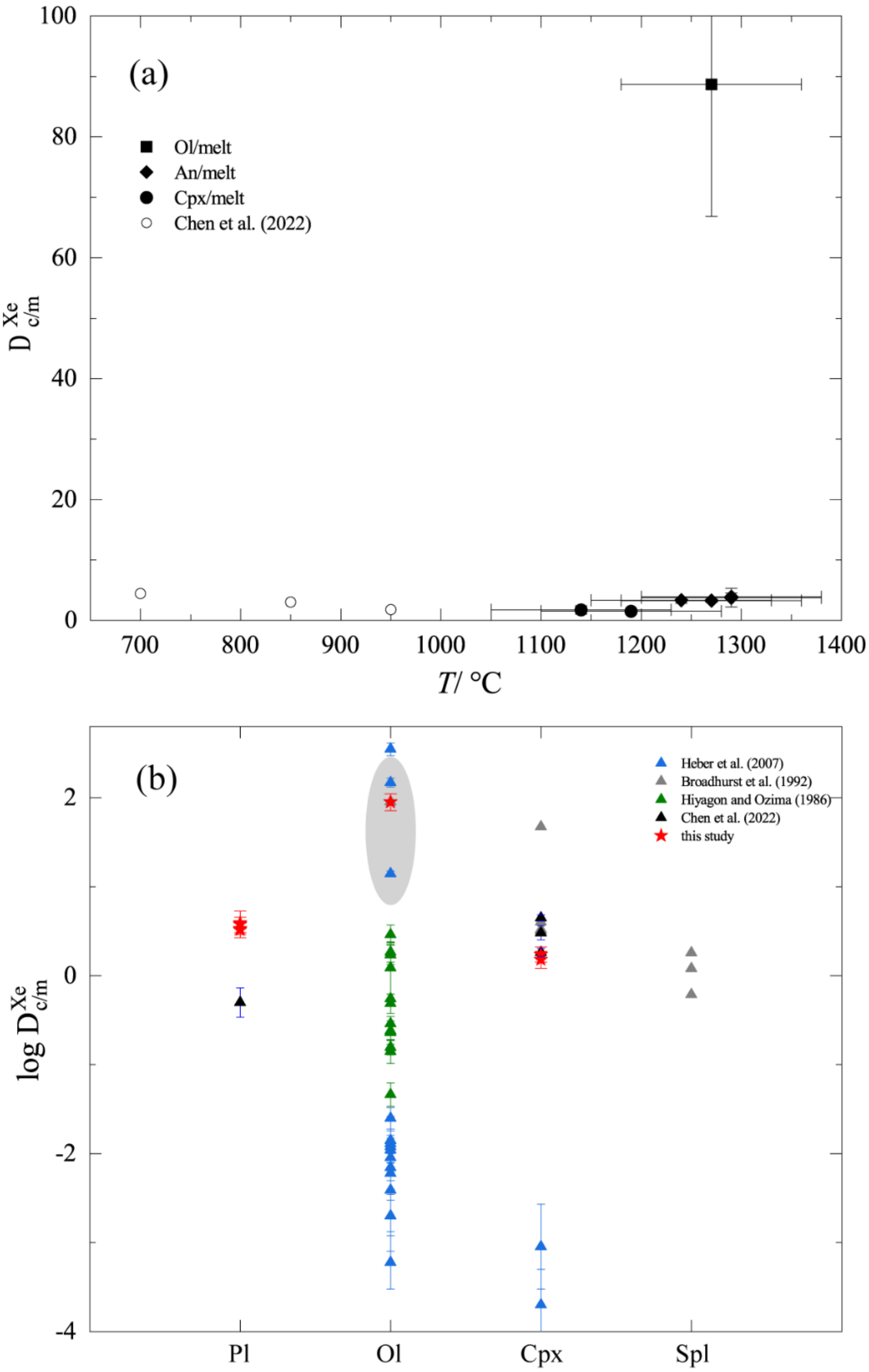

Fig. 4-3. Xenon crystal/melt partition coefficients. (a) for all investigated systems; (b) compared with literature data: Heber et al. (2007) (blue); Broadhurst et al. (1992) (grey); Hiyagon and Ozima (1986) (green), Chen et al. (2022) (black); Pl, plagioclase; Ol, olivine; Cpx, clinopyroxene; Spl. spinel; Grey area for Ol-melt system represents the results from ex-situ measurements with mass spectrometry analyses.

4.3.2 Xe behaviour in polymineralic plagioclase-clinopyroxene-basalt system

Clinopyroxene can form plentiful of solid solutions in the Ca-Mg-Fe-Al-Na system (Morimoto 1988; Deer et al. 2013). In anorthite (An)-clinopyroxene (Cpx) system, An transforms to Cpx at higher *P* while Cpx is absent or in smaller amounts at lower *P* (Green and Hibberson, 1974). We hence investigated Xe distribution in An-Cpx-melt system.

Upon heating, Xe fluorescence signal of Xe Kα lines were discovered in both ‘crystal-rich’ and ‘melt-rich’ patterns (Fig. 4-4). At higher *P* (2.2 GPa), clinopyroxene was the only detected stable crystal phase, with a more intense Xe fluorescence signal in ‘crystal-rich’ compared to ‘melt-rich’ pattern (Fig. 4-1). However, when *P* decreased below 1.5 GPa, the anorthite diffraction signal was systematically observed (Fig. 4-4). Xe fluorescence signal in ‘crystal-rich’ pattern was more intense than in that of melt pattern. Interestingly, Xe fluorescence signal in Cpx crystal remarkably decreased, indicating Xe was extracted from Cpx to An.

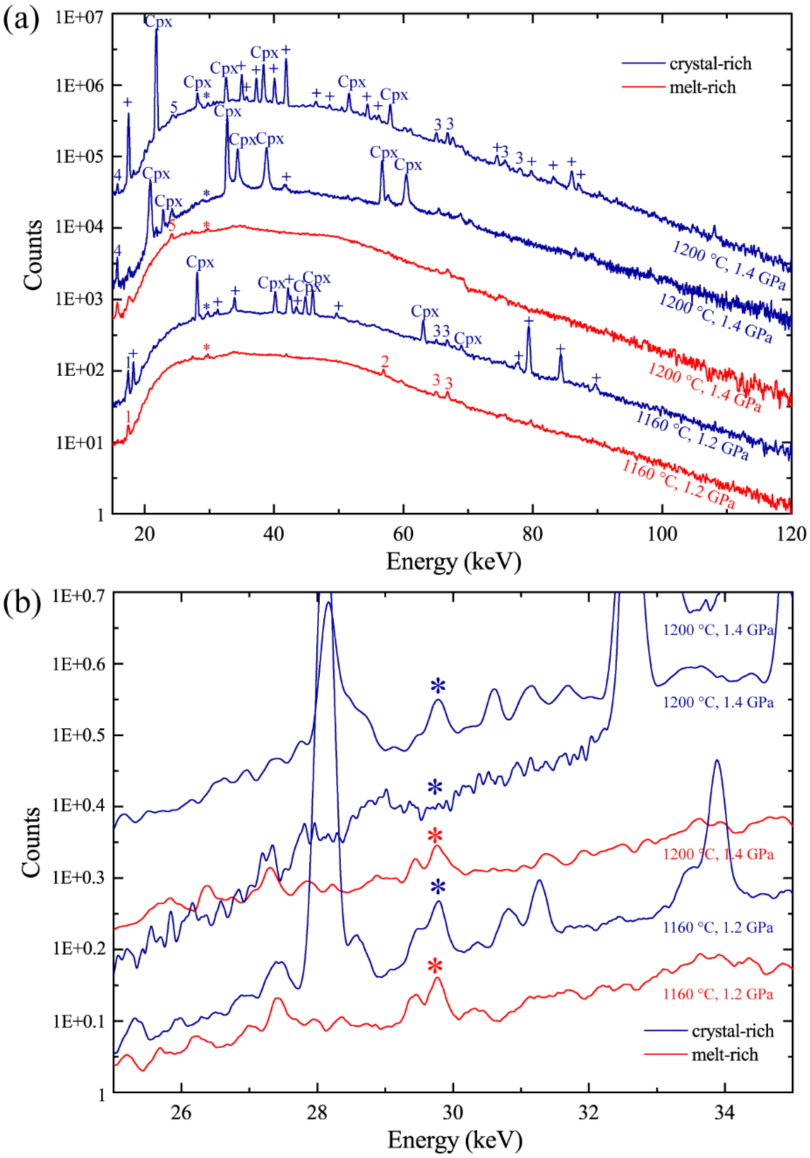

Fig. 4-4. *In situ* energy-dispersive patterns from PE press experiments. (a) EDX spectra for coexisting melt (red) and crystal-rich (blue) patterns collected at 10.0252º; (b) zoom on Xe fluorescence signal. Asterisks denote Xe Kα fluorescence ray (29.78 keV); + represents anorthite diffraction; Cpx for clinopyroxene diffraction; 1-5 from beamline elements: 1, Mo fluorescence; 2, MgO diffraction; 3, Pt fluorescence; 4, Zr fluorescence; and 5, In fluorescence. Note the W absorption edge at 69 keV.

To obtain phase fractions in 'crystal-rich' patterns, EDX data were processed by normalizing intensities with live time and slits size, and converting energy to scattering vector, q (Fig 4-2b), and further converted into conventional angle-dispersive data for Rietveld analysis (Fig 4-5) using methods described in Neuling and Holzapfel (1992).

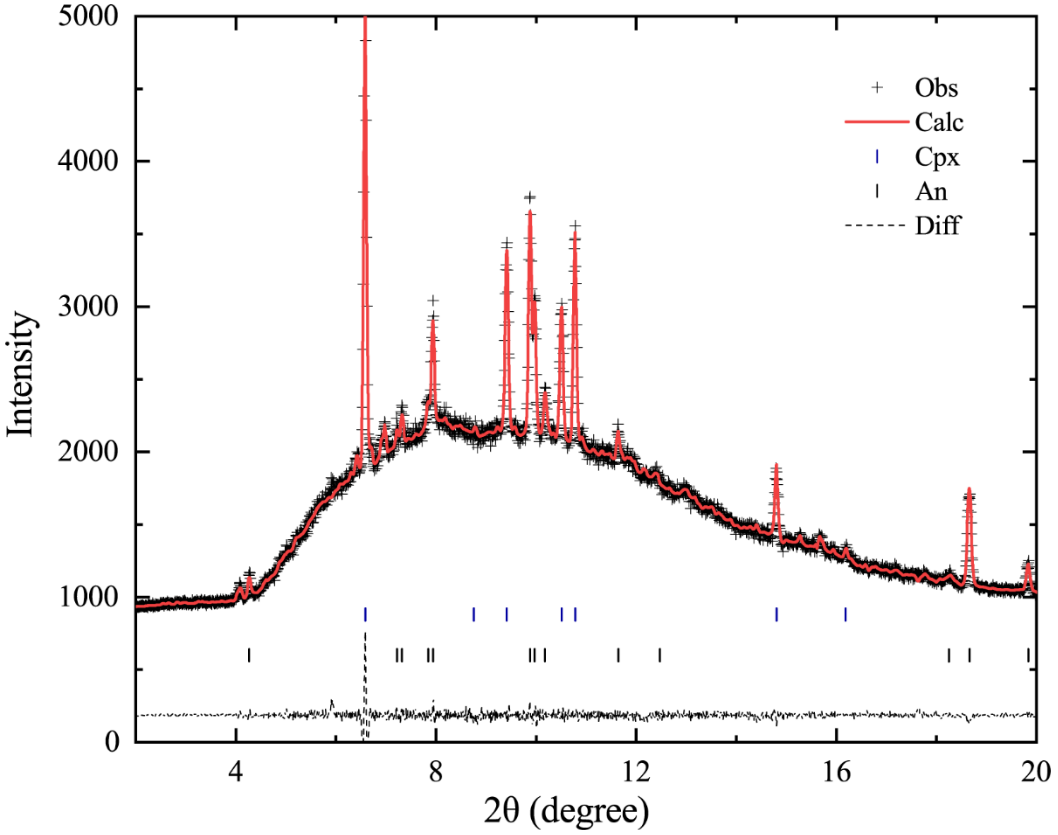

Fig. 4-5. Converted angle-dispersive data of An-Cpx-melt system at 1160 °C, 1.2 GPa.

Assuming $D^{Xe}_{An/m}$ keeps constant with an average value of 3.57, Xe contents were determined following the same strategy as described above. Results are summarized in Table 4-4. Xe concentration significantly reduced in both melt and clinopyroxene phases with the appearance of anorthite.

Table 4-4

Phase proportions, densities and Xe concentrations. In brackets: uncertainties.

			melt-rich		crystal-rich			Xe content		
Run	P (GPa)	T (°C)	X_c (%)	X_m (%)	X_m (%)	X_{Cpx} (%)	X_{An} (%)	$Xe_{m/g}$ (wt%)	Xe_{An} (wt%)	Xe_{Cpx} (wt%)
HPT4	0.9	1155	0	100	23.6	56.8	19.6	0.029 (0.003)	0.097 (0.009)	0.012 (0.003)
	1.4	1200	0	100	42.4	38.6	19.0	0.026 (0.002)	0.087 (0.019)	0.009 (0.003)

1.1	1140	0	100	45.2	14.0	40.8	0.033 (0.002)	0.110 (0.017)	0.012 (0.006)
1.2	1160	0	100	46.9	36.1	17.0	0.032 (0.009)	0.105 (0.031)	0.006 (0.002)

Our *in situ* high *P*-*T* measurements show that Xe is a compatible element in clinopyroxene with $D^{Xe}_{Cpx/m}$ reaching 1.72 at 2.2 GPa (Fig. 4-2). However, anorthite would have a negative effect on $D^{Xe}_{Cpx/m}$, with an extreme extraction of Xe from clinopyroxene to anorthite, resulting in $D^{Xe}_{Cpx/m}$ far less than 1 (Fig. 4-6).

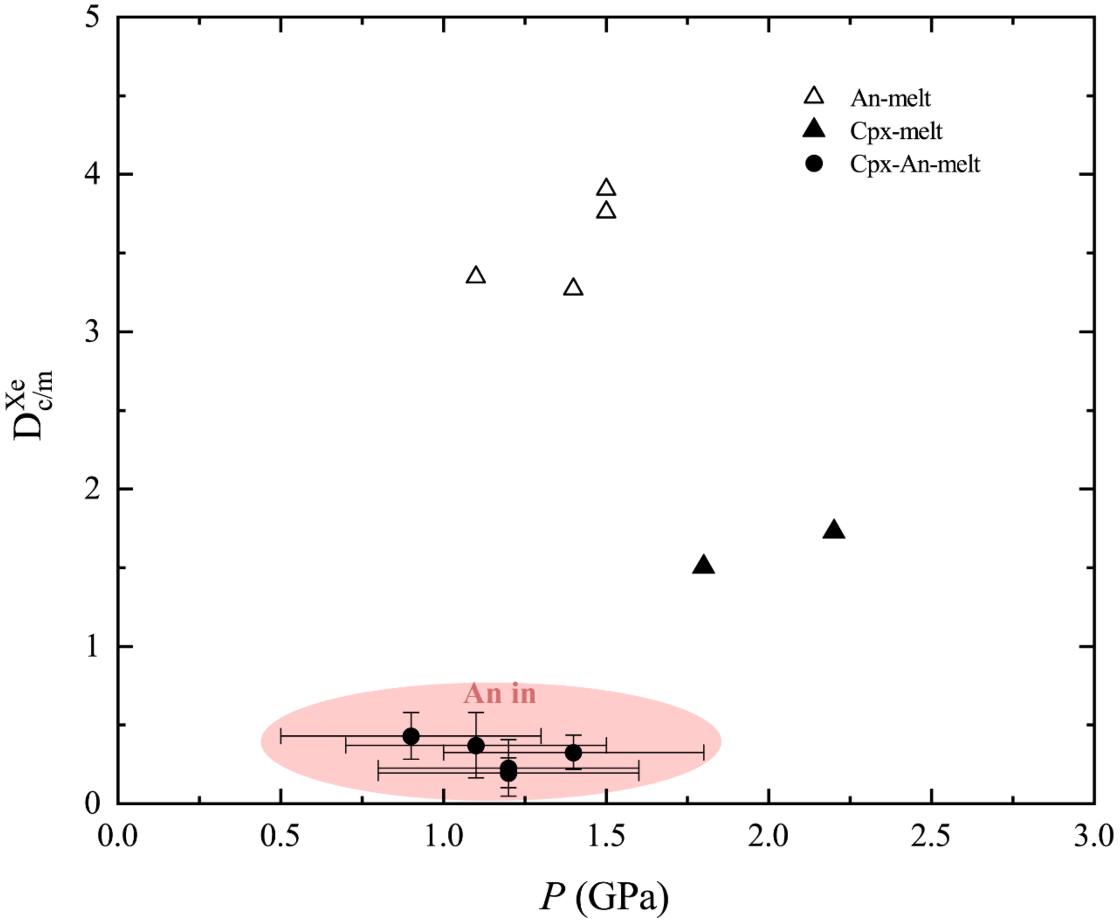

Fig. 4-6. Partition coefficient of Xe. Hollow data for $D_{An/m}^{Xe}$, solid data for $D_{Cpx/m}^{Xe}$. Red area indicates Cpx-An-melt system. Cpx: clinopyroxene; An: anorthite.

4.3.3 Characterization of quenched samples

Chemical analyses of starting glasses and samples recovered from in-situ measurements are summarized in Table 4-5. Based on SEM and EPMA analyses, the synthesized starting glass of Xe-doped basalt is chemically homogeneous.

Table 4-5

Chemical composition in wt% obtained from EPMA. Analyses are based on 10-20 data points, in brackets: standard deviation.

Run	Phase	Na_2O	K_2O	FeO	CaO	MgO	SiO_2	Al_2O_3	Xe	total
PC197	An (95)	1.13 (0.23)	0.19 (0.04)		17.16 (0.17)		46.40 (0.38)	32.31 (0.27)	< DL	97.19
	Cpx (5)			10.43 (0.21)	2.35 (0.17)	29.72 (0.25)	49.52 (0.99)	8.52 (0.84)	< DL	
	glass	1.10 (0.05)	0.95 (0.08)	9.40 (0.7)	11.70 (0.32)	8.42 (0.14)	49.86 (0.58)	18.97 (0.36)	< DL	100.70
PC202	glass			13.00 (0.33)	13.67 (0.39)	10.19 (0.16)	44.93 (0.74)	17.55 (0.31)	0.05 (0.01)	99.40
PC229	Cpx			11.00 (0.41)	14.82 (0.32)	13.20 (0.21)	45.81 (0.32)	16.86 (0.27)	< DL	101.69
	glass			11.45 (0.99)	14.03 (0.27)	12.00 (0.31)	45.20 (0.75)	17.14 (0.21)	< DL	99.84
PC265	Ol			9.80 (0.89)		48.84 (0.76)	42.13 (0.39)		< DL	100.76
	glass			3.85 (0.62)	13.80 (0.21)	11.27 (0.44)	48.45 (0.29)	21.47 (0.16)	< DL	98.85
HPT1	Cpx			2.00 (0.41)	17.53 (2.56)	16.69 (3.05)	49.59 (1.41)	16.41 (1.65)	< DL	102.21
	glass	2.17 (0.11)	1.78 (0.11)	1.32 (0.12)	9.92 (0.41)	4.81 (0.32)	55.55 (0.45)	23.72 (0.25)	< DL	99.27
HPT2	Ol			8.81 (0.85)		51.16 (1.15)	42.26 (0.44)		< DL	102.22

	glass			4.86 (0.19)	15.27 (0.27)	13.04 (0.27)	49.00 (0.64)	18.71 (0.37)	< DL	100.89
HPT4	An (60)	1.87 (0.11)	0.07 (0.04)		17.30 (0.63)		48.76 (0.28)	32.33 (1.97)	< DL	100.32
	Cpx (40)	0.18 (0.04)		0.81 (0.35)	14.96 (0.97)	26.91 (1.13)	49.32 (0.86)	9.29 (1.15)	< DL	101.01
	glass	1.07 (0.18)	0.07 (0.01)	0.64 (0.32)	15.38 (1.09)	15.01 (0.93)	48.68 (0.51)	19.28 (0.64)	< DL	99.88

PC: from PC press runs; HPT: from in-situ PE press experiments; An, anorthite; Cpx, clinopyroxene; Ol, olivine; DL, detection limit.

EDX analyses confirmed the presence of Xe bubbles trapped in An (Fig. 4-7a), Cpx (Fig. 4-7c) and Ol (Fig. 4-7d and e) crystals, interpreted as Xe diffusing out of the crystal network during *T*-quenching as previously observed during in situ x-ray diffraction experiments (Sanloup et al., 2011). Interestingly, sub-micron Xe bubbles trapped in melt were only detected in Cpx-melt system (Fig. 4-7c), corresponding to the smallest value of $D_{Cpx/m}^{Xe}$ compared to $D_{An/m}^{Xe}$ and $D_{ol/m}^{Xe}$ measured from in-situ experiments. At higher pressure (> 1.8 GPa), Cpx was the only stable crystal phase from recovered sample (Fig. 4-7g), while anorthite crystal occupied a large proportion at low pressure (Fig. 4-7i). No Xe bubbles are observed in or at the periphery of quenched crystals from in-situ experiments (Fig. 4-7g, h and i) due to the relatively low initial Xe content. On the contrary, we found a very different behaviour of Kr in plagioclase coexisting with felsic melt (Fig. 4-7j), where bright Kr bubbles are mainly located at the edge of crystals, interpreting as Kr diffusing out from the crystal voids at ambient conditions. Despite the finding of the Kr bonding to oxygen in melts via insertion into the melt ring structure (Crepisson et al., 2018b), Kr cannot fit in Si-O tetrahedra of crystals by substitution of Si due to the larger Kr-O distance (2.49 ± 0.1 Å) compared to the Xe-O bond length of 2.10 ± 0.1 Å (Probert, 2010; Crepisson et al., 2019). This short bond length is due to Xe being oxidized, not neutral, and having a stronger covalent bond to oxygen than krypton does (at least in magmas). Hence oxidized Xe has a smaller ionic radius than Kr.

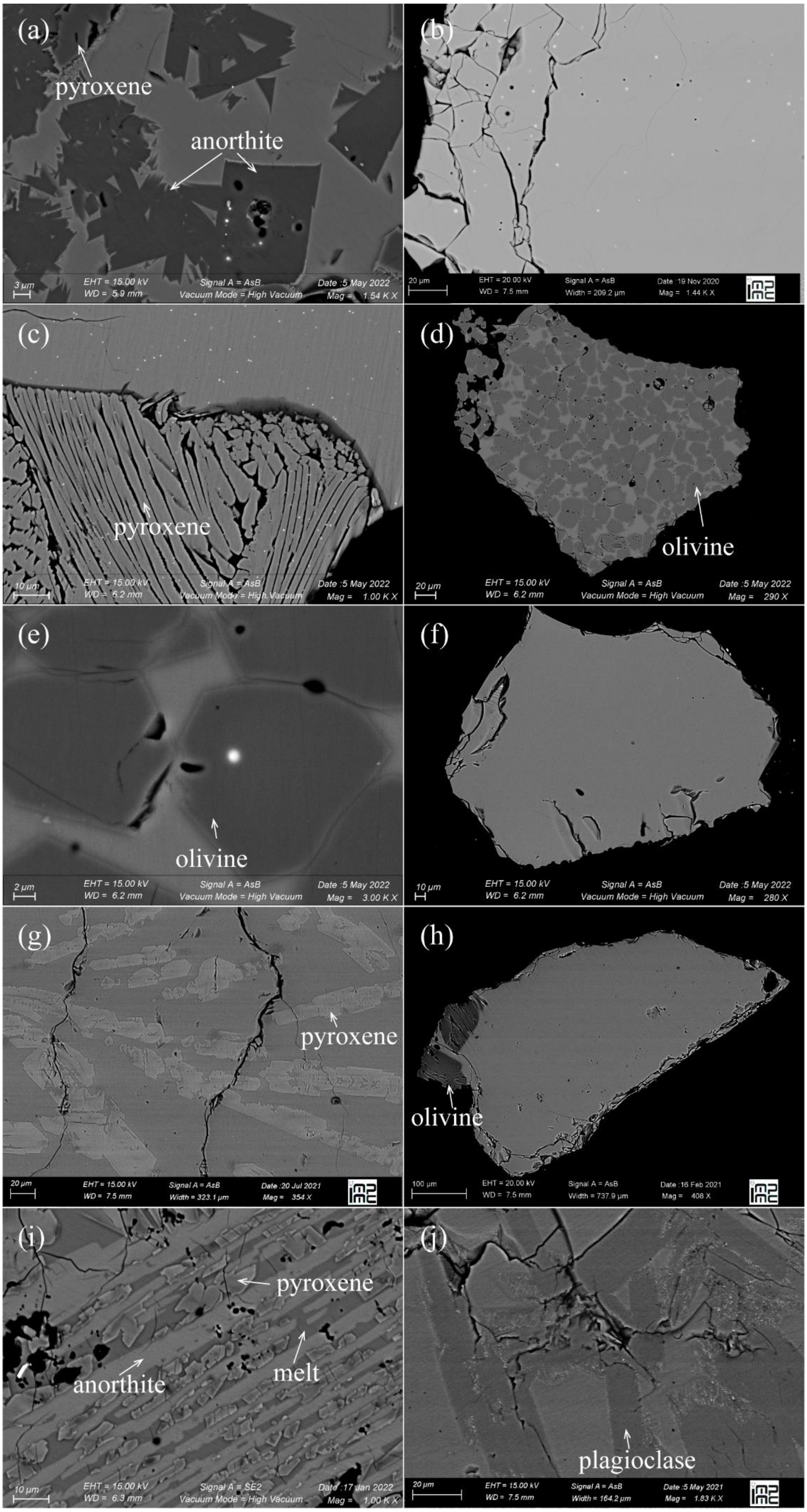
(a)
pyroxene
anorthite
3 µm EHT = 15.00 kV WD = 5.9 mm Signal A = AsB Vacuum Mode = High Vacuum Date :5 May 2022 Mag = 1.54 K X
(b)
20 µm EHT = 20.00 kV WD = 7.5 mm Signal A = AsB Width = 209.2 µm Date :19 Nov 2020 Mag = 1.44 K X
(c)
pyroxene
10 µm EHT = 15.00 kV WD = 6.2 mm Signal A = AsB Vacuum Mode = High Vacuum Date :5 May 2022 Mag = 1.00 K X
(d)
olivine
20 µm EHT = 15.00 kV WD = 6.2 mm Signal A = AsB Vacuum Mode = High Vacuum Date :5 May 2022 Mag = 290 X
(e)
olivine
2 µm EHT = 15.00 kV WD = 6.2 mm Signal A = AsB Vacuum Mode = High Vacuum Date :5 May 2022 Mag = 3.00 K X
(f)
10 µm EHT = 15.00 kV WD = 6.2 mm Signal A = AsB Vacuum Mode = High Vacuum Date :5 May 2022 Mag = 280 X
(g)
pyroxene
20 µm EHT = 15.00 kV WD = 7.5 mm Signal A = AsB Width = 323.1 µm Date :20 Jul 2021 Mag = 354 X
(h)
olivine
100 µm EHT = 20.00 kV WD = 7.5 mm Signal A = AsB Width = 737.9 µm Date :16 Feb 2021 Mag = 408 X
(i)
pyroxene
anorthite
melt
10 µm EHT = 15.00 kV WD = 6.3 mm Signal A = SE2 Vacuum Mode = High Vacuum Date :17 Jan 2022 Mag = 1.00 K X
(j)
plagioclase
20 µm EHT = 15.00 kV WD = 7.5 mm Signal A = AsB Width = 164.2 µm Date :5 May 2021 Mag = 1.83 K X

Fig. 4-7. SEM images of starting glass and high *P-T* quenched samples. (a) Run PC197, anorthite (dark) + basaltic melt (grey), about 5% clinopyroxene detected without Xe trapped (grey crystal at the upper left and low right).; (b) PC202, Xe-doped basalt glass; (c) PC229, clinopyroxene + basaltic melt; (d) PC265, olivine (dark) + basaltic melt (grey); (e) zoomed on olivine crystal; (f) PC265, a piece of pure basaltic glass with no Xe bubble detected (g) HPT1, clinopyroxene + basaltic melt; (h) HPT2, olivine (dark) + basaltic melt (grey); (i) HPT4, clinopyroxene + anorthite + basaltic melt; and (j) PC223, plagioclase (dark) + felsic melt (grey), with Kr bubbles trapped at the edge of the plagioclase crystals. Bright dots in (a), (b), (c), (d) and (e) are Xe bubbles.

4.3.4 Xe storage at depths

We now turned to simulate Xe distribution in olivine mineral and residual MO with two models of crystallization: (1) fractional crystallization as the standard model for evaluating the effect of MO crystallization (Kato et al., 1988); and (2) equilibrium crystallization coupled with atmospheric loss (Hirschmann, 2016) (Fig. 4-8). In the latter model, a MO was assumed to be overlayed by an atmosphere and equilibrating with crystallized olivine, where the mass of a volatile dissolved in the magma ocean is related to its solubility imposed by the vapor partial pressure (P) of the atmosphere. For Xe, it can be defined as:

$$P_{Xe} = M_{atmosphere}^{Xe} \cdot g/A \tag{4.2}$$

where M represents the total mass of Xe, g is the gravitational acceleration (9.8 m/s^2), A is the surface area of the planet (5.1×10^{14} m^2). And from the mass balance, we can get:

$$M^{Xe} = M_{MO}^{Xe} + M_{olivine}^{Xe} + M_{atmosphere}^{Xe} \tag{4.3}$$

where M^{Xe} is equal to the product of concentration c and the mass of reservoir i:

$$M_i^{Xe} = c_i^{Xe} \cdot m_i \tag{4.4}$$

and equilibrium between MO and olivine can be expressed as:

$$D_{olivine/MO}^{Xe} = c_{olivine}^{Xe} / c_{MO}^{Xe} \tag{4.5}$$

equilibrium between the MO and atmosphere can be approximately given by the Henry's law:

$$c_{MO}^{Xe} = S_{Xe} \cdot P_{Xe} \tag{4.6}$$

where *S* is the Henrian constant. Combining Equation 4.2 to 4.6 gives:

$$M^{Xe} = M_{atmosphere}^{Xe} \cdot \left[1 + \frac{S_{Xe} \cdot g}{A} \cdot (m_{MO} + m_{olivine} \cdot D_{olivine/MO}^{Xe})\right] \tag{4.7}$$

Assuming that MO was formed by the whole molten upper mantle during impacts (e.g., Abe, 1997) with a 55 vol. % of olivine (e.g., Gaherty et al., 1999), initial Xe concentration was 50 ppt representing of the average Xe content in EC (Crabb and Anders 1981; Patzer and Schultz, 2002) and $D_{Ol/m}^{Xe}$ kept constant for 88.7 (indeed partition coefficient can be effected by *P* and *T*, however we use the only gotten one at 2 GPa), fractional crystallization process could give an upper limit of Xe storage at depth, which causes a larger Xe enrichment in Ol compared to equilibrium crystallization (Fig. 4-8a), with a storage of hundreds to thousands ppt Xe (Fig. 4-8b), the decrease of Xe concentration in Ol is due to the growing fraction of crystals. When considering Xe loss to atmosphere, the inferior limit of Xe concentration in Ol can be up to 176 ppt with equilibrium crystallization. We address that neither of both models are unlikely to be perfect representatives, but could constrain the range of Xe allocation. Besides, 8 to 12 atmospheric masses of Xe are missing compared to the chondritic noble gas concentration trend (Bekaert et al., 2020), corresponding to a ^{132}Xe concentration of 1.1×10^{-14} mol/g to 1.7×10^{-14} mol/g if stored in the crust and upper mantle (Rzeplinski et al., 2022). Only 50 ppt of Xe stored in upper mantle or 10 ppb Xe in lower continental crust is sufficient (Sanloup, 2020) to solve the entire amount of the 'missing Xe' (Ozima and Podosek, 1999). Our model thus indicates the whole missing Xe could be stored in terrestrial upper mantle. Moreover, natural Xe excesses have also been reported in xenoliths (Hennecke and Manuel, 1975a; Poreda and Farley; 1992; Czuppon et al., 2009) with a ^{132}Xe concentration ranging from 1.2×10^{-16} mol/g to 3.8×10^{-15} mol/g. The natural sample nevertheless can only give a lower limit of the relevant Xe content at depth due to the loss of Xe on geological timescales.

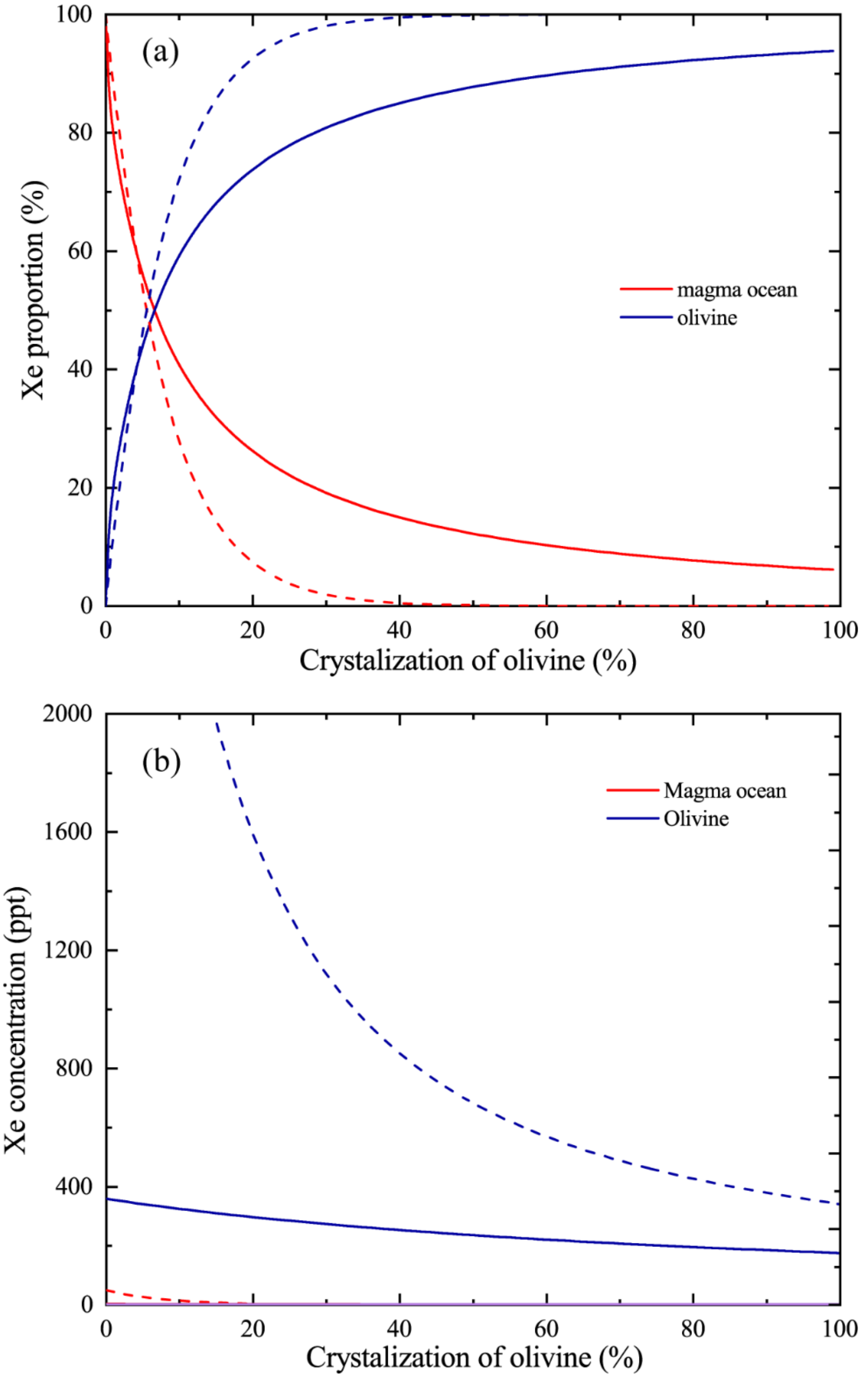

Fig. 4-8. Xe distribution with the crystallization of olivine in MO. (a) Xe proportion (equal to $c_i/(c_{Mo}+c_{olivine})$, c is the concentration) and (b) Xe concentration in crystalized olivine and residual MO; dashed lines for fractional crystallization process; solid lines for equilibrium crystallization considering degassing process.

The discovery of relatively low solubility of Ar in minerals (< 0.015 wt.%) and high solubility in ultramafic liquid (~1.5 wt.%) suggests it is incompatible during MO crystallization (Jackson et al., 2021). Light noble gases like Ar are so far considered as dissolving in interstitial voids in the melt and glass structure (Carroll and Stolper, 1993).

Besides, as discussed before, Kr cannot fit in Si-O tetrahedra of crystals by substitution of Si due to the larger Kr-O distance. Consequently, the high compatibility of Xe is unique among other noble gases. We hence propose a scenario to explain the riddle of 'missing Xe' (Fig 4-9). The isotopic composition of Earth points out that it mainly consists of EC meteorites (Dauphas, 2017), which likewise contributed to terrestrial volatile elements (Piani et al., 2020). Xe likely inherited from EC was partially retained in Ol, Cpx and An minerals as a compatible element during the crystallization of undergoing MOs of pre-planetary bodies, which further entered to the differentiate silicate crust and upper mantle. Yet there is still a part of Xe released into the magma during crystallization, and eventually degassed to the atmosphere. However, crystallization-induced Xe in the primitive atmosphere could have been partly or entirely lost at the proto-planetary stage with a series of giant impacts (Schlichting and Mukhopadhyay, 2018). Based on the ratio of He/Ne isotopes, at least two separate magma ocean degassing and atmospheric loss processes occurred during terrestrial accretion (Tucker and Mukhopadhyay, 2014). The Xe isotopic fractionation of +2.3 ± 0.2‰ per a.m.u. measured in sanidine feldspar and olivine crystals compressed at high *P* and *T* (Rzeplinski et al., 2022) indicates a succession of magma oceans and atmospheric loss on proto-planets at the planetary embryo stage of more than 10 times in order to explain the observed +35 ‰ per a.m.u. signature of the atmosphere compared to CI chondrites. Xe isotopes in the deep mantle show a chondritic component compared to that of atmosphere (Holland et al., 2009; Mukhopadhyay, 2012; Caracausi et al., 2016), indicating the later MOs may not homogenize the whole mantle, or recycling of early Archean atmosphere at depth as atmospheric depletion in Xe light isotopes occurred throughout the Archean (Pujol et al., 2011; Holland et al., 2013; Avice 2017, 2018; Almayrac et al., 2021). The secondary atmosphere was generated by degassing during the magma ocean stage after the Moon-forming impact. Indeed, CI chondrites and comets could deliver Xe to the secondary atmosphere during later veneer, contributing to the initial Xe isotopic feature (U-Xe). However, the late veneer contribution was insufficient to overprint the volatile characteristics obtained during the accretion phase (Halliday, 2013). Instead, it was continuously revamped by subsequent magma production and eruption throughout geological times, eventually overprinted by released heavy Xe at the end of the Archean. Besides, Xe can efficiently transfer from mantle to crust (both continental and oceanic) in later magmatic processes throughout Earth's history due to the preference to plagioclase in polymineralic plagioclase-clinopyroxene-basalt system, leading to the enrichment of Xe in crustal reservoir (e.g., Drescher et al., 1998).

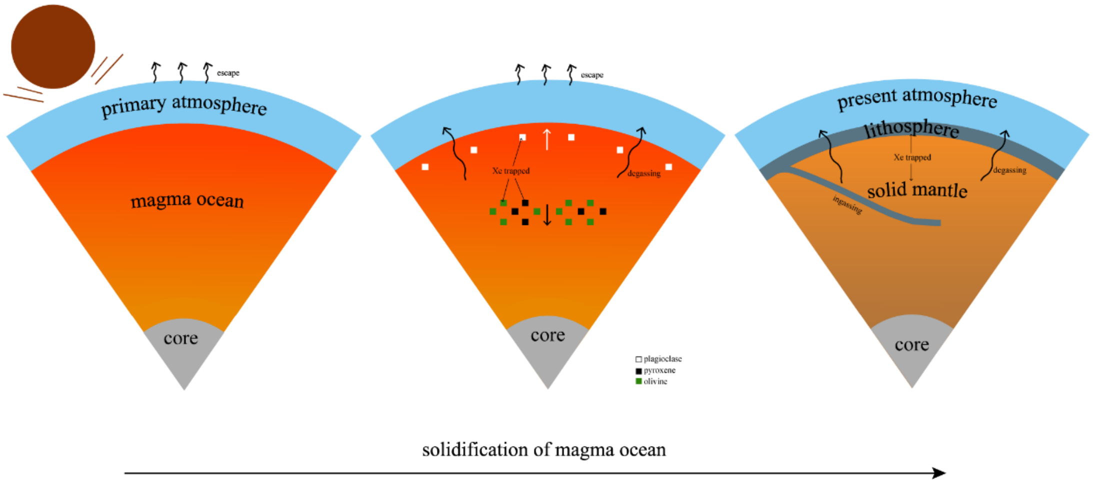

Fig. 4-9. Schematic section of the Xe storage at depths during solidification of magma oceans.

Chapter 5: Xenon behavior in fluids at depth

This chapter studied the local structure of Xe in aqueous fluids, and its effect on Xe distribution behaviour between aqueous fluids and minerals using in-situ X-ray diffraction (XRD) and X-ray fluorescence (XRF) analyses. We systematically investigated Xe-fluids structure by comparing Xe-doped and undoped samples under pressure. The preliminary result shows a Xe-O distance similar to that in Xe hydrates, which may imply Xe is in a clathrate environment in the fluid, different from mechanisms in minerals and melts. In particular, Xe partitioning between fluids and crystal has been quantified, with Xe being partially retained within fluids.

5.1. Introduction

As previously mentioned, we now have good understanding of the local structure of Xe in silicate minerals and melts (Sanloup et al., 2005, 2011; Probert, 2010; Kalinowski et al., 2014; Leroy et al., 2018). However, there is no study of Xe retention mechanism in aqueous fluids, whereas it is fundamental to constrain Xe distribution between water/magma or water/minerals system. Clathrate hydrates (or gas hydrates), ice-like crystalline inclusion compounds of water and natural gas (or other organic materials) that usually form spontaneously at high *P* and low *T*, have long been regarded as a crucial carrier of noble gases to the giant planets. They have been discovered at oceanic seafloor and permafrost regions on Earth (e.g., Kvenvolden, 1998, 1999), or potentially exist in comets (Delsemme and Wenger, 1970; Iro et al., 2003), with three molecular structures at near-ambient conditions: two cubic structures named structure I (CS-I) and structure II (CS-II), and a hexagonal structure (SH). Interestingly, all noble gases can form clathrate hydrates with H_2O via van der Waals interactions, with a decrease of stability from Xe to Ne (Dyadin et al., 1999). Among the noble gases, Xe molecule is too large to fit in CS-II but can remain stable in CS-I up to 1.8 GPa, transfer to a hexagonal clathrate phase at higher *P* (Sanloup et al., 2002a), and decompose into solid Xe and ice VII above 2.5 GPa (Dyadin et al., 1996; Sanloup et al., 2002a). Besides, unlike pure water high-density amorphous ice, cubic clathrate hydrates exhibit a sharp, first-order-like transition to an amorphous state when compressed at low *T*, with a stable amorphous Xe hydrate above 3 GPa (Carvalho et al., 2021).

Besides, the convecting mantle noble gas isotopic and elemental composition can be explained by subduction of sediment and seawater-dominated pore fluids by analyzing Xe and Kr isotopes in mantle-derived well gases (Holland and Ballentine, 2006). Subduction of noble gases could occur either by storage in seawater filling porous sediments (Holland and Ballentine, 2006), or by retention in hydrous minerals (Kendrick et al., 2011; Smye et al., 2017) in channels and ring sites formed by a pair of six-member (Si, Al)O^{4}_{-4}. Xenon has a relatively high solubility in serpentinite (3.29×10^{-9} mol/g), which is ten times more than that of Ar (Krantz et al., 2019). However, it remains unknown that to what extent of Xe could be released with aqueous fluids or be retained in the slab and enter into the mantle during subduction processes due to the lack of knowledge of partition coefficients. Moreover, some studies show that there are weak bonds between noble gases and halogens via van der Waals interactions (Rohrbacher et al., 2000; Beswick et al., 2012; Nunzi et al., 2019). The aim of this study is to determine the behavior of Xe in H_2O and brine system under *P*, and further investigate how these retention mechanisms affect Xe partitioning between mineral and fluids. In terms of chemical composition, we use plagioclase in co-existence with H_2O/brine solution, and explore Xe behavior using resistive-heating diamond anvil cell, with in-situ high energy (42.7 keV) X-ray fluorescence and X-ray diffraction set-up up to 6 GPa and 1000 ºC.

5.2. Methods

The composition and synthesis of starting plagioclase glass ($Ab_{80}An_{20}$) were described in section 3.2.1. Besides, 1 mol/L NaCl solution was used to simulate the brine system.

5.2.1 Diamond-anvil cell experiments with *in situ* monochromatic x-ray probes

In-situ high energy synchrotron X-ray diffraction and fluorescence data at the extreme conditions were collected at beamline P02.2, Petra III (DESY, Hamburg). Symmetric large opening DACs (70°) equipped with Boelher-Almax seats and 800 mm diameter culet diamonds were used to generate high *P*-*T* conditions (Boehler et al., 2004). Laser drilled Re gasket was used as sample chamber, loaded with Xe-doped Pl glass. Resistive-heating was achieved using the internal heating technique developed by Fei and Mao (1994) using a Pt wire (cf, section 2.1.2). *T* was recorded by a type S thermocouple located on the edge of the gasket closed to the sample chamber. Pressure at ambient *T* was measured by ruby fluorescence, and was monitored at high *T* from Raman signal of pieces of ruby (Dewaele et al., 2008) and $SrB_4O_7{:}Sm^{2+}$ (Rashchenko et al., 2015). Synchrotron XRD and XRF analyses were performed using a 3 × 8 mm^2 focused monochromatic x-ray beam at 42.7 keV, following the same strategy as in previous studies (Bureau et al., 2016; Leroy et al., 2019). At each *T* step, *P* was firstly monitored from ruby and $SrB_4O_7{:}Sm^{2+}$ Raman signal, angle-dispersive diffraction patterns were recorded on a CsI bonded amorphous silicon detector (Perkin Elmer XRD 1621) to identify phases (i.e., crystalline vs fluids) and the local structure of the aqueous fluid from its radial distribution function (RDF). In-situ X-ray diffraction data were collected for six different loadings (Table 5-1), two on the plagioclase (0.5 wt% Xe) + H_2O composition, one on plagioclase (0.5 wt% Xe) + 1 mol/L NaCl composition, two on the undoped plagioclase + H_2O composition, and one on the plagioclase (0.15 wt% Xe) + H_2O composition (Fig. 5-1). Upon glass transition *T*, XRD was performed on the sample to find two positions (one optimizing crystalline signal = ‘crystal-rich’, and one optimizing H_2O signal = ‘H_2O-rich’), following by XRF measurements on each position. For each run, X-ray diffraction patterns were collected with an empty gasket inserted in the DAC at room conditions as the baseline patterns. The XRD patterns were integrated from the images with Fit2D software (Hammersley, 1998) and the diffraction peaks were modelled from pseudo-Voigt function using Fullprof software (Rodríguez-Carvajal, 1993). XRF signal was collected on a Vortex® 60-EX silicon drift detector with a collection time of 900s. Xe Kα and Kβ rays (29.78 and 33.62 KeV) were used to quantify Xe concentrations. For XRF, quantification of Xe content from signal intensity was calibrated in-situ in the DAC at room conditions by filling a gasket with 0.5 wt% Xe-doped starting glass (PC242) as a standard.

Table 5-1

Summary of diamond-anvil cell runs.

Run	Starting composition	Quenched products
Cell1	plagioclase glass (1.0 wt% Xe) + H_2O	crystal + H_2O
Cell3	plagioclase glass (1.0 wt% Xe) + 1 mol/L NaCl	crystal + H_2O
Cell4	undoped plagioclase glass + H_2O	crystal + H_2O
Cell5	plagioclase glass (1.0 wt% Xe) + H_2O	crystal + H_2O
Cell6	undoped plagioclase glass + H_2O	crystal + H_2O
Cell7	plagioclase glass (0.15 wt% Xe) + H_2O	crystal + H_2O

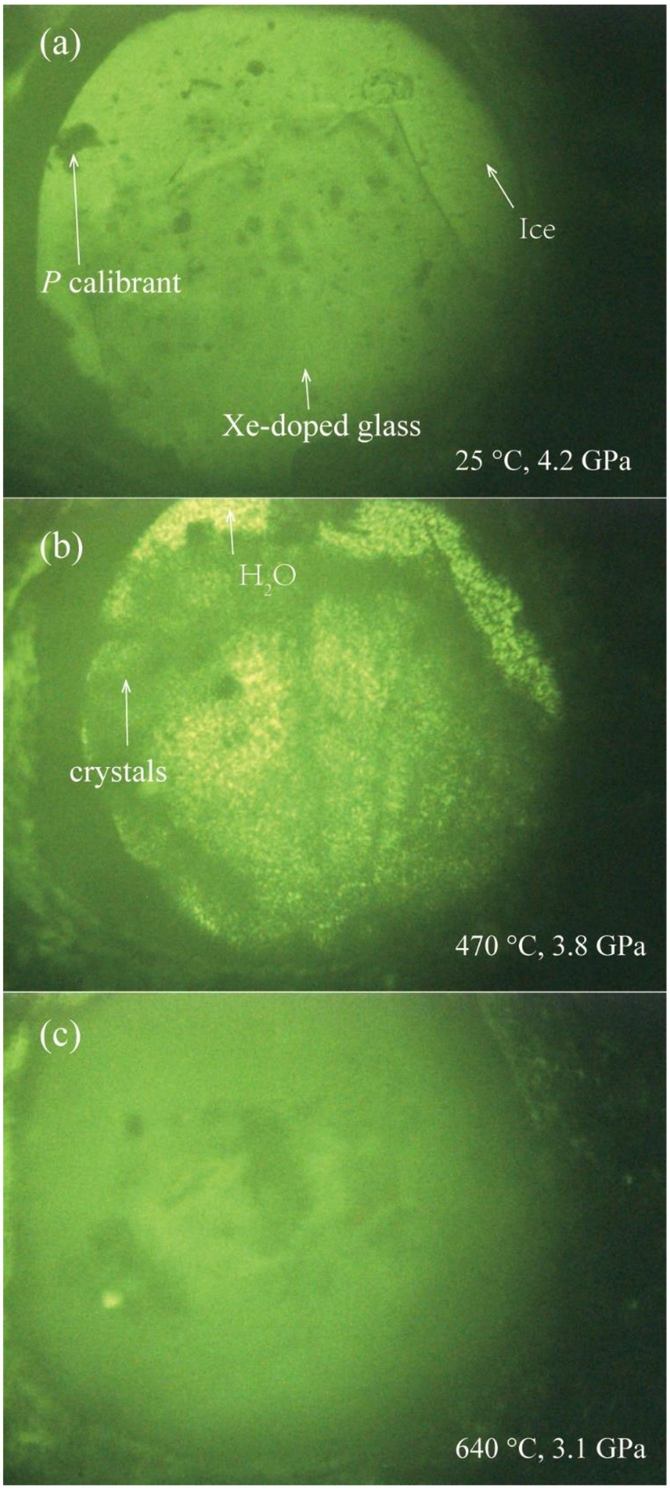

Fig. 5-1. Images observed by the optical microscope for run Cell5. At (a) room *T*; (b) 470 ºC; and (c) 640 ºC. H_2O existed as ice phase detected by XRD measurements at room *T* due to the relatively high *P*. About 450-500 ºC, recrystallization happened with tiny crystals (black) appearing. This process was fast, with only crystal and H_2O signal but no melt signal detected with XRD at higher *T* (600 ºC). The images were undistinguished above 600 ºC due to the poor quality.

5.2.2 Pressure determination

Ruby and $SrB_4O_7:Sm^{2+}$ were used as pressure sensors in our in-situ experiments (Fig. 5-2). Both of them showed a consistency of *P* at *T* less than 200 ºC, but have respective limitations at high *T* (cf, chapter 2.1.2). Therefore, to estimate *P* at *T* > 600 ºC in our experiments, the DAC was quenched after reaching the highest *T*, and measured *P* at ambient conditions as the *P* at the highest *T* (For example, for Cell4, 1.6 GPa measured at room conditions was taken as the *P* at 800 ºC). A calibration curve was further made combining the *P* read from Sm_4O_7 and quenched *P*. We address that the estimated *P* at high *T* only gives an inferior limit in this way.

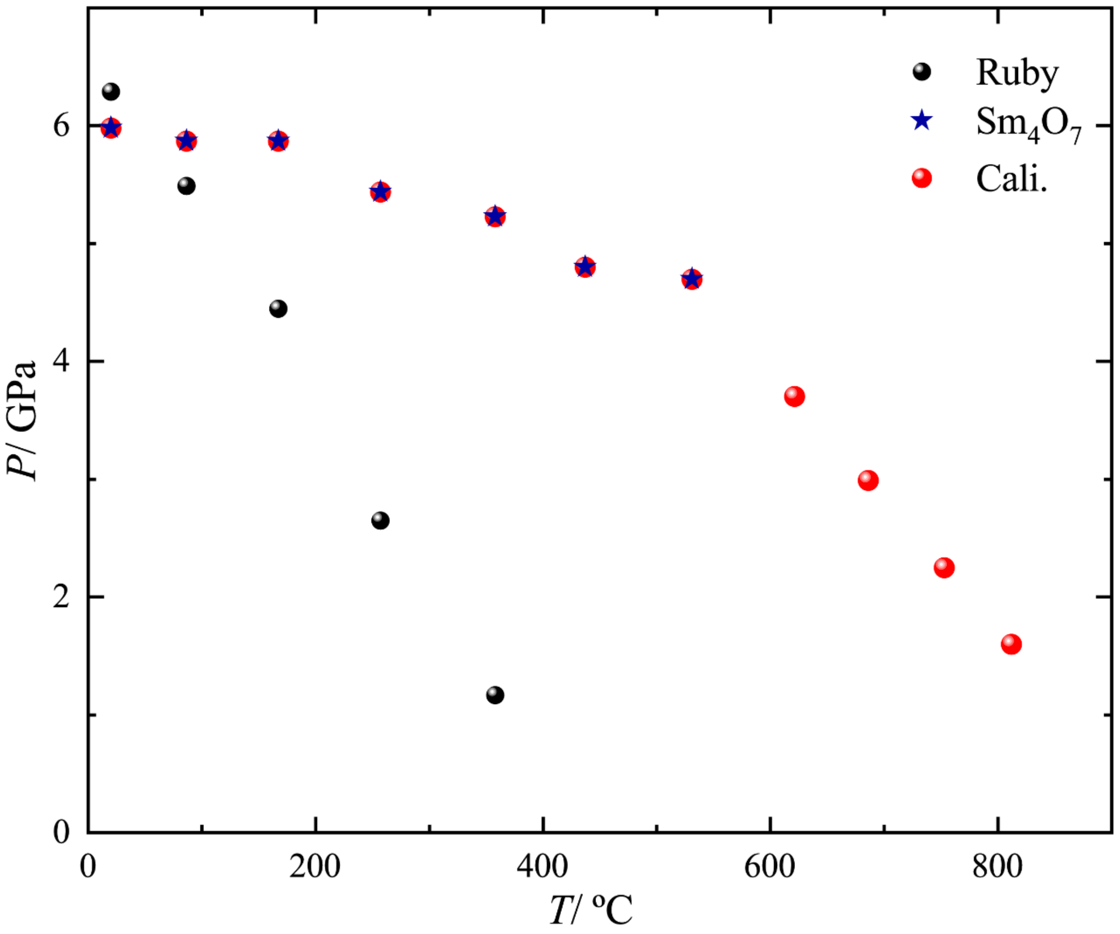

Fig. 5-2. Pressure determination for run Cell4. $SrB_4O_7:Sm^{2+}$ dissolved around 500-600 ºC. Final *P* (1.6 GPa) was measured on ruby quenched to room conditions.

5.2.3 Ex-situ chemical analyses

Quenched samples together with starting glasses were put in epoxy resin and polished for scanning electron microscopy and electron microprobe analyses.

A Zeiss Ultra 55 field emission scanning electron microscope (SEM) was used with a working distance of 7.5 mm and a voltage of 20 kV for detection of Xe. Major elements were analyzed using a Cameca SX-FIVE electron microprobe analyzer (EPMA) on the Camparis platform. The beam was focused to 15 μm diameter on the sample. Accelerating voltage was set to 15 kV, with 5 nA beam current for Na, Ca, Al, Si and 40 nA for Xe, 10s counting time for per element on both peak and background. Xe calibration was established following the procedure developed by Montana et al. (1993) by measuring the counts for the neighbouring elements, I (CuI) and Cs (CsCl).

5.3. Results and discussion

5.3.1 Total structure description

Data corrections were made according to the methods employed by Sanloup and de Grouchy (2018). X-ray diffraction data were collected on fluids using both Xe-doped and plain samples as X-ray diffraction is not chemically-selective. After baseline subtraction (empty DAC patterns), X-ray diffraction intensity data were converted into the structure factor *S(q)*, which represents the normalized amplitude of the waves scattering from a sample, using the Ashcroft-Langreth formalism (cf. section 2.2.4). The total radial distribution function *G(r)* was calculated by Fourier transform of the structure factor:

$$G(r) = \frac{1}{2\pi^2 rn}\int_0^{\infty} qS(q)\sin(rq)\,dq \tag{5.1}$$

where $n = \frac{\rho N_A}{N}$, M the mean atomic molar mass, and ρ the density.

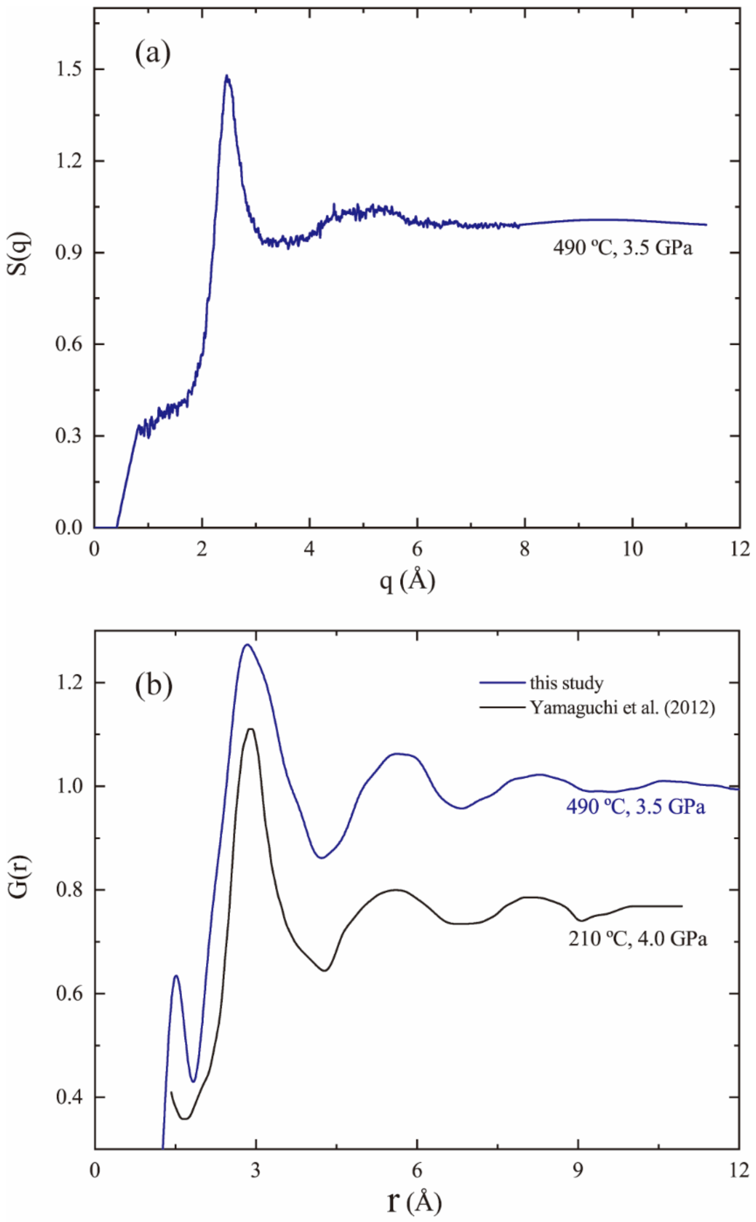

Fig. 5-3. Structure factors *S(q)* of aqueous fluids (H_2O) at high pressure and corresponding radial distribution functions, *G(r)* for run Cell6.

Fig. 5-3 shows the structure factors and corresponding total radial distribution functions of H_2O with the plain composition at 490 ºC, 3.5 GPa in run Cell6. The first and second diffuse peaks appeared at around 2.9 Å and 5.6 Å upon heating (Fig. 5-3b), concomitantly with the disappearance of crystalline ice diffraction peaks. The feature of G(r) is in satisfactory agreement with previous study of pure H_2O at 210 ºC, 4 GPa (Yamaguchi et al., 2002) with no changes observed. However, an additional contribution was detected at ~ 3.7 Å above 300 ºC for the Xe-doped experiments (Fig.

5-4). Indeed Xe can form compounds with H and O, with a Xe-H bond length of 1.7-1.8 Å in Xe-O-H and Xe-C-H compounds (Khriachtchev et al., 2008), and a Xe-O bond of 1.99-2.29 Å in Xe-doped quartz (Probert, 2010) or 2.05 Å in Xe-doped melt (Leroy et al., 2018). These distances are much shorter than the observed distance in Xe-doped H_2O system. Instead, Carvalho et al. (2021) found the O-Xe contacts at ~ 3.65 Å in two dodecahedral 5^{12} cages (D cages) and ~ 3.7-3.8 Å in six tetrakaidekahedral $5^{12}6^2$ cages (T cages) from 2.3 to 5 GPa in Xe clathrate hydrate cubic structure I, which belongs to Pm-3n space group with lattice parameter a of ~ 12 Å (McMullan and Jeffrey, 1965). This may suggest a repulsive interaction considering that the van der Waals radii are 2.16 and 1.59 Å for Xe and the O atom, respectively (Bondi, 1964). We hence attribute the newly observed peak at 3.7 ± 0.1 Å to the Xe clathrate environment in the fluid.

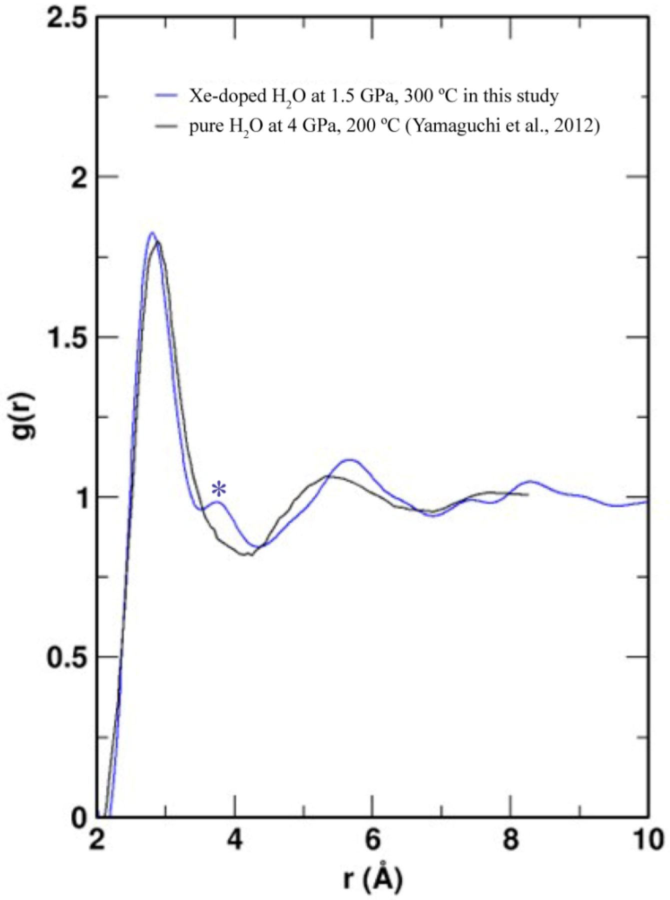

Fig. 5-4. Radial distribution function, g(r) of H_2O with initial 0.15 wt% Xe-doped plagioclase glass in run Cell7. The asterisk suggests the additional contribution observed for Xe-doped H_2O.

To investigate possible effect of Xe content on the intensity of the additional contribution, as well as the effect of halogens on the Xe-H_2O structure, experiments were also conducted with higher Xe concentrations (run Cell 1 and 5) and NaCl solution (run Cell 3). Data are however still in processing.

5.3.2 Xe partitioning behaviour

Recrystallization was observed above the glass transition *T* around 450-500 °C (450 °C for H_2O-saturated albite glass, Romano et al., 1994, but higher for H_2O-saturated anorthite, Richet et al., 1996) and kept stable until quenching for all DAC runs (Fig. 5-1b, 5-5b, c, and Fig. 5-6a). The observation of jadeite and quartz in recovered samples suggests the cells maintained high *P* at high *T*. H_2O and Xe diffused out during decompression, illustrating the crucial need of in-situ measurements.

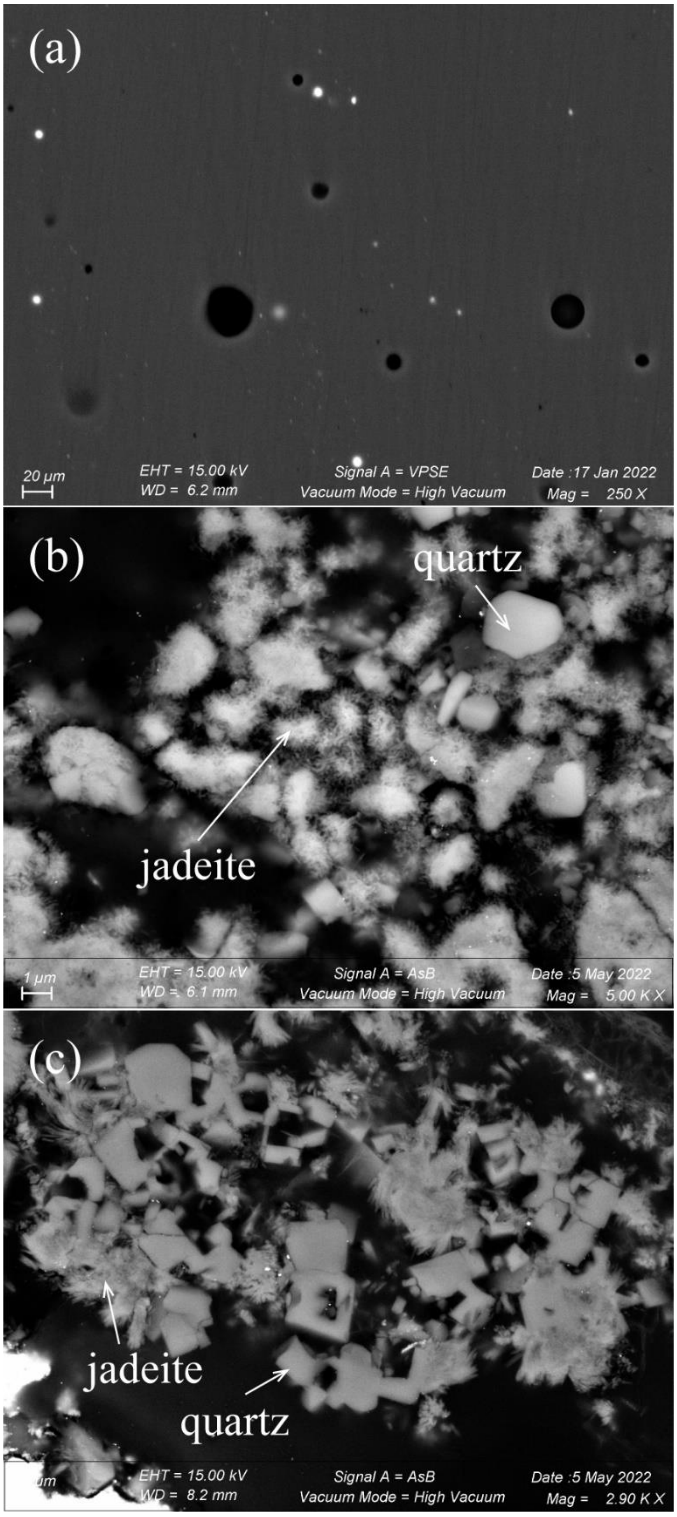

Fig. 5-5. SEM images of samples recovered from *HP-HT* experiments. (a) The starting Xe-doped $Ab_{80}An_{20}$ glass (PC242); quenched samples recovered from DAC experiments of (b) run Cell5, and (c) run Cell6. Jadeite and quartz existed as stable phases, the black areas in (b) and (c) are epoxy.

Xe content was determined using the fluorescence signal of Xe Kα lines (Fig. 5-6b) processed with PyMCA software with the declaration of attenuation by absorption of air, Be window and diamond anvils (Solé et al., 2007). At 650 °C for run Cell3, H_2O proportion is more than 95% in the 'H_2O-rich' pattern thus we assume it can represent the Xe content in pure H_2O. For a mixture of 'crystal-rich' pattern, data were treated in a multilayer way (c.f. section 3.3.1).

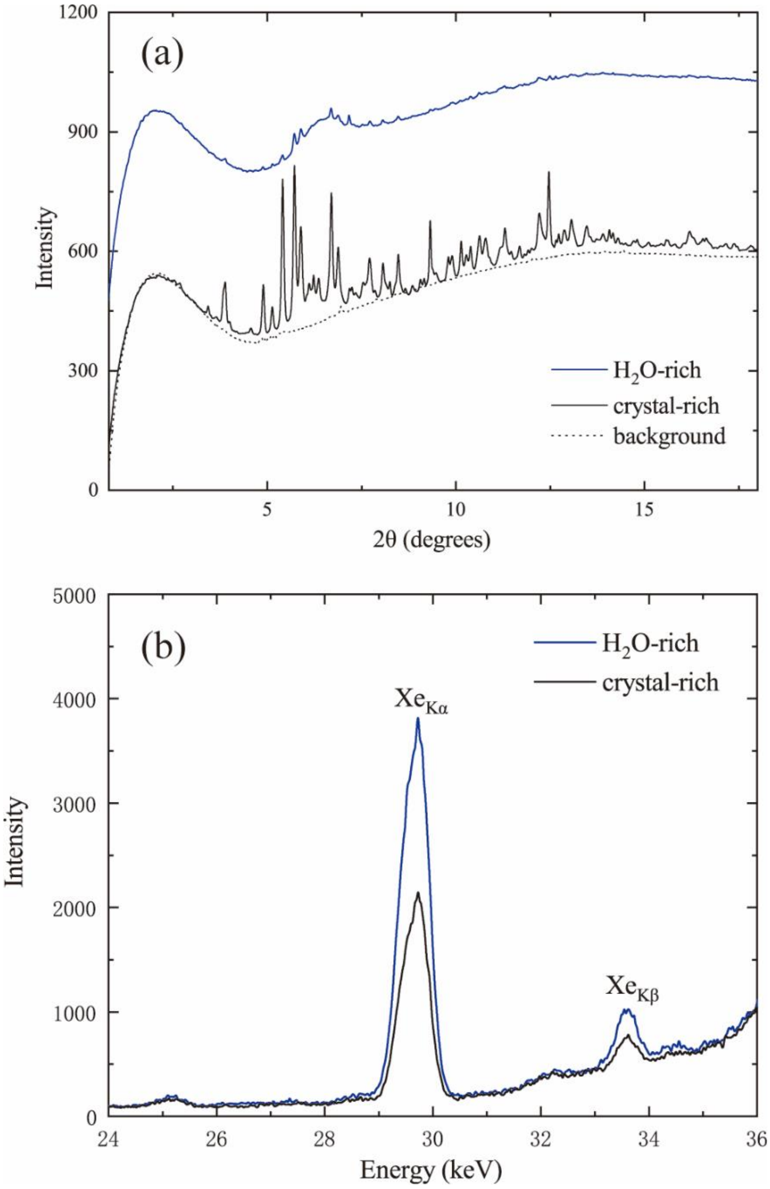

Fig. 5-6. (a) X-ray diffraction spectra; (b) corresponding x-ray fluorescence spectra, collected at 3 GPa and 650 °C (run Cell3). Crystal-rich is in black and H_2O-rich is in blue. Dotted line: background obtained using an empty gasket in the DAC. The Xe Kα and Kβ fluorescence rays are observed at 29.78 keV and 33.62 keV, respectively.

Due to the extensive distribution of crystals, pure H_2O signal was difficult to detected at high *T* (Fig. 5-1c). Only two data points were collected (Table 5-2). The relatively higher Xe contents in run Cell3 is because of the use of a bigger piece of Xe-doped starting glass. In both runs the higher Xe concentrations are found in fluids (H_2O or brine) phase, indicating Xe preferentially goes into aqueous fluids rather than into the crystals. Due to the existence of inseparable jadeite and quartz crystals at *HP-HT* conditions, the obtained $D^{Xe}_{f/c}$ actually represents $D^{Xe}_{fluids/(jadeite+quartz)}$. We address that the values of measured $D^{Xe}_{f/c}$ (11-13) are much lower than $D^{Xe}_{f/m}$ between H_2O and molten HPG at similar *T* (from 190-2750 at 680-760 °C, Leroy et al., 2019). This is consistent with our previous measurements on crystal/melt Xe partitioning, as crystals prove to be retained more Xe than melt. The values of $D^{Xe}_{f/c}$ remain constant for pure H_2O and brine system under the same *P-T* conditions, suggest halogens may have little influence on Xe distribution behaviour, and structural related data need to be analyzed in future.

Table 5-2

Xe concentrations and partition coefficients. in brackets: uncertainties

Run	*T (°C)* (80)	*P (GPa)* (0.5)	Xe_{fluid} (*wt%*)	$Xe_{crystal}$ (*wt%*)	$D^{Xe}_{f/c}$
Cell3	650	3.0	0.834 (0.116)	0.066 (0.007)	12.67 (1.17)
Cell5	640	3.1	0.578 (0.142)	0.052 (0.008)	11.12 (1.06)

$Xe_{crystal}$, Xe content in crystal; Xe_{fluid}, Xe content in aqueous fluids; uncertainties derived from noise to signal ratio of fluorescence signal intensity (10-20 %) and phases proportions (~10 %).

Subduction process is key to constrain the evolution of mantle noble gases and mediate the global cycling of elements over the Earth's history. Up to 80% of current Xe and

100% of non-radiogenic Ar and Kr could come from recycling atmospheric noble gases (Holland and Ballentine, 2006). Besides, measurements on exhumed portions of oceanic and continental lithosphere show that terrigeneous lithologies and hydrated oceanic slab are able to host significant quantities of noble gases (Honda et al., 2012; Kendrick et al., 2013, 2015; Baldwin and Das, 2015, Dai et al., 2016, Guo et al., 2017). For example, serpentinite, the altered oceanic lithospheric mantle, is a dominant volatile-rich carrier in subducting plates with a high Xe solubility of 3.29×10^{-9} mol/(g·bar) (Krantz et al., 2019) as well as up to 15 wt% H_2O (Rüpke et al., 2014). When cold slabs descend into the warm mantle, fluids (H_2O) released by metamorphic dehydration can effectively extract Xe and impact a noble gas signature into the mantle wedge, triggering partial melting as it crosses the wet solidus (Tatsumi, 1989). Besides, Xe partitioning between granitic melt and aqueous fluid was investigated using in-situ X-ray fluorescence measurements, finding Xe degasses only at low temperature but remains within the melt at high temperature (Leroy et al., 2019), part of injected Xe could be therefore retained in melts at depth and further enter into the crust. In addition, Xe could be delivered to mantle through cold subduction zones where less amount of H_2O is released from the slabs (Smye et al., 2017). We address that the obtained $D^{Xe}_{f/c}$ is not so large that a fraction of Xe can still be retained and recycled into the deep Earth, especially for serpentinites with large Xe solubility, leading to the mantle noble gases budget.

Chapter 6: Conclusions and Perspectives

In this thesis, xenon partitioning behaviour has been investigated for both minerals/melt and minerals/fluids systems at high pressure and temperature, including three major minerals of the continental crust and the upper mantle (olivine, clinopyroxene and plagioclase); felsic and basaltic melt; as well as pure H_2O and brine solution. The structure of Xe-doped aqueous fluids has been studied with different initial Xe content.

In-situ studies need to be favored to investigate Xe partitioning behaviour as Xe escapes from the silicate network and forms bubbles upon quenching.

A new protocol has been established to in-situ measure element partitioning at high *P-T* conditions throughout the work presented in this thesis. For this purpose, xenon concentration in phases was determined using not only classical XRF data obtained using monochromatic x-ray beam but also x-ray fluorescence signal on energy dispersive diffraction data. The target system is hydrous albite-anorthite as its melting point is achievable using resistive-heating DACs (used for "classical" XRD). XRF from EDX data is compatible with the use of large volume presses on synchrotrons such as DESY and the APS, with good Xe fluorescence signal even for 200 ppm Xe. We describe the advantages of x-ray energy dispersive technique to record simultaneously Xe concentration (from fluorescence peaks) and structural information (from diffraction peaks) on each co-existing phase, i.e., crystals and melt. This method is very promising for a more systematic investigation of element partitioning at higher *P-T* conditions.

X-ray diffraction made it possible to in-situ determine phases at high pressure, to probe the structure of element incorporation in liquids and determine a nearest-neighbour bond distances.

X-ray tomography made it possible to visualize interior features within solid samples and figure out phase proportions at experimental conditions when attenuation contrasts are sufficiently large. However, for some samples the measured X-ray intensity attenuation were similar between phases, it could not give useful imaging (Fig. 6-1).

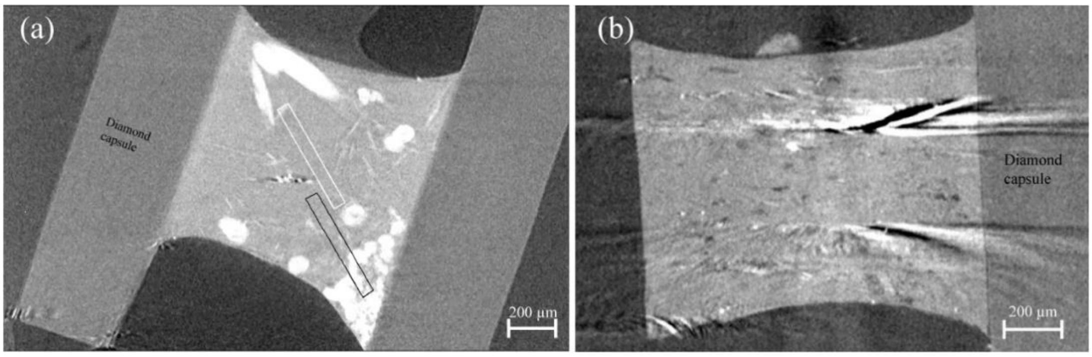

Fig. 6-1. X-ray tomography for (a) clinopyroxene-felsic melt system for run HH357 (cf. chapter 2); (b) clinopyroxene-anorthite-basaltic melt system for run HPT4 (cf. chapter 3). The attenuation contrasts between phases in latter basaltic system are too small to get useful imaging.

In this situation, X-ray diffraction made it possible to calculate the phase proportions (1) of crystal/melt via amorphous intensity and crystalline intensity, and (2) of crystal/crystal by Rietveld refinement. It also proves difficulty to determine location of small Xe content at a specific site by Rietveld refinement.

In the felsic system, xenon is moderately incompatible in plagioclase, but compatible in clinopyroxene and yields a negative correlation with T due to the decrease of trivalent elements in crystal phase. This indicates Xe is preferentially stored in minerals during continental crust partial melting processes.

In the basaltic system, xenon is compatible in all plagioclase/clinopyroxene/olivine crystals, with a highest partition coefficient in olivine/melt system. Xe is thus preferentially retained in minerals upon solidification of magma oceans, and only partially degassed, favouring the very early retention of Xe as a trace element in planetary interiors. Further work on Xe isotopic fractionation in olivine is now needed.

In the clinopyroxene-anorthite-basaltic melt system, xenon concentration is significantly reduced in clinopyroxene with the appearance of anorthite, indicating Xe is efficiently extracted from clinopyroxene to anorthite. This may suggest a way to transfer Xe from mantle to crust (both continental and oceanic) in later magmatic processes throughout Earth's history.

In the crystal-fluids system, Xe was proved to preferentially go into the fluid phase, with Xe fluid/crystal partition coefficient of 11-13. This could help us constrain the content of Xe recycling at subduction zones, as Xe will be extracted from the subducting slab via the release of fluids by metamorphic dehydration. Fluid composition (brine solution) was found to have little influence on fluid/crystal partition coefficient.

We also found a new peak at around 3.7 Å in Xe-fluids system, which is much larger than Xe-H bond length (1.7-1.8 Å) and Xe-O bond length (1.99-2.29 Å), but similar to the Xe-O van der Waals bond length in Xe hydrates. We attributed this contribution to Xe hydrate-like environment in the fluid, different from Xe local environment in minerals and melts.

The mechanism of incorporation in silicate minerals may different for Xe and Kr. Our primary results on Kr-doped plagioclase showing that bright Kr bubbles are mainly located at the edges of crystals (cf, Appendix II) rather than inside as for Xe. This may indicate Kr diffusing out from the crystal voids at ambient conditions or Kr adsorption on crystals surface. Further work is now needed to quantify Kr partitioning behaviour between minerals/melt.

References

Abe, Y., 1997. Thermal and chemical evolution of the terrestrial magma ocean. Physics of the Earth and Planetary Interiors 100, 27-39.

Abe, Y., Matsui, T., 1985. The formation of an impact-generated H2O atmosphere and its implications for the early thermal history of the Earth. Journal of Geophysical Research: Solid Earth 90, C545-C559.

Abràmoff, M.D., Magalhães, P.J., Ram, S.J., 2004. Image processing with ImageJ. Biophotonics international 11, 36-42.

Ahrens, T.J., 1993. Impact erosion of terrestrial planetary atmospheres. Annual Review of Earth and Planetary Sciences 21, 525-555.

Albarede, F., 2009. Volatile accretion history of the terrestrial planets and dynamic implications. Nature 461, 1227-1233.

Alexander, C.O.D., Bowden, R., Fogel, M., Howard, K., Herd, C., Nittler, L., 2012. The provenances of asteroids, and their contributions to the volatile inventories of the terrestrial planets. Science 337, 721-723.

Allègre, C.J., 1987. Isotope geodynamics. Earth and Planetary Science Letters 86, 175-203.

Allègre, C.J., Moreira, M., Staudacher, T., 1995. ^{4}He/^{3}He dispersion and mantle convection. Geophysical Research Letters 22, 2325-2328.

Allègre, C.J., Staudacher, T., Sarda, P., 1987. Rare gas systematics: formation of the atmosphere, evolution and structure of the Earth's mantle. Earth and Planetary Science Letters 81, 127-150.

Allègre, C.J., Staudacher, T., Sarda, P., Kurz, M., 1983. Constraints on evolution of Earth's mantle from rare gas systematics. Nature 303, 762-766.

Almayrac, M.G., Broadley, M.W., Bekaert, D.V., Hofmann, A., Marty, B., 2021. Possible discontinuous evolution of atmospheric xenon suggested by Archean barites. Chemical Geology 581, 120405.

Ander, E., Ebihara, M., 1982. Solar-system abundances of the elements: Geochem. Cosmochim. Acta 46, 2363-2380.

Anders, E., Owen, T., 1977. Mars and Earth: Origin and abundance of volatiles. Science 198, 453-465.

Avice, G., Marty, B., Burgess, R., 2017. The origin and degassing history of the Earth's atmosphere revealed by Archean xenon. Nature communications 8, 1-9.

Avice, G., Marty, B., Burgess, R., Hofmann, A., Philippot, P., Zahnle, K., Zakharov, D., 2018. Evolution of atmospheric xenon and other noble gases inferred from Archean to Paleoproterozoic rocks. Geochimica et Cosmochimica Acta 232, 82-100.

Baldwin, S.L., Das, J., 2015. Atmospheric Ar and Ne returned from mantle depths to the Earth’s surface by forearc recycling. Proceedings of the National Academy of Sciences 112, 14174-14179.

Ballentine, C.J., Marty, B., Sherwood Lollar, B., Cassidy, M., 2005. Neon isotopes constrain convection and volatile origin in the Earth's mantle. Nature 433, 33-38.

Balsiger, H., Altwegg, K., Bar-Nun, A., Berthelier, J.-J., Bieler, A., Bochsler, P., Briois, C., Calmonte, U., Combi, M., De Keyser, J., 2015. Detection of argon in the coma of comet 67P/Churyumov-Gerasimenko. Science advances 1, e1500377.

Basford, J., Dragon, J., Pepin, R., Coscio Jr, M., Murthy, V., 1973. Krypton and xenon in lunar fines, Lunar and Planetary Science Conference Proceedings, p. 1915.

Batiza, R., Bernatowicz, T., Hohenberg, C., Podosek, F., 1979. Relations of noble gas abundances to petrogenesis and magmatic evolution of some oceanic basalts and related differentiated volcanic rocks. Contributions to Mineralogy and Petrology 69, 301-313.

Bekaert, D.V., Avice, G., Marty, B., Henderson, B., Gudipati, M.S., 2017. Stepwise heating of lunar anorthosites 60025, 60215, 65315 possibly reveals an indigenous noble gas component on the Moon. Geochimica et cosmochimica Acta 218, 114-131.

Bekaert, D.V., Broadley, M.W., Marty, B., 2020. The origin and fate of volatile elements on Earth revisited in light of noble gas data obtained from comet 67P/Churyumov-Gerasimenko. Scientific reports 10, 1-18.

Benz, W., Cameron, A., 1990. Terrestrial effects of the Giant Impact. Origin of the Earth, 61-67.

Bernatowicz, T., Podosek, F., Honda, M., Kramer, F., 1984. The atmospheric inventory of xenon and noble gases in shales: the plastic bag experiment. Journal of Geophysical Research: Solid Earth 89, 4597-4611.

Besson, J., Nelmes, R., Hamel, G., Loveday, J., Weill, G., Hull, S., 1992. Neutron

powder diffraction above 10 GPa. Physica B: Condensed Matter 180, 907-910.
Beswick, J., Halberstadt, N., Janda, K., 2012. Structure and dynamics of noble gas-halogen and noble gas ionic clusters: when theory meets experiment. Chemical Physics 399, 4-16.

Bieri, R., Koide, M., Goldberg, E.D., 1964. Noble gases in sea water. Science 146, 1035-1037.

Boehler, R., De Hantsetters, K., 2004. New anvil designs in diamond-cells. High Pressure Research 24, 391-396.

Boettcher, S.L., Qiti, G., Montana, A., 1989. A simple device for loading gases in high-pressure experiments. American Mineralogist 74, 1383-1384.

Bondi, A.v., 1964. van der Waals volumes and radii. The Journal of physical chemistry 68, 441-451.

Bouhifd, M.A., Jephcoat, A.P., Heber, V.S., Kelley, S.P., 2013. Helium in Earth's early core. Nature Geoscience 6, 982-986.

Bowyer, T.W., Schlosser, C., Abel, K.H., Auer, M., Hayes, J.C., Heimbigner, T.R., McIntyre, J.I., Panisko, M.E., Reeder, P.L., Satorius, H., 2002. Detection and analysis of xenon isotopes for the comprehensive nuclear-test-ban treaty international monitoring system. Journal of environmental radioactivity 59, 139-151.

Boyd, F., England, J., 1960. Apparatus for phase-equilibrium measurements at pressures up to 50 kilobars and temperatures up to 1750° C. Journal of Geophysical Research 65, 741-748.

Broadhurst, C.L., Drake, M.J., Hagee, B.E., Bernatowicz, T.J., 1990. Solubility and partitioning of Ar in anorthite, diopside, forsterite, spinel, and synthetic basaltic liquids. Geochimica et Cosmochimica Acta 54, 299-309.

Broadhurst, C.L., Drake, M.J., Hagee, B.E., Bernatowicz, T.J., 1992. Solubility and partitioning of Ne, Ar, Kr and Xe in minerals and synthetic basaltic melts. Geochimica et Cosmochimica Acta 56, 709-723.

Broadley, M.W., Barry, P.H., Bekaert, D.V., Byrne, D.J., Caracausi, A., Ballentine, C.J., Marty, B., 2020. Identification of chondritic krypton and xenon in Yellowstone gases and the timing of terrestrial volatile accretion. Proceedings of the National Academy of Sciences 117, 13997-14004.

Brock, D.S., Schrobilgen, G.J., 2011. Synthesis of the missing oxide of xenon, XeO2, and its implications for Earth's missing xenon. Journal of the American Chemical

Society 133, 6265-6269.

Brooker, R., Du, Z., Blundy, J., Kelley, S., Allan, N., Wood, B., Chamorro, E., Wartho, J.-A., Purton, J., 2003. The ‘zero charge’partitioning behaviour of noble gases during mantle melting. Nature 423, 738-741.

Bureau, H., Auzende, A.-L., Marocchi, M., Raepsaet, C., Munsch, P., Testemale, D., Mézouar, M., Kubsky, S., Carrière, M., Ricolleau, A., 2016. Modern and past volcanic degassing of iodine. Geochimica et Cosmochimica Acta 173, 114-125.

Burnard, P., Graham, D., Turner, G., 1997. Vesicle-specific noble gas analyses of "popping rock": implications for primordial noble gases in Earth. Science 276, 568-571.

Caffee, M., Hudson, G., Velsko, C., Huss, G., Alexander Jr, E., Chivas, A., 1999. Primordial noble gases from Earth's mantle: identification of a primitive volatile component. Science 285, 2115-2118.

Caldwell, W.A., Nguyen, J.H., Pfrommer, B.G., Mauri, F., Louie, S.G., Jeanloz, R., 1997. Structure, bonding, and geochemistry of xenon at high pressures. Science 277, 930-933.

Canup, R.M., Asphaug, E., 2001. Origin of the Moon in a giant impact near the end of the Earth's formation. Nature 412, 708-712.

Caracausi, A., Avice, G., Burnard, P.G., Füri, E., Marty, B., 2016. Chondritic xenon in the Earth’s mantle. Nature 533, 82-85.

Caro, G., Bourdon, B., Birck, J.-L., Moorbath, S., 2003. 146 Sm–142 Nd evidence from Isua metamorphosed sediments for early differentiation of the Earth's mantle. Nature 423, 428-432.

Carroll, M.R., Stolper, E.M., 1993. Noble gas solubilities in silicate melts and glasses: New experimental results for argon and the relationship between solubility and ionic porosity. Geochimica et Cosmochimica Acta 57, 5039-5051.

Carvalho, P.H.B., Mace, A., Andersson, O., Tulk, C.A., Molaison, J., Lyubartsev, A.P., Nangoi, I.M., Leitão, A.A., Häussermann, U., 2021. Pressure-induced amorphization of noble gas clathrate hydrates. Physical Review B 103, 064205.

Chambers, J.E., 2004. Planetary accretion in the inner Solar System. Earth and Planetary Science Letters 223, 241-252.

Chamorro-Perez, E., Gillet, P., Jambon, A., Badro, J., McMillan, P., 1998. Low argon solubility in silicate melts at high pressure. Nature 393, 352-355.

Chassefière, E., Leblanc, F., 2004. Mars atmospheric escape and evolution; interaction with the solar wind. Planetary and Space Science 52, 1039-1058.

Chaston, J., 1975. The oxidation of the platinum metals. Platinum Metals Review 19, 135-140.

Chudinovskikh, L., Boehler, R., 2001. High-pressure polymorphs of olivine and the 660-km seismic discontinuity. Nature 411, 574-577.

Clarke, W.B., Beg, M., Craig, H., 1969. Excess 3He in the sea: Evidence for terrestrial primodal helium. Earth and Planetary Science Letters 6, 213-220.

Chen, Q., Sanloup, C., Bureau, H., Rzeplinski, I., Glazyrin, K., and Farla, R., 2022. Compatible behaviour of Xe in feldspar at deep crust conditions. Journal of Geophysical Research: Solid Earth (submitted).

Coes Jr, L., 1962. Synthesis of minerals at high pressures. Modern very high pressure techniques, 137-150.

Colin, A., Moreira, M., Gautheron, C., Burnard, P., 2015. Constraints on the noble gas composition of the deep mantle by bubble-by-bubble analysis of a volcanic glass sample from Iceland. Chemical Geology 417, 173-183.

Crabb, J., Anders, E., 1981. Noble gases in E-chondrites. Geochimica et Cosmochimica Acta 45, 2443-2464.

Crépisson, C., Blanchard, M., Lazzeri, M., Balan, E., Sanloup, C., 2018a. New constraints on Xe incorporation mechanisms in olivine from first-principles calculations. Geochimica et Cosmochimica Acta 222, 146-155.

Crépisson, C., Sanloup, C., Blanchard, M., Hudspeth, J., Glazyrin, K., Capitani, F., 2019. The Xe-SiO2 system at moderate pressure and high temperature. Geochemistry, Geophysics, Geosystems 20, 992-1003.

Crépisson, C., Sanloup, C., Cormier, L., Blanchard, M., Hudspeth, J., Rosa, A.D., Mathon, O., Irifune, T., 2018b. Kr environment in feldspathic glass and melt: A high pressure, high temperature X-ray absorption study. Chemical Geology 493, 525-531.

Criss, J. W., and Birks, L. S., 1968. Calculation methods for fluorescent x-ray spectrometry. Empirical coefficients versus fundamental parameters. Analytical Chemistry, 40(7), 1080-1086.

Ćuk, M., Stewart, S.T., 2012. Making the Moon from a fast-spinning Earth: A giant impact followed by resonant despinning. science 338, 1047-1052.

Czuppon, G., Matsumoto, T., Handler, M.R., Matsuda, J.-i., 2009. Noble gases in spinel peridotite xenoliths from Mt Quincan, North Queensland, Australia: undisturbed MORB-type noble gases in the subcontinental lithospheric mantle. Chemical Geology 266, 19-28.

Dai, L.-Q., Zheng, Y.-F., He, H.-Y., Zhao, Z.-F., 2016. Postcollisional mafic igneous rocks record recycling of noble gases by deep subduction of the continental crust. Lithos 252, 135-144.

Dasgupta, R., Chi, H., Shimizu, N., Buono, A.S., Walker, D., 2013. Carbon solution and partitioning between metallic and silicate melts in a shallow magma ocean: Implications for the origin and distribution of terrestrial carbon. Geochimica et Cosmochimica Acta 102, 191-212.

Dauphas, N., 2003. The dual origin of the terrestrial atmosphere. Icarus 165, 326-339.

Dauphas, N., 2017. The isotopic nature of the Earth's accreting material through time. Nature 541, 521-524.

De Grouchy, C. J. (2016). The Influence of Trace Element Incorporation on the Structure of Silicate Melts and Glasses at High Pressure (Doctoral dissertation, The University of Edinburgh).

Delsemme, A., Wenger, A., 1970. Physico-chemical phenomena in comets-I: Experimental study of snows in a cometary environment. Planetary and Space Science 18, 709-715.

Dewaele, A., Pépin, C., Geneste, G., Garbarino, G., 2017. Reaction between nickel or iron and xenon under high pressure. High Pressure Research 37, 137-146.

Dewaele, A., Torrent, M., Loubeyre, P., Mezouar, M., 2008. Compression curves of transition metals in the Mbar range: Experiments and projector augmented-wave calculations. Physical Review B 78, 104102.

Dewaele, A., Worth, N., Pickard, C.J., Needs, R.J., Pascarelli, S., Mathon, O., Mezouar, M., Irifune, T., 2016. Synthesis and stability of xenon oxides Xe 2 O 5 and Xe 3 O 2 under pressure. Nature chemistry 8, 784-790.

Drake, M.J., Righter, K., 2002. Determining the composition of the Earth. Nature 416, 39-44.

Drescher, J., Kirsten, T., Schäfer, K., 1998. The rare gas inventory of the continental crust, recovered by the KTB Continental Deep Drilling Project. Earth and Planetary Science Letters 154, 247-263.

Dyadin, Y.A., Larionov, E., Aladko, E.Y., Manakov, A.Y., Zhurko, F., Mikina, T., Komarov, V.Y., Grachev, E., 1999. Clathrate formation in water-noble gas (hydrogen) systems at high pressures. Journal of Structural Chemistry 40, 790-795.

Dyadin, Y.A., Larionov, E.G., Mikina, T.V., Starostina, L.I., 1996. Clathrate hydrate of xenon at high pressure. Mendeleev communications 2, 44-45.

Elkins-Tanton, L.T., 2008. Linked magma ocean solidification and atmospheric growth for Earth and Mars. Earth and Planetary Science Letters 271, 181-191.

Elkins-Tanton, L.T., 2012. Magma oceans in the inner solar system. Annual Review of Earth and Planetary Sciences 40, 113-139.

Eremets, M.I., Gregoryanz, E.A., Struzhkin, V.V., Mao, H.-k., Hemley, R.J., Mulders, N., Zimmerman, N.M., 2000. Electrical conductivity of xenon at megabar pressures. Physical Review Letters 85, 2797.

Errandonea, D., Somayazulu, M., Häusermann, D., Mao, H., 2003. Melting of tantalum at high pressure determined by angle dispersive x-ray diffraction in a double-sided laser-heated diamond-anvil cell. Journal of Physics: Condensed Matter 15, 7635.

Farla, R., Bhat, S., Sonntag, S., Chanyshev, A., Ma, S., Ishii, T., Liu, Z., Néri, A., Nishiyama, N., Faria, G.A., 2022. Extreme conditions research using the large-volume press at the P61B endstation, PETRA III. Journal of synchrotron radiation 29.

Farley, K., Neroda, E., 1998. Noble gases in the earth's mantle. Annual Review of Earth and Planetary Sciences 26, 189-218.

Fei, Y., Mao, H.-k., 1994. In situ determination of the NiAs phase of FeO at high pressure and temperature. Science 266, 1678-1680.

Fischer-Gödde, M., Kleine, T., 2017. Ruthenium isotopic evidence for an inner Solar System origin of the late veneer. Nature 541, 525-527.

Gaherty, J.B., Wang, Y., Jordan, T.H., Weidner, D.J., 1999. Testing plausible upper-mantle compositions using fine-scale models of the 410-km discontinuity. Geophysical Research Letters 26, 1641-1644.

Genda, H., Abe, Y., 2005. Enhanced atmospheric loss on protoplanets at the giant impact phase in the presence of oceans. Nature 433, 842-844.

Genda, H., Brasser, R., Mojzsis, S., 2017. The terrestrial late veneer from core disruption of a lunar-sized impactor. Earth and Planetary Science Letters 480, 25-32.

Gerber, R., 2004. Formation of novel rare-gas molecules in low-temperature matrices. Annu. Rev. Phys. Chem. 55, 55-78.

Goettel, K.A., Eggert, J.H., Silvera, I.F., Moss, W.C., 1989. Optical evidence for the metallization of xenon at 132 (5) GPa. Physical review letters 62, 665.

Goldschmidt, V., 1929. The distribution of the chemical elements. Nature 124, 15-17.

Gonnermann, H.M., Mukhopadhyay, S., 2009. Preserving noble gases in a convecting mantle. Nature 459, 560-563.

Grevesse, N., Asplund, M., Sauval, A., 2005. The new solar chemical composition. EAS Publications Series 17, 21-30.

Grochala, W., 2007. Atypical compounds of gases, which have been called ‘noble’. Chemical Society Reviews 36, 1632-1655.

Guillot, B., Sator, N., 2012. Noble gases in high-pressure silicate liquids: A computer simulation study. Geochimica et Cosmochimica Acta 80, 51-69.

Guo, W., He, H., Hilton, D.R., Zheng, Y., Su, F., Liu, Y., Zhu, R., 2017. Recycled noble gases preserved in podiform chromitites from Luobusa, Tibet. Chemical Geology 469, 97-109.

Hall, H.T., 1967. High pressure apparatus: ram-in-tie-bar multianvil presses. The Review of Physical Chemistry of Japan 37, 63-71.

Halliday, A.N., 2013. The origins of volatiles in the terrestrial planets. Geochimica et Cosmochimica Acta 105, 146-171.

Hamano, Y., Ozima, M., 1978. Earth-atmosphere evolution model based on Ar isotopic data. Advances in Earth and Planetary Sciences 3, 155-171.

Hammersley, A., 1998. computer program FIT2D. ESRF, Grenoble.

Harper Jr, C.L., Jacobsen, S.B., 1996. Noble gases and Earth's accretion. Science, 1814-1818.

Hart, R., Hogan, L., Dymond, J., 1985. The closed-system approximation for evolution of argon and helium in the mantle, crust and atmosphere. Chemical Geology: Isotope Geoscience section 52, 45-73.

Heber, V.S., Baur, H., Bochsler, P., McKeegan, K.D., Neugebauer, M., Reisenfeld, D.B., Wieler, R., Wiens, R.C., 2012. Isotopic mass fractionation of solar wind: Evidence from fast and slow solar wind collected by the Genesis mission. The Astrophysical Journal 759, 121.

Heber, V.S., Brooker, R.A., Kelley, S.P., Wood, B.J., 2007. Crystal–melt partitioning of noble gases (helium, neon, argon, krypton, and xenon) for olivine and clinopyroxene. Geochimica et Cosmochimica Acta 71, 1041-1061.

Hébrard, E., Marty, B., 2014. Coupled noble gas–hydrocarbon evolution of the early Earth atmosphere upon solar UV irradiation. Earth and Planetary Science Letters 385, 40-48.

Helffrich, G., 2000. Topography of the transition zone seismic discontinuities. Reviews of Geophysics 38, 141-158.
Hennecke, E.W., Manuel, O., 1975a. Noble gases in an Hawaiian xenolith. Nature 257, 778-780.

Hennecke, E.W., Manuel, O., 1975b. Noble gases in CO2 well gas, Harding county, New Mexico. Earth and Planetary Science Letters 27, 346-355.

Hermann, A., Schwerdtfeger, P., 2014. Xenon suboxides stable under pressure. The Journal of Physical Chemistry Letters 5, 4336-4342.

Hermans, P., Weidinger, A., 1948. Quantitative x-ray investigations on the crystallinity of cellulose fibers. A background analysis. Journal of Applied Physics 19, 491-506.

Hirschmann, M.M., 2016. Constraints on the early delivery and fractionation of Earth's major volatiles from C/H, C/N, and C/S ratios. American Mineralogist 101, 540-553.

Hiyagon, H., Ozima, M., 1982. Noble gas distribution between basalt melt and crystals. Earth and Planetary Science Letters 58, 255-264.

Hiyagon, H., Ozima, M., 1986. Partition of noble gases between olivine and basalt melt. Geochimica et Cosmochimica Acta 50, 2045-2057.

Hiyagon, H., Ozima, M., Marty, B., Zashu, S., Sakai, H., 1992. Noble gases in submarine glasses from mid-oceanic ridges and Loihi seamount: constraints on the early history of the Earth. Geochimica et Cosmochimica Acta 56, 1301-1316.

Holland, G., Ballentine, C.J., 2006. Seawater subduction controls the heavy noble gas composition of the mantle. Nature 441, 186-191.

Holland, G., Cassidy, M., Ballentine, C.J., 2009. Meteorite Kr in Earth's mantle suggests a late accretionary source for the atmosphere. Science 326, 1522-1525.

Holland, G., Lollar, B.S., Li, L., Lacrampe-Couloume, G., Slater, G., Ballentine, C., 2013. Deep fracture fluids isolated in the crust since the Precambrian era. Nature 497, 357-360.

Holland, T.J.B., Powell, R., 1998. An internally consistent thermodynamic data set for phases of petrological interest. Journal of metamorphic Geology 16, 309-343.

Honda, M., McDougall, I., 1998. Primordial helium and neon in the Earth-a speculation on early degassing. Geophysical research letters 25, 1951-1954.

Honda, M., McDougall, I., Patterson, D.B., Doulgeris, A., Clague, D.A., 1993. Noble gases in submarine pillow basalt glasses from Loihi and Kilauea, Hawaii: a solar component in the Earth. Geochimica et Cosmochimica Acta 57, 859-874.

Honda, M., Reynolds, J., Roedder, E., Epstein, S., 1987. Noble gases in diamonds: Occurrences of solarlike helium and neon. Journal of Geophysical Research: Solid Earth 92, 12507-12521.

Horlait, D., Faure, R., Thomas, B.A., Devert, N., Amany, M.-L., Carlot, G., Gilabert, É., 2021. A new thermo-desorption laser-heating setup for studying noble gas diffusion and release from materials at high temperatures. Review of Scientific Instruments 92, 124102.

Horowitz, P., Howell, J.A., 1972. A scanning x-ray microscope using synchrotron radiation. Science 178, 608-611.

Hunten, D.M., Pepin, R.O., Walker, J.C., 1987. Mass fractionation in hydrodynamic escape. Icarus 69, 532-549.

Huston, J.L., Studier, M.H., Sloth, E.N., 1964. Xenon tetroxide: mass spectrum. Science 143, 1161-1162.

Iro, N., Gautier, D., Hersant, F., Bockelée-Morvan, D., Lunine, J.I., 2003. An interpretation of the nitrogen deficiency in comets. Icarus 161, 511-532.

Jackson, C.R., Parman, S.W., Kelley, S.P., Cooper, R.F., 2013. Constraints on light noble gas partitioning at the conditions of spinel-peridotite melting. Earth and Planetary Science Letters 384, 178-187.

Jackson, C.R., Williams, C.D., Du, Z., Bennett, N.R., Mukhopadhyay, S., Fei, Y., 2021. Incompatibility of argon during magma ocean crystallization. Earth and Planetary

Science Letters 553, 116598.

Janssens, K., Vincze, L., Vekemans, B., Adams, F., Haller, M., Knöchel, A., 1998. Use of lead-glass capillaries for micro-focusing of highly-energetic (0–60 keV) synchrotron radiation. Journal of Analytical Atomic Spectrometry 13, 339-350.

Janssens, K.H., Adams, F., Rindby, A., 2000. Microscopic X-ray fluorescence analysis. Wiley Chichester.

Javoy, M., Kaminski, E., Guyot, F., Andrault, D., Sanloup, C., Moreira, M., Labrosse, S., Jambon, A., Agrinier, P., Davaille, A., 2010. The chemical composition of the Earth: Enstatite chondrite models. Earth and Planetary Science Letters 293, 259-268.

Kalinowski, J., Räsänen, M., Gerber, R.B., 2014. Chemically-bound xenon in fibrous silica. Physical Chemistry Chemical Physics 16, 11658-11661.

Kaneoka, I., Takaoka, N., Aoki, K.-I., 1977. Rare gases in a phlogopite nodule and a phlogopite-bearing peridotite in South African kimberlites. Earth and Planetary Science Letters 36, 181-186.

Kaneoka, I., Takaoka, N., Clague, D.A., 1983. Noble gas systematics for coexisting glass and olivine crystals in basalts and dunite xenoliths from Loihi Seamount. Earth and Planetary Science Letters 66, 427-437.

Kato, T., Ringwood, A., Irifune, T., 1988. Experimental determination of element partitioning between silicate perovskites, garnets and liquids: constraints on early differentiation of the mantle. Earth and Planetary Science Letters 89, 123-145.

Kendrick, M.A., Honda, M., Pettke, T., Scambelluri, M., Phillips, D., Giuliani, A., 2013. Subduction zone fluxes of halogens and noble gases in seafloor and forearc serpentinites. Earth and Planetary Science Letters 365, 86-96.

Kendrick, M.A., Honda, M., Vanko, D.A., 2015. Halogens and noble gases in Mathematician Ridge meta-gabbros, NE Pacific: implications for oceanic hydrothermal root zones and global volatile cycles. Contributions to Mineralogy and Petrology 170, 1-20.

Kendrick, M.A., Scambelluri, M., Honda, M., Phillips, D., 2011. High abundances of noble gas and chlorine delivered to the mantle by serpentinite subduction. Nature Geoscience 4, 807-812.

Khriachtchev, L., Isokoski, K., Cohen, A., Räsänen, M., Gerber, R.B., 2008. A small neutral molecule with two noble-gas atoms: HXeOXeH. Journal of the American Chemical Society 130, 6114-6118.

Kleine, T., Mezger, K., Palme, H., Scherer, E., Münker, C., 2005. Early core formation in asteroids and late accretion of chondrite parent bodies: Evidence from 182Hf-182W in CAIs, metal-rich chondrites, and iron meteorites. Geochimica et Cosmochimica Acta 69, 5805-5818.

Kleine, T., Münker, C., Mezger, K., Palme, H., 2002. Rapid accretion and early core formation on asteroids and the terrestrial planets from Hf–W chronometry. Nature 418, 952-955.

Kono, Y., Irifune, T., Higo, Y., Inoue, T., Barnhoorn, A., 2010. *P-V-T* relation of MgO derived by simultaneous elastic wave velocity and in situ X-ray measurements: A new pressure scale for the mantle transition region. Physics of the Earth and Planetary Interiors 183, 196-211.

Kono, Y., Kenney-Benson, C., Park, C., Shen, G., Wang, Y., 2013. Anomaly in the viscosity of liquid KCl at high pressures. Physical Review B 87, 024302.

Kono, Y., Park, C., Kenney-Benson, C., Shen, G., Wang, Y., 2014. Toward comprehensive studies of liquids at high pressures and high temperatures: Combined structure, elastic wave velocity, and viscosity measurements in the Paris–Edinburgh cell. Physics of the Earth and Planetary Interiors 228, 269-280.

Krantz, J. A., Parman, S. W., & Kelley, S. P., 2019. Recycling of heavy noble gases by subduction of serpentinite. Earth and Planetary Science Letters, 521, 120-127.

Krummenacher, D., Merrihue, C., Pepin, R., Reynolds, J., 1962. Meteoritic krypton and barium versus the general isotopic anomalies in meteoritic xenon. Geochimica et Cosmochimica Acta 26, 231-249.

Kunz, J., Staudacher, T., Allegre, C.J., 1998. Plutonium-fission xenon found in Earth's mantle. Science 280, 877-880.

Kurz, M., Jenkins, W., Hart, S., 1982. Helium isotopic systematics of oceanic islands and mantle heterogeneity. Nature 297, 43-47.

Kurz, M.D., Curtice, J., Fornari, D., Geist, D., Moreira, M., 2009. Primitive neon from the center of the Galápagos hotspot. Earth and Planetary Science Letters 286, 23-34.
Kvenvolden, K.A., 1988. Methane hydrate—a major reservoir of carbon in the shallow geosphere? Chemical geology 71, 41-51.

Kvenvolden, K.A., 1999. Potential effects of gas hydrate on human welfare. Proceedings of the National Academy of Sciences 96, 3420-3426.

Labrosse, S., Hernlund, J., Coltice, N., 2007. A crystallizing dense magma ocean at the base of the Earth’s mantle. Nature 450, 866-869.

Lange, M., Ahrens, T.J., 1982. Impact induced dehydration of serpentine and the evolution of planetary atmospheres. Journal of Geophysical Research: Solid Earth 87, A451-A456.

Larson, A.C., Von Dreele, R.B., 1994. Gsas. Report lAUR, 86-748.

Le Losq, C., Neuville, D.R., Moretti, R., Roux, J., 2012. Determination of water content in silicate glasses using Raman spectrometry: Implications for the study of explosive volcanism. American Mineralogist 97, 779-790.

Lee, K.K., Steinle-Neumann, G., 2006. High-pressure alloying of iron and xenon: “Missing” Xe in the Earth's core? Journal of Geophysical Research: Solid Earth 111.

Leroy, C., Bureau, H., Sanloup, C., Raepsaet, C., Glazirin, K., Munsch, P., Harmand, M., Prouteau, G., Khodja, H., 2019. Xenon and iodine behaviour in magmas. Earth and Planetary Science Letters 522, 144-154.

Leroy, C., Sanloup, C., Bureau, H., Schmidt, B.C., Konôpková, Z., Raepsaet, C., 2018. Bonding of xenon to oxygen in magmas at depth. Earth and Planetary Science Letters 484, 103-110.

Liermann, H.-P., Merkel, S., Miyagi, L., Wenk, H.-R., Shen, G., Cynn, H., Evans, W.J., 2009. Experimental method for in situ determination of material textures at simultaneous high pressure and high temperature by means of radial diffraction in the diamond anvil cell. Review of scientific instruments 80, 104501.

Liu, J., 2016. High pressure x-ray diffraction techniques with synchrotron radiation. Chinese Physics B 25, 076106.

Liu, W., Li, B., 2006. Thermal equation of state of $(Mg_{0.9}Fe_{0.1})_2SiO_4$ olivine. Physics of the Earth and Planetary Interiors 157, 188-195.

Lodders, K., 2003. Solar system abundances and condensation temperatures of the elements. The Astrophysical Journal 591, 1220.

Long, D.A., 1977. Raman spectroscopy. New York 1.

Mackwell, S.J., Dimos, D., Kohlstedt, D.L., 1988. Transient creep of olivine: point-defect relaxation times. Philosophical Magazine A 57, 779-789.

Mahaffy, P., Niemann, H., Alpert, A., Atreya, S., Demick, J., Donahue, T., Harpold, D., Owen, T., 2000. Noble gas abundance and isotope ratios in the atmosphere of Jupiter from the Galileo Probe Mass Spectrometer. Journal of Geophysical Research: Planets 105, 15061-15071.

Maier, W.D., Barnes, S.J., Campbell, I.H., Fiorentini, M.L., Peltonen, P., Barnes, S.-J., Smithies, R.H., 2009. Progressive mixing of meteoritic veneer into the early Earth’s deep mantle. Nature 460, 620-623.

Malfait, W.J., 2018. Vibrational properties of glasses and melts, Magmas Under Pressure. Elsevier, pp. 211-236.

Malfait, W.J., Seifert, R., Petitgirard, S., Mezouar, M., Sanchez-Valle, C., 2014. The density of andesitic melts and the compressibility of dissolved water in silicate melts at crustal and upper mantle conditions. Earth and Planetary Science Letters 393, 31-38.

Marchi, S., Canup, R., Walker, R., 2018. Heterogeneous delivery of silicate and metal to the Earth by large planetesimals. Nature geoscience 11, 77-81.

Marty, B., 2012. The origins and concentrations of water, carbon, nitrogen and noble gases on Earth. Earth and Planetary Science Letters 313, 56-66.

Marty, B., Altwegg, K., Balsiger, H., Bar-Nun, A., Bekaert, D., Berthelier, J.-J., Bieler, A., Briois, C., Calmonte, U., Combi, M., 2017. Xenon isotopes in 67P/Churyumov-Gerasimenko show that comets contributed to Earth's atmosphere. Science 356, 1069-1072.

Marty, B., Avice, G., Sano, Y., Altwegg, K., Balsiger, H., Hässig, M., Morbidelli, A., Mousis, O., Rubin, M., 2016. Origins of volatile elements (H, C, N, noble gases) on Earth and Mars in light of recent results from the ROSETTA cometary mission. Earth and Planetary Science Letters 441, 91-102.

Matsubara, K., Matsuda, J.i., Nagao, K., Kita, I., Taguchi, S., 1988. Xe in amorphous silica: A new thermometer in geothermal systems. Geophysical Research Letters 15, 657-660.

Matsuda, J., Sudo, M., Ozima, M., Ito, K., Ohtaka, O., Ito, E., 1993. Noble gas partitioning between metal and silicate under high pressures. Science 259, 788-790.

Matsuda, J.-i., Matsubara, K., 1989. Noble gases in silica and their implication for the terrestrial “missing” Xe. Geophysical Research Letters 16, 81-84.

Matsui, T., Abe, Y., 1986. Evolution of an impact-induced atmosphere and magma ocean on the accreting Earth. Nature 319, 303-305.

Mazor, E., Heymann, D., Anders, E., 1970. Noble gases in carbonaceous chondrites. Geochimica et Cosmochimica Acta 34, 781-824.

McMillan, P.F., Jakobsson, S., Holloway, J.R., Silver, L.A., 1983. A note on the Raman spectra of water-bearing albite glasses. Geochimica et Cosmochimica Acta 47, 1937-1943.

McMillan, P.F., Poe, B.T., Gillet, P., Reynard, B., 1994. A study of SiO2 glass and supercooled liquid to 1950 K via high-temperature Raman spectroscopy. Geochimica et Cosmochimica Acta 58, 3653-3664.

McMullan, R.K., Jeffrey, G., 1965. Polyhedral clathrate hydrates. IX. Structure of ethylene oxide hydrate. The Journal of Chemical Physics 42, 2725-2732.

Meng, Y., Shen, G., Mao, H., 2006. Double-sided laser heating system at HPCAT for in situ x-ray diffraction at high pressures and high temperatures. Journal of Physics: Condensed Matter 18, S1097.

Meshik, A., Hohenberg, C., Pravdivtseva, O., Kapusta, Y.S., 2001. Weak decay of 130 Ba and 132 Ba: Geochemical measurements. Physical Review C 64, 035205.

Meshik, A., Mabry, J., Hohenberg, C., Marrocchi, Y., Pravdivtseva, O., Burnett, D., Olinger, C., Wiens, R., Reisenfeld, D., Allton, J., 2007. Constraints on neon and argon isotopic fractionation in solar wind. Science 318, 433-435.

Mizuno, H., Nakazawa, K., Hayashi, C., 1980. Dissolution of the primordial rare gases into the molten Earth's material. Earth and Planetary Science Letters 50, 202-210.

Montana, A., Guo, Q., Boettcher, S., White, B.S., Brearley, M., 1993. Xe and Ar in high-pressure silicate liquids. American Mineralogist 78, 1135-1142.

Morard, G., 2006. Les systèmes Fe-FeS et Fe-S-Si à haute pression et haute température: implications pour les noyaux des corps planétaires. Paris, Institut de physique du globe.

Morard, G., Mezouar, M., Bauchau, S., Álvarez-Murga, M., Hodeau, J.-L., Garbarino, G., 2011. High efficiency multichannel collimator for structural studies of liquids and low-Z materials at high pressures and temperatures. Review of Scientific Instruments 82, 023904.

Moreira, M., 2013. Noble gas constraints on the origin and evolution of Earth’s volatiles. Geochemical Perspectives 2, 229-230.

Moreira, M., Allègre, C.-J., 2002. Rare gas systematics on Mid Atlantic ridge (37–40 N). Earth and Planetary Science Letters 198, 401-416.

Moreira, M., Charnoz, S., 2016. The origin of the neon isotopes in chondrites and on Earth. Earth and Planetary Science Letters 433, 249-256.

Moreira, M., Kunz, J., Allegre, C., 1998. Rare gas systematics in popping rock: isotopic and elemental compositions in the upper mantle. Science 279, 1178-1181.

Moreira, M., Staudacher, T., Sarda, P., Schilling, J.-G., Allègre, C.J., 1995. A primitive plume neon component in MORB: The Shona ridge-anomaly, South Atlantic (51–52° S). Earth and Planetary Science Letters 133, 367-377.

Moreira, M., Valbracht, P., Staudacher, T., Allègre, C., 1996. Rare gas systematics in Red Sea ridge basalts. Geophysical research letters 23, 2453-2456.

Mukhopadhyay, S., 2012. Early differentiation and volatile accretion recorded in deep-mantle neon and xenon. Nature 486, 101-104.

Mukhopadhyay, S., Parai, R., 2019. Noble gases: a record of Earth's evolution and mantle dynamics. Annual Review of Earth and Planetary Sciences 47, 389-419.

Neuling, H., Holzapfel, W., 1992. Rietveld analysis for energy dispersive X-ray diffraction under high pressure with synchrotron radiation. High Pressure Research 8, 655-660.

Neuville, D.R., Cormier, L., Massiot, D., 2006. Al coordination and speciation in calcium aluminosilicate glasses: Effects of composition determined by 27Al MQ-MAS NMR and Raman spectroscopy. Chemical geology 229, 173-185.

Neuville, D.R., Mysen, B.O., 1996. Role of aluminium in the silicate network: In situ, high-temperature study of glasses and melts on the join SiO2-NaAlO2. Geochimica et Cosmochimica Acta 60, 1727-1737.

Nunzi, F., Cesario, D., Belpassi, L., Tarantelli, F., Roncaratti, L.F., Falcinelli, S., Cappelletti, D., Pirani, F., 2019. Insight into the halogen-bond nature of noble gas-chlorine systems by molecular beam scattering experiments, ab initio calculations and charge displacement analysis. Physical Chemistry Chemical Physics 21, 7330-7340.

Ozima, M., 1975. Ar isotopes and Earth-atmosphere evolution models. Geochimica et Cosmochimica Acta 39, 1127-1134.

Ozima, M., Podosek, F., 1999. Formation age of Earth from 129I/127I and 244Pu/238U systematics and the missing Xe. Journal of Geophysical Research: Solid Earth 104, 25493-25499.

Ozima, M., Podosek, F.A., 2002. Noble gas geochemistry. Cambridge University Press.
Ozima, M., Zahnle, K., 1993. Mantle degassing and atmospheric evolution: Noble gas view. Geochemical Journal 27, 185-200.

Ozima, M., Zashu, S., 1988. Solar-type Ne in Zaire cubic diamonds. Geochimica et Cosmochimica Acta 52, 19-25.

Palma, R.L., Rao, M.N., Rowe, M.W., Koeberl, C., 1997. Krypton and xenon fractionation in North American tektites. Meteoritics & Planetary Science 32, 9-14.

Parai, R., Mukhopadhyay, S., 2018. Xenon isotopic constraints on the history of volatile recycling into the mantle. Nature 560, 223-227.

Parai, R., Mukhopadhyay, S., Standish, J., 2012. Heterogeneous upper mantle Ne, Ar and Xe isotopic compositions and a possible Dupal noble gas signature recorded in basalts from the Southwest Indian Ridge. Earth and Planetary Science Letters 359, 227-239.

Patzer, A., Schultz, L., 2002. Noble gases in enstatite chondrites II: The trapped component. Meteoritics & Planetary Science 37, 601-612.

Pearce, N. J., Perkins, W. T., Westgate, J. A., Gorton, M. P., Jackson, S. E., Neal, C. R., & Chenery, S. P., 1997. A compilation of new and published major and trace element data for NIST SRM 610 and NIST SRM 612 glass reference materials. Geostandards newsletter, 21(1), 115-144.

Pepin, R.O., 1991. On the origin and early evolution of terrestrial planet atmospheres and meteoritic volatiles. Icarus 92, 2-79.

Pepin, R.O., 2006. Atmospheres on the terrestrial planets: Clues to origin and evolution. Earth and Planetary Science Letters 252, 1-14.

Péron, S., Moreira, M., 2018. Onset of volatile recycling into the mantle determined by xenon anomalies. Geochemical Perspectives Letters, 21-25.

Péron, S., Moreira, M., Agranier, A., 2018. Origin of light noble gases (He, Ne, and Ar) on Earth: A review. Geochemistry, Geophysics, Geosystems 19, 979-996.

Péron, S., Moreira, M., Colin, A., Arbaret, L., Putlitz, B., Kurz, M.D., 2016. Neon isotopic composition of the mantle constrained by single vesicle analyses. Earth and Planetary Science Letters 449, 145-154.

Péron, S., Moreira, M., Putlitz, B., Kurz, M., 2017. Solar wind implantation supplied light volatiles during the first stage of Earth accretion. Geochemical Perspectives

Letters, 151-159.

Péron, S., Mukhopadhyay, S., Kurz, M.D., Graham, D.W., 2021. Deep-mantle krypton reveals Earth's early accretion of carbonaceous matter. Nature 600, 462-467.

Petitgirard S, Borchert M, Andrault D et al., 2012. An in situ approach to study trace element partitioning in the laser heated diamond anvil cell. Rev. Sci. Instr. 83:013904.

Pető, M.K., Mukhopadhyay, S., Kelley, K.A., 2013. Heterogeneities from the first 100 million years recorded in deep mantle noble gases from the Northern Lau Back-arc Basin. Earth and Planetary Science Letters 369, 13-23.

Philippe, J., Le Godec, Y., Mezouar, M., Berg, M., Bromiley, G., Bergame, F., Perrillat, J., Alvarez-Murga, M., Morand, M., Atwood, R., 2016. Rotating tomography Paris–Edinburgh cell: a novel portable press for micro-tomographic 4-D imaging at extreme pressure/temperature/stress conditions. High Pressure Research 36, 512-532.

Phillipsi, M., Colville, A., Ribbe, P., 1971. The crystal structures of two oligoclases: A comparison with low and high albite. Zeitschrift für Kristallographie-Crystalline Materials 133, 43-65.

Piani, L., Marrocchi, Y., Rigaudier, T., Vacher, L.G., Thomassin, D., Marty, B., 2020. Earth's water may have been inherited from material similar to enstatite chondrite meteorites. Science 369, 1110-1113.

Porcelli, D., Halliday, A., 2001. The core as a possible source of mantle helium. Earth and Planetary Science Letters 192, 45-56.

Porcelli, D., Wasserburg, G., 1995. Mass transfer of helium, neon, argon, and xenon through a steady-state upper mantle. Geochimica et Cosmochimica Acta 59, 4921-4937.

Porcelli, D., Wasserburg, G., 1995. Mass transfer of xenon through a steady-state upper mantle. Geochimica et cosmochimica acta 59, 1991-2007.

Poreda, R., Farley, K., 1992. Rare gases in Samoan xenoliths. Earth and Planetary Science Letters 113, 129-144.

Potts, P.J., Webb, P.C., 1992. X-ray fluorescence spectrometry. Journal of Geochemical Exploration 44, 251-296.

Prescher, C., and Prakapenka, V. B., 2015. DIOPTAS: a program for reduction of two-dimensional X-ray diffraction data and data exploration. High Pressure Research, 35(3), 223-230.

Probert, M.I.J., 2009. An ab initio study of xenon retention in α-quartz. Journal of physics: Condensed matter 22, 025501.

Pujol, M., Marty, B., Burgess, R., 2011. Chondritic-like xenon trapped in Archean rocks: A possible signature of the ancient atmosphere. Earth and Planetary Science Letters 308, 298-306.

Pujol, M., Marty, B., Burnard, P., Philippot, P., 2009. Xenon in Archean barite: Weak decay of 130Ba, mass-dependent isotopic fractionation and implication for barite formation. Geochimica et Cosmochimica Acta 73, 6834-6846.

Raquin, A., Moreira, M., 2009. Atmospheric 38Ar/36Ar in the mantle: implications for the nature of the terrestrial parent bodies. Earth and Planetary Science Letters 287, 551-558.

Raquin, A., Moreira, M.A., Guillon, F., 2008. He, Ne and Ar systematics in single vesicles: mantle isotopic ratios and origin of the air component in basaltic glasses. Earth and Planetary Science Letters 274, 142-150.

Rashchenko, S.V., Kurnosov, A., Dubrovinsky, L., Litasov, K.D., 2015. Revised calibration of the Sm: SrB_4O_7 pressure sensor using the Sm-doped yttrium-aluminum garnet primary pressure scale. Journal of Applied Physics 117, 145902.

RD, S., KC, J., 1977. Abundances and isotopic compositions of rare gases in granites. Geochemical Journal 11, 75-90.

Ribas, I., Guinan, E.F., Güdel, M., Audard, M., 2005. Evolution of the solar activity over time and effects on planetary atmospheres. I. High-energy irradiances (1-1700 Å). The Astrophysical Journal 622, 680.

Richet, P., Lejeune, A.-M., Holtz, F., Roux, J., 1996. Water and the viscosity of andesite melts. Chemical Geology 128, 185-197.

Rietveld, H., 1967. Line profiles of neutron powder-diffraction peaks for structure refinement. Acta Crystallographica 22, 151-152.

Rietveld, H.M., 1969. A profile refinement method for nuclear and magnetic structures. Journal of applied Crystallography 2, 65-71.

Rindby, A., Engström, P., Janssens, K., 1997a. The use of a scanning X-ray microprobe for simultaneous XRF/XRD studies of fly-ash particles. Journal of synchrotron radiation 4, 228-235.

Rindby, A., Engström, P., Janssens, K., Osan, J., 1997b. Micro-distribution of heavy elements in highly inhomogeneous particles generated from μ-beam XRF/XRD analysis. Nuclear Instruments and Methods in Physics Research Section B: Beam Interactions with Materials and Atoms 124, 591-604.

Ringwood, A.E., 1968. Phase transformations in the mantle. Earth and Planetary Science Letters 5, 401-412.

Ringwood, A.E., 1970. Phase transformations and the constitution of the mantle. Physics of the Earth and Planetary Interiors 3, 109-155.

Rivoldini, A., Van Hoolst, T., Verhoeven, O., Mocquet, A., Dehant, V., 2011. Geodesy constraints on the interior structure and composition of Mars. Icarus 213, 451-472.

Rodriguez-Carvajal, J., 1990. program FULLPROF. Laboratoire Léon Brillouin (CEA-CNRS) Version 3.

Rodríguez-Carvajal, J., 1993. Recent advances in magnetic structure determination by neutron powder diffraction. Physica B: Condensed Matter 192, 55-69.

Rohrbacher, A., Halberstadt, N., Janda, K.C., 2000. The Dynamics of Noble Gas—Halogen Molecules and Clusters. Annual Review of Physical Chemistry 51, 405-433.

Romano, C., Dingwell, D.B., Sterner, S.M., 1994. Kinetics of quenching of hydrous feldspathic melts: quantification using synthetic fluid inclusions. American Mineralogist 79, 1125-1134.

Rubin, M., Altwegg, K., Balsiger, H., Bar-Nun, A., Berthelier, J.-J., Briois, C., Calmonte, U., Combi, M., De Keyser, J., Fiethe, B., 2018. Krypton isotopes and noble gas abundances in the coma of comet 67P/Churyumov-Gerasimenko. Science advances 4, eaar6297.

Rüpke, L.H., Morgan, J.P., Hort, M., Connolly, J.A., 2004. Serpentine and the subduction zone water cycle. Earth and Planetary Science Letters 223, 17-34.

Rzeplinski, I., Sanloup, C., Gilabert, E., Horlait, D., 2022. Hadean isotopic fractionation of xenon retained in deep silicates. Nature (accepted).

Sakai, R., Nagahara, H., Ozawa, K., Tachibana, S., 2014. Composition of the lunar magma ocean constrained by the conditions for the crust formation. Icarus 229, 45-56.

Sanloup, C., 2020. Noble Gas Reactivity in Planetary Interiors. Frontiers in Physics 8.

Sanloup, C., Bonev, S.A., Hochlaf, M., Maynard-Casely, H.E., 2013. Reactivity of xenon with ice at planetary conditions. Physical Review Letters 110, 265501.

Sanloup, C. and de Grouchy, C. J., 2018. X-ray diffraction structure measurements. In Magmas under pressure (pp. 137-153). Elsevier.

Sanloup, C., Hemley, R.J., Mao, H.k., 2002. Evidence for xenon silicates at high pressure and temperature. Geophysical research letters 29, 30-31-30-34.

Sanloup, C., Mao, H.-k., Hemley, R.J., 2002. High-pressure transformations in xenon hydrates. Proceedings of the National Academy of Sciences 99, 25-28.

Sanloup, C., Schmidt, B., Gudfinnsson, G., Dewaele, A., Mezouar, M., 2011. Xenon and Argon: A contrasting behavior in olivine at depth. Geochimica et Cosmochimica Acta 75, 6271-6284.

Sanloup, C., Schmidt, B.C., Perez, E.M.C., Jambon, A., Gregoryanz, E., Mezouar, M., 2005. Retention of xenon in quartz and Earth's missing xenon. Science 310, 1174-1177.

Sano, Y., Marty, B., Burnard, P., 2013. Noble gases in the atmosphere, The noble gases as geochemical tracers. Springer, pp. 17-31.

Sarda, P., Graham, D., 1990. Mid-ocean ridge popping rocks: implications for degassing at ridge crests. Earth and Planetary Science Letters 97, 268-289.

Sarda, P., Moreira, M., Staudacher, T., Schilling, J.G., Allègre, C.J., 2000. Rare gas systematics on the southernmost Mid-Atlantic Ridge: Constraints on the lower mantle and the Dupal source. Journal of Geophysical Research: Solid Earth 105, 5973-5996.

Sarda, P., Staudacher, T., Allegre, C.J., 1985. ^{40}Ar^{36}Ar in MORB glasses: constraints on atmosphere and mantle evolution. Earth and Planetary Science Letters 72, 357-375.
Sarda, P., Staudacher, T., Allègre, C.J., 1988. Neon isotopes in submarine basalts. Earth and Planetary Science Letters 91, 73-88.

Sautter, V., Toplis, M., Wiens, R., Cousin, A., Fabre, C., Gasnault, O., Maurice, S., Forni, O., Lasue, J., Ollila, A., 2015. In situ evidence for continental crust on early Mars. Nature Geoscience 8, 605-609.

Schlichting, H.E., Mukhopadhyay, S., 2018. Atmosphere impact losses. Space Science Reviews 214, 1-31.

Schmidt, B.C., Keppler, H., 2002. Experimental evidence for high noble gas solubilities in silicate melts under mantle pressures. Earth and Planetary Science Letters 195, 277-290.

Selig, H., Claassen, H.H., Chernick, C.L., Malm, J.G., Huston, J.L., 1964. Xenon tetroxide: preparation and some properties. Science 143, 1322-1323.

Shi, Y., Neuefeind, J., Ma, D., Page, K., Lamberson, L.A., Smith, N.J., Tandia, A., Song, A.P., 2019. Ring size distribution in silicate glasses revealed by neutron scattering first sharp diffraction peak analysis. Journal of Non-Crystalline Solids 516, 71-81.

Shibata, T., Takahashi, E., Matsuda, J.-i., 1998. Solubility of neon, argon, krypton, and xenon in binary and ternary silicate systems: a new view on noble gas solubility. Geochimica et Cosmochimica Acta 62, 1241-1253.

Shibata, T., Takahashi, E., Ozima, M., 1994. Noble gas partition between basaltic melt and olivine crystals at high pressures. Noble Gas Geochemistry and Cosmochemistry, 343-354.

Shimada, M. 1972. Melting of albite at high pressures under conditions. Journal of Physics of the Earth 20, 59-70.

Simabuco, S., Nascimento Filho, V., 1994. Quantitative analysis by energy dispersive X-ray fluorescence by the transmission method applied to geological samples. Scientia Agricola 51, 197-206.

Smye, A.J., Jackson, C.R., Konrad-Schmolke, M., Hesse, M.A., Parman, S.W., Shuster, D.L., Ballentine, C.J., 2017. Noble gases recycled into the mantle through cold subduction zones. Earth and Planetary Science Letters 471, 65-73.

Solé, V.A., Papillon, E., Cotte, M., Walter, P., Susini, J.A., 2007. A multiplatform code for the analysis of energy-dispersive X-ray fluorescence spectra. Spectrochimica Acta Part B: Atomic Spectroscopy 62, 63-68.

Sparks Jr, C., Raman, S., Yakel, H., Gentry, R., Krause, M., 1977. Search with synchrotron radiation for superheavy elements in giant-halo inclusions. Physical Review Letters 38, 205.

Speziale, S., Zha, C.S., Duffy, T.S., Hemley, R.J., Mao, H.k., 2001. Quasi-hydrostatic compression of magnesium oxide to 52 GPa: Implications for the pressure-volume-temperature equation of state. Journal of Geophysical Research: Solid Earth 106, 515-528.

Srinivasan, B., 1976. Barites: anomalous xenon from spallation and neutron-induced reactions. Earth and Planetary Science Letters 31, 129-141.

Staudacher, T., 1987. Upper mantle origin for Harding County well gases. Nature 325, 605-607.

Staudacher, T., Allègre, C.J., 1982. Terrestrial xenology. Earth and Planetary Science Letters 60, 389-406.

Staudacher, T., Allègre, C.J., 1988. Recycling of oceanic crust and sediments: the noble gas subduction barrier. Earth and Planetary Science Letters 89, 173-183.

Staudacher, T., Allègre, C.J., 1989. Noble gases in glass samples from Tahiti: Teahitia, Rocard and Mehetia. Earth and planetary science letters 93, 210-222.

Staudacher, T., Kurz, M.D., Allègre, C.J., 1986. New noble-gas data on glass samples from Loihi Seamount and Hualalai and on dunite samples from Loihi and Reunion Island. Chemical Geology 56, 193-205.

Staudacher, T., Sarda, P., Allègre, C.J., 1990. Noble gas systematics of Réunion island, Indian Ocean. Chemical geology 89, 1-17.

Stavrou, E., Yao, Y., Goncharov, A.F., Lobanov, S.S., Zaug, J.M., Liu, H., Greenberg, E., Prakapenka, V.B., 2018. Synthesis of xenon and iron-nickel intermetallic compounds at Earth’s core thermodynamic conditions. Physical Review Letters 120, 096001.

Stevenson, D.J., 1987. Origin of the moon-The collision hypothesis. Annual review of earth and planetary sciences 15, 271-315.

Swindle, T., Caffee, M., Hohenberg, C., 1986. Xenon and other noble gases in shergottites. Geochimica et Cosmochimica Acta 50, 1001-1015.

Tatsumi, Y., 1989. Migration of fluid phases and genesis of basalt magmas in subduction zones. Journal of Geophysical Research: Solid Earth 94, 4697-4707.

Templeton, D.H., Zalkin, A., Forrester, J., Williamson, S.M., 1963. Crystal and molecular structure of xenon tetrafluoride. Journal of the American Chemical Society 85, 242-242.

Tolstikhin, I., O'Nions, R., 1994. The Earth's missing xenon: a combination of early degassing and of rare gas loss from the atmosphere. Chemical geology 115, 1-6.

Tonks, W.B., Melosh, H.J., 1993. Magma ocean formation due to giant impacts. Journal of Geophysical Research: Planets 98, 5319-5333.

Tribaudino, M., Angel, R.J., Cámara, F., Nestola, F., Pasqual, D., Margiolaki, I., 2010. Thermal expansion of plagioclase feldspars. Contributions to Mineralogy and Petrology 160, 899-908.

Trieloff, M., Kunz, J., Allègre, C.J., 2002. Noble gas systematics of the Réunion mantle plume source and the origin of primordial noble gases in Earth's mantle. Earth and Planetary Science Letters 200, 297-313.

Trieloff, M., Kunz, J., Clague, D.A., Harrison, D., Allègre, C.J., 2000. The nature of pristine noble gases in mantle plumes. Science 288, 1036-1038.

Trinquier, A., Birck, J.-L., Allegre, C.J., 2007. Widespread 54Cr heterogeneity in the inner solar system. The Astrophysical Journal 655, 1179.

Tucker, J.M., Mukhopadhyay, S., 2014. Evidence for multiple magma ocean outgassing and atmospheric loss episodes from mantle noble gases. Earth and Planetary Science Letters 393, 254-265.

Tucker, J.M., Mukhopadhyay, S., Schilling, J.-G., 2012. The heavy noble gas composition of the depleted MORB mantle (DMM) and its implications for the preservation of heterogeneities in the mantle. Earth and Planetary Science Letters 355, 244-254.

Turekian, K., 1959. The terrestrial economy of helium and argon. Geochimica et Cosmochimica Acta 17, 37-43.

Valbracht, P.J., Staudacher, T., Malahoff, A., Allègre, C.J., 1997. Noble gas systematics of deep rift zone glasses from Loihi Seamount, Hawaii. Earth and Planetary Science Letters 150, 399-411.

Vickery, A.M., Melosh, H.J., 1990. Atmospheric erosion and impactor retention in large impacts, with application to mass extinctions. Global catastrophes in Earth history 247, 289-300.

Villard P. Combination of argon with water. C R Hebd Seances Acad Sci. (1896) 123:377.

Wang, K., Lu, X., Liu, X., Zhou, M., Yin, K., 2022. Partitioning of noble gases (He, Ne, Ar, Kr, Xe) during Earth's core segregation: a possible core reservoir for primordial noble gases. Geochimica et Cosmochimica Acta.

Wang, Z., Becker, H., 2013. Ratios of S, Se and Te in the silicate Earth require a volatile-rich late veneer. Nature 499, 328-331.

Warren, P.H., 2011. Stable-isotopic anomalies and the accretionary assemblage of the Earth and Mars: A subordinate role for carbonaceous chondrites. Earth and Planetary Science Letters 311, 93-100.

Wetherill, G.W., 1985. Occurrence of giant impacts during the growth of the terrestrial planets. Science 228, 877-879.

Wetherill, G.W., 1990. Formation of the Earth. Annual Review of Earth and Planetary Sciences 18, 205-256.

Williams, C.D., Mukhopadhyay, S., 2019. Capture of nebular gases during Earth's accretion is preserved in deep-mantle neon. Nature 565, 78-81.

Wilke M, Appel K, Vincze L et al., 2010. A confocal set-up for micro-XRF and XAFS experiments using diamond-anvil cells. J. Synch. Rad. 17:669-675.

Wood, J.A., Dickey Jr, J.S., Marvin, U.B., Powell, B.N., 1970. Lunar anorthosites and a geophysical model of the moon. Geochimica et Cosmochimica Acta Supplement 1, 965.

Yamada, A., Wang, Y., Inoue, T., Yang, W., Park, C., Yu, T., Shen, G., 2011. High-pressure x-ray diffraction studies on the structure of liquid silicate using a Paris–Edinburgh type large volume press. Review of Scientific Instruments 82, 015103.

Yamaguchi, T., Fujimura, K., Uchi, K., Yoshida, K., Katayama, Y., 2012. Structure of water from ambient to 4 GPa revealed by energy-dispersive X-ray diffraction combined with empirical potential structure refinement modeling. Journal of Molecular Liquids 176, 44-51.

Yan, J., Doran, A., MacDowell, A., Kalkan, B., 2021. A tungsten external heater for BX90 diamond anvil cells with a range up to 1700 K. Review of Scientific Instruments 92, 013903.

Yin, Q., Jacobsen, S., Yamashita, K., Blichert-Toft, J., Télouk, P., Albarede, F., 2002. A short timescale for terrestrial planet formation from Hf–W chronometry of meteorites. Nature 418, 949-952.

Yokochi, R., Marty, B., 2004. A determination of the neon isotopic composition of the deep mantle. Earth and Planetary Science Letters 225, 77-88.

Zahnle, K.J., Gacesa, M., Catling, D.C., 2019. Strange messenger: A new history of hydrogen on Earth, as told by Xenon. Geochimica et Cosmochimica Acta 244, 56-85.

Zahnle, K.J., Kasting, J.F., Pollack, J.B., 1988. Evolution of a steam atmosphere during Earth's accretion. Icarus 74, 62-97.

Zha, C.-S., Mibe, K., Bassett, W.A., Tschauner, O., Mao, H.-K., Hemley, R.J., 2008. P-V-T equation of state of platinum to 80 GPa and 1900 K from internal resistive heating/x-ray diffraction measurements. Journal of Applied Physics 103, 054908.

Zhang, Y., Zindler, A., 1989. Noble gas constraints on the evolution of the Earth's atmosphere. Journal of Geophysical Research: Solid Earth 94, 13719-13737.

Zhu, L., Liu, H., Pickard, C.J., Zou, G., Ma, Y., 2014. Reactions of xenon with iron and nickel are predicted in the Earth's inner core. Nature chemistry 6, 644-648.

Appendix I/Summary of piston-cylinder runs

Experimental conditions for piston cylinder experiments.

Run	*P* (GPa)	*T* (°C)	Samples	Noble gases detected?
PC149	2.0	1500	$Ab_{80}An_{20}$ + Xe + 12wt% H_2O	NO
PC151	2.0	1500	$Ab_{80}An_{20}$ + Xe + 12wt% H_2O	NO
PC155	2.0	1500	$Ab_{80}An_{20}$ + Xe + 12wt% H_2O	NO
PC158	2.0	1500	Fo-Di-Q + Xe + H_2O	NO
PC159	1.8	1500	Fo-Di-Q + Xe + H_2O	NO
PC160	2.2	1500	$Ab_{80}An_{20}$ + Xe + 12wt% H_2O	NO
PC161	2.2	1500	$Ab_{80}An_{20}$ + Xe + 12wt% H_2O	NO
PC162	2.2	1500	$Ab_{80}An_{20}$ + Xe + 12wt% H_2O	YES
PC163	2.2	1500	Fo-Di-Q + Xe + H_2O	NO
PC164	2.2	1450	Fo-Di-Q + Xe + H_2O	YES
PC178	3.2	1450	Xe + lherzolite + H_2O	NO
PC182	3.2	1700	Xe + lherzolite	YES
PC183	2.2	1700	Xe + lherzolite	NO
PC185	2.2	1720	Xe + lherzolite	NO
PC186	2.2	1720	Xe + lherzolite	NO
PC187	2.2	1700	Xe + lherzolite	NO
PC188	2.2	1690	Xe + lherzolite	NO
PC193	2.2	1500	Basalt + Xe	NO
PC194	2.2	1500	Basalt + Xe	NO
PC195	2.2	1600	Basalt + Xe	NO
PC196	1.0	1650	K-Na fledspar + Xe	NO
PC197	1.1	1250	K-Na fledspar + basalt + Xe	YES
PC202	2.2	1610	Basalt + Xe	YES
PC203	1.6	1290	Labradorite + basalt glass+ Xe	NO

PC213	2.7	1600	Basalt + Kr	NO
PC214	2.7	1550	Basalt + Kr	NO
PC215	2.3	1550	Basalt + Kr	NO
PC216	2.3	1450	Basalt + Kr	NO
PC220	2.4	1240	Basalt + Xe	YES
PC221	2.3	1340	a: Basalt + Xe b: $Ab_{80}An_{20}$ + Kr	YES
PC222	2.7	1450	$Ab_{80}An_{20}$ + Kr	YES
PC223	3.3	1400	$Ab_{80}An_{20}$ + Kr	YES
PC228	2.8	1600	Basalt + Xe	YES
PC229	2.5	1650	Basalt + Xe	YES
PC230	2.3	1650	Basalt + Xe	NO
PC231	2.2	1600	Basalt + Xe	YES
PC232	2.2	1600	Basalt + Xe	YES
PC233	2.3	1600	Basalt + Xe	NO
PC234	1.7	1600	Lherzolite + Xe	YES
PC242	2.3	1500	$Ab_{80}An_{20}$ + Xe	YES
PC252	1.9	1600	a: PC234a b: PC234b	YES
PC256	1.9	1550	Basalt + Xe	YES
PC257	1.7	1250	a: Basalt + Xe b: PC256b	NO
PC258	1.7	1250	a: Basalt + Xe b: PC256b	NO
PC260	2.2	1500	Basalt + Xe	NO
PC261	2.2	1400	Basalt + Xe	NO
PC262	2.2	1300	Basalt + Xe	NO
PC263	2.2	1300	a: PC231a b: PC220b	NO
PC264	1.8	1000	Basalt + Xe	YES
PC265	1.3	1200	Basalt + Xe	YES

Ab is for albite; An for anorthite; Fo for forsterite; Di for diopside; Q for quartz.

Appendix II/Kr partition experiments

Here we introduce the attempts to carry out measurements on Kr distribution behaviour in crystal/melt system. Kr can only be measured from ex-situ experiments as Kr cannot be in-situ probed with XRF in diamond at high *P* (Kr Kα fluorescence rays is at ~12.65 keV, overlapped with strong diamond fluorescence signal). Thus several experiments were conducted in piston-cylinder press (cf, Appendix I) and analyzed with recovered samples. Unlike Xe mostly found inside crystals, recovered samples (PC222a and PC223) both show that Kr bubbles are located at the edges of the crystal (Fig. 1), with an extraordinary enrichment in the area of interaction of melt and crystals (Fig. 1b). This may indicate a very different environment for Xe and Kr incorporation with minerals. Our preliminary results suggest Kr cannot fit in Si-O tetrahedra of crystals by substitution of Si but store in the voids or defects due to a larger ionic radius of Kr-O (2.49 ± 0.1 Å) than that of oxidized Xe (2.10 ± 0.1 Å). The next step is to measure Kr concentration in both phases and determine the partition coefficients.

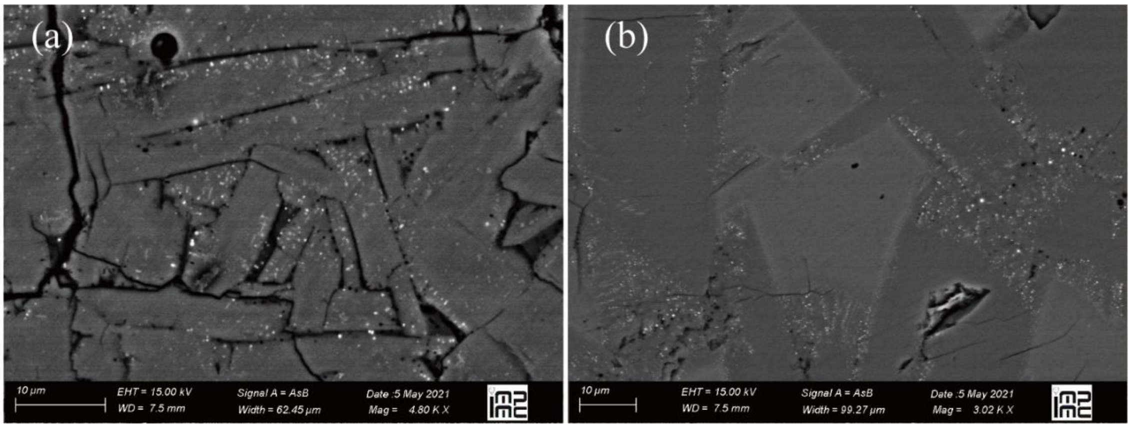

Fig. 1. SEM images for (a) PC222a; (b) PC223. Bright dots mainly existed at the edge of crystals are Kr bubbles.

Appendix III/EPMA analyses

EMPA of starting plagioclase samples.

n° of analysis	Sample	Na_2O	K_2O	FeO	CaO	MgO	SiO_2	Al_2O_3	Xe	total
1 / 1 .	$Ab_{80}An_{20}$	9.28	-0.02	0.05	4.46	0.00	62.99	25.23		101.99
2 / 1 .	$Ab_{80}An_{20}$	8.58	0.04	-0.06	4.46	0.00	63.14	25.42		101.58
3 / 1 .	$Ab_{80}An_{20}$	9.04	0.02	-0.03	4.41	0.01	63.21	25.08		101.74
4 / 1 .	$Ab_{80}An_{20}$	9.04	0.03	-0.12	4.44	0.01	63.49	24.82		101.71
6 / 1 .	$Ab_{80}An_{20}$	8.97	0.06	0.07	4.53	-0.01	62.83	25.37		101.82
7 / 1 .	$Ab_{80}An_{20}$	7.86	0.05	-0.06	4.36	-0.01	62.50	25.22		99.92
9 / 1 .	$Ab_{80}An_{20}$	8.11	0.03	-0.01	4.35	-0.02	62.40	26.09		100.95
10 / 1 .	$Ab_{80}An_{20}$	8.06	0.02	0.03	4.55	0.01	62.97	25.71		101.35
11 / 1 .	$Ab_{80}An_{20}$	8.89	0.00	0.02	4.51	0.01	62.82	25.81		102.06
12 / 1 .	$Ab_{80}An_{20}$	8.15	0.05	0.04	4.38	0.00	62.10	25.38		100.10
13 / 1 .	$Ab_{80}An_{20}$	8.37	0.03	0.03	4.61	0.00	62.76	25.28		101.08
14 / 1 .	$Ab_{80}An_{20}$	8.47	0.02	0.04	4.52	-0.01	62.17	25.32		100.53
15 / 1 .	$Ab_{80}An_{20}$	8.66	0.01	-0.06	4.39	-0.02	62.42	25.89		101.29
16 / 1 .	$Ab_{80}An_{20}$	8.72	0.02	-0.09	4.56	-0.01	62.81	25.29		101.30
18 / 1 .	$Ab_{80}An_{20}$	7.88	0.03	0.02	4.44	-0.02	65.30	25.31		102.96

EMPA of synthesized plagioclase samples.

n° of analysis	Sample	Na_2O	K_2O	FeO	CaO	MgO	SiO_2	Al_2O_3	Xe	total
39 / 1 .	PC162a	4.77	0.03	-0.06	3.73	0.06	58.18	22.01	0.16	88.88
40 / 1 .	PC162a	5.11	0.00	-0.02	3.79	0.03	59.55	23.16	0.16	91.78
41 / 1 .	PC162a	5.09	0.01	0.00	3.89	0.06	57.58	22.17	0.13	88.93
42 / 1 .	PC162a	4.68	0.04	-0.04	3.84	0.02	57.78	22.56	0.15	89.04

43 / 1 .	PC162a	4.81	0.03	0.00	3.76	0.06	58.03	22.08	0.13	88.90
44 / 1 .	PC162a	5.01	0.02	-0.04	3.67	0.00	57.44	21.94	0.16	88.20
45 / 1 .	PC162a	5.19	0.05	-0.03	3.89	0.04	58.79	22.46	0.12	90.51
46 / 1 .	PC162a	4.66	-0.01	0.04	3.38	0.02	53.07	20.27	0.13	81.56
47 / 1 .	PC162a	4.94	0.01	0.04	3.83	0.05	58.81	22.54	0.13	90.35
48 / 1 .	PC162a	4.78	0.00	-0.02	3.69	0.04	58.03	21.18	0.16	87.86
49 / 1 .	PC162a	5.08	0.04	0.04	3.67	0.06	57.83	22.21	0.16	89.09
50 / 1 .	PC162a	5.86	0.01	0.03	3.82	0.06	59.09	23.06	0.15	92.08
51 / 1 .	PC162a	5.02	0.01	-0.02	3.79	0.05	59.29	22.74	0.16	91.04
52 / 1 .	PC162a	4.95	0.03	0.02	3.70	0.04	58.80	22.06	0.15	89.75
53 / 1 .	PC162a	5.32	0.02	0.02	3.84	0.03	58.12	22.36	0.16	89.87
54 / 1 .	PC162a	4.94	0.03	-0.01	3.73	0.08	58.40	22.21	0.13	89.51
55 / 1 .	PC162a	5.23	0.06	0.01	3.95	0.09	58.98	22.75	0.13	91.20
56 / 1 .	PC162a	5.29	0.02	0.00	3.90	0.04	59.07	22.66	0.13	91.11
57 / 1 .	PC162a	5.00	0.02	0.03	3.68	0.05	58.25	22.18	0.16	89.37
58 / 1 .	PC162a	4.96	0.03	0.00	3.84	0.05	59.80	22.92	0.16	91.76
59 / 1 .	PC162a	4.98	0.05	0.03	3.93	0.04	59.85	20.58	0.14	89.60
60 / 1 .	PC162a	5.05	0.09	0.03	3.95	0.04	58.18	22.01	0.15	89.50
61 / 1 .	PC162a	5.21	0.02	0.03	3.72	0.05	59.13	22.85	0.16	91.17

62 / 1 .	PC162b	4.23	0.05	-0.02	3.21	1.07	55.27	20.53	0.01	84.35
63 / 1 .	PC162b	4.63	0.11	-0.12	3.21	0.99	55.64	19.71	0.02	84.19
64 / 1 .	PC162b	4.93	0.03	0.07	3.62	1.13	56.61	20.53	0.02	86.94
65 / 1 .	PC162b	4.91	0.06	0.11	3.53	1.11	56.24	20.55	0.02	86.53
66 / 1 .	PC162b	4.54	0.12	0.03	3.45	1.09	54.52	20.10	0.01	83.86
67 / 1 .	PC162b	5.17	0.05	-0.04	3.29	1.16	55.47	20.11	0.03	85.24

68 / 1 .	PC162b	4.65	0.06	-0.04	3.22	1.05	53.42	20.15	0.03	82.54
69 / 1 .	PC162b	5.44	0.07	-0.07	3.53	1.10	57.04	20.82	0.00	87.93
70 / 1 .	PC162b	5.46	0.04	0.01	3.58	1.13	56.12	20.80	0.03	87.17
72 / 1 .	PC162b	5.24	0.04	-0.06	3.25	1.04	57.20	20.12	0.03	86.86
73 / 1 .	PC162b	4.76	0.06	-0.01	3.40	1.00	56.06	21.03	0.01	86.31
74 / 1 .	PC162b	4.85	0.05	0.11	3.54	1.07	56.90	20.47	0.03	87.02
75 / 1 .	PC162b	4.69	0.05	0.15	3.09	1.05	55.94	20.12	0.02	85.11
76 / 1 .	PC162b	4.75	0.02	-0.10	3.32	1.18	57.21	20.58	0.02	86.98
77 / 1 .	PC162b	4.86	0.08	0.06	3.43	1.19	56.76	20.11	0.01	86.50
78 / 1 .	PC162b	4.98	0.06	0.03	3.54	1.21	58.11	20.88	0.03	88.84

EMPA of recovered plagioclase samples from in-situ experiments.

n° of analysis	Sample	Na_2O	K_2O	FeO	CaO	MgO	SiO_2	Al_2O_3	Xe	total
230 / 1 .	Cell5melt	4.85	0.06	0.01	4.79	0.07	65.29	24.38	0.15	99.60
231 / 1 .	Cell5melt	6.78	0.03	-0.01	4.49	0.04	63.50	24.18	0.12	99.13
232 / 1 .	Cell5melt	7.86	0.04	0.00	4.27	0.05	62.88	24.01	0.16	99.27
233 / 1 .	Cell5melt	8.04	-0.03	-0.14	4.35	0.10	62.29	24.16	0.16	98.93
234 / 1 .	Cell5melt	8.06	0.12	-0.06	4.75	0.09	62.88	23.26	0.13	99.23
235 / 1 .	Cell5melt	8.07	0.08	0.03	4.32	0.09	63.49	23.66	0.16	99.90
236 / 1 .	Cell5melt	7.41	0.07	-0.01	4.49	0.06	62.37	23.04	0.15	97.58
237 / 1 .	Cell5melt	8.30	0.07	-0.06	4.70	0.05	63.58	24.15	0.16	100.95
238 / 1 .	Cell5melt	7.31	0.04	-0.05	4.32	0.06	63.65	24.79	0.15	100.27
239 / 1 .	Cell5melt	6.08	-0.02	-0.04	4.49	0.03	64.69	24.77	0.14	100.14
48 / 1 .	HH355melt	5.19	0.16	0.01	1.30	0.02	68.72	15.55		90.95
49 / 1 .	HH355melt	5.24	0.26	-0.03	0.99	-0.01	64.68	13.99		85.12

50 / 1 .	HH355melt	5.04	0.31	-0.08	1.27	0.02	64.55	13.28		84.39
51 / 1 .	HH355melt	4.77	0.31	-0.01	1.07	-0.01	66.86	15.07		88.06
52 / 1 .	HH355melt	4.44	0.32	0.04	1.40	0.01	69.28	15.43		90.92
53 / 1 .	HH355melt	4.06	0.43	0.02	1.38	0.02	70.23	15.49		91.63
54 / 1 .	HH355melt	5.31	0.34	0.05	1.28	0.02	67.02	15.09		89.11
56 / 1 .	HH355melt	4.34	0.21	-0.01	1.17	0.00	63.55	14.02		83.28
57 / 1 .	HH355melt	5.80	0.32	0.05	1.11	0.00	67.68	14.83		89.79
58 / 1 .	HH355melt	5.02	0.23	-0.11	1.32	0.02	64.64	15.05		86.17
59 / 1 .	HH355melt	4.89	0.32	0.01	1.28	0.02	66.44	15.07		88.03
60 / 1 .	HH355melt	3.67	0.22	-0.01	1.23	0.04	68.09	14.81		88.05
61 / 1 .	HH355melt	5.11	0.19	-0.01	1.11	0.01	66.70	14.78		87.89
62 / 1 .	HH355crystal	8.52	-0.02	-0.05	10.78	3.79	54.40	25.76		103.18
63 / 1 .	HH355crystal	8.84	-0.01	-0.01	9.76	2.87	53.37	26.79		101.61
64 / 1 .	HH355crystal	7.02	-0.02	-0.03	13.67	5.85	52.69	23.60		102.78
65 / 1 .	HH355crystal	12.21	-0.05	-0.08	3.52	0.55	57.54	26.46		100.15
66 / 1 .	HH355crystal	9.52	-0.04	0.01	8.73	3.02	53.91	24.24		99.39
67 / 1 .	HH355crystal	6.62	0.02	-0.02	11.36	5.14	51.94	23.32		98.38
68 / 1 .	HH355crystal	7.03	-0.01	0.01	13.61	6.08	52.18	22.01		100.91
69 / 1 .	HH355crystal	6.88	-0.01	-0.02	13.57	6.35	51.87	21.62		100.26
70 / 1 .	HH355crystal	8.91	0.02	0.08	9.72	4.02	54.58	23.35		100.68
71 / 1 .	HH355crystal	12.14	0.00	0.07	4.89	1.48	58.98	24.88		102.44
72 / 1 .	HH355crystal	7.74	0.00	0.03	12.27	4.94	52.91	23.31		101.2
73 / 1 .	HH355crystal	7.40	-0.03	0.05	12.62	5.43	52.40	22.43		100.3
74 / 1 .	HH355crystal	6.84	-0.01	-0.04	14.37	6.88	52.84	21.09		101.97

11 / 1 .	HH357melt	5.44	0.23	-0.02	2.53	0.97	58.46	18.07	85.68
12 / 1 .	HH357melt	9.20	0.19	0.01	2.39	0.95	59.53	17.63	89.9
13 / 1 .	HH357melt	9.28	0.20	-0.01	2.25	0.81	59.63	17.21	89.37
14 / 1 .	HH357melt	6.69	0.19	0.00	2.55	1.05	61.51	18.23	90.22
15 / 1 .	HH357melt	7.81	0.22	-0.02	2.28	1.19	60.10	17.64	89.22
16 / 1 .	HH357melt	7.96	0.21	-0.08	2.35	1.23	60.40	17.34	89.41
17 / 1 .	HH357melt	7.82	0.23	0.08	2.38	1.05	59.98	17.68	89.22
18 / 1 .	HH357melt	7.48	0.22	-0.04	2.49	0.92	60.81	16.46	88.34
19 / 1 .	HH357melt	7.48	0.29	0.00	2.38	1.12	57.88	17.20	86.35
20 / 1 .	HH357melt	9.22	0.23	0.00	2.49	1.05	59.02	17.08	89.09
21 / 1 .	HH357melt	7.85	0.17	0.08	2.50	1.03	60.59	17.69	89.91
22 / 1 .	HH357melt	7.66	0.26	0.02	2.40	1.18	60.13	17.70	89.35
23 / 1 .	HH357melt	7.44	0.25	0.03	2.60	0.92	61.42	18.18	90.84
24 / 1 .	HH357melt	7.32	0.20	0.14	2.61	1.19	60.56	17.65	89.67
25 / 1 .	HH357melt	6.93	0.25	-0.01	2.50	0.73	60.50	17.55	88.45
26 / 1 .	HH357melt	7.93	0.24	-0.03	2.65	0.88	60.73	17.06	89.46
27 / 1 .	HH357crystal	6.09	0.01	0.05	14.09	9.29	55.58	17.94	103.05
28 / 1 .	HH357crystal	7.07	0.00	-0.08	13.05	8.45	55.39	17.80	101.68
29 / 1 .	HH357crystal	6.36	0.05	0.02	13.43	8.40	56.01	17.94	102.21
30 / 1 .	HH357crystal	6.53	0.04	0.06	14.00	8.65	55.37	18.52	103.17
31 / 1 .	HH357crystal	7.96	0.00	0.12	12.23	7.18	56.67	19.33	103.49
32 / 1 .	HH357crystal	5.90	0.03	0.08	14.72	9.11	55.22	18.58	103.64
33 / 1 .	HH357crystal	5.49	-0.03	0.12	15.74	9.29	53.87	18.41	102.89
35 / 1 .	HH357crystal	6.43	-0.01	-0.03	13.50	8.90	55.94	17.91	102.64
36 / 1 .	HH357crystal	7.92	0.01	-0.08	12.25	8.00	56.54	18.56	103.2
37 / 1 .	HH357crystal	7.39	0.02	0.02	12.96	8.35	56.32	17.47	102.53

39 / 1 .	HH357crystal	8.64	0.00	0.00	10.80	6.65	56.61	20.96		103.66
40 / 1 .	HH357crystal	5.86	0.00	-0.07	14.90	8.91	54.92	18.95		103.47
41 / 1 .	HH357crystal	7.88	-0.03	0.00	11.87	7.19	56.77	20.11		103.79
42 / 1 .	HH357crystal	5.78	-0.04	0.03	14.54	8.62	52.73	18.31		99.97
43 / 1 .	HH357crystal	6.83	0.03	0.08	13.66	8.57	55.56	17.83		102.56

EMPA of synthesized basaltic samples from piston-cylinder runs.

n° of analysis	Sample	Na_2O	K_2O	FeO	CaO	MgO	SiO_2	Al_2O_3	Xe	total
45 / 1 .	PC197melt	1.18	0.91	8.83	12.10	8.51	49.46	19.10		100.09
46 / 1 .	PC197melt	1.06	1.05	9.36	11.70	8.40	49.87	19.45		100.89
47 / 1 .	PC197melt	1.04	0.89	9.76	11.81	8.58	49.21	18.98		100.27
48 / 1 .	PC197melt	1.11	1.04	9.85	12.13	8.55	49.67	19.41		101.76
49 / 1 .	PC197melt	1.01	0.94	9.61	11.85	8.39	50.59	18.81		101.2
50 / 1 .	PC197melt	1.15	0.94	9.73	11.91	8.52	50.54	19.12		101.91
51 / 1 .	PC197melt	1.11	1.01	9.09	12.02	8.44	51.05	19.33		102.05
52 / 1 .	PC197melt	1.15	0.93	9.60	11.60	8.30	50.57	18.74		100.89
53 / 1 .	PC197melt	1.00	1.13	9.59	11.84	8.48	49.87	19.29		101.2
54 / 1 .	PC197melt	1.20	1.05	9.99	11.93	8.34	50.31	19.26		102.08
55 / 1 .	PC197melt	1.12	0.91	9.21	11.62	8.40	49.77	19.28		100.31
56 / 1 .	PC197melt	1.08	0.94	9.55	11.90	8.56	50.44	18.49		100.96
57 / 1 .	PC197melt	1.15	0.79	9.50	11.64	8.33	49.54	18.93		99.88
58 / 1 .	PC197melt	1.13	1.02	9.87	11.18	8.81	49.93	18.83		103.07
36 / 1 .	PC197crystal	1.13	0.19	1.52	17.16	0.61	46.40	32.31		99.32
37 / 1 .	PC197crystal	1.02	0.33	5.41	9.93	13.81	50.77	21.46		102.73
45 / 1 .	PC256crystal	0.00	0.02	8.09	0.36	50.38	41.45	0.10		100.4
46 / 1 .	PC256crystal	-0.01	0.02	10.59	0.35	49.78	41.76	0.13		102.62

47 / 1 .	PC256crystal	0.03	-0.02	10.22	0.26	50.15	42.25	0.12		103.01
48 / 1 .	PC256crystal	0.02	0.01	10.03	0.31	49.49	42.42	0.05		102.33
49 / 1 .	PC256crystal	-0.01	0.01	10.23	0.32	50.68	42.55	0.11		103.89
50 / 1 .	PC256crystal	-0.01	0.03	7.82	0.45	51.55	42.54	0.13		102.51
51 / 1 .	PC256crystal	0.03	-0.02	8.32	0.27	51.59	42.01	0.13		102.33
52 / 1 .	PC256crystal	-0.02	-0.01	8.91	0.30	49.87	41.42	0.06		100.53
53 / 1 .	PC256crystal	0.05	-0.03	8.98	0.32	49.66	42.17	0.11		101.26
11 / 1 .	PC256melt	0.16	-0.02	4.29	13.65	11.37	48.66	21.36		99.47
12 / 1 .	PC256melt	0.20	0.03	3.42	13.95	11.17	48.25	21.59		98.61

EMPA of recovered basaltic samples from in-situ experiments.

n° of analysis	Sample	Na_2O	K_2O	FeO	CaO	MgO	SiO_2	Al_2O_3	Xe	total
44 / 1 .	HPT2melt	0.08	-0.01	5.20	15.67	13.20	49.40	18.94		102.48
45 / 1 .	HPT2melt	0.07	0.04	4.84	15.26	13.07	48.78	18.81		100.87
46 / 1 .	HPT2melt	0.03	0.03	4.32	15.02	12.97	49.23	19.08		100.68
47 / 1 .	HPT2melt	0.11	0.07	4.81	15.16	12.42	47.53	17.75		97.85
48 / 1 .	HPT2melt	0.14	0.01	5.00	15.17	12.96	49.10	19.15		101.53
49 / 1 .	HPT2melt	0.13	0.06	4.99	15.26	13.10	49.18	19.27		101.99
50 / 1 .	HPT2melt	0.11	-0.02	4.94	15.07	13.00	49.65	18.86		101.61
51 / 1 .	HPT2melt	0.05	0.00	4.81	14.97	13.00	49.65	18.78		101.26
52 / 1 .	HPT2melt	0.09	-0.05	4.85	15.06	13.16	49.05	18.32		100.48
53 / 1 .	HPT2melt	0.12	0.02	5.07	15.31	13.30	48.79	18.84		101.45
54 / 1 .	HPT2melt	0.08	0.02	4.90	15.55	13.17	49.49	19.10		102.31
55 / 1 .	HPT2melt	0.13	0.00	5.19	15.34	13.10	49.72	18.90		102.38
56 / 1 .	HPT2melt	0.08	-0.03	4.97	15.14	12.77	48.39	18.54		99.86
57 / 1 .	HPT2melt	0.09	0.04	4.91	15.43	13.26	48.45	18.79		100.97

58 / 1 .	HPT2melt	0.07	0.00	4.87	14.97	12.94	48.59	18.89	100.33
59 / 1 .	HPT2melt	0.07	0.05	4.83	15.48	13.43	48.42	18.78	101.06
60 / 1 .	HPT2melt	0.07	-0.01	4.86	15.61	13.19	48.47	18.97	101.16
61 / 1 .	HPT2melt	0.07	0.02	4.81	15.43	12.91	49.96	18.69	101.89
62 / 1 .	HPT2melt	0.09	0.04	4.98	15.29	12.84	48.81	18.94	100.99
63 / 1 .	HPT2melt	0.10	-0.06	4.78	15.75	13.10	49.08	18.35	101.1
64 / 1 .	HPT2melt	0.09	0.02	4.74	14.78	12.96	49.57	18.72	100.88
65 / 1 .	HPT2melt	0.01	-0.02	5.02	15.25	13.05	49.51	19.10	101.92
66 / 1 .	HPT2melt	0.09	0.04	4.81	15.28	13.68	48.62	18.61	101.13
67 / 1 .	HPT2melt	0.10	0.03	4.85	15.26	13.24	49.09	18.35	100.92
68 / 1 .	HPT2melt	0.12	0.00	4.67	15.92	13.16	49.56	18.34	101.77
69 / 1 .	HPT2melt	0.12	0.03	4.59	15.02	12.66	49.65	18.59	100.66
70 / 1 .	HPT2melt	0.08	0.01	4.54	14.86	12.43	47.34	17.84	97.1
71 / 1 .	HPT2crystal	0.02	-0.01	8.89	0.39	52.12	42.30	0.00	103.71
72 / 1 .	HPT2crystal	0.02	-0.01	8.06	0.33	52.09	42.84	0.09	103.42
73 / 1 .	HPT2crystal	0.00	0.00	9.43	0.31	51.02	42.37	0.05	103.18
75 / 1 .	HPT2crystal	-0.03	0.01	8.84	0.32	52.53	41.75	0.03	103.45
76 / 1 .	HPT2crystal	0.01	0.05	8.32	0.38	52.44	42.42	0.11	103.73
77 / 1 .	HPT2crystal	-0.01	-0.03	8.17	0.28	51.76	41.86	0.21	102.24
78 / 1 .	HPT2crystal	-0.02	0.01	7.73	0.40	51.14	43.00	0.09	102.35
79 / 1 .	HPT2crystal	0.00	0.03	8.57	0.35	52.49	42.08	0.10	103.62
80 / 1 .	HPT2crystal	-0.05	-0.01	7.92	0.39	52.57	41.73	0.03	102.58
81 / 1 .	HPT2crystal	-0.01	0.00	7.93	0.22	51.80	42.55	0.14	102.63
82 / 1 .	HPT2crystal	-0.04	0.00	8.49	0.35	51.38	42.56	0.11	102.85
83 / 1 .	HPT2crystal	-0.02	0.02	8.48	0.36	51.89	42.28	0.06	103.07
84 / 1 .	HPT2crystal	0.03	0.01	7.68	0.34	52.43	42.16	0.06	102.71

99 / 1 .	HPT1melt	2.25	1.72	1.45	9.56	4.74	55.67	23.86	99.25
100 / 1 .	HPT1melt	2.27	1.83	1.32	9.84	4.59	55.62	24.13	99.60
101 / 1 .	HPT1melt	2.06	1.72	1.45	9.94	4.67	55.69	23.92	99.45
102 / 1 .	HPT1melt	2.14	1.79	1.41	9.61	4.70	55.66	23.88	99.19
103 / 1 .	HPT1melt	2.31	1.81	1.24	10.07	4.63	54.74	23.69	98.49
104 / 1 .	HPT1melt	2.21	1.92	1.35	9.53	4.72	56.01	23.66	99.40
105 / 1 .	HPT1melt	2.10	1.89	1.32	10.05	4.81	55.26	23.44	98.87
106 / 1 .	HPT1melt	2.23	1.78	1.24	9.86	4.81	56.20	23.54	99.66
107 / 1 .	HPT1melt	1.98	1.53	1.07	10.87	5.65	55.11	23.34	99.55
108 / 1 .	HPT1melt	1.95	1.66	1.28	10.61	5.50	54.99	23.33	99.32
109 / 1 .	HPT1melt	2.03	1.52	1.19	10.39	5.36	54.87	22.67	98.03
110 / 1 .	HPT1melt	2.02	1.55	1.28	10.41	5.34	55.06	22.89	98.55
111 / 1 .	HPT1melt	1.96	1.51	1.02	10.05	5.10	54.59	22.89	97.12
112 / 1 .	HPT1melt	2.11	1.66	1.17	10.52	5.03	55.05	23.30	98.84
113 / 1 .	HPT1melt	2.21	1.66	1.33	10.06	4.72	56.29	23.42	99.69
114 / 1 .	HPT1melt	2.00	1.54	1.06	10.35	4.80	55.94	23.82	99.51
115 / 1 .	HPT1melt	2.06	1.63	1.19	10.25	5.08	54.23	23.66	98.10
116 / 1 .	HPT1melt	1.94	1.60	1.12	10.34	5.13	54.93	23.06	98.12
117 / 1 .	HPT1melt	2.24	1.92	1.14	9.34	4.41	55.95	22.93	97.93
118 / 1 .	HPT1melt	2.09	1.92	1.36	9.98	4.63	55.89	22.93	98.8
121 / 1 .	HPT1melt	2.25	1.76	1.15	9.56	4.55	56.00	23.09	98.36
122 / 1 .	HPT1melt	2.26	1.89	1.37	9.36	4.31	56.06	22.93	98.18
123 / 1 .	HPT1melt	2.19	1.80	1.40	9.43	4.16	55.87	23.64	98.49
124 / 1 .	HPT1melt	2.27	1.86	1.41	9.87	4.14	55.96	23.80	99.31
125 / 1 .	HPT1crystal	0.24	0.06	2.13	15.49	18.76	49.18	16.58	102.44

126 / 1 .	HPT1crystal	0.30	0.02	2.31	17.75	17.72	49.59	16.18	103.87
127 / 1 .	HPT1crystal	0.31	0.02	1.72	20.04	14.92	48.54	17.11	102.66
128 / 1 .	HPT1crystal	0.27	0.02	1.68	20.96	14.02	47.36	18.72	103.03
130 / 1 .	HPT1crystal	0.27	0.02	1.74	18.42	16.14	48.89	16.66	102.14
131 / 1 .	HPT1crystal	0.27	-0.03	2.01	17.71	17.00	49.02	15.90	101.88
132 / 1 .	HPT1crystal	0.42	0.22	1.82	19.11	15.06	49.78	16.67	103.08
133 / 1 .	HPT1crystal	0.18	0.05	2.29	17.19	17.71	49.22	16.58	103.22
134 / 1 .	HPT1crystal	0.18	0.05	2.56	14.22	20.81	50.68	14.86	103.36
135 / 1 .	HPT1crystal	0.27	0.03	1.95	18.85	15.71	48.29	17.14	102.24
136 / 1 .	HPT1crystal	0.21	0.03	1.89	18.22	17.09	48.82	15.89	102.15
137 / 1 .	HPT1crystal	0.57	0.34	2.02	16.51	15.81	50.80	17.27	103.32
138 / 1 .	HPT1crystal	0.26	0.00	2.03	17.87	17.72	48.84	15.79	102.51
139 / 1 .	HPT1crystal	0.35	0.23	2.22	16.80	16.21	50.37	16.37	102.55
140 / 1 .	HPT1crystal	0.28	0.05	1.85	20.61	14.83	48.03	16.82	102.47
141 / 1 .	HPT1crystal	0.28	0.11	2.22	17.72	17.21	49.56	15.79	102.89
142 / 1 .	HPT1crystal	0.26	0.02	2.15	18.82	16.37	49.16	16.91	103.69
144 / 1 .	HPT1crystal	0.19	0.08	2.41	16.73	18.44	49.02	14.97	101.84
145 / 1 .	HPT1crystal	0.15	0.06	2.49	15.47	19.57	49.49	15.51	102.74
146 / 1 .	HPT1crystal	0.20	0.02	2.64	13.32	21.45	50.66	14.63	102.92
147 / 1 .	HPT1crystal	0.25	-0.01	1.19	21.59	14.92	49.05	16.06	103.05
148 / 1 .	HPT1crystal	0.29	0.03	1.38	19.87	16.08	49.22	15.34	102.21
149 / 1 .	HPT1crystal	0.31	0.05	0.95	21.96	13.86	48.66	15.95	101.74
150 / 1 .	HPT1crystal	0.26	0.00	1.60	18.94	16.68	50.22	15.50	103.2
151 / 1 .	HPT1crystal	0.40	0.12	2.19	16.42	16.58	50.40	16.87	102.98
152 / 1 .	HPT1crystal	0.26	0.00	2.60	14.71	20.11	49.82	15.21	102.71
153 / 1 .	HPT1crystal	0.21	0.01	2.35	14.47	20.26	50.13	15.69	103.12

154 / 1 .	HPT1crystal	0.28	0.02	1.82	18.82	16.96	49.58	14.85		102.33

Appendix IV/Image plates for X-ray diffraction

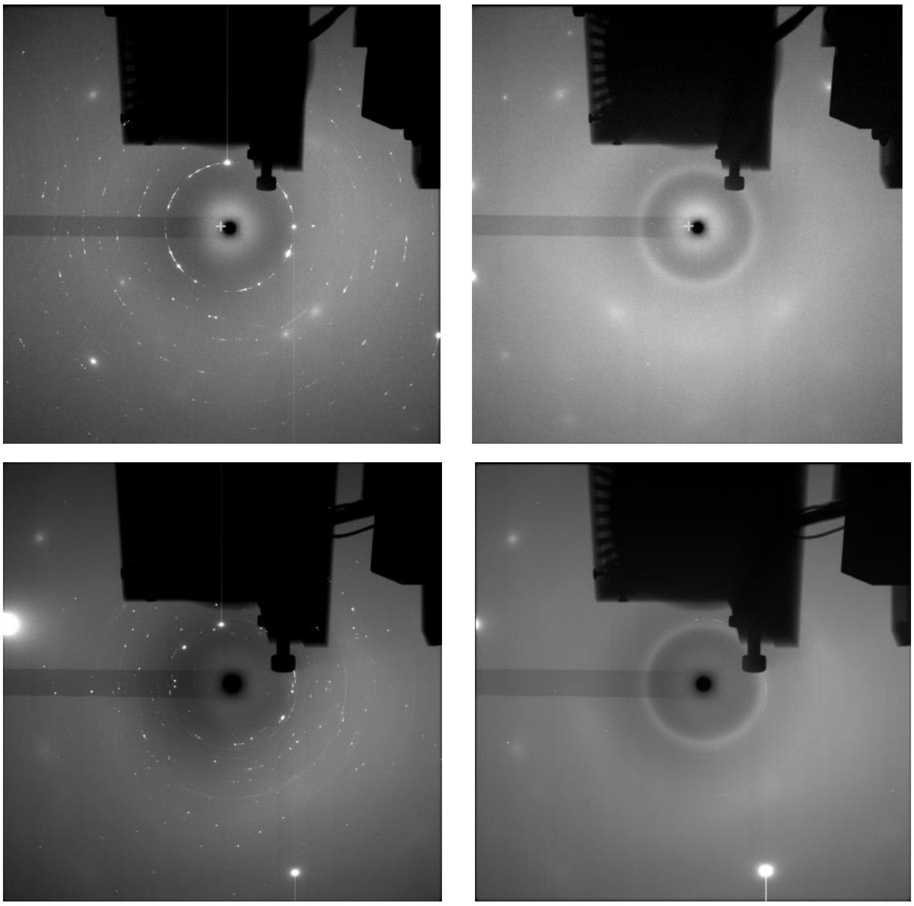

Image plate for run Cell6 of plain H_2O at 6.1 GPa and 25 ºC (top left), at 3.5 GPa and 490 ºC (top right), and for Cell7 of Xe-bearing H_2O at 1.2 GPa and 25 ºC (bottom left), at 1.5 GPa and 300 ºC (bottom right).

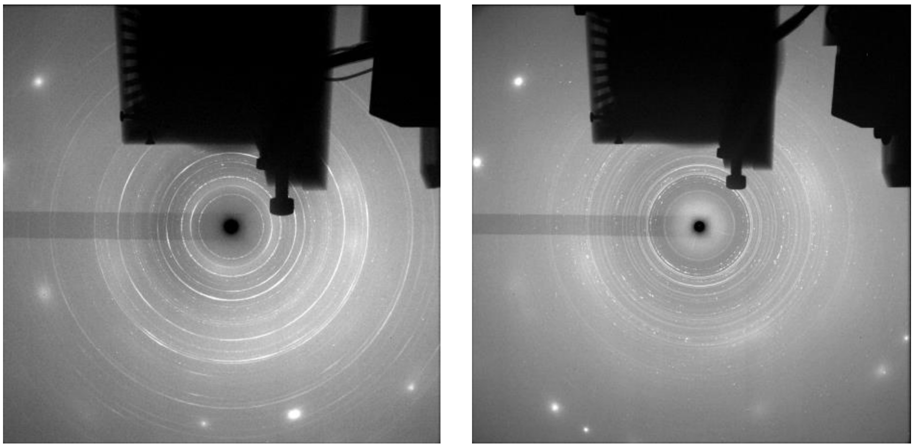

Image plate for run Cell5 of Xe-bearing plagioclase at 2.0 GPa and 1010 ºC (left), and for Cell3 of Xe-bearing jadeite+quartz at 3.0 GPa and 650 ºC (left).